The Influences of Strain Rate on Mechanical Properties and Deformation Mechanisms of High-Mn and Medium-Mn TWIP-TRIP Steels

By

Jake Tyler Benzing

Dissertation

Submitted to the Faculty of the

Graduate School of Vanderbilt University

in partial fulfillment of the requirements

for the degree of

DOCTOR OF PHILOSOPHY

in

Interdisciplinary Materials Science

May 11, 2018

Nashville, Tennessee

Approved:

James Wittig, Ph.D.

Greg Walker, Ph.D.

James Bentley, Ph.D.

Çağlar Oskay, Ph.D.

Ashok Choudhury, Ph.D.

ACKNOWLEDGEMENTS

This work was supported by the US National Science Foundation, Division of Materials Research under grant DMR1309258, NSF EPS 1004083, the Max-Planck-Institut für Eisenforschung, Düsseldorf, the Center for Electron Microscopy and AnalysiS at The Ohio State University, the Advanced Steel Processing and Products Research Center at Colorado School of Mines and the National Institute of Standards and Technology in Gaithersburg, MD. Work at the Molecular Foundry was supported by the Office of Science, Office of Basic Energy Sciences, of the U.S. Department of Energy under Contract No. DE-AC02-05CH11231. Work at Oak Ridge National Laboratory was supported by a Center for Nanophase Materials Science proposal (CNMS2014-291).

This research is the result of many collaborations and would not be possible without the support and guidance from many people. I am extremely grateful for the valuable guidance and direction from my advisor, Prof. James Wittig, who patiently instructed me on advanced characterization techniques, introduced me to German culture and pushed me to become a better scientist. I am also grateful for the extensive hands-on TEM instruction and guidance provided by Prof. James Bentley throughout my graduate research experiences. I would like to thank Prof. Çağlar Oskay for giving me the opportunity to gain experience with constitutive modeling, Prof. Greg Walker for generously providing an infra-red camera for my research at Colorado School of Mines and Prof. Ashok Choudhury for always providing new perspectives on how my graduate experience and research relates to the grand scheme. I am very grateful for the research directions and excellent mentoring from Dr. Dean Pierce, who helped pave the way for my Ph.D. research.

I would like to thank Prof. Dierk Raabe for the continued support, as well as the insightful guidance during my summers at the Max-Planck-Institut für Eisenforschung, Düsseldorf. I am especially grateful for fruitful conversations with Dr. Dirk Ponge during alloy design of a medium-Mn steel and for providing thermodynamic predictions. Many thanks are given to Angelika Bobrowski and Katja Angenendt for instruction on TEM and SEM sample preparation and respective instrumentation practices. I would like to thank Dr. Baptiste Gault, Dr. Lutz Morsdorf and Alisson Kwiatkowski da Silva for the atom probe tomography work and Prof. Jeongho Han for providing the medium-Mn material. Aniruddha Dutta is gratefully acknowledged for work with the dilatometer and help with X-ray diffraction. In addition to the previous MPIE colleagues mentioned, Dr. Mathias Millitzer, Dr, Ania Koprek, Dr. Christian Baron, Dr. Andrew Breen, Dr. Torsten Schwarz, Dr. Phillip Kurnsteiner, Dr. Won Seok, Avinash Hariharan and Zhuangming Li are just some of the many colleagues that I had the pleasure of working with at the MPIE. Not only did my colleagues at the MPIE make me feel extremely welcome during every summer (in a country foreign to me), but they also introduced me to their individual cultures and for that I am eternally grateful.

I would also like to thank Prof. Mike Mills, Prof. Glenn Daehn, Dr. Tim Smith, Dr. Lee Casalena, Dr. Jason Johnson and Geoff Taber at The Ohio State University who not only gave me the opportunity to work in their labs as an undergraduate research assistant, but gave me the courage and support to apply to graduate school and pursue my doctoral degree. I will never forget all of the great experiences from The Ohio State University, during both undergraduate and graduate research experiences. I would not be in this position if not for your help along every step of the way. I would also like to thank Prof. Kip Findley and Dr. Whitney Poling for their support with mechanical testing at Colorado School of Mines (during multiple visits) and for continued academic instruction in the area of advanced high strength steels as our work led to the first peer-reviewed journal publication from my Ph.D. research. I really can't thank you both enough. Special thanks to Oscar Terrazas and Sean Mills for letting me stay at their apartments while visiting CSM. You are both true friends.

Special thanks to Jim Ciston and Colin Ophus at NCEM for providing fantastic atomic resolution images as well as to Alex Belianinov for the fantastic image processing software to further characterize atomic columns. These results still continue to amaze me. Many thanks to Prof. Guil Gualda for letting me use the SEM with EBSD in the Geology lab at Vanderbilt, which allowed for many opportunities to independently use the technique on a different platform. Thanks to James McBride for always being patient with me on the TEM at Vanderbilt and for always being available when I needed help the most (when instrumentation and operation does not agree). I am also very grateful for the extensive mechanical testing completed by Dr. Bill Luecke and Dr. Steve Mates at NIST in Gaithersburg. Your hard work and continued patience gave me the chance to gather and analyze results that were essential for completing this dissertation. Thank you so much.

Everyone in the BioPhotonics Center at Vanderbilt is gratefully acknowledged for welcoming me into your group, laughing at my jokes, providing excellent company throughout my graduate career during long hours in the office and most importantly inviting me to Fluids Lab. You are all very kind and accepting people who will always remain my friends. Thank you for everything that you do day in and day out. It is an honor to have a cubicle in your building.

I need to express extra thanks to my family for always believing in me and supporting me throughout my life and all of the obstacles I've encountered along the way. I would truly not be here today without you and I am truly grateful for the unconditional love and support.

Finally, I would like to express my whole-hearted love to my girlfriend Megan. I can't thank you enough for your empathetic understanding, continued patience and steadfast support throughout the past three years.

TABLE OF CONTENTS

Page

Chapter

LIST OF TABLES

Table Page

LIST OF FIGURES

ACRONYMS

(AHSS)	advanced high strength steels
(TWIP)	twinning-induced plasticity
(TRIP)	transformation-induced plasticity
(SFE)	stacking fault energy
(FCC)	face centered cubic
(BCC)	body centered cubic
(HCP)	hexagonal close packed
(DSA)	dynamic strain aging
(HR)	high resolution
(TEM)	transmission electron microscopy
(STEM)	scanning transmission electron microscopy
(EDS)	energy dispersive spectroscopy
(BF-TEM)	bright-field TEM
(DF-TEM)	dark-field TEM
(SAED)	selected area electron diffraction
(CBED)	convergent beam electron diffraction
(HAADF)	high angle annular dark field
(PCA)	principal component analysis
(SEM)	scanning electron microscopy
(EBSD)	electron backscatter diffraction
(KAM)	kernel average misorientation
(IPF)	inverse pole figure
(ECCI)	electron channeling contrast imaging
(UFG)	ultrafine-grained
(XRD)	X-ray diffraction
(APT)	atom probe tomography
(DIC)	digital image correlation
(UE)	uniform elongation
(TE)	total elongation
(YS)	yield strength
(UTS)	ultimate tensile strength
(PSE)	product of strength and elongation
(AFM)	anti-ferro magnetic
(PM)	paramagnetic
(DM)	delocalized moment
(LE)	local equilibrium
(CPFE)	crystal plasticity finite element

CHAPTER 1

1. INTRODUCTION

Within the past few decades, advanced high strength steels (AHSS) have been incorporated into automotive vehicles to reduce their weight and improve the strength of structural components [1][2][3]. More stringent fuel economy standards and crash safety tests continue to drive the implementation and evolution of AHSS. The U.S. Environmental Protection Agency and the National Highway Traffic Safety Administration requires a fleet wide fuel economy average of 54.5 mpg by 2025, (including passenger cars and light trucks) [4]. The Insurance Institute for Highway Safety continues to develop more rigorous new crash safety tests, such as the small overlap frontal crash test implemented in 2012 [5]. The new small overlap frontal crash test raises challenging alloy design issues that may be resolved in part with new generations of AHSS [1]. In comparison to lighter-weight materials, (such as aluminum and magnesium alloys that reduce total vehicle weight), AHSS offer a significant improvement in crash safety and production cost, meaning AHSS are the favored material of choice for automotive lightweighting [6].

The design, testing and qualification of second and third generation AHSS have progressed rapidly and will ultimately provide critical solutions for improved crash performance and weight reduction of automotive vehicles in the near future. The combination of both high strength and high ductility is a characteristic feature in second and third generation AHSS and depends on microstructures that are engineered to contain austenite [7][8]. The deformation behavior and thus mechanical properties of austenite can be tuned through careful alloying and thermo-mechanical processing [9]. High-Mn and medium-Mn twinning-induced and transformation-induced plasticity (TWIP/TRIP) steels have garnered significant attention because the tunable deformation mechanisms in the austenite provide excellent combinations of strength and ductility. However, there are still many aspects of the processing-structure-property relationships in these steels that are not well understood. More specifically, a fundamental understanding of the deformation mechanisms of TWIP-TRIP steels at high strain rates (experienced during crashes and advanced forming processes) will be beneficial for implementing these steels into automotive vehicles and designing future generations of AHSS [10]. Under crash conditions, steel components are subjected to a wide range of strain rates, most of which can be simulated with tensile tests in the strain rate range from $\dot{\varepsilon} = 10^{-2}$ /s to $\dot{\varepsilon} = 10^{3}$ /s [11]. As such, the structure-property information from high strain rate tensile testing is potentially useful for alloy design and crystal plasticity models to predict the performance of sheet steel forming behavior and automotive crash response of components in the vehicle body.

1.1 Research Objectives

The goal of this work is to gain an understanding of the effects of strain rate on the mechanical properties and deformation mechanisms in next generation steels where austenite is a major (second generation AHSS) and minor (third generation AHSS) microstructural constituent. Adiabatic heating is an inherent consequence of high strain rate deformation and could have an effect on the temperature-dependent austenitic stacking fault energy (SFE). As stacking fault energy influences which deformation mechanism dominates [12], indirectly raising the stacking fault energy through adiabatic heating could alter strength and ductility at high strain rates. The effect of strain rate ($\dot{\varepsilon} = 10^{-4}$ /s to $\dot{\varepsilon} = 10^{3}$ /s) on the strain-induced austenite-to-martensite transformation rate was previously studied in first generation TRIP, second generation austenitic stainless and third-generation TRIP steels [13][14][15][16][17][18][19]. In first generation TRIP steels, there was little to no significant difference in the transformation rate of retained austenite for strain rates from $\dot{\varepsilon} = 10^{-2}$ /s to $\dot{\varepsilon} = 10^{2}$ /s) [13][14]. In second generation austenitic stainless steels, a decrease in the transformation rate was noted at higher strain rates and attributed to adiabatic heating, which stabilized the austenite [15][16][17][18]. There was no significant difference in the transformation rate of third generation quenched and partitioned steels (from strain rates of $\dot{\varepsilon} = 10^{-4}$ /s to $\dot{\varepsilon} = 10^{2}$ /s), whereas third generation medium-Mn TRIP steels did show evidence of reduced transformation rate of the austenite at higher strain rates [19]. The difference in transformation rate of third generation steels is related to the stabilizing effects of adiabatic heating of the tensile specimen and the level of strain at which a majority of the transformation takes place [19]. A study on a medium-Mn steel that contains large amounts of carbon ($C > 0.5$ wt%) and is thus fully austenitic before tensile deformation, provided evidence of a TRIP-to-TWIP transition with increasing strain rate. This transition was attributed to a strain rate dependence of the critical resolved shear stress of epsilon martensite, rather than effects of adiabatic heating on stacking fault energy [20]. Finally, a previous study on austenitic FeMnC and FeMnSiAl TWIP steels revealed contrasting behaviors. The FeMnC steel, which deformed in part through dynamic strain aging (DSA), showed an obvious decrease in density of twin boundaries at higher strain rates, while the DSA-free FeMnSiAl steel did not show any strain rate sensitivity of twinning density for all studied strain rates (from $\dot{\varepsilon} = 10^{-4}$ /s to $\dot{\varepsilon} = 10^{0}$ /s) [21].

The present study is in part a continuation of extensive work by Pierce on Fe-22/25/28Mn-3Al-3Si steels [22]. More specifically, these non-commercial steels were developed to study the influences of stacking fault energy on deformation mechanisms in austenite, helped by the straightforward imaging procedures associated with studying coarse-grained nonferromagnetic high-Mn steels. The stacking fault energies of these high-Mn steels were experimentally determined using weak-beam dark-field transmission electron microscopy (TEM) [23][24] and incorporated elastic constants measured by a novel combination of orientation imaging microscopy and nano-indentation [25]. The Fe-25Mn-3Al-3Si steel deforms by a combination of planar dislocation glide and secondary deformation mechanisms [12][26]. The SFE value of 21±3 mJ/m^2 promotes twinning-induced plasticity as the dominant mode of secondary deformation with some evidence of transformation-induced plasticity in the form of hexagonal ε-martensite [12]. When deformed at room temperature and quasi-static strain rates, these secondary deformation mechanisms contribute to high strain-hardening rates as seen in Figure 1-1. However, the Fe-22Mn-3Al-3Si steel showed little evidence of twinning (mostly hexagonal ε-martensite), which translated to a higher yield and ultimate tensile strengths, a higher strain hardening rate before 0.25 plastic true strain and still moderate ductility, (see Figure 1-1). Furthermore, Pierce *et al.* showed the influence of Mn-content and SFE on the mechanical properties of high-Mn steels and that an optimal SFE between 15 and 39 mJ/m^2 produces the highest product of [ultimate tensile] strength and [total] elongation (PSE), due in large part to combined dislocation glide and secondary deformation, the latter producing obstacles to subsequent dislocation motion [12].

The first part of the present study expands on the work of Pierce [22] by investigating the influences of strain rate on the deformation mechanisms and mechanical properties of the Fe-25Mn-3Al-3Si TWIP-TRIP steel. The second part of the present study deals with designing an industrially relevant medium-Mn steel alloy, (manageable compositions that decrease cost, increase weldability and maintain an appropriate combination of strength and ductility). The medium-Mn steel contains austenite as a minor microstructural constituent, but another requirement of the alloy design includes producing austenite with a stacking fault energy similar to that of the Fe-25Mn-3Al-3Si TWIP-TRIP steel (~21 mJ/m^2) within the multi-phase microstructure to investigate the TWIP and TRIP mechanisms in a complex microstructure. By studying the non-commercial single-phase high-Mn steels with an austenite SFE of ~21 mJ/m^2, the effects of strain rate on the deformation mechanisms and mechanical properties can be better understood in this industrially relevant multi-phase medium-Mn steel, where austenite is a minor microstructural constituent.

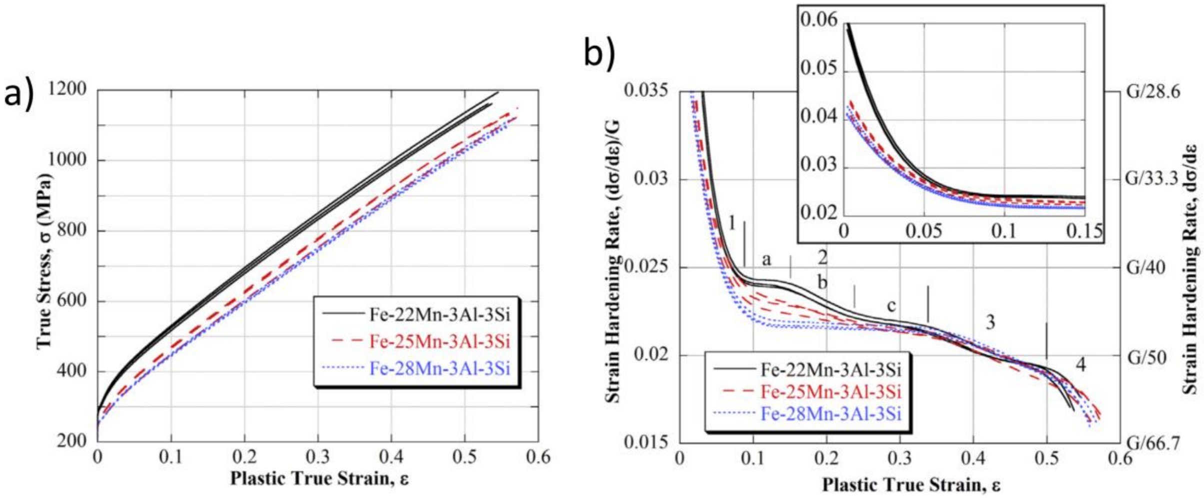

Figure 1-1: a) True stress and b) strain-hardening rate vs. plastic true strain for the Fe-22/25/28Mn-3Al-3Si steels deformed at room temperature and quasi-static strain rates. The strain hardening stages are labeled 1-4 at approximate locations and all curves terminate at maximum uniform elongation. Figure from Pierce et al. [12].

The present work focuses on:

- Measuring the effects of strain rate (using servo-hydraulic tension and strain rates from $\dot{\varepsilon} = 10^{-4}$ /s to $\dot{\varepsilon} = 10^{2}$ /s) on the mechanical properties of an ultra-low carbon austenitic Fe-25Mn-3Al-3Si (wt%) TWIP-TRIP steel, including in-situ temperature measurements of the tensile specimens.

- Determining the influence of adiabatic heating on deformation mechanisms in the single-phase high-Mn TWIP-TRIP steel after interrupted testing at high strain rates (with servo-hydraulic tension and uniaxial ring expansion for strain rates from $\dot{\varepsilon} = 10^{-4}$ /s to $\dot{\varepsilon} = 10^{3}$ /s) using a variety of advanced characterization techniques.
- Designing an ultra-low carbon medium-Mn multi-phase steel with an intrinsic austenitic stacking fault energy similar to that of the Fe-25Mn-3Al-3Si (wt%) TWIP-TRIP steel (21±3 mJ/m^2), including an in-depth study of the microstructural evolution during intercritical annealing.
- Measuring the effects of strain rate (using servo-hydraulic tension and Kolsky-bar testing at strain rates from $\dot{\varepsilon} = 10^{-4}$ /s to $\dot{\varepsilon} = 10^{2}$ /s) and annealing time on the mechanical properties of a multi-phase medium-Mn Fe-12Mn-3Al-0.05C (wt%) multi-phase steel, including in-situ temperature and strain measurements of the tensile specimens.
- Determining which deformation mechanisms are activated in the multi-phase medium-Mn steel during quasi-static and high strain rates to inform predictive models for future design of AHSS.

1.2 Dissertation Overview

Chapter 2 contains a literature review of AHSS and identifies the differences between thermo-mechanical processing, microstructure and mechanical properties of all three generations. Deformation mechanisms in high-Mn and medium-Mn steels are discussed in detail. High strain-rate deformation is explained in the context of strain-rate sensitivity of steel, mechanical-testing recommendations, adiabatic heating of tensile specimens and complex deformation behaviors of various AHSS. A perspective of the present work in regards to contributions to the literature is also provided.

The design and execution of experimental methods is presented in Chapter 3 Experimental procedures include thermo-mechanical processing, specimen machining, mechanical testing, in-situ temperature measurements and data acquisition at high strain rates. Also, sample preparation and methods of advanced characterization techniques, such as electron backscatter diffraction (EBSD), electron channeling-contrast imaging (ECCI), bright- and dark-field transmission electron microscopy, convergent-beam and selected-area electron diffraction, energy-dispersive spectroscopy, atom-probe tomography and X-ray diffraction are introduced.

The results in Chapter 4 are organized into sub-sections by mechanical testing method and steel alloy investigated. For the high-Mn steel, characterization results from uniaxial ring expansions are discussed and important conclusions are outlined regarding the presence of planar defects after high strain-rate deformation. Mechanical properties from servo-hydraulic tensile testing of the high-Mn steel are discussed in the context of in-situ measurements of adiabatic heating, a thermodynamic-based SFE model and post-mortem characterization of the planar defects in interrupted samples. Strict conclusions are drawn regarding the effects of strain rate on positive strain-rate sensitivities in mechanical properties and influences of adiabatic heating on TWIP-TRIP mechanisms. The alloy design process and main considerations in alloy design of a multi-phase medium-Mn steel are presented, including a detailed study of the compositional and morphological evolution during intercritical annealing. The effects of strain rate and annealing time on mechanical properties, when deformed with servo-hydraulic tension and Kolsky-bar testing, are presented and discussed for the medium-Mn steel. In-situ temperature measurements of adiabatic heating and in-situ digital image correlation measurements of strain are shown for all strain rates and two heat treatment conditions. Key conclusions are drawn regarding the effect of annealing time and morphology of ultrafine-grained phases on the deformation mechanisms responsible for the deformed microstructure, specifically in the context of individual contributions of each microstructural constituent to the overall strain hardening behavior.

In Chapter 5, a summary of the major results precedes the provided list of conclusions that are drawn regarding the influences of strain rate on mechanical properties and deformation mechanisms of high-Mn and medium-Mn TWIP-TRIP steels. Chapter 6 includes suggested directions for future work, such as the influence of environment temperature on deformation mechanisms in high-Mn steels, constitutive modeling of strain-hardening behavior in multi-phase medium-Mn steels and parametric studies for future AHSS design.

CHAPTER 2

2. LITERATURE REVIEW

2.1 Mechanical Properties of Advanced High Strength Steels

One of the main incentives behind AHSS research and development originates with the pressing need to adhere to federal standards of automotive fuel economy by reducing vehicle weight without sacrificing passenger safety. Material supply and production costs are also major driving forces. Figure 2-1 shows a map of tensile properties (total elongation and tensile strength) and categorizes AHSS into 3 generations based on respective products of strength and elongation (PSE) in units of MPa% [27]. Second generation AHSS, such as austenitic stainless and high-Mn steels, where both TRIP and TWIP effects are possible [28] [29][30][31], clearly have the largest PSE among all AHSS due to their high capacity to strain harden (refer to engineering stress-strain curve of TWIP steel in Figure 2-2). However, a drawback of most TWIP steels for automotive applications is a relatively low yield strength (also evident in Figure 2-2). Such considerations are important for understanding AHSS design and the three generations will be described in more detail below.

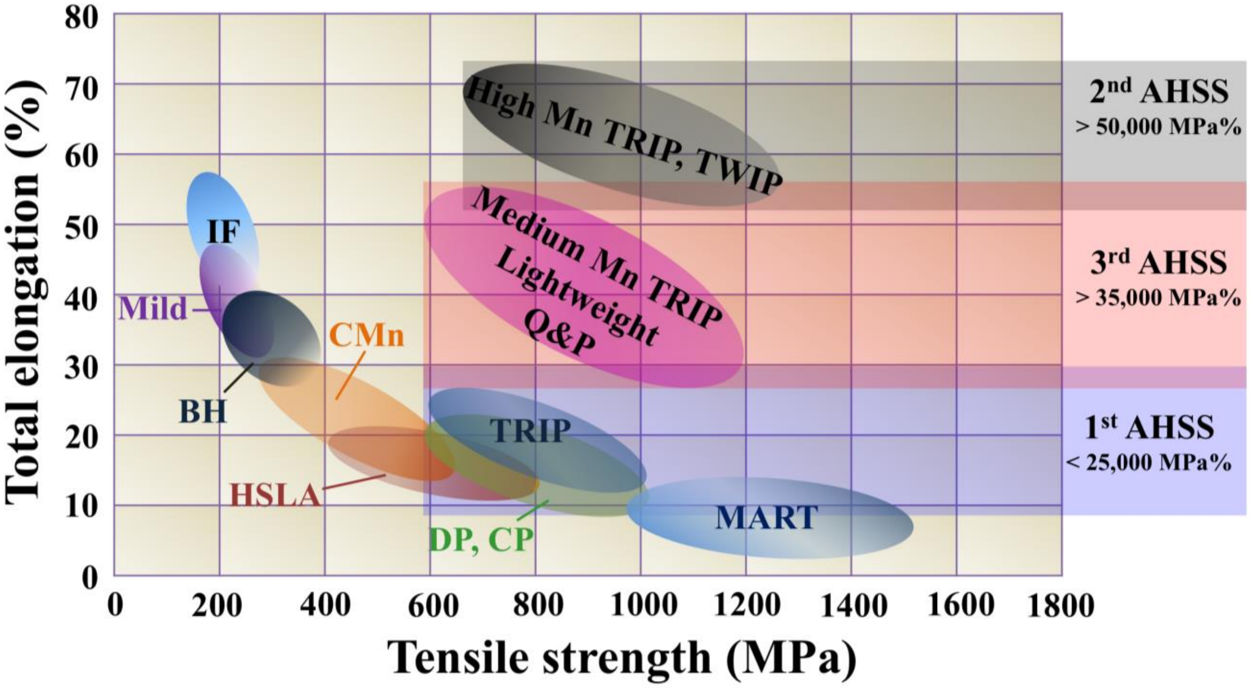

Figure 2-1: Total elongation versus tensile strength map of 1st, 2nd and 3rd generation advanced high strength steels, categorized by respective products of strength and elongation in units of MPa%. Figure from Lee *et. al* [27].

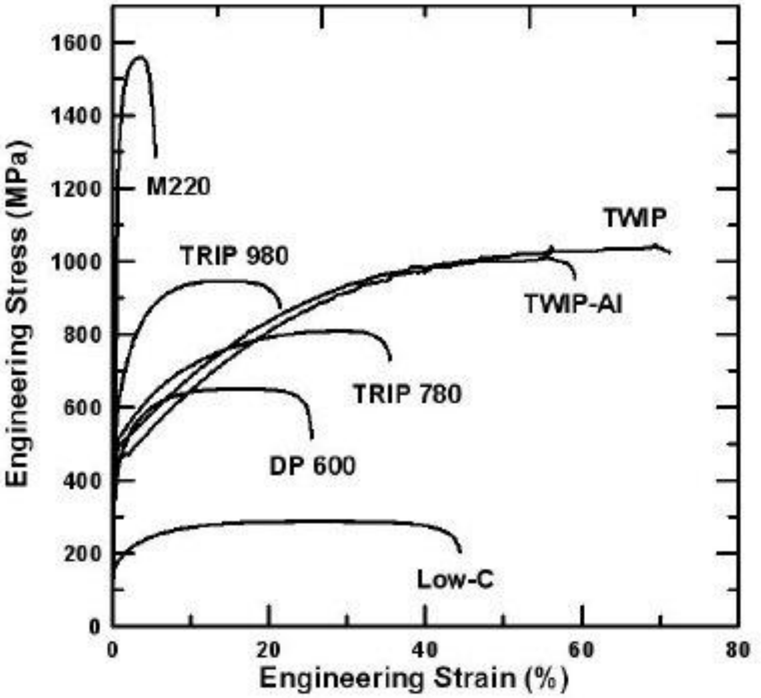

Figure 2-2: Engineering stress-strain tensile curves from all generations of advanced high strength steels, (deformed at room temperature at quasi-static strain rates). Figure from Ronevich [32].

First generation AHSS is a term used to encompass categories of steels that manipulate orientations and compositions of ferritic (α) and/or martensitic (α') microstructures, such as: mild, interstitial-free (IF), bake-hardenable (BH), carbon-manganese (CMn), high-strength low-alloy (HSLA), dual-phase (DP), complex-phase (CP), transformation-induced plasticity (TRIP), and martensitic (MART) steels [33][27]. The tradeoff in mechanical properties between fully martensitic and fully ferritic microstructures is typically characterized as a banana curve when total elongation (TE) is plotted vs. ultimate tensile strength (UTS), seen in Figure 2-1. Furthermore, fully martensitic microstructures possess ultimate tensile strengths in the range of 1-2 GPa and total elongations of 10% or less, whereas fully ferritic coarse-grained microstructures can achieve total elongations up to ~50%, but the ultimate tensile strengths usually do not exceed 0.5 GPa [27], as seen in Figure 2-2. DP steels consist of a ferrite matrix with varying amounts of martensite and produce high UTS values with comparable ductility and are being incorporated into automotive structures [3][34]. First generation TRIP steels are quite unique, as compared to other generations of TRIP steels, as the microstructure contains ferrite, bainite, retained austenite and sometimes martensite [3]. Austenite (γ) is stabilized mostly by carbon in these TRIP steels and is further stabilized when carbide/cementite formation is suppressed by alloying additions, such as Al and Si [35]. Although first generation AHSS have been successful in a variety of applications, TRIP steels, (20-30% TE & 0.5-1 GPa UTS), show a promising direction for new automotive steels as the extra contribution to strain hardening at higher strain levels (from the transformation of a small volume fraction of retained austenite) surpasses the typical trade-off between high strength martensite and ductile ferrite [36].

Second generation AHSS is the term used to describe the different types of austenitic (γ) steels which possess a large PSE. Austenite is a close-packed structure of Fe and is stabilized at room temperature (RT) when Fe is alloyed by more than approximately 17 wt% with γ-stabilizers (Ni, Mn, Al, C) [27]. Austenitic stainless steels utilize large amounts of Ni, Cr, Nb, Ti & Si, plus some Mn & Mo, while high-Mn twinning-induced plasticity (TWIP) and/or high-Mn TRIP steels utilize large amounts of Mn, and smaller amounts of Al, Si & C. The variation in RT quasi-static mechanical properties of austenite is mainly due to differences in barriers to dislocation glide and dominating deformation mechanisms, which are influenced by alloy content and stacking fault energy [12]. Although second generation AHSS have superior strain-hardening rates and large uniform elongations, a drawback for automotive applications is the relatively low yield strength, especially in carbon-lean alloys. Other commercial drawbacks of second generation AHSS for automotive applications are increased cost and decreased weldability, which are both related to the substantial amount of alloying required to stabilize a fully austenitic microstructure [27].

An optimally balanced 3rd generation AHSS consists of an alloying content below 17 wt. % and a multi-phase microstructure (α′/α/γ) to respectively balance cost and appropriate mechanical properties. Ideal mechanical properties of a third generation AHSS include yield strengths greater than 0.5 GPa and ultimate tensile strengths greater than 1 GPa at levels of uniform elongation equal to or greater than 30 % [36][33][37][38]. The types of third generation steels capable of achieving these desired properties are medium-Mn TWIP/TWIP steels, lightweight steels and quenched & partitioned TRIP steels [1][2]. Medium-Mn steels generally exhibit an α′ martensitic microstructure after hot and cold rolling, but intercritical annealing in the α+γ phase field produces a multi-phase microstructure with ultrafine-grained (UFG) phases and equilibrium volume fraction of reverted austenite that ranges between 20 and 50%. Mechanical properties of a third generation AHSS ideally exhibit low strain hardening rates at low levels of strain and higher strain hardening rates as total strain accumulates, a behavior that is related to the accommodation of deformation in each phase. Studies investigating deformation mechanisms and mechanical properties of medium-Mn steels have reported the effects of intercritical annealing temperature on phase quantity/grain sizes [36][39]. Other researchers of medium-Mn steels and TWIP steels have observed static and dynamic strain aging effects (respectively termed Lüders bands and Portevin-Le Châtelier or PLC bands) which can lead to plastic instabilities during deformation. Such strain aging effects are influenced by microstructure, composition, dislocation mobility, temperature and strain rate [40][41][42][43][44][45][46]. Moreover, a broad range of microstructures observed in steels containing a medium amount of Mn and produced with a variety of thermo-mechanical processing steps have exhibited a wide range of mechanical properties, which depend on bulk composition, intercritical annealing temperature/time, cooling/heating rate, grain size, relative phase fraction, mechanical stability of a given phase and phase morphology [27][39][47][48][49][50][51][52][53][54][55][56][57][58][59].

2.2 High-Mn Twinning and Transformation-induced Plasticity Steels

High-Mn twinning-induced and transformation-induced plasticity (TWIP/TRIP) steels exhibit promising properties for automotive applications due to their exceptional combination of strength and ductility. The product of ultimate tensile strength (UTS) and total elongation (TE) typically ranges between 42,000 and 68,000 MPa·% [12][60][61], which is superior to many other AHSS grades. The superior energy absorption capability of these steels could also play a critical role in improving crash performance for future vehicle designs. The work of Frommeyer at the Max-Planck-Institut für Eisenforschung in Düsseldorf, Germany

[29][30][62][63] was critical for renewed interest in Hadfield and high-Mn steels. Hadfield steels are austenitic steels with 11-14 wt% Mn and 1-1.3 wt% C that transform to martensite under applied stress (therefore useful for railroad applications) and have high work hardening rates that usually include dynamic strain aging (serrated flow stresses) [64]. This research group studied the structure-property relationships of various high-Mn alloy compositions (Fe-15/20/25/30Mn-1/2/3Al-1/2/3Si) and were able to tune microstructures that contained large amounts of austenite, which formed α′/ε- martensite and mechanical twins during deformation. One of the alloys studied in this dissertation (Fe-25Mn-3Al-3Si wt%) that Frommeyer originally designed [29] was selected due to the interesting combination of TWIP-TRIP mechanisms identified by Pierce [31] and the best room temperature elongation of the mentioned high-Mn alloys. Although Mn has a negligible effect on solid solution strengthening [65], the Mn atoms stabilize the Fe-based FCC lattice at room temperature and allow for tunable deformation mechanisms and mechanical properties [29][31].

Typically, high-Mn (15-30 wt%) TWIP and/or TRIP steels are composed of metastable or stable austenite and are alloyed with Al, Si, Cr, C and N [60][66][30][67][61][68][69][54]. The deformation mechanisms and tensile properties of TWIP and/or TRIP steels can exhibit a strong dependence on temperature and stacking-fault energy (SFE) [12][66]. Si generally reduces the SFE, while C, Mn and Al increase the SFE of austenite [70][71][72]. These steels deform by a combination of dislocation glide and secondary deformation mechanisms such as mechanical twinning and/or ε_{hcp}-martensite formation [26][12]. Austenitic high-Mn steels with relatively high SFE (approximately 50 mJ/m^2 and greater) deform primarily by dislocation glide. As the SFE decreases from ~50 to ~20 mJ/m^2, mechanical twinning becomes increasingly favorable and the steel deforms by both dislocation glide and mechanical twinning. With decreasing SFE below ~20 mJ/m^2, these steels typically deform by a combination of dislocation glide and a diffusionless martensitic phase transformation, where the austenite phase transforms to hexagonal ε-martensite [12][68][23][29][66][72][73][74]. The martensite platelets and mechanical twins act as planar obstacles, reduce the mean free path of non-coplanar dislocation glide and produce back stresses, resulting in a high strain-hardening rate, delayed necking, and large uniform elongations [75][76][60][66][30][67][61][68][77][78].

The close-packed FCC slip system of {111} glide planes and <110> slip directions in austenite is visualized in Figure 2-3a. The dissociation of a full a/2 <110> dislocation to two a/6 <112> partial dislocations is schematically introduced in Figure 2-3b/c. The mechanisms by which mechanical twins and ε-martensite form are closely related to the glide of a/6 <112> partial dislocations, which successively displace atoms on {111} planes in the FCC lattice [79][20][80][30][81][77]. Partial dislocations both trail and lead a stacking fault on {111} glide planes (see Figure 2-4) and can either transform planes of the FCC lattice to HCP as is the case of ε-martensite or in the case of mechanical twinning (a reorientation of the FCC lattice). The separation distance between partial dislocations is generally speaking inversely proportional to the intrinsic stacking fault energy, (i.e. closely spaced partials have a higher SFE than widely separated partials), which is related to the repulsive forces of anisotropic elasticity and the restorative forces of the SFE [82][83][22]. The purpose of the repulsive force is to reduce strain energy between the partials, the magnitude of which is proportional to the square of the Burgers vector [84].

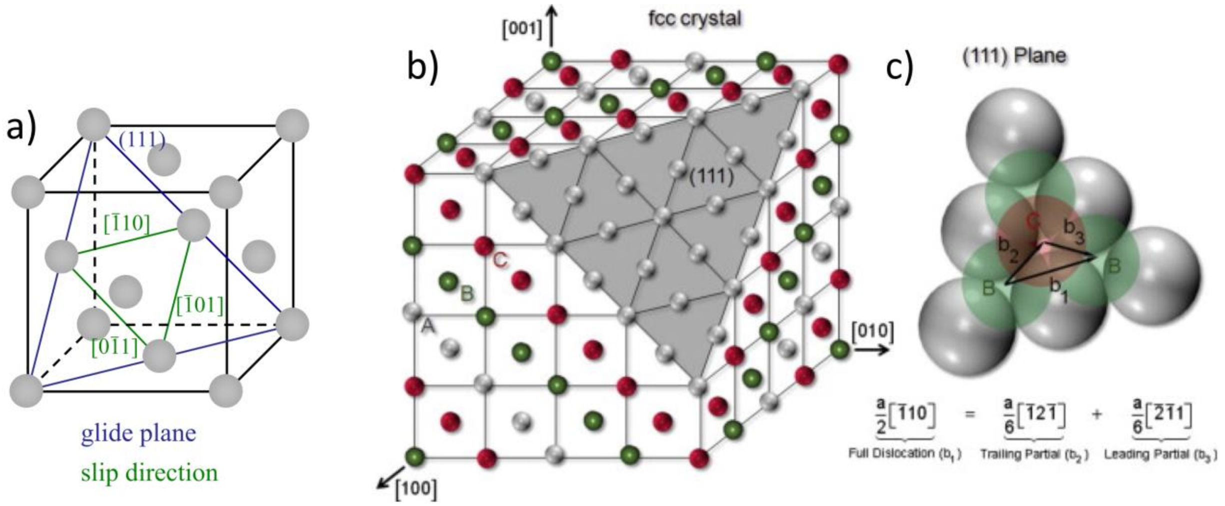

Figure 2-3: a) Slip system in one unit-cell of the FCC lattice: each {111} plane contains three <110> directions. b) The A-B-C (silver-green-red) stacking sequence of {111} planes in a multiple unit-cell lattice, and the cut-away dark gray section highlights the specific (111) plane. A full dislocation (b1)of a/2 <110> type dissociates into two Shockley partials (b2 and b3) of a/6 <112> type. The 3-dimensional dissociation is shown in part c). Figure a) from Gottstein [85] and b-c) from Chowdhury *et. al* [86].

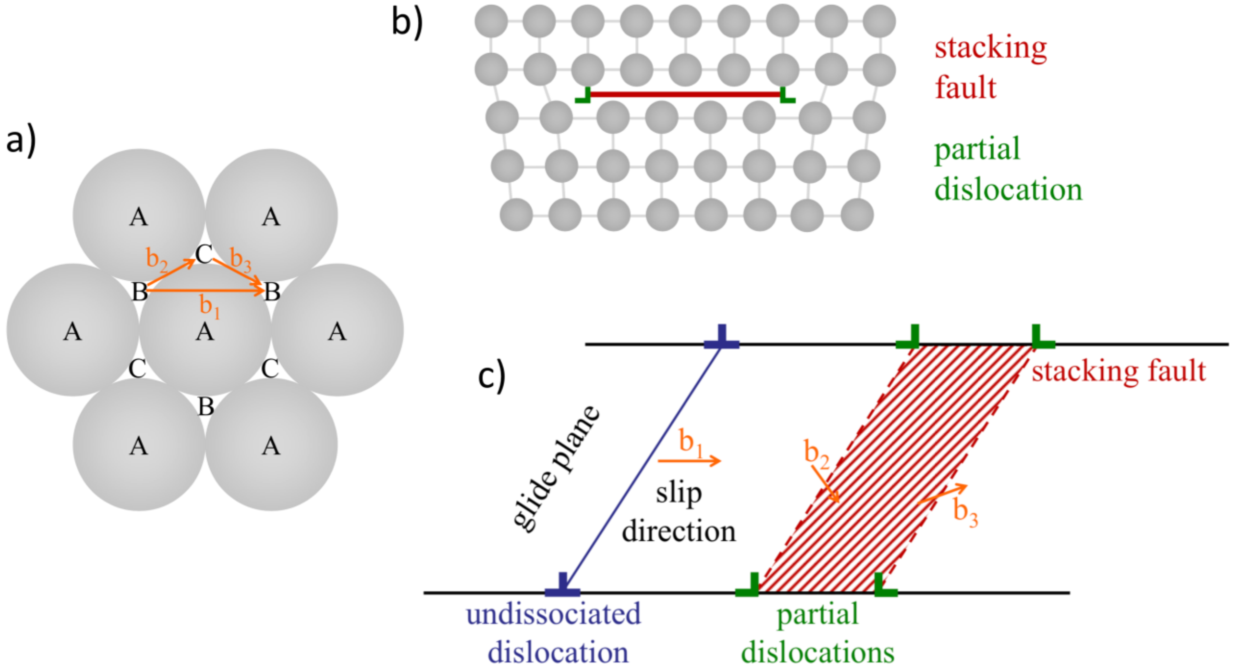

Figure 2-4: a) stacking sequence of closed-packed {111} planes in the FCC lattice, including a full dislocation (b1) and its dissociated partials (b2 and b3). The trailing and leading partial dislocations can widely separate to form a stacking fault, as shown in b) and c). Figures from Gottstein [85].

As stated previously, the intrinsic austenitic stacking fault energy (γ_{isf}), in units of mJ/m^2, can be tuned for phase transformation, deformation twinning, and dislocation glide, based on temperature and alloy composition [60][66][30][67][61][68][69]. All SFE values mentioned refer to intrinsic SFE values (as opposed to energies related to extrinsic stacking faults) unless stated otherwise. SFE values of austenitic alloys reported in the literature for Fe-(20-32)Mn-Cr-C alloys [87], Co-15-45Ni-14Cr-Mo alloys [88], Fe-Mn-C TWIP steels [89], and Fe-18Cr-10Ni-C-N alloys [90] have reported twinning is possible for SFE values ranging from 12 to 48 mJ/m^2 (see Figure 2-5). Further, the combination of both mechanical twinning and ε-martensite has been observed for SFE values ranging from 8 to 21 mJ/m^2 (see Figure 2-5). Further, Shiekhelsouk *et al.* [91] studied polycrystalline TWIP steel through constitutive modeling and concluded that forest dislocations dominated short-range barriers to dislocation mobility during early levels of strain, grain size and twin spacing of primary twin systems had an effect on the dislocation mean free path at mid-to-late levels of strain (acting as long-range barriers to dislocation motion) and multiple twin systems produced an effect on the mean free path and work hardening rate only at late levels of strain accumulation.

A schematic representation of how the deformation twinning mechanism could occur through passage of Shockley partials on successive {111} planes is shown in Figure 2-6 [79]. In this regard, the twinning mechanism is closely related to the formation of ε-martensite where a Shockley partial would pass through every second {111} plane. Twin boundaries in face centered cubic (FCC) materials are classically described by a mirror reflection (180° rotation) of the matrix lattice and the twinned lattice. It is important to note that the mechanism described in Figure 2-6 is not the only proposed mechanism for twinning. Steinmetz *et al.* [77] developed a multiscale dislocation density-based model for the strain hardening behavior of TWIP steel, which included nucleation driving forces described in detail by Mahajan *et al.* [92] and showed close agreement with experimental results. Mahajan *et al.* [92] proposed that two full dislocations on neighboring {111} planes split into faults and react to produce three Shockley partials on adjacent planes (a three-layer stacking fault). Idrissi *et al.* [93] investigated twinning in a Fe-20Mn-1.2C steel and specifically mentioned that twin nucleation models proposed by Miura *et al.* [94] and Cohen *et al.* [95] best explained the behaviors observed. The MTN model, (named after Miura Takamura and Narita [94]) proposed that dislocations pile-up at Lomer dislocations (at the junction of a primary and cross slip plane) and react to form two Shockley partials and a Frank sessile dislocation of the a/3<111> type. This double layer extrinsic stacking fault would serve as the twin nucleus. Cohen and Weertman [95] proposed that the twin nucleus forms due to pile-up stresses at Cottrel-Lomer locks, which forces a full dislocation to dissociate into a sessile Frank partial screw dislocation and a glissile Shockley partial. Comparatively, Gutierrez-Urrutia and Raabe [96] mentioned Cottrel-Lomer locks near dislocation cells played a significant role during stage 2 of strain hardening. In this work [96] the authors studied the dislocation and twin substructure evolution and observed that the initial increase in the strain hardening rate of a Fe-22Mn-0.6C TWIP steel was due to the nucleation of dislocation cells, which decreased in size to form highly dense dislocation walls. The authors additionally noted that mechanical twinning significantly influenced strain hardening after 0.1 true strain. Furthermore, other work by Idrissi [97] showed that the carbon content has a significant effect on the morphology and internal dislocation structure of deformation twins. Mechanical twins in the carbon-rich steels were thinner and contained more sessile dislocations (compared to carbon-lean steels) and were observed to act as more effective barriers to dislocation glide [97].

Some of the first investigations of hexagonal ε-martensite formation (by Olson and Cohen [98]) detailed the orientation relationship with austenite as $(111)_{\gamma}||(0001)_{\varepsilon}/[1\text{-}10]_{\gamma}||[1\text{-}210]_{\varepsilon}$. The close-packed planes and directions of ε-martensite are parallel to the listed slip system in austenite and can form in austenite during quenching (if cooling temperatures cross the martensite start temperature with a sufficient rate) or during tensile deformation. Typically, a SFE of 20 mJ/m^2 or less (see Figure 2-5) translates to an increased stability of the hexagonal close packed (HCP) phase relative to the FCC phase and promotes nucleation of ε-martensite [98]. However, in-situ TEM measurements by Brooks *et al.* [99] showed that the nucleation of epsilon may not be as simple as the passage of a Shockley partial on every second {111} plane in austenite. The authors observed ε-martensite nucleation near the collection of irregularly spaced stacking faults and the ε-martensite thickens with increased deformation. This group of stacking faults provides energetically favorable regions for hexagonal lattices as the slight contraction in spacing between fault planes helps to minimize the interfacial energy between FCC and HCP stacking sequences. Since mechanical properties of Fe-Mn-Al-Si steels depend on SFE [100], alloy design requires accurate SFE predictions as a function of temperature and composition. Alternatively, De Cooman *et al.* [101] proposed that the stress value at which twinning initiates is inversely related to temperature (assuming the SFE value remains below 45 mJ/m^2). Traditionally, thermodynamic descriptions do not consider the stacking fault character and use constant values for FCC/HCP interfacial and strain energy parameters because the variation with respect to temperature is not well understood. In reality, the interfacial energy likely decreases with increasing temperature [102]. This subject will be discussed further in Sections 4.2.5 and 4.2.9.

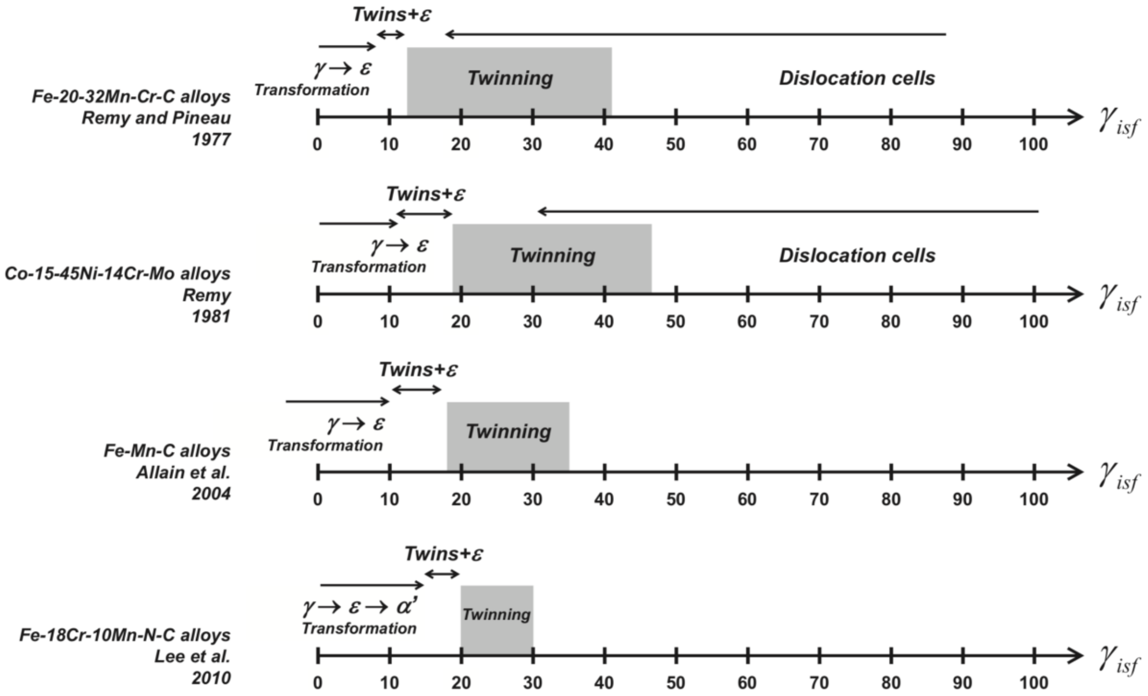

Figure 2-5: Ranges of the intrinsic austenitic stacking fault energy γ_{isf} (in units of mJ/m^2) for phase transformation, deformation twinning, and dislocation glide in FCC γ-Fe alloys reported in the literature for Fe-(20- 32)Mn-Cr-C alloys [87], Co-15-45Ni-14Cr-Mo alloys [88], Fe-Mn-C TWIP steels [89], and Fe-18Cr-10Ni-C-N alloys [90]. The relation between the γ_{isf} axis and $\Delta G^{\gamma \rightarrow \varepsilon}$ is also indicated, assuming that $2 \text{ x } \sigma^{\gamma \rightarrow \varepsilon} = 15$ mJ/m^2. Composite figure from De Cooman *et al.* [101].

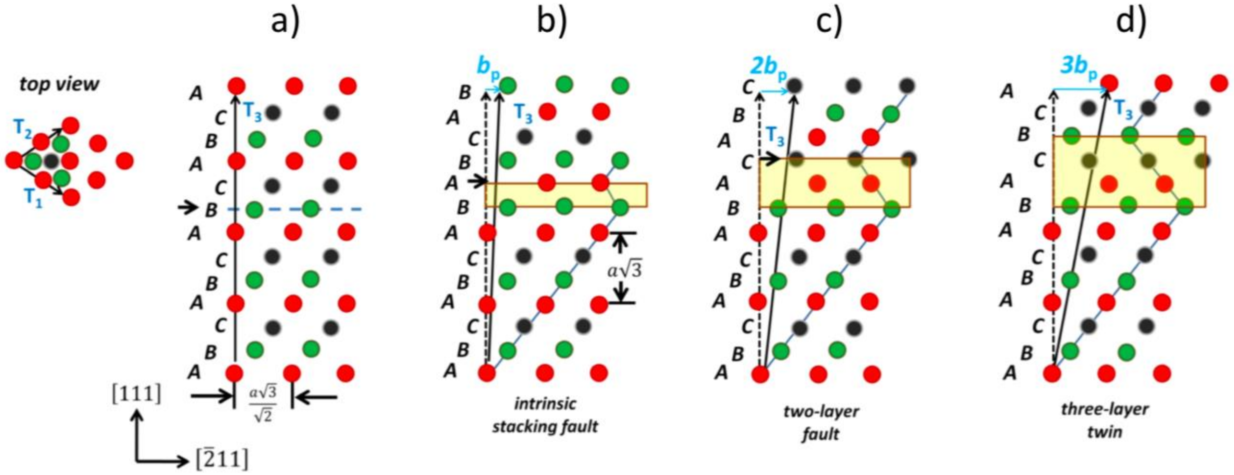

Figure 2-6: Schematic representation of deformation twinning: a) perfect FCC lattice with an A-B-C stacking sequence b) one-layer (intrinsic) stacking fault c) two-layer (extrinsic) stacking fault and d) three-layer (twin) planar fault. The black horizontal arrows indicate the successive {111} planes on which Shockley partials – Burgers vector of $b_p = a/6<112>$ type – are passed. The translation vector T_3 maintains the FCC stacking between the neighboring unit cells. Figure from Kibey et al. [79], adapted by Saeed-Akbari [103].

2.3 Medium-Mn Twinning and Transformation-induced Plasticity Steels

Medium-Mn steels are considered third generation advanced high strength steels and aim to fill the property gap between first and second generation AHSS by offsetting the outstanding mechanical properties of second generation AHSS with the low cost of first generation AHSS [33]. Medium-Mn steels generally exhibit a fully deformed martensitic microstructure after hot and cold rolling, but designing a multi-phase medium-Mn microstructure requires an additional intercritical annealing step (seen in Figure 2-7a). The volume fraction of reverted austenite measured at room temperature after all thermo-mechanical processing steps, depends on annealing time and annealing temperature [27].

Early work by Miller [104] showed how additions of Ni can be used to stabilize austenite at room temperature after intercritical annealing and the amount of austenite also depends on % cold reduction (see Figure 2-7b). Mn is currently used instead of Ni to stabilize austenite due to cost benefits, while C is usually minimized due to welding concerns [105]. The partitioning of Mn and C from martensite to form austenite and partitioning of Al from austenite to martensite and ferrite during intercritical annealing in the $\gamma+\alpha$ phase field (temperatures between Ac_1 and Ac_3) control the amount, size, composition and stacking fault energy of the reverted austenite [105].

Chen et al. [106] measured greater Mn and C concentrations in austenite at lower annealing temperatures in a Fe-5.1Mn-1.4Ni-0.2Si-0.035C wt% steel (10.4Mn-0.12C wt% at 600 °C vs 7.7Mn-0.07C wt% at 650°C). Studies on medium-Mn steels with bulk carbon concentrations ranging from 0.2 to 0.4 wt% have shown how cementite formation and dissolution at low-angle lath martensite boundaries caused sluggish formation of reverted austenite during early stages of intercritical annealing, rather than reversion depending only on partitioning of Mn and C from ferrite to austenite [107][108]. Atom probe tomography (APT) results in one of the studies [108] showed a Mn concentration of 28 at.% Mn in a 30 nm-sized carbide vs 10 at.% Mn in austenite for an Fe-10Mn-3Al-2Si-0.3C wt% steel (cold-rolled and annealed for 10 min at 700 °C). Another study [109] on a quenched and partitioned medium-Mn steel (AISI 9260 steel containing approximately 0.6 wt% C) provided evidence of transition carbide formation before partitioning of Mn and C from ferrite to austenite. Han et al. even observed what is believed to be cementite particles in SEM micrographs after 10 s of annealing at 620 °C in a Fe-9Mn-0.05C (wt%) alloy, but noted all cementite particles had dissolved after 30 s of annealing [109]. Another study by Han et al. [110] on a Fe-9Mn-0.05C (wt%) alloy demonstrated that heating rates below 15 °C/s revealed cementite formation whereas heating rates above 15 °C/s did not exhibit cementite formation, (both heat treatments involving heating to 650 °C or greater and promptly quenching to room temperature without isothermal holding). Other studies on low-carbon (< 0.2 wt%) medium-Mn steels observe co-segregation of C and Mn during early stages of austenite nucleation followed by a moving ferrite/austenite interface during partitioning, which depends on the diffusion of Mn and thus the local equilibrium between ferrite and austenite [111][112]. Seol *et al.* noted that precipitation of κ carbides, [$(Fe,Mn)Al_3C_x$], requires compositions of Mn < 8 wt%, 5<Al<8 wt%, C < 0.3 wt% [113] and Raabe *et al.* showed if the [Al] was greater than 10 % then the L12 κ would precipitate during quenching [114]. The medium-Mn alloy in the present work should not contain kappa carbides due to insufficient levels of Al and C.

Typically, increasing cold reduction increases the amount of retained austenite for the same annealing time and temperature due to an increase in the nucleation rate of austenite and directly translates to faster diffusion paths for the partitioned elements [115]. Also, in medium-Mn steels, microstructures produced from cold-rolling and intercritical annealing are usually exhibit equiaxed ferrite and austenite grains, (related to the numerous partitioning pathways afforded by the high dislocation density). On the other hand hot-rolling and intercritical annealing tends to produce microstructures in medium-Mn steels that are usually more elongated in nature, resembling the acicular martensitic microstructure prior to annealing, plate-like interfaces and prior austenite grain boundaries providing the preferred partitioning pathways (see Figure 2-7c/d) [104][109]. However, fully equiaxed microstructures may require cold rolling on the order of 60-85% cold-reduction in thickness of the plate and intercritical annealing times of 16 h or greater [104].

Recent work by Zhang *et al.* [59] on a cold-rolled Fe-7.14Mn-0.23Si-0.14C-0.06Al steel observed an elongated microstructure after an intercritical annealing for 3 min at 620 °C, which was used to simulate continuous casting conditions. Annealing times from 12 h to 96 h, which demonstrated batch annealing conditions, produced more equiaxed grains in the cold-rolled Fe-7.14Mn-0.23Si-0.14C-0.06Al steel [59]. However, it is important to note that a special annealing step (620 °C for 12 h) was completed in between hot-rolling and cold-rolling, meaning the intercritical annealing times mentioned above (3 min through 96 h) are actually considered the second annealing step after hot-rolling. Other work involving extra thermo-mechanical processing steps includes a study by He *et al.* [116] which utilized a liquid nitrogen bath in between steps of hot rolling and intercritical annealing to improve the mechanical stability of retained austenite and led to improvements of ductility and strength during tensile testing.

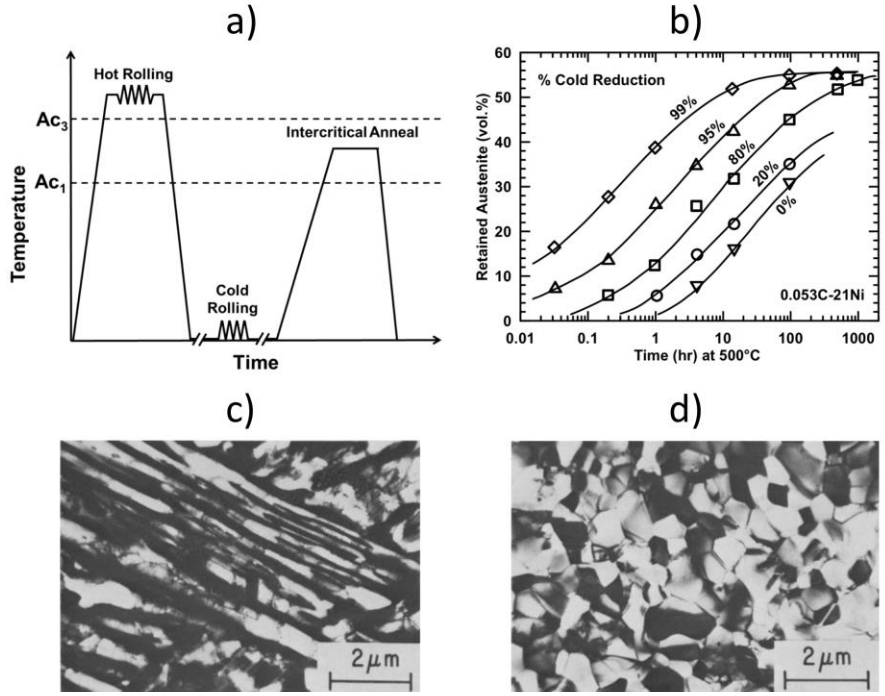

Figure 2-7: a) Example of the basic processing sequence involved in typical thermo-mechanical processing steps used for medium-Mn steel production. b) Curves showing the effect of cold work on austenite transformation time during an intercritical anneal of a 0.053C- 21Ni (wt.%) steel. TEM micrographs of the ferrite-austenite microstructures of a 0.11C-5.7Mn (wt.%) steel with an initially martensitic microstructure after hot rolling that were c) annealed for 16 h at 600 °C and d) cold-rolled (60-85%) then annealed for 16 h at 600 °C. Figures a-d) from Miller [104], but a) and b) redrawn by Poling [19].

The austenite-to-α′-martensite transformation depends on both chemical and mechanical driving forces [117][118]. Chemical driving forces mostly depend on differences in Gibbs free energies, as shown in Figure 2-8a. Initially, during thermo-mechanical processing steps of medium-Mn steels, the martensite start temperature (M_s) is usually above room temperature, which is why quenching after hot rolling and homogenization, especially at fast cooling rates, produces a microstructure with both austenite and martensite [39]. Mainly, the chemical driving force is extremely high and the homogenized [prior] austenite does not contain enough Mn to be stable at room temperature and a large portion is transformed to athermal martensite. The fraction of martensite (f_m) can be predicted using contributions from alloy composition (see Equation 2-1 where compositions in weight % are positive if the element increases the M_s temperature and negative if the element reduces the M_s temperature) and quench temperature (see Equation 2-2) using the Koistinen-Marburger relationship [119][120][121]. After cold rolling, the medium-Mn microstructure is deemed fully deformed martensite, which will be discussed in more detail. During intercritical annealing the partitioning elements diffuse and create ultrafine-grained stable austenite. The reverted austenite is stable at room temperature because the M_s temperature is driven below room temperature [118] during the super-saturation of austenite with Mn and C as discussed previously. However, if the intercritical annealing temperature is too high and cooling rate too fast, fresh athermal stress-assisted martensite can form again. Previous work [39] on medium-Mn steels demonstrates that an increase in intercritical annealing temperature increases the austenite volume fraction retained at room temperature, up until a specific temperature ($T_{\gamma\text{-max}}$), above which the austenite volume fraction decreases. The decrease in austenite fraction after intercritical annealing with temperatures above $T_{\gamma\text{-max}}$ is due to the formation of fresh athermal martensite during cooling (this temperature varies strongly with carbon content and moderately with parent grain size) [39][122]. Further, in original work on multi-phase medium-Ni steels [104] Miller observed a decrease in hardness and increase in austenite fraction with increasing annealing temperature up until $T_{\gamma\text{-max}}$, but hardness rapidly increased and austenite fraction rapidly decreased with increasing temperatures above the $T_{\gamma\text{-max}}$. Lee et al. observed an increase in austenite fraction from 10 to 25% for respective annealing times of 1 h and 24 h at the same annealing temperature of 600 °C, (Tγ-max = 650 °C for the Fe-6Mn-0.3C wt% alloy) [39].

$M_s(^\circ C) = 539 - [423 \times (wt\%\ C)] - [30.4 \times (wt\%\ Mn)] - [7.5 \times (wt\%\ Si)] + [30 \times (wt\%\ Al)]$

(Equation 2-1)

M_s = martensite start temperature

$$f_m = 1 - e^{-1.1 \times 10^{-2}(M_s - QT)} \qquad \text{(Equation 2-2)}$$

f_m = fraction of stress-assisted martensite retained at room temperature
QT = quench temperature

In terms of deformation-induced martensite, mechanical driving forces become more dominant [118] and the roles of stress-assisted vs. strain-induced nucleation must be considered. As M_s decreases relative to room temperature (or alternatively as the environment temperature increases above the M_s), the chemical driving forces of Gibbs free energies (transformation from gamma to α'-martensite) decrease while mechanical driving forces increase (U' seen in Figure 2-8a). The temperature at which the chemical and mechanical driving forces are equal ($M_s\sigma$) indicates the point at which α'-martensite nucleation sites transition from stress-assisted to strain-induced [117] (nucleation is assisted by inelastic stress in the austenite between M_s and $M_s\sigma$ and occurs at stresses below the yield strength of the austenite [123]). This transition is typically associated with negative strain-rate sensitivities [20][19].

Martensite nucleation theory developed by Olson and Cohen [118] (see Figure 2-8b) describes a non-linear relationship between temperature and stress for the regime of strain-induced nucleation. This is an important point to resolve because the TRIP mechanism here becomes more complex and is usually associated with low-SFE materials [124]. First, yielding occurs through slip in the austenite and when stresses increase locally through accumulation plastic deformation, nucleation sites of α'-martensite develop at the intersections of planar defects on non-coplanar slip systems. Specifically, the intersections of two hexagonal ε-martensite plates, ε-martensite and mechanical twins, ε-martensite and stacking faults or twins and stacking faults are possible combinations that nucleate strain-induced α′ martensite within an austenite grain [118][125][99][126][127][128][129][130]. As such, the Olson-Cohen model seen in Equation 2-3 shows that the strain-induced alpha prime martensite fraction (f_{α}') depends on the rate of planar-defect formation (α), the probability of planar-defect intersections becoming a martensite nuclei (β), and plastic strain (ε). The β parameter is related to the chemical driving force, α is inversely related to the stacking fault energy, (meaning α and β both depend on temperature), and the exponent n is typically assumed to be 2 for equiaxed grains and even higher for non-equiaxed/textured austenite grains [118]. Temperatures above M_d, where the Gibbs free energy favors austenite over martensite, austenite is stable against strain-induced transformation to α′-martensite.

$$f_{\alpha}' = 1 - \exp\left(-\beta(1 - \exp(-\alpha\varepsilon))^{n}\right) \qquad \text{(Equation 2-3)}$$

f_{α}' = fraction of strain-induced α′-martensite
β = probability that planar-defect intersections create an α′-martensite nucleus
α = rate of planar-defect formation
ε = plastic strain
n = parameter that relates the austenite morphology to schmid factor

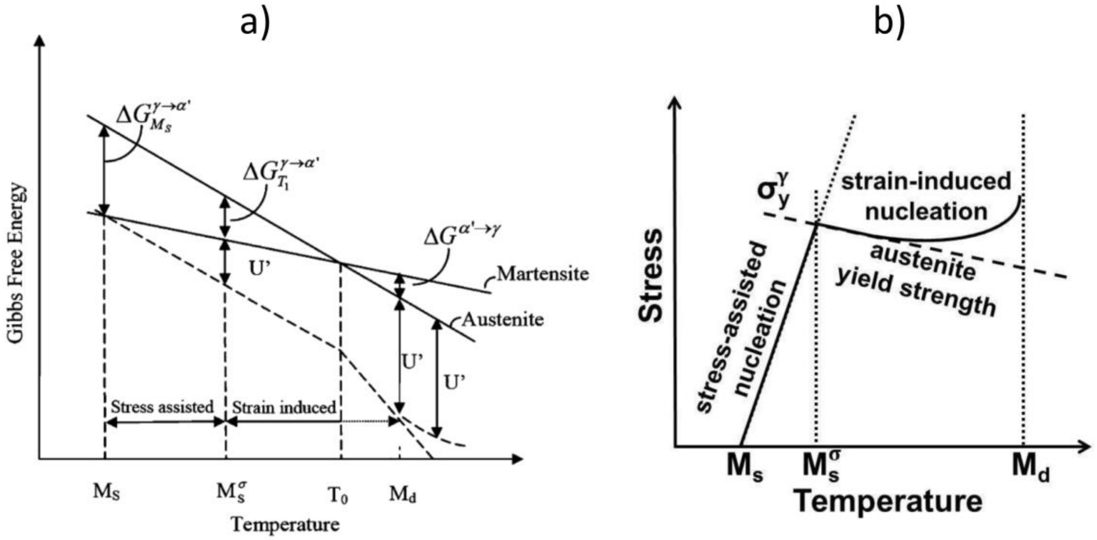

Figure 2-8: a) Gibbs free energies of austenite and martensite as a function of temperature. b) Schematic presentation of stress-assisted (before yielding) and strain-induced nucleation of deformation-induced martensite formation. $M_s\sigma$ is the temperature at which the deformation-induced martensite formation is switched from the stress-assisted mechanism to the strain-induced mechanism. Figure a) from Curtze *et al.* [117] and b) from Olson and Cohen [118], but redrawn by Poling [19].

Differences in stress-assisted and strain-induced nucleation are schematically represented and identified with TEM from work by DeCooman and Gibbs [124], as seen in Figure 2-9. Stress-assisted martensite is defined as the type of martensite that can be produced during quenching with fast cooling rates (given the right set of M_s and quench temperatures) by stresses that are less than the yield strength of austenite. The predominant driving force of stress-assisted nucleation is chemical-based (i.e. the driving force of Gibbs free energy). Strain-induced martensite is defined as the type of martensite that nucleates after the material is strained and contains a high density of dislocations and preferential nucleation sites near the intersection of planar defects and partial dislocations. Mechanical driving forces provide the favorable nucleation of strain-induced nucleation of martensite, rather than chemical driving forces. For lower intercritical annealing temperatures (slightly below $T_{\gamma\text{-max}}$ seen in Figure 2-9c), athermal martensite is not observed in the austenite after quenching (Figure 2-9a) as predicted [7], which means the austenite-to-α′-martensite transformation will only be strain-induced (since room temperature is greater than $M_s\sigma$) and must occur during tensile deformation. However, when room temperature lies between M_s and $M_s\sigma$, partial or full transformation of austenite can occur during quenching from higher intercritical annealing temperatures and thus prior to tensile deformation [124] as predicted in Figure 2-9c and shown in Figure 2-9b.

The study by DeCooman *et al.* [124] also revealed a strong dependence of mechanical properties on intercritical annealing temperature (see Figure 2-10a), based on in-situ neutron diffraction measurements during tensile deformation (see Figure 2-10b and Figure 2-10c). The α′-fraction was estimated by subtracting the neutron measurements of austenite, ε-martensite and intercritical ferrite fractions from 100 pct. Shaded regions in Figure 2-10b and Figure 2-10c also include yield-point elongation. Moreover, the lowest intercritical annealing temperature of 575 °C had the highest yield strength, second largest total elongation, the most amount of yield-point elongation through Lüders banding, the smallest transformation rate of austenite (see Figure 2-10b) and a relatively low UTS. However, strain-induced martensite transformation did occur readily in the 600 °C annealed sample after 10% engineering strain (see Figure 2-10d). The intercritical annealing temperature of 650 °C that produced athermal martensite during quenching had nearly the opposite mechanical behavior of the 575 °C annealing temperature (low yield strength, low elongation and low amount of yield-point elongation as shown in Figure 2-10a and Figure 2-10c). A high transformation rate as seen in Figure 2-10c, is indicative of a low SFE, early transformation at 2% engineering strain (see Figure 2-10e) and a high UTS (Figure 2-10a).

Predicted room-temperature stacking fault energies in the work by DeCooman *et al.* [124] are based on measured austenite compositions after annealing and quenching and ranged from 12 mJ/m^2 for the 575 °C annealing temperature to 1 mJ/m^2 for the 650 °C annealing temperature, which indicates that twinning is not a likely mechanism and a full transformation of austenite to α'-martensite is likely. Also, the lower the SFE, the higher the transformation rate of austenite. Other recent work [54][131] has shown that an increase of the intercritical annealing temperature decreases the Mn content in austenite and also decreases the SFE of the austenite. The SFE is important for determining TWIP and TRIP effects in the γ phase during deformation [39][132][55][133][56][134]. As Mn diffusion in austenite is sluggish, the reverted grains tend to be ultra-fine in size (less than 1 μm in diameter) [107]. As compared to fully austenitic steels, Gutierrez-Urrutia et al. [135] observed that decreasing the grain size from 50 to 3 μm reduced the activity of mechanical twinning, but did not completely suppress the secondary deformation mechanism.

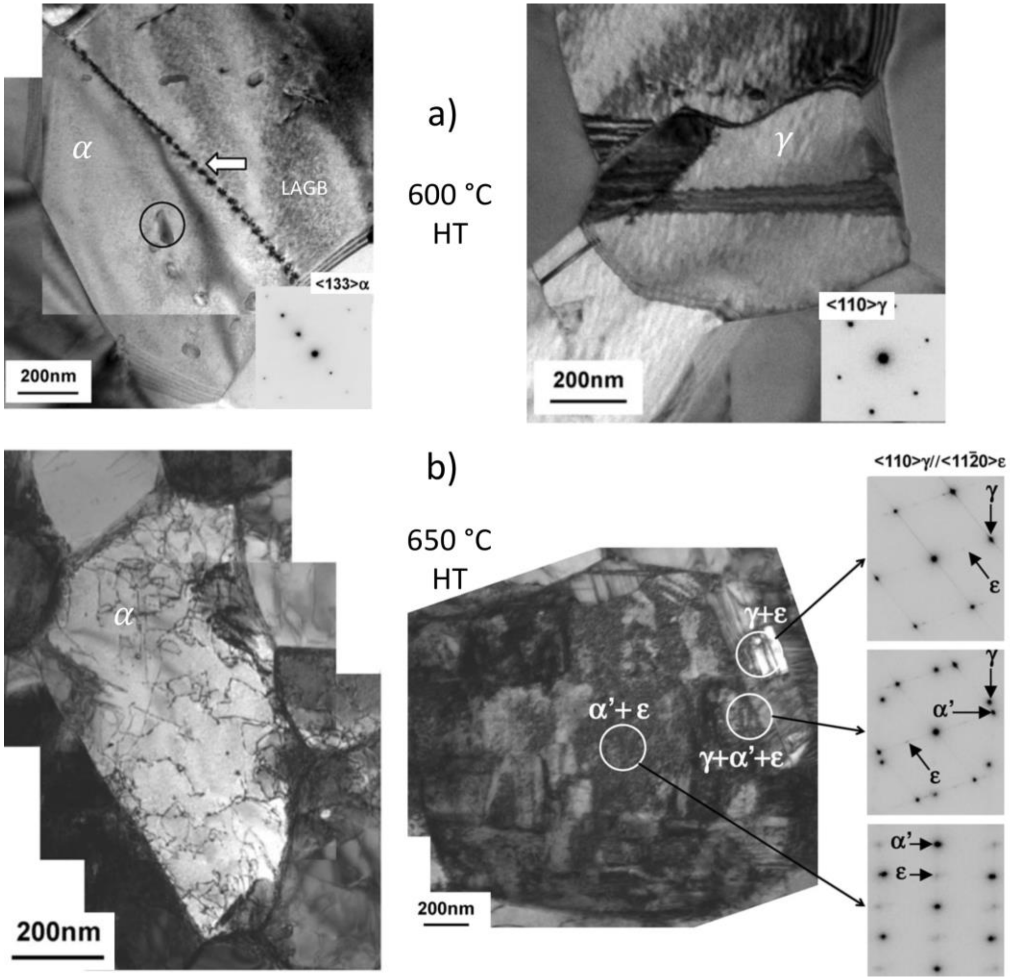
α
LAGB
<133>α
200nm
a)
600 °C
HT
γ
<110>γ
200nm
α
200nm
b)
650 °C
HT
α'+ ε
γ+α'+ε
γ+ε
200nm
<110>γ//<11$\bar{2}$0>ε
γ
ε
γ
α'
ε
α'
ε

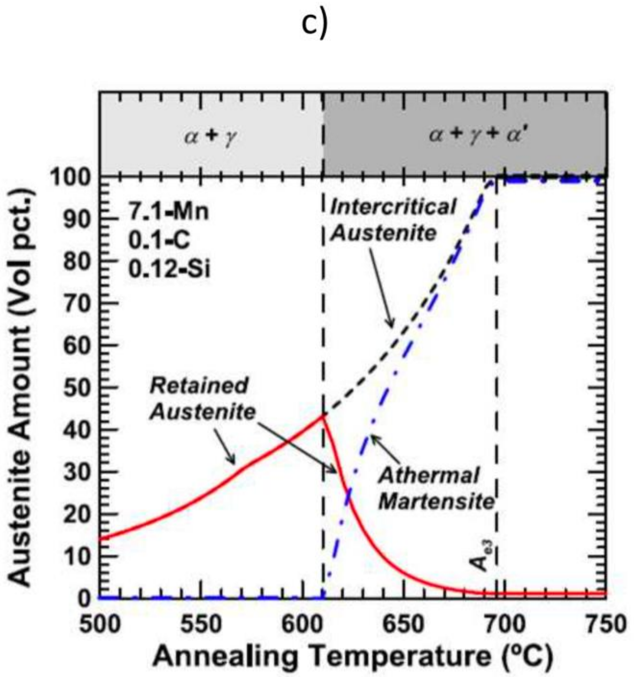
c)
α + γ
α + γ + α'
7.1-Mn
0.1-C
0.12-Si
Intercritical Austenite
Retained Austenite
Athermal Martensite
A_{e3}
Austenite Amount (Vol pct.)
0
10
20
30
40
50
60
70
80
90
100
500
550
600
650
700
750
Annealing Temperature (ºC)

Figure 2-9: 7.1Mn-0.12Si-0.1C TRIP steel annealed for 168 h at a) 600 °C and b) 650 °C, followed by water quenching. BF-TEM images (with inset SAED patterns) were recorded prior to any tensile testing. a) The UFG microstructure annealed at 600 °C for 168 h is predominately dislocation free, while the UFG microstructure b) annealed at 650 °C for 168 h has dislocation tangles in the ferrite, and some fully transformed austenite grains, consistent with c) the predicted austenite stability. Figure a-b from De Cooman *et al.* [124] and c) from Gibbs [7].

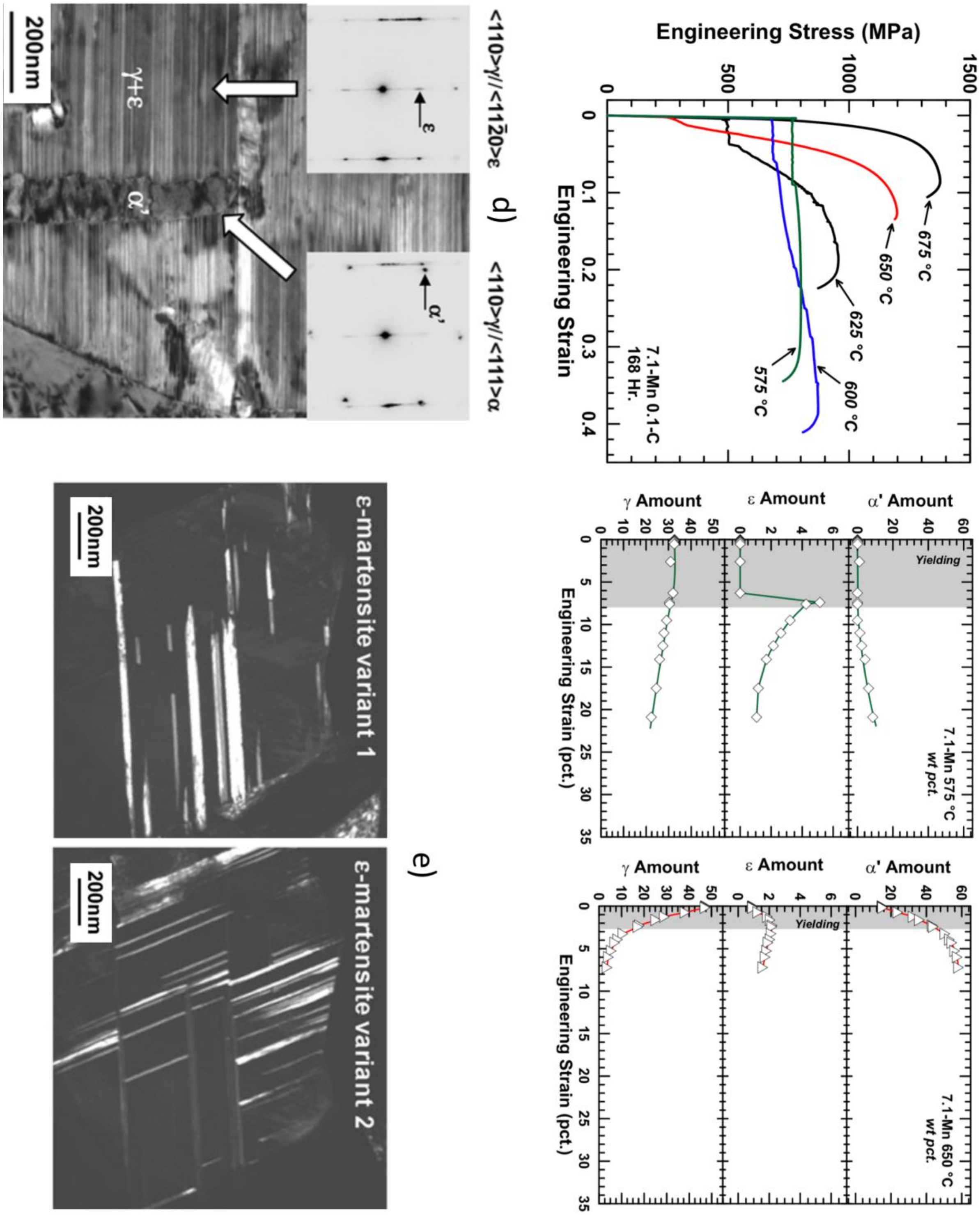

Figure 2-10: a) Quasi-static engineering stress-strain curves from room-temperature tensile testing of the 7.1Mn-0.12Si-0.1C steel annealed for 168 h at the temperatures listed on the figure and water quenched. Relative austenite and martensite fractions as a function of engineering strain measured with in-situ neutron diffraction for the b) 575 °C and c) 650 °C heat treatments. d) Bright-field TEM images (with inset SAED patterns) of an austenite grain in a sample annealed at 600 °C and deformed to 10 % engineering strain shows a high density of ε-

martensite plates, which locally nucleated strain-induced α′-martensite. e) Dark-field TEM images of an austenite grain in a sample annealed at 650 °C and deformed to 2 % engineering strain shows multiple variants of ε-martensite. Figures a-c) from Gibbs [7] and figures d-e) from De Cooman *et al.* [124].

Recently, both static and dynamic strain-aging effects have been observed in engineering stress-strain curves and high frame-rate thermal imaging for medium-Mn TRIP steels with equiaxed microstructures of ultrafine-grained ferrite and austenite [40][41][42][43][44][45][46]. The static aging process is characterized by an upper yield point, lower yield point and yield-point elongation when interstitial atoms such as carbon diffuse to and pin edge dislocations. The pinned dislocations are less mobile and when new dislocations are generated with increasing dislocation density, the stress drops from the upper to the lower yield point. Yield-point elongation in low-carbon ferritic steels typically crosses the gauge section of a tensile specimen through a heterogenous band (Lüders banding) and is associated with a low work-hardening rate [136]. The Lüders banding in medium-Mn TRIP steels is more complex as the heterogenous deformation not only increases the dislocation density of ferrite grains, but also initiates stress-assisted ε-martensite transformation of austenite grains [124]. Dynamic strain-aging effects (serrated plastic flow after Lüders banding) has been observed for many medium-Mn steels and examples are shown in Figure 2-10a for specimens intercritically annealed at 600 and 625 °C. The dynamic strain aging is typically characterized with large steps of change in stress and fine serrations in between. Some studies have associated the re-arrangement of interstitial atoms in austenite during a strain-induced transformation as the leading cause of serrations in the tensile curve (after Lüders banding has occurred) [40][41]. Other studies attribute the relatively low activation energy of short-range diffusion of C in dislocations cores [137], C-vacancy complexes, as well rearrangement of C-Mn couples during reorientation of the lattice through the passage of a stacking fault through the FCC lattice [42]. C-Mn couples have been theorized to show prominent behavior in low SFE TRIP steels as the low SFE translates to more widely separated partials and more favorable orientations for pinning stacking faults [42]. Finally, there are many types of dynamic strain-aging events (various types of serrations named Portevin-Le Châtelier bands can exhibit step-wise or jerky flow in stress-strain curves during initiation and propagation of deformation bands) and are similarly attributed in other respects as related to interactions of interstitial carbon with a stacking fault [138]. Moreover, Lüders banding is not practical for complex geometries of automotive parts as some areas become thinner than expected during forming operations and can lead to premature failure, while dynamic strain again can also lead to localized plastic instabilities and premature cracking [42][43][44][45][46]. Therefore, careful analysis of the mechanical properties, composition and microstructure of the medium-Mn steel investigated in this work will be discussed later in the context of such plastic instabilities.

Multi-phase modeling of medium-Mn steels is an important aspect in understanding and predicting alloy design of next-generation AHSS. Matlock et al. predicted the area of opportunity in mechanical properties, appropriate for third generation steels, by applying Mileiko’s composite model [139] and varying the phase fraction of austenite and α′-martensite [33]. In terms of TRIP steel, Ma and Hartmaier were able to include a martensite nucleation parameter, (based on plastic deformation of austenite), to differentiate between the anisotropy of stress-assisted and strain-induced martensitic transformations [140]. However, a recent trend in advanced high-strength steel design includes finite element frameworks to model deformation, with the goal of predicting strain localization in multi-phase steels and informing design strategies. Latypov et al [141] obtained all of the experimentally determined information about the microstructure with electron backscatter (EBSD) maps and concurrently simulated tensile deformation and microstructural changes through 50 % engineering strain using appropriate constitutive models outlined by previous work [142][143]. Moreover, microstructure-based finite-element models may ultimately provide answers that sufficiently explain the complex strain-hardening behavior of multi-phase steels and will assist in the design of next-generation advanced high-strength steels.

2.4 High Strain-Rate Deformation

High strain rates can be achieved in a few ways, mainly the split-Hopkinson bar test, uniaxial ring expansion, dynamic torsion and servo-hydraulic tension [142][143]. The range of strain rates necessary to determine an effect on microstructure involves the consideration of adiabatic heating (not present at quasi-static strain rates) for strain rates approximately greater than $\dot{\varepsilon} = 10^{-3}$ /s. Viscous dislocation-drag kinetics are considered at ultra-high strain rates, (greater than $\dot{\varepsilon} = 10^{3}$ /s), since dislocation velocity approaches the speed of transverse sound waves [146]. Relevant to this work is the transition from quasi-static to low dynamic strain rates ($\dot{\varepsilon} = 10^{-4}$ /s to $\dot{\varepsilon} = 10^{3}$ /s) [11], which can be used to simulate crash conditions and speeds of forming operations. Challenges involving measurement of load, strain and temperature at high rates tends to push the limits of data acquisition and processing, but will be discussed in the following section. As shown in Figure 2-11, TWIP steels possess the highest specific energy absorption of all advanced high-strength steels when axial crush tests are deformed at rates of $\dot{\varepsilon} = 10^{2}$ /s.

One measure of strain-rate sensitivity is measured as the change in flow stress at constant strain, with respect to strain rate [147]. If the stress component increases linearly with respect to strain rate, the material is said to have a positive m coefficient, where m is the slope of the relevant stress vs. strain rate. Flow-stress relationships may be understood as a dynamic interaction of lattice resistance (Peierls barrier), strength of dislocation interactions, interstitial and solid-solution hardening and grain boundaries [148]. However, planar defects also need to be considered in the flow-stress equation as they provide obstacles to subsequent dislocation motion, which is a strengthening mechanism. Gray's review [147] went on to classify some common metals into three groups: pure FCC, BCC & HCP and a special group consisting of alloyed FCC and/or BCC or HCP which deforms primarily by dislocation slip, but eventually develops deformation twinning as a secondary mechanism. Figure 2-12 relates the generalized evolution of mechanical properties with respect to decreasing temperature and increasing strain rate for each of the three groups. High strain rates can have similar effects on flow stress as low temperatures due to the thermal and athermal components of flow stress [149].

$$\sigma = \sigma_a + \sigma_0(\dot{\varepsilon},T) + \sigma_p(\dot{\varepsilon},T,\varepsilon) \qquad \text{(Equation 2-4)}$$

σ = flow stress
σ_a = athermal term (long-range barriers)
σ_0 = frictional term (short-range Peirels barriers)
σ_p = thermally-activated term (other short-range barriers)
$\dot{\varepsilon}$ = strain-rate
T = Temperature
ε = strain

Seen in Equation 2-4, σ_a is the athermal component of flow stress, which stems from long-range barriers to dislocation motion that cannot be overcome by thermal energy, such as grain boundaries, precipitates or dislocation substructures [149]. The Peierels barrier, or frictional component of flow stress (σ_0) represents the stress required to overcome lattice friction and depends on strain rate and temperature. The thermally-activated term (σ_p) is similar to the frictional term in that both depend on strain rate and temperature, but in this case also represents the storage of dislocations (accumulated through strain) [18]. Thermal components in flow stress originates with short-range obstacles to dislocation motion, which can be overcome by thermal energy [150]. For body centered cubic (BCC) metals, the primary short-range barrier is the Peirels stress (σ_0) and for FCC is dislocation forests (related to σ_p), which translates to differences in strain-rate sensitivities for pure BCC and pure FCC materials [150]. Solute atoms can also act as thermally-activated short-range barriers, especially Si in high-Mn austenitic steels, which will be discussed in section 4.2.9 through the context of high strain-rate behavior [65].

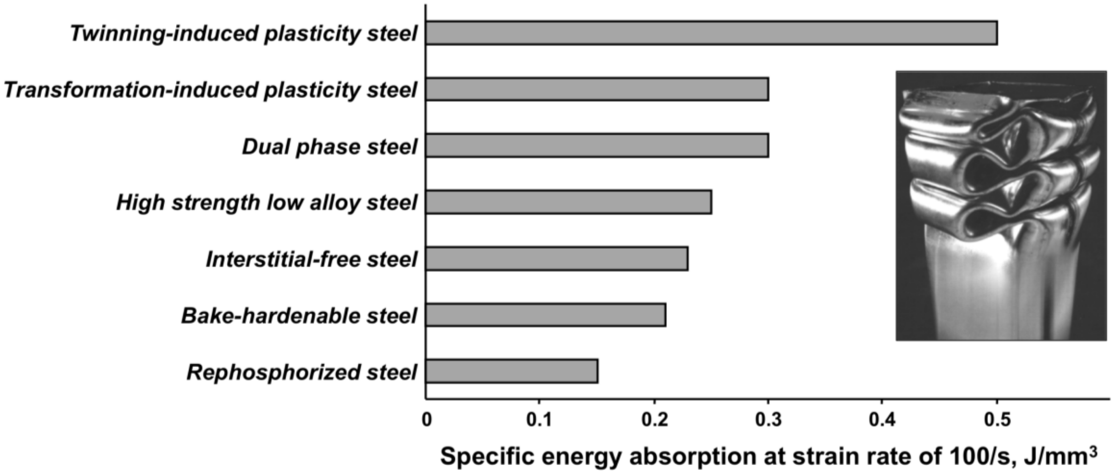

Figure 2-11: A qualitative comparison of the crash performance properties (obtained after high strain rate axial crush tests) of various generations of advanced high strength steels. Figure from De Cooman *et al.* [101].

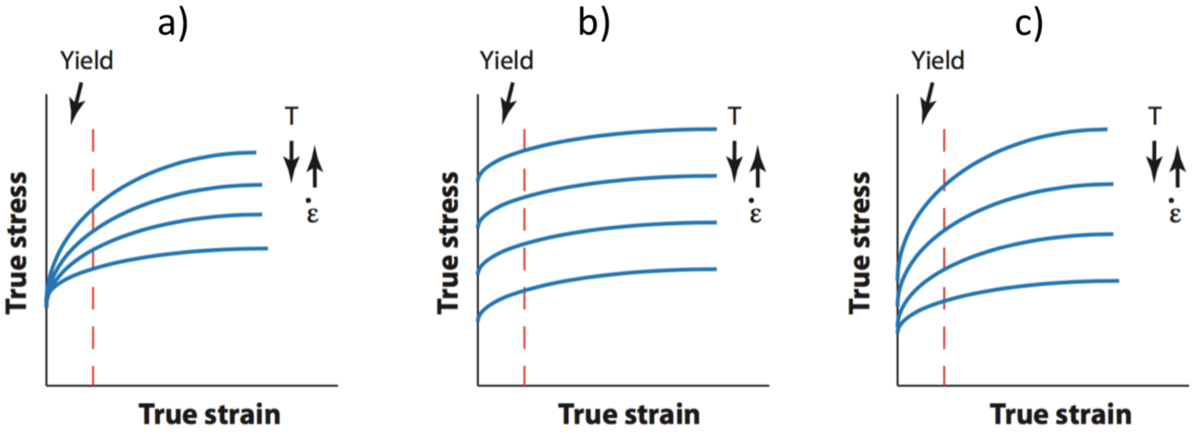

Figure 2-12: The generalized effect of an increase in strain rate on true stress-strain curves for: a) pure FCC b) pure BCC & pure HCP c) alloyed FCC and/or BCC and HCP which develop deformation twinning. Figure from Gray [148].

Campbell *et al.* [151] studied annealed mild steel (a microstructure with polycrystalline BCC crystal structure) and measured a positive strain-rate sensitivity of the lower yield stress (see Figure 2-13). Specifically, lower yield stress increases linearly with strain rate for various temperatures (195 K to 373 K), where the thermal component dominates (from $\dot{\varepsilon} = 10^{-2}$ /s to $\dot{\varepsilon} = 10^{3}$ /s). However, at strain rates of $\dot{\varepsilon} = 10^{4}$ /s and greater, where viscous drag influences dislocation velocity, the lower yield stress increases in a parabolic manner with increasing strain rate. These observations are consistent with the expectation that the Peirels barrier in BCC metals contributes to strong positive strain-rate sensitivity when thermally-activated and time-dependent short-range barriers dominate the contribution to yield stress by inhibiting dislocation mobility [150] as generalized in Figure 2-12b. To clarify, if long-range dislocation interactions dominate a given stress component, little to no strain-rate sensitivity is expected [149], which is the case when mild steel is deformed at high temperatures (493 K and 713 K) and strain rates below $\dot{\varepsilon} = 10^{3}$ /s [151].

Thermally-activated dislocation mobility in alloyed FCC steels, such as Hadfield steels also shows a strongly positive strain-rate sensitivity of the flow stress to thermally-activated and time-dependent short-range barriers [152] as the yield strength in Figure 2-14a nearly doubles, (an increase of approximately 500 MPa), when increasing strain rate from $\dot{\varepsilon} = 10^{-3}$ /s to $\dot{\varepsilon} = 10^3$ /s. The generalized behavior of alloyed FCC metals in Figure 2-12c, (increasing strain rate increases yield strength and strain-hardening rate), nearly matches the results of the Hadfield steel (see Figure 2-14a) and Figure 2-14b shows the steep increase in stress at $\dot{\varepsilon} = 10^3$ /s for various values of true plastic strain, which is attributed to viscous drag on dislocations [152]. In contrast, pure FCC materials such as copper only exhibit a modest increase in yield stress of approximately 100 MPa when strain rate is increased 7 orders of magnitude (see Figure 2-15), which is consistent with the behavior described in Figure 2-12a.

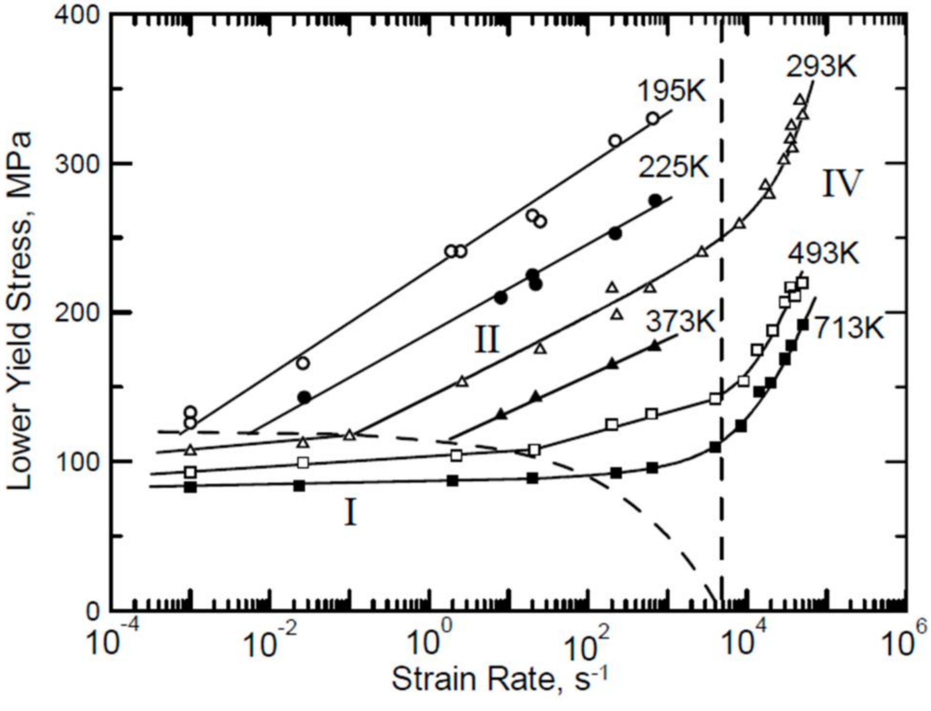

Figure 2-13: Strain rate and temperature dependence of lower yield stress in an annealed mild steel, organized by areas of dominating contributions such as I) athermal components II) thermal components and IV) viscous drag of dislocation velocity. Figure re-plotted by Bruce [153] from Campbell *et al.* [151].

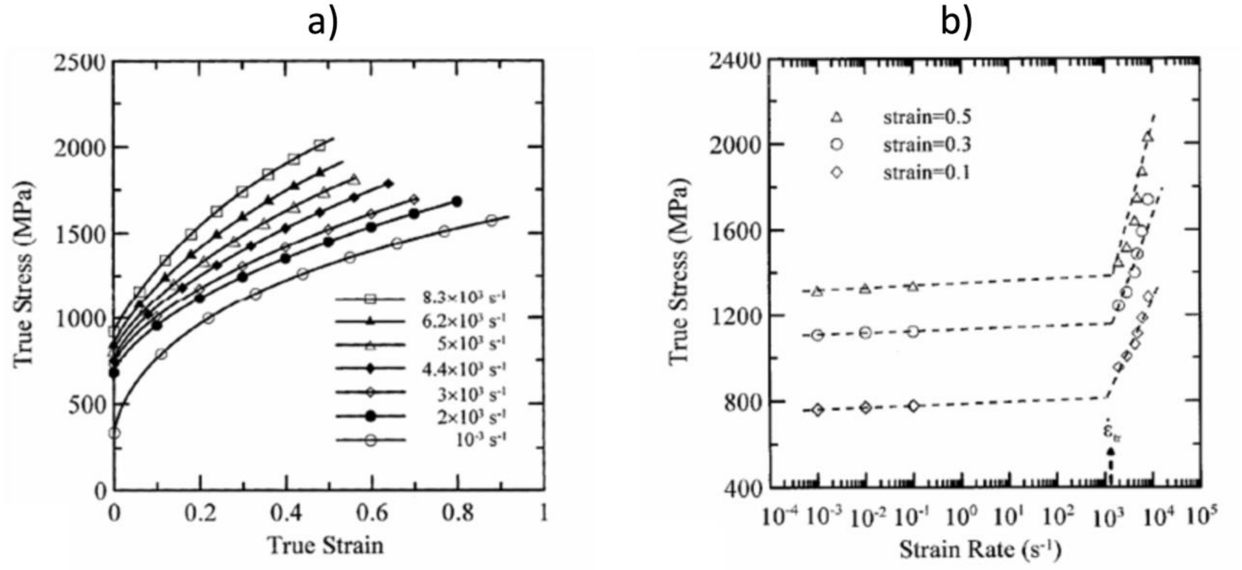

Figure 2-14: a) True stress-strain curves and b) strain-rate dependence of flow stress of a Hadfield Steel for room temperature tensile tests. Figure from Lee et al. [152].

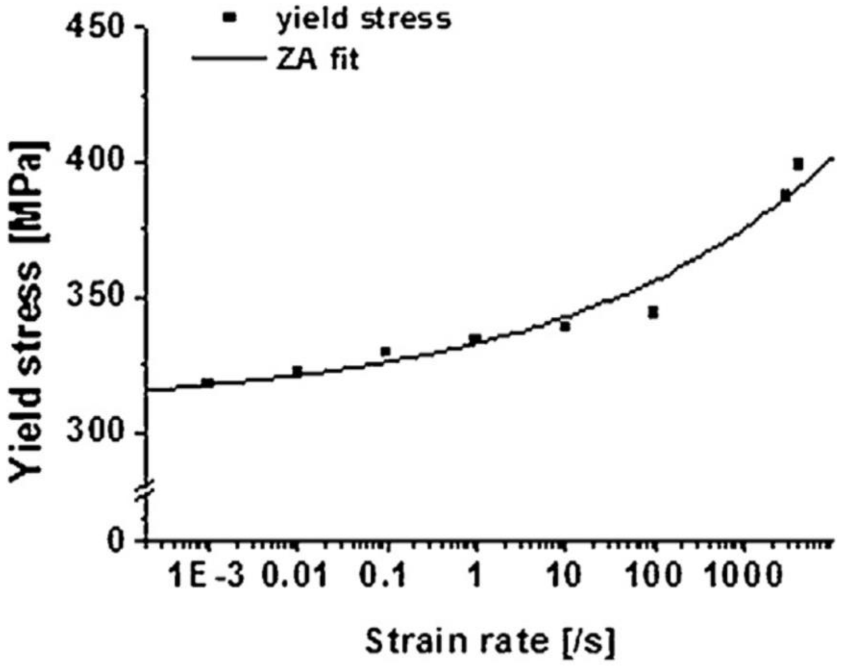

Figure 2-15: Strain rate dependence of yield stress in OFHC Cu (ZA is the Zerilli and Armstrong model). Figure from Huh *et al.* [154].

2.4.1 Mechanical-Testing Recommendations and Interruption at High Strain Rates

A fundamental understanding of the deformation mechanisms of TWIP-TRIP steels at high strain rates will be beneficial for implementing these steels into automotive vehicles and designing future TWIP-TRIP steel grades, particularly as it relates to the response of TWIP-TRIP steels to high strain rates experienced during crashes and advanced forming processes [10]. Under crash conditions, steel components are subjected to a wide range of strain rates, most of which can be simulated with tensile tests in the strain rate range of $\dot{\varepsilon} = 10^{-2}$ /s to $\dot{\varepsilon} = 10^{3}$ /s [11]. Implementation of complex geometries and varying thicknesses of automotive body parts requires a deeper understanding of TWIP-TRIP steel behavior at high strain rates, since many studies on sheet steels have shown an influence of specimen thickness on mechanical properties [155][156][157][158][159]. Interrupted tests are essential for gaining an in-depth understanding of how next-generation steels behave at high strain rates. Interrupted high-rate tests with electromagnetic forming have been reported as far back as 1982 and allow for characterization of the microstructure at appropriate levels of strain [160]. Choi *et al.* [161] measured the volume fraction of retained austenite in two different TRIP sheet steels as a function of strain at rates up to $\dot{\varepsilon} = 6 \times 10^{2}$ /s with the use of an interruption device during high strain-rate tensile testing. The methodology to interrupt high strain-rate tensile tests developed by Choi *et al.* was used in the present work. As such, the structure-property information from high strain-rate tensile tests is potentially useful for models to predict the performance of sheet steel forming behavior and automotive crash response of components in the vehicle body.

2.4.2 Adiabatic Heating

A fraction of plastic deformation is converted to heat during tensile testing and can raise the temperature of the tensile specimen, depending on the rate of plastic deformation [150]. High strain-rate tensile testing does not allow sufficient time for heat to diffuse from the interior of a tensile specimen to the free surfaces, which leads to adiabatic heating. Since adiabatic heating is a product of higher strain rates and SFE is sensitive to temperature, understanding the deformation mechanisms as a function of strain rate for microstructures containing austenite requires quantitative measures of the heat produced during a tensile test [68]. Work by Rodríquez-Martínez *et al.* [17] employed a novel method of in-situ measurements of temperature with a high speed thermal camera during high strain testing of AISI 304 stainless steel at room temperature (see Figure 2-16). The heat generated throughout the gauge section after yielding increased almost linearly as a function of true strain up until the point of necking, upon which the temperature increased dramatically.

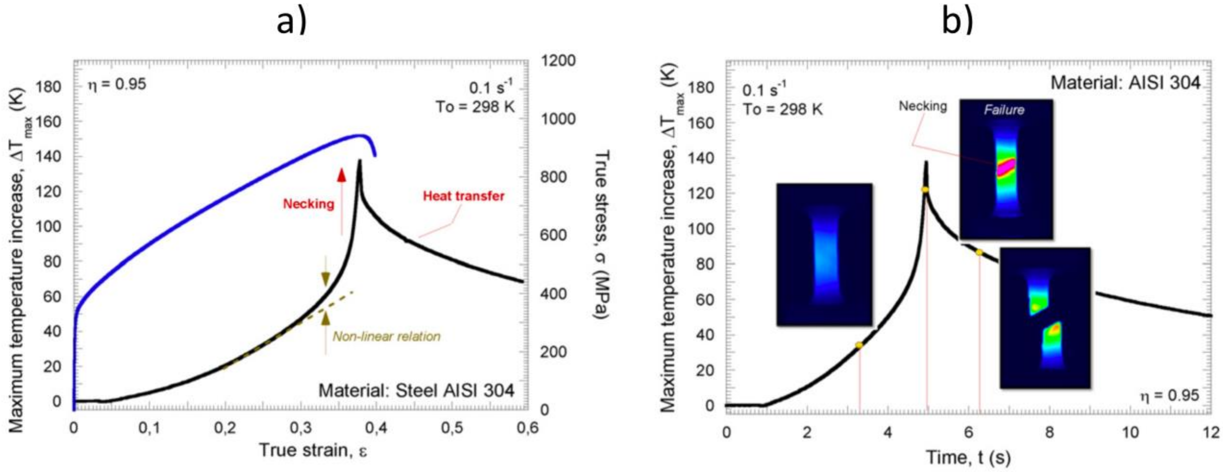

Figure 2-16: a) Maximum temperature increase and true stress as a function of true strain for AISI 304 stainless steel deformed at room temperature. B) Maximum temperature increase as a function of time in AISI 304 stainless steel. Figure from Rodríquez-Martínez *et al.* [17].

$$\Delta T = \frac{\beta}{\rho C_p} \int_0^{\varepsilon} \sigma d\varepsilon \qquad \text{(Equation 2-5)}$$

ΔT = change in temperature
β = conversion efficiency (plastic work to heat)
ρ = mass density
C_p = heat capacity
ε = plastic strain

Equation 2-5 shows the predicted change in temperature (ΔT) as a function of plastic strain (ε) and stress (σ), where β is the efficiency of conversion of plastic work to heat, C_p is the heat capacity and ρ is the material's mass density [150]. Novel experimental techniques have been utilized to measure the amount of retained austenite and rise in adiabatic heating via non-contact methods for TRIP and DP steels [162]. In the case of third generation AHSS, work by Poling [19] on QP980 (Fe-1.79Mn-1.52Si-0.039Al-0.2C in wt%) and TRIP7Mn (Fe-7.14Mn-0.23Si-0.056Al-0.14C in wt%) steels studied the effect of strain rate on mechanical properties using servo-hydraulic tension (see Figure 2-17a/b) and measured the change in temperature at UTS using a high-rate data-acquisition thermocouple system at strain rates from $\dot{\varepsilon} = 1\text{x}10^{-3}$ /s to $\dot{\varepsilon} = 1\text{x}10^{2}$ /s. Most importantly, the adiabatic heating model used in the study on the TRIP7Mn steel, (see specific values as related to Equation 2-5 in Figure 2-17d), confirmed that the heat generated during tensile deformation did not reach adiabatic conditions until a strain rate of $\dot{\varepsilon} = 1\text{x}10^{-1}$ /s and greater. This is an important point of discussion in the next section as related to relative stability of austenite and the TRIP mechanisms, as well as suppression of dynamic strain aging in the medium-Mn AHSS.

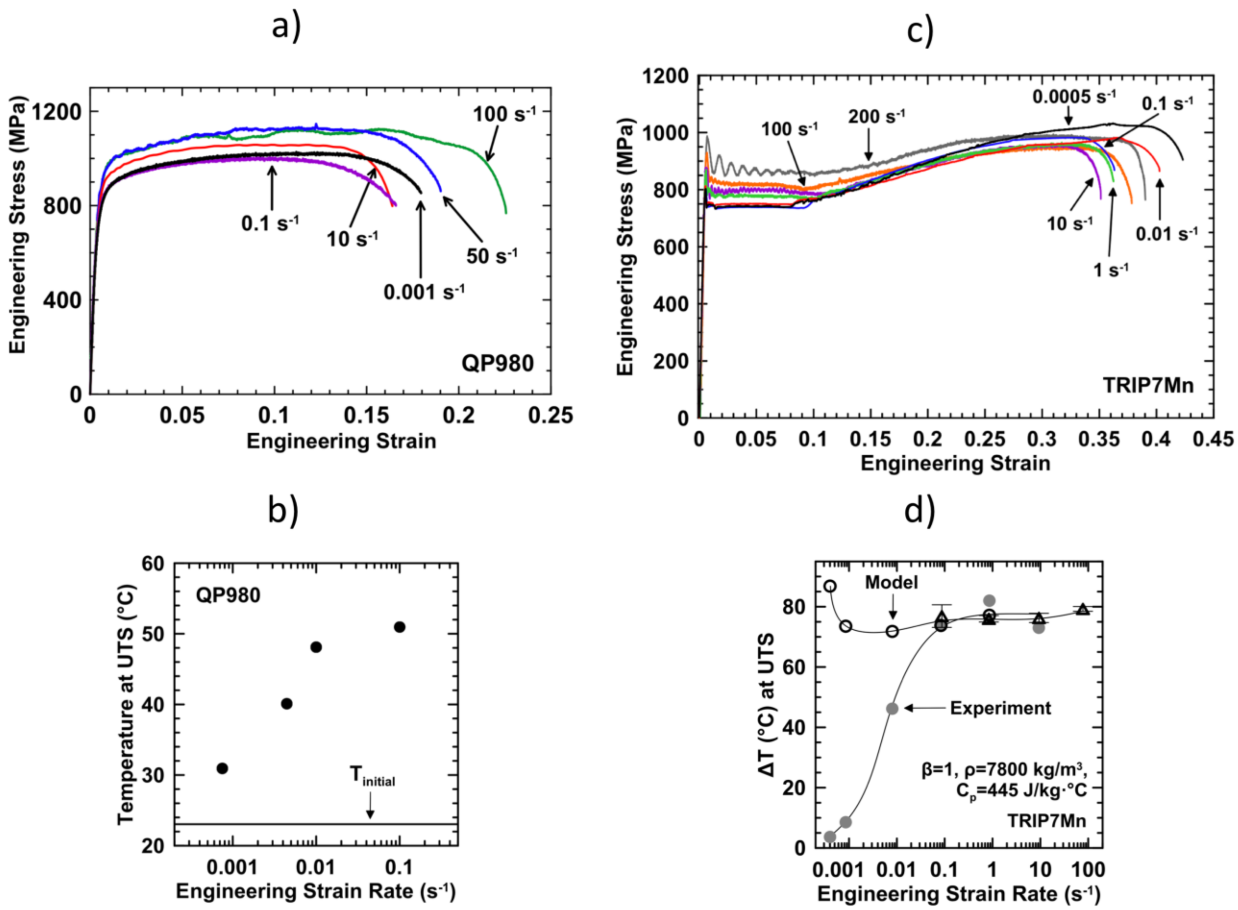

Figure 2-17: a) Engineering stress-strain curves for quenched and partitioned 980 steel deformed at strain rates from $\dot{\varepsilon}$ = 1x10^{-3} /s to $\dot{\varepsilon}$ = 1x10^{2} /s at room temperature and b) corresponding temperatures at UTS. c) Engineering stress-strain curves for TRIP7Mn steel deformed at strain rates from $\dot{\varepsilon}$ = 5x10^{-4} /s to $\dot{\varepsilon}$ = 2x10^{2} /s at room temperature, plus d) corresponding change in temperature at UTS for a given strain rate and an adiabatic heating model. Figures from Poling [19].

2.4.3 Effects of Strain Rate on Deformation Mechanisms in High-Mn and Medium-Mn Steels

In the high strain-rate condition, some FCC metals that possess a high SFE and do not normally twin under quasi-static deformation, may actually twin easily at the high stress levels associated with high rates of plastic strain [148]. The second fold of these conditions reveals that certain materials, which already favor twinning at intermediate environment temperatures and strain rates, may display an increase in twinning density in more extreme conditions when viscous drag of dislocations contributes more significantly to flow stress, as compared to the equilibration of heat [148]. Although temperature influences SFE, which influences mechanical properties, temperature also has a direct effect on mechanical twinning. Specifically, Steinmetz et al [77] showed that an increase in temperature from 293 to 473 K delayed the onset of twinning from 0.1 to 0.18 true strain in a high-Mn TWIP steel, due to an increase in critical stress for twinning. Effectively, at 473 K the strain-hardening rate was lower at early levels of strain as compared to 293 K, but the twin volume fraction after 0.4 true strain was nearly the same. At 673 K and above, the typical boost in strain-hardening rate due to twinning is nearly absent, which means the onset of twinning was delayed to high levels of strain such that the change in twin volume fraction never reached its full potential as compared to room temperature. However, when considering only yielding behavior in AHSS, short-range barriers have been shown to be the leading causes of increases in strain-rate sensitivity for ferritic stainless, austenitic stainless, dual-phase, quenched and partitioned and TRIP steels (see Figure 2-18). The strain-rate sensitivity of the ferritic stainless steel was nearly the same as the austenitic stainless steels, indicating the BCC Peirels barriers have similar contributions (in terms of order of magnitude) as thermally-activated short-range FCC barriers.

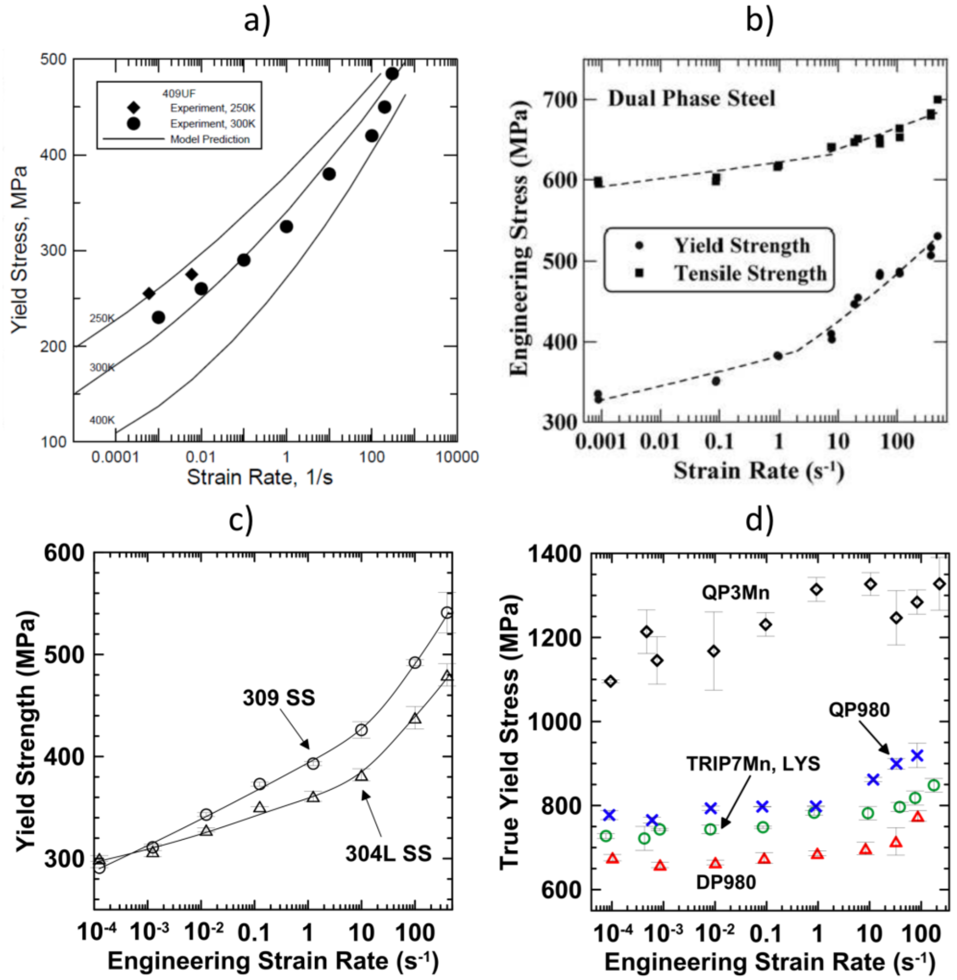

Figure 2-18: Yield stress versus strain rate measured at room temperature for a) 409 ULTRA FORM® ferritic stainless steel, b) a commercial dual phase steel, c) 309 and 304L stainless steels and d) dual-phase 980, quenched and partitioned 980, quenched and partitioned 3Mn and TRIP 7Mn steels, (LYS is the lower yield stress measured after yield-point elongation). Figure a) from Clarke *et al.* [163], b) from Bruce [153] c) from Lichtenfeld *et al.* [16] and d) from Poling [19].

The work of Grässel *et al.* [30] is of particular interest for the first half of the present study on a Fe-25Mn-3Al-3Si wt% steel as the high strain-rate mechanical properties were previously measured with sub-sized tensile samples using multiple mechanical testing methods. The results seen in Figure 2-19 show a strong strain-rate sensitivity of the yield and ultimate tensile strengths, which was not discussed in detail as the focus of the paper pointed more towards the other high-Mn steel alloy development and the effects of temperature on mechanical properties. Grässel *et al.* [30] measured a small negative strain-rate sensitivity of uniform elongation and attributed the observation to adiabatic heating, but the relative increase in temperature during testing was never measured. Further, only twinning was observed in TEM and no high strain-rate tests were interrupted to investigate the evolution of the microstructure. As Pierce [31] identified the combination of twins and hexagonal ε-martensite, the present work will investigate the role of strain rate on any changes in microstructural evolution that may occur due to changes in stacking fault energy. A study by Curtze *et al.* [68] measured the effects of stacking fault energy, temperature and strain rate for Fe-Mn-Al-Si steels. The chemical and magnetic contributions to SFE are shown in Figure 2-20a and the effect of temperature on SFE is represented in Figure 2-20b. Mainly, all Fe-Mn-Al-Si steels possessed room-temperature SFE values between 20 and 45 mJ/m^2 (the twinning-dominated regime) and the alloy with a RT SFE of 42 mJ/m^2 (labeled TWIP 3) would need to be deformed at a temperature of approximately 85 °C to change the SFE to a value that would suppress twinning. Furthermore, all three TWIP steels had positive strain-rate sensitivities of YS and UTS (see Figure 2-20c). Notably, increasing the strain-rate from $\dot{\varepsilon}$ = 1x10^{-3} /s to $\dot{\varepsilon}$ = 1x10^3 /s increased the uniform and total elongations of the TWIP steel with the RT SFE of 21 mJ/m^2 (labeled TWIP 1) whereas the TWIP steel with the RT SFE of 42 mJ/m^2 (labeled TWIP 3) exhibited a reduction in uniform and total elongations, which was attributed to an increase in SFE through adiabatic heating [68].

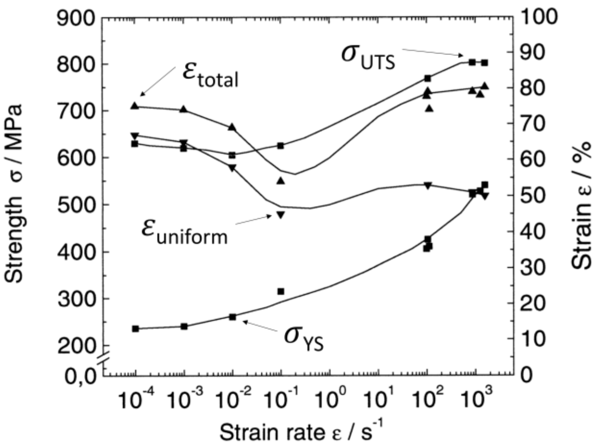

Figure 2-19: Strain rate dependence of yield strength (0.2% offset), ultimate tensile strength, uniform elongation and total elongation for a Fe-25Mn-3Al-3Si (wt%) steel deformed at room temperature. Figure from Grässel [30].

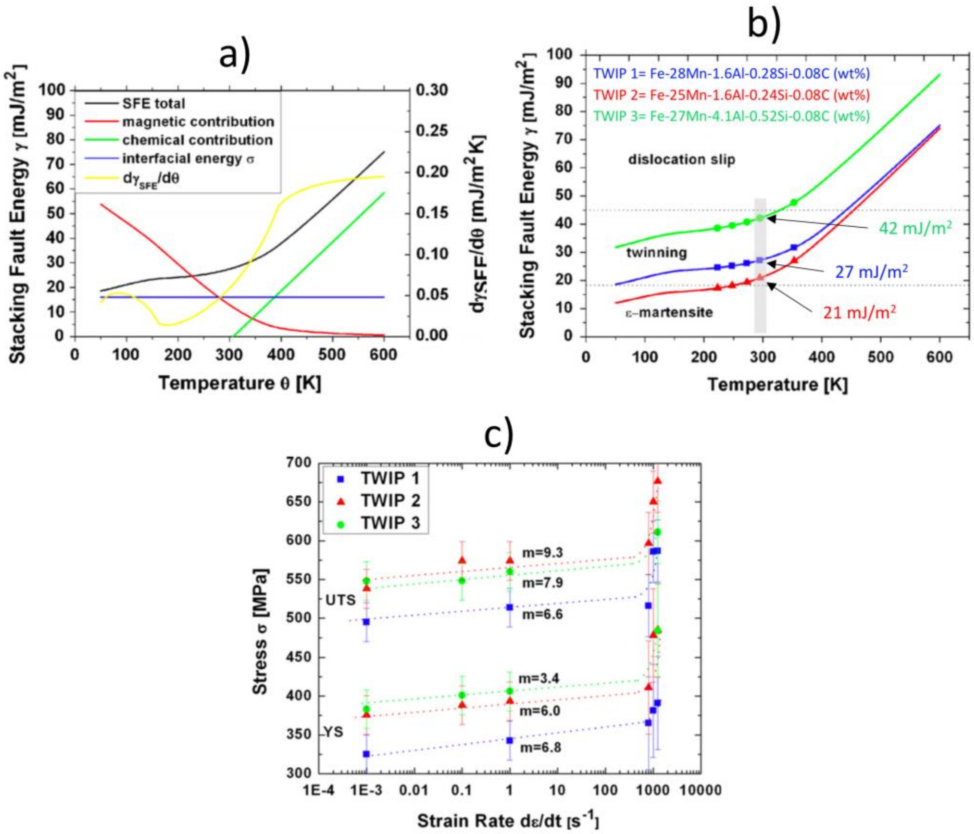

Figure 2-20: a) Stacking fault energy of TWIP 1 as a function of temperature (θ) broken down into components of chemical, magnetic and interfacial contributions. B) Stacking fault energies of the 3 TWIP alloys as a function of temperature (θ). Room temperature values are highlighted. c) Strain rate dependence of yield strength and ultimate tensile strengths of 3 TWIP steels. Slope $m = d\sigma/d \ln\dot{\varepsilon}$ is the strain-rate sensitivity factor. Figures from Curtze *et al.* [68].

The effect of strain rate (from $\dot{\varepsilon} = 1\text{x}10^{-5}$ /s to $\dot{\varepsilon} = 1\text{x}10^{-1}$ /s) on mechanical properties and deformation mechanisms was studied previously for a Fe-12Mn-0.6C TWIP steel [20]. The authors concluded that lower strain rates favor austenite to ε-martensite TRIP effects whereas high strain rates favor mechanical twinning of austenite, (TWIP effects). The strain-rate dependence of the plasticity enhancement was due to a critically resolved shear stress (CRSS) dependence of the ε-martensite on temperature, rather than the slight increase in SFE due to adiabatic heating. Furthermore, Lee *et al.* [20] also reported that with increasing strain rate, the strain-hardening rate initially decreased and then increased again. The highest strain-hardening value achieved was at the lowest strain rate when TRIP effects dominated and the strain-hardening values had a minimum at 10^{-3} ε/s when TRIP & TWIP effects were in competition [20]. However, this fully austenitic steel contained Portevin-Le Chatelier bands during deformation, due to the significant amount of carbon present. Another study by Yang *et al.* [21] investigated two austenitic steels that revealed contrasting behaviors. The DSA-free FeMnSiAl steel did not show any strain-rate sensitivity of twinning density for all studied strain rates (from $\dot{\varepsilon} = 10^{-4}$ /s to $\dot{\varepsilon} = 10^{0}$ /s) and exhibited a strong positive strain-rate sensitivity of the YS, UTS and PSE (see Figure 2-21a) [21]. The FeMnC steel, which deformed in part through dynamic strain-aging (DSA) at quasi-static strain rates, showed an obvious decrease in density of twin boundaries and DSA activity at higher strain rates and a negative strain-rate sensitivity of the YS and UTS (see Figure 2-21b) [21]. It is possible that negative strain-rate sensitivity can occur in steels due to the influences from a change in twinning and/or transformation rate of austenite, as well as the critical strain for onset of DSA [20][164]. As DSA activity declines with increasing strain rate during room-temperature tensile tests, strain rate sensitivity of the UTS becomes negative [19].

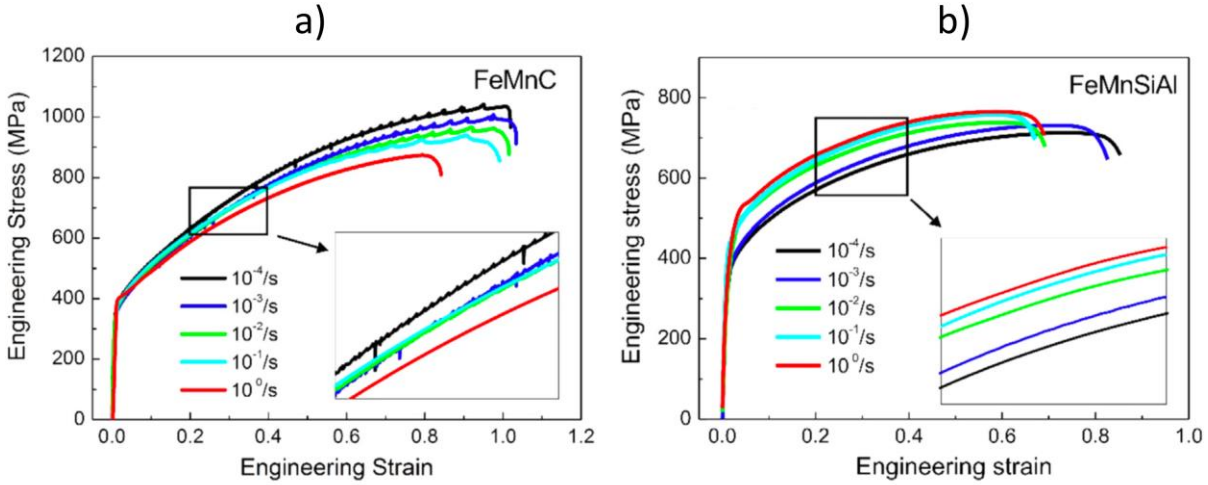

Figure 2-21: Tensile engineering stress-strain curves of a) FeMnC and b) FeMnSiAl TWIP steels deformed at strain rates from $\dot{\varepsilon} = 1\text{x}10^{-4}$ /s to $\dot{\varepsilon} = 1\text{x}10^{0}$ /s at room temperature. Figures from Yang *et al.* [21].

For room-temperature tensile tests at quasi-static strain rates, there are many articles that have investigated deformation mechanisms and mechanical properties of medium-Mn steels by reporting the effect of intercritical annealing temperature, phase size and phase fractions of the microstructure [39][55][56][165][54] as has been discussed previously in section 2.3. Extensive work by Poling [19] on a TRIP7Mn steel included changing the environment test temperature and strain rate to study mechanical properties (Figure 2-22a) and used an interruption device [13] and X-ray diffraction to measure the transformation rate of retained austenite (see Figure 2-22b). The TRIP7Mn steel (Fe-7.14Mn-0.23Si-0.056Al-0.14C in wt%) consisted of an equiaxed ferrite-austenite UFG microstructure and had significant static aging (Lüders banding) and dynamic strain aging during room temperature quasi-static servo-hydraulic tensile tests. Poling [19] noted that adiabatic heating causes an increase in austenite stability, (less TRIP activity due to an increase in SFE), during high strain-rate tests at all test temperatures and the test temperature of 70 °C showed the greatest stability. Also, the discontinuous serrated plastic flow disappeared at high strain rates and was attributed to adiabatic heating. The disappearance of DSA at high strain rates, specimen self-heating at high levels of plastic strain and significant adiabatic heating at high strain-rates all contributed to the negative strain rate sensitivities of the UTS and UE (see Figure 2-22d/f). However, the upper and lower YS had positive strain-rate sensitivities, indicating the short-range barriers played a significant role during yielding of the multi-phase medium-Mn TRIP steel. Increasing temperature generally decreased strength and increased ductility (see Figure 2-22c/e) for the same steel [19]. To contrast and compare the work by Poling [19], the transformation rate of austenite was not affected by strain rate and adiabatic heating in a TRIP700 steel (Fe-1.6Mn-1.5Al-0.22C-0.05Si supplied by Thyssen-Krupp Stahl AG), but an increase in environment temperature stabilized the austenite by increasing the SFE [14], as shown in Figure 2-23. Poling concluded several reasons for the disparity between high strain-rate test results of various TRIP steels, including more heat dissipation during testing from miniature specimens, differences in thermal conductivity, initial austenite content and grain size/morphology [19].

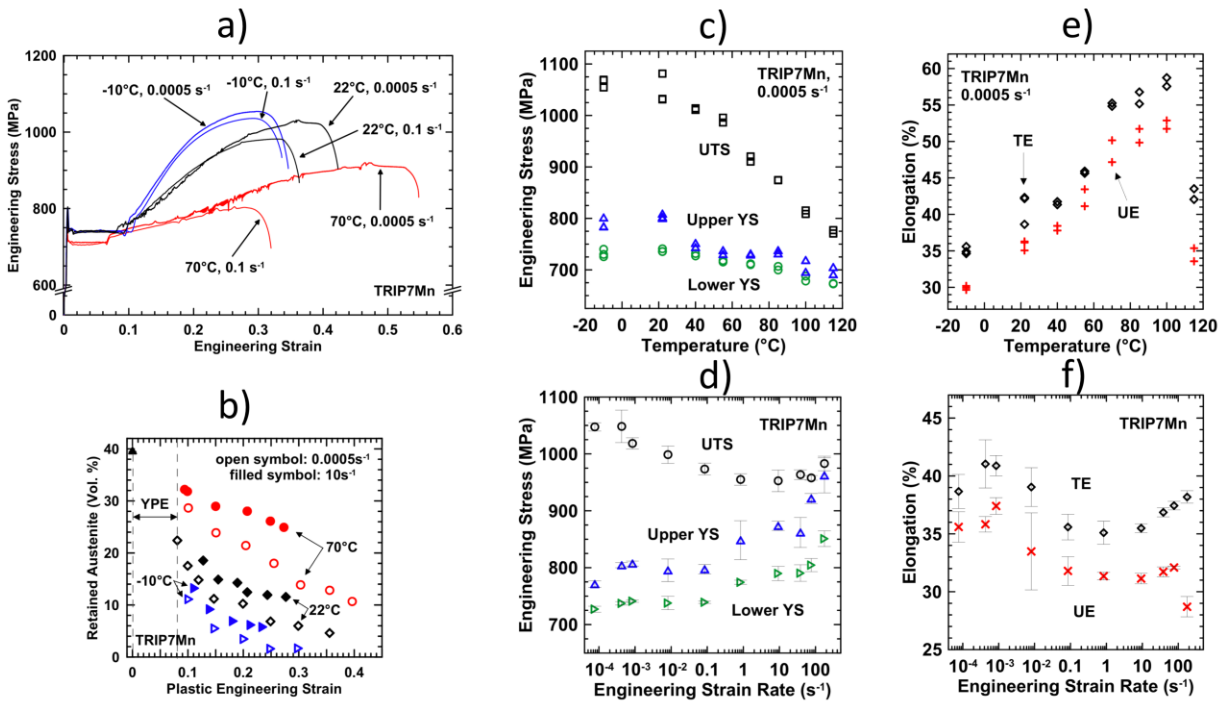

Figure 2-22: a) Engineering stress-strain curves for TRIP7Mn steel from tensile tests at strain rates of $\dot{\varepsilon} = 5\text{x}10^{-4}$ /s to $\dot{\varepsilon} = 1\text{x}10^{-1}$ /s and temperatures of -10, 22 and 70 °C, plus the corresponding changes in retained austenite volume % as a function of plastic engineering strain. Dependence of yield strengths and ultimate tensile strenghts on c) temperature and d) strain rate. Dependence of uniform and total elongation on e) temperature and f) strain rate. Figures from Poling [19].

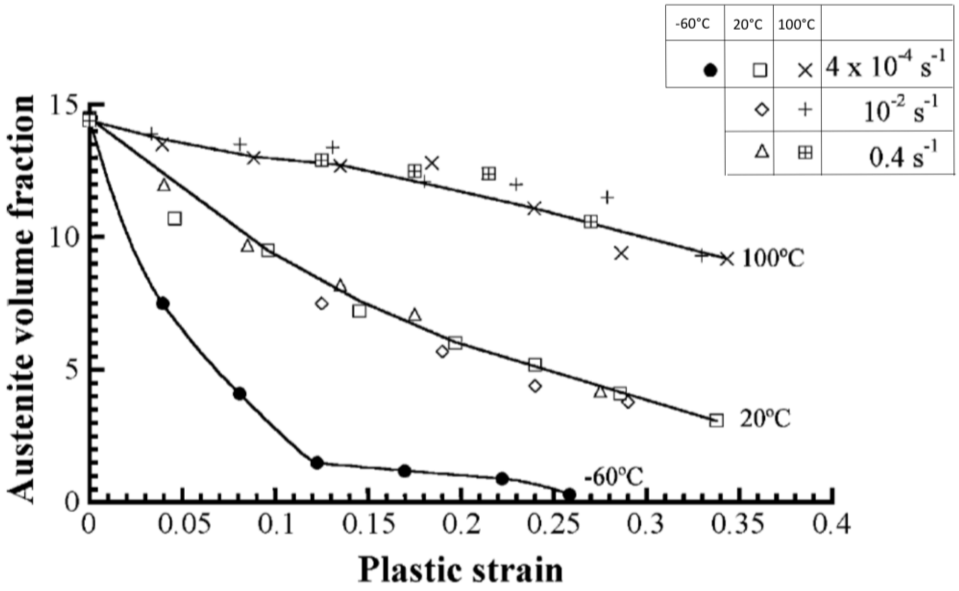

Figure 2-23: Tensile test results for TRIP700 steel tested at strain rates from $\dot{\varepsilon} = 4\text{x}10^{-4}$ /s to $\dot{\varepsilon} = 4\text{x}10^{-1}$ /s for three different temperatures (- 60, 20 and 100 °C). Figures from Jiménez *et al.* [14].

2.5 Objectives and Goals

There is strong agreement in the literature concerning the effects of environment test temperature on tensile properties and stacking fault energy of austenite in second and third generation AHSS. An increase in environment test temperature diminishes strength and work-hardening rate, increases the stacking fault energy of austenite and decreases the transformation rate of austenite [12][13][14][77][68][19][21][148][60][66][30][67][61][68][69]. However, based on the literature presented in this chapter, there is significant scatter and disagreement regarding the effects of strain rate and adiabatic heating on the martensite transformation rate and activity of twinning during high strain-rate deformation. Depending on the austenite fraction, morphology, grain size, phase composition and stacking fault energy, an increase in strain-rate can lead to a decrease in martensite transformation rate [15][16][17][18][19], an increase in density of mechanical twinning [21][148], a transition from transformation-dominated to twinning-dominated plasticity-enhancing mechanisms [20], or no effect at all on the transformation rate [13][14]. The effect of adiabatic heating is certainly more prevalent at higher strain-rates and high levels of accumulated strain, but based on which strengthening mechanisms are used in various high-Mn and medium-Mn steels, the temperature and strain-rate contributions to the thermal component of flow stress can result in various strain-rate sensitivities of UTS [19][149][150][65][18]. These differentiations of course become more complex in multi-phase steels that deform in part by static and dynamic strain-aging phenomena [40][41][42][43][44][45][46]. Finally, it is possible that more than one of the proposed twinning mechanisms contribute to strain-hardening in a single TWIP steel, plus sensitivities of twinning and dislocation substructures to interstitial content likely contribute to the complex work-hardening behavior of TWIP and TWIP-TRIP steels [79][77][92][93][94][95][96][97].

The goal of this work is to gain a fundamental understanding of the effects of strain rate on the mechanical properties and deformation mechanisms in non-commercial and industrially relevant AHSS. The present research uses advanced characterization techniques and novel in-situ temperature measurement methods during mechanical testing to investigate the fundamental behavior of two AHSS. Where austenite is a major or a minor microstructural constituent (high-Mn and medium-Mn steels respectively) the effect of strain rate on changes in strength, ductility and work-hardening rate of advanced high strength steels are measured. Deformed microstructures are characterized to study the influence of strain rate on the dominant deformation mechanisms in single-phase and multi-phase steels, when austenite SFE is held constant. Specimen heating measurements are used to predict the changes in stacking fault energy using a thermodynamic model to investigate to what degree adiabatic heating affects deformation mechanisms in and tensile properties of TWIP-TRIP steels. Important aspects in alloy design of next generation AHSS such as annealing temperature, bulk composition and constituent composition are considered in regard to austenite SFE and the effects of annealing time on phase fraction and grain size were measured. The effect of annealing time on high strain-rate behavior was also investigated. A range of empirical techniques and results were considered so as to inform constitutive modeling of an AHSS, which allowed for prediction of next generation AHSS properties using tunable parameters relevant for AHSS design.

CHAPTER 3

3. EXPERIMENTAL METHODS

3.1 Materials and Thermo-Mechanical Processing

3.1.1 Fe-25Mn-3Al-3Si Steel

The high-Mn steel alloy, [Fe-24.8Mn-2.99Al-3.03Si-0.019C-<0.001O wt%], was induction melted, cast into an ingot in an Ar atmosphere and thermo-mechanically processed by hot rolling at 1100 °C to produce two 10-mm thick plates. One plate was further processed for uniaxial ring expansion testing and the other for servo-hydraulic tension.

A 50% cold-rolled reduction was applied to one of the 10-mm thick plates to produce a 5-mm thick plate and then recrystallized for 0.5 h in air atmosphere at 900 °C. This plate was used for machining uniaxial ring expansion specimens, where the height of the ring is the thickness of the plate (5 mm). Grain size analysis using ASTM E112 [166] yielded a 20 µm average grain size.

The other 10-mm thick plate was sectioned in half to study the effect of sheet thickness on servo-hydraulic tensile properties. The plate halves were further hot-rolled to 3.0 and 2.2 mm, then a 50% cold-rolled reduction was applied to respectively create 1.5 and 1.1 mm sheets. These sheets were recrystallized for 0.5 h in air at 900 °C. Parallel plate grinding was used to remove the oxide scale and produced final sheet thicknesses of 1.15 and 0.95 mm. Grain size analysis using ASTM E112 [166] yielded a 21 µm average grain size for both sheet thicknesses (1.15 mm and 0.95 mm). Thus, the 1.15 mm thick sheet has a slightly higher thickness-to-grain-size ratio.

3.1.2 Fe-12Mn-3Al-0.05C Steel

The medium-Mn steel alloy, An ingot of [Fe-12.27Mn-3.01Al-0.046C-<0.001O] (wt%) was induction melted, cast into an ingot in an Ar atmosphere and thermo-mechanically processed by hot rolling at 900 °C to 3.4 mm thickness, homogenized in an Ar atmosphere at 1100°C for 2 h, water-quenched to room temperature, (below the Ms temperature) and cold-rolled to 1.7 mm, (a 50 % reduction in thickness), to produce a fully deformed martensitic microstructure. To study the effect of annealing time, samples were annealed at 585 °C for 0.5, 8 and 48 h. Grain size measurements with electron backscatter diffraction of the ultrafine-grained multi-phase microstructure will be discussed in section 4.3.2.

3.2 Specimen Machining and Mechanical Testing

3.2.1 Uniaxial Ring Expansion of High-Mn Steel

High strain-rate uniaxial ring expansion was used to study microstructures after interruption at high strain rates at The Ohio State University. Eight sets of three concentric rings were machined from the 5 mm plate with inner diameters of 15.9, 25.4 & 50.8 mm (a drawing of the concentric rings shown in Figure 3-1a). Wall thicknesses of each ring were chosen such that the same radius/thickness ratio was achieved to keep a consistent hoop-stress state, (when modeled as a thin-walled pressure vessel) [167]. The expansion method was equipped with a large bank capacitor to deliver large amounts of energy on the order of kJ in extremely short timeframes (a few µs) to vaporize an Al wire, which expands an elastomer and eventually the ring of steel, (setup seen in Figure 3-2). A laser was mounted away from the test setup and pointed orthogonally to the outer wall of the expanding ring. The change in frequency is used to calculate velocity and acceleration of the expanded ring via photonic Doppler velocimetry (pDv) [167].

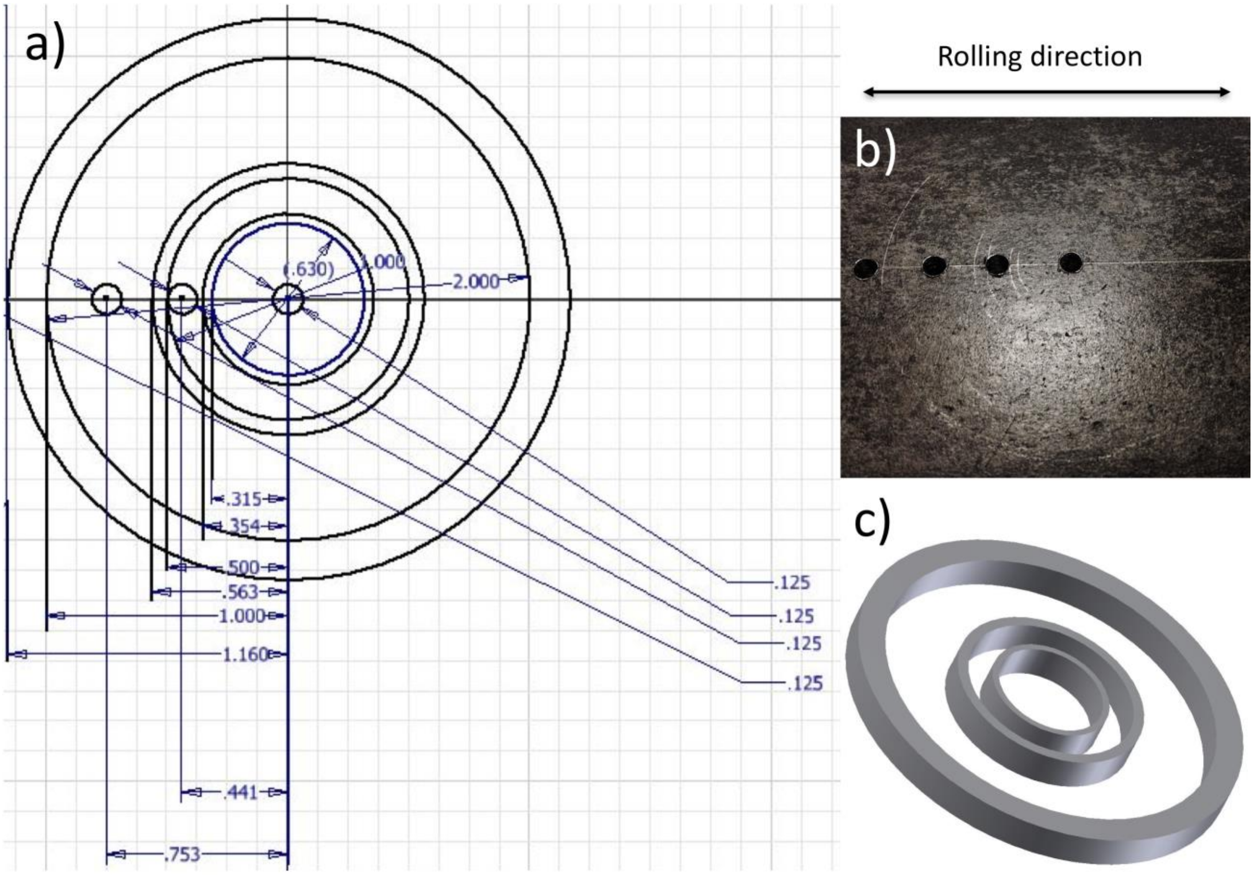

Figure 3-1: a) Drawing of uniaxial ring expansion specimens (units in inches) such that the height of rings is equal to the thickness of the plate. b) specimens were machined along the rolling direction and holes were appropriately drilled to feed the wire through for electro-discharge machining of the c) concentric set of rings.

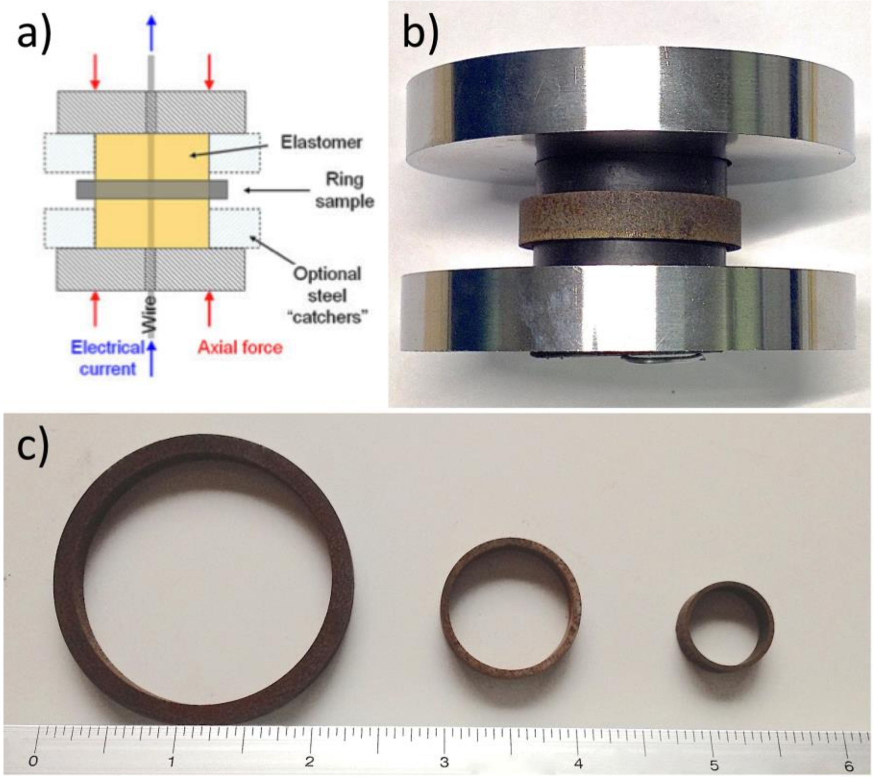

Figure 3-2: a) Schematic of the uniaxial ring expansion setup and b) the actual setup with a medium-sized ring. c) A comparison of the unexpanded ring sizes is shown (ruler units in inches).

3.2.2 Servo-Hydraulic Tension of High-Mn Steel

Tensile specimens for elongation to failure and interruption were wire electro-discharge machined with dimensions as indicated in Figure 3-3, based on specimen designs from Choi *et al.* and Addessio [161][168]. The 3.05 mm radius of the grip notches on the interruption geometry were further notched with a slow speed diamond saw blade to ensure interruption after the desired deformation in the gauge section. The schematic of the interruption device is shown in Figure 3-4. Tensile testing was performed at Colorado School of Mines with a MTS 810 high-rate servo-hydraulic testing system. The system was comprised of a 500 kN capacity frame with a 50 kN capacity actuator. A 400 kN Kistler piezoelectric load washer was used to measure load. Data acquisition rates up to 2.5 MHz are attained through the National Instruments oscilloscope software program VirtualBench Scope™ and a National Instruments 12-bit data acquisition board with four data channels. A two-valve system and a slack adapter on the actuator allow the actuator to move at low and high rates. Strain was measured with a high elongation Vishay EP-08-250BG-120 strain gauge adhered to the specimen with Vishay M-Bond A-12. However, the strain gauge often detached prior to necking of the specimen as the strain gauge is only rated up to a total strain of 0.2. For tests at $\dot{\varepsilon} = 2\text{x}10^1$ /s and slower, the engineering strain rate prior to debonding was used to extrapolate the strain data to fracture. Total strain in every mechanical test was corroborated with caliper measurements of the gauge length before and after tension testing (see Figure 3-5a-b). Specimens were strained in tension at various strain rates (from $\dot{\varepsilon} = 2\text{x}10^{-4}$ /s to $\dot{\varepsilon} = 2\text{x}10^2$ /s) either to failure or to specific strain levels using the interruption device and technique developed by Choi *et al.* [161].

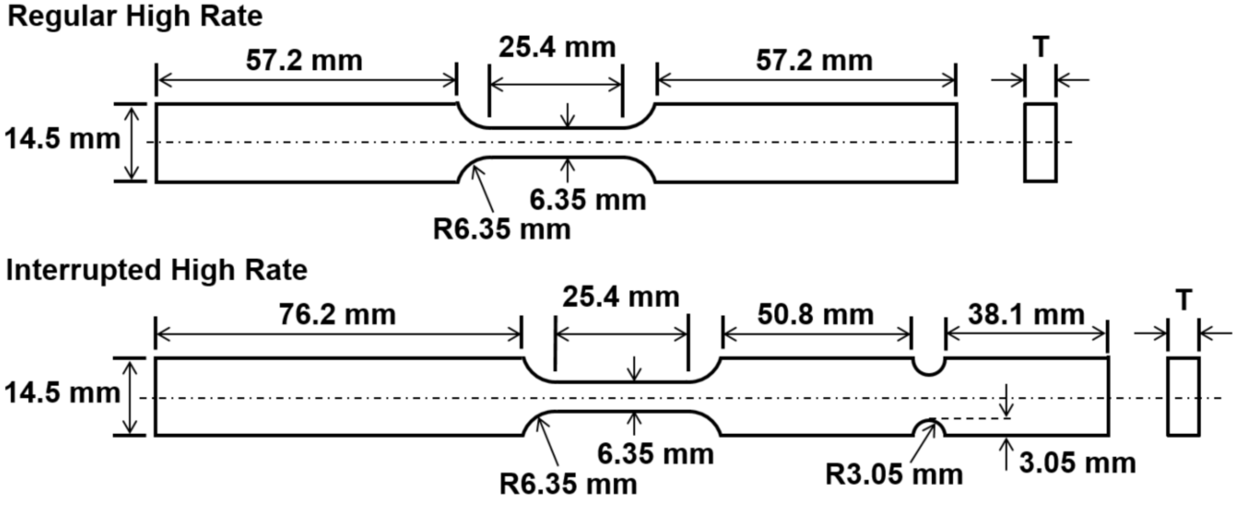

Figure 3-3: Drawing of fabricated tensile specimens for failure and interruption at high strain rates, (T is sheet thickness), based on previous studies [161][168].

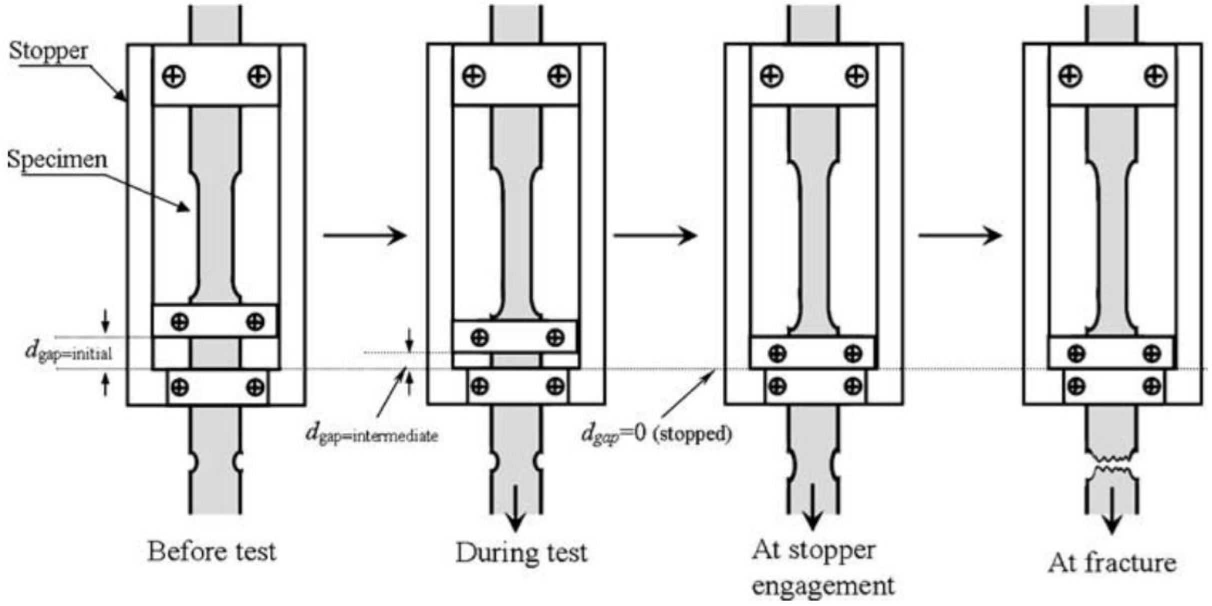

Figure 3-4: Schematic of stopper dynamics during high strain rate interruption of sheet metals. Figure from Choi *et al.* [161].

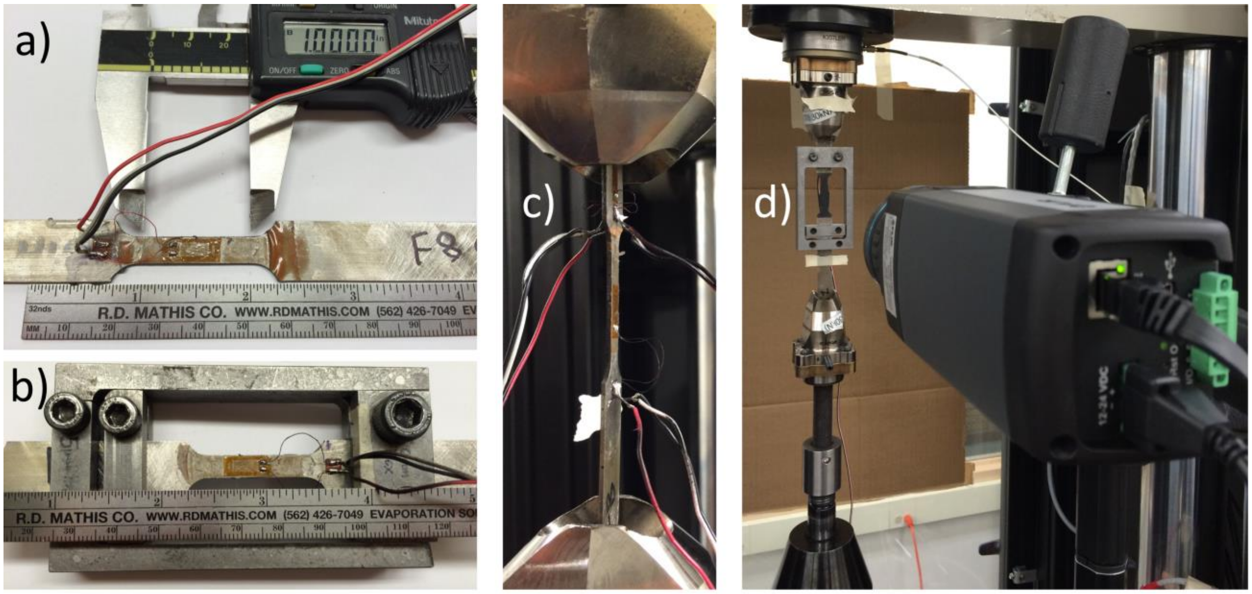

Figure 3-5: a) Strain gauged pull to failure tensile specimen with a 1 inch (25.4 mm) gauge length and the setup with the b) interruption geometry and device (ruler units in inches). c) Setup of a pull to failure test at $\dot{\varepsilon} = 10^2$ /s with a plastic strain gauge mounted on the gauge length and two elastic gauges mounted on the grip section near the load washer. d) Representative thermal camera view of the tensile specimen, in this case during an interrupted test, (note the black spraypaint on the side viewed by the camera).

3.2.3 Servo-Hydraulic Tension of Medium-Mn Steel and Digital-Image Correlation

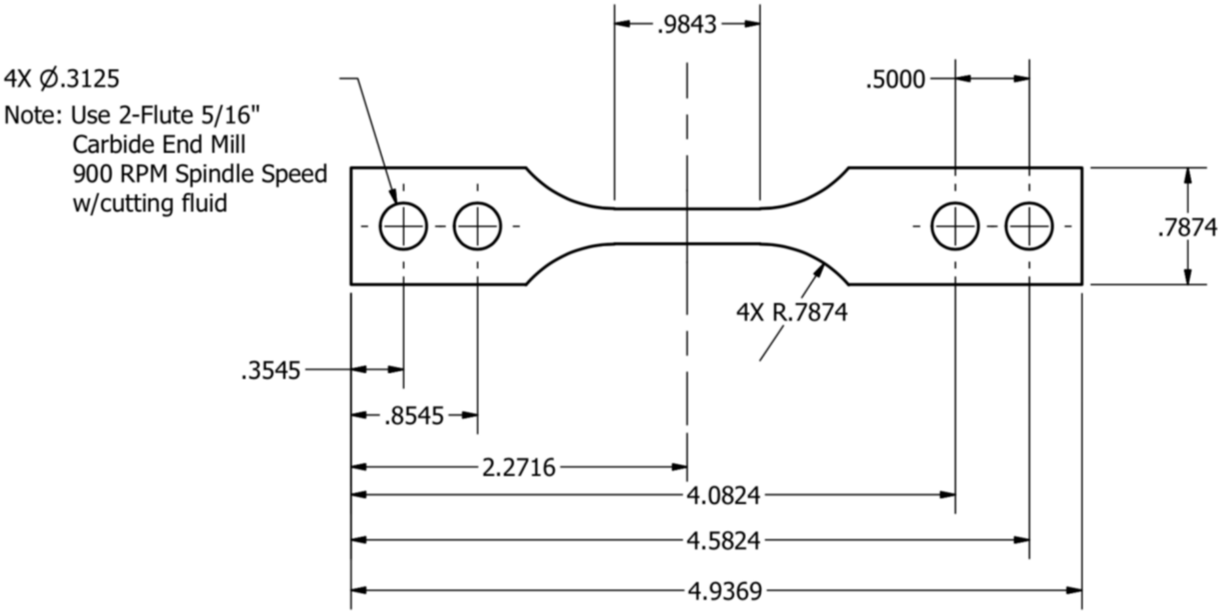

Figure 3-6: Servo-hydraulic specimen geometry for grip-loaded and pin-loaded geometries. Dimensions are expressed in inches.

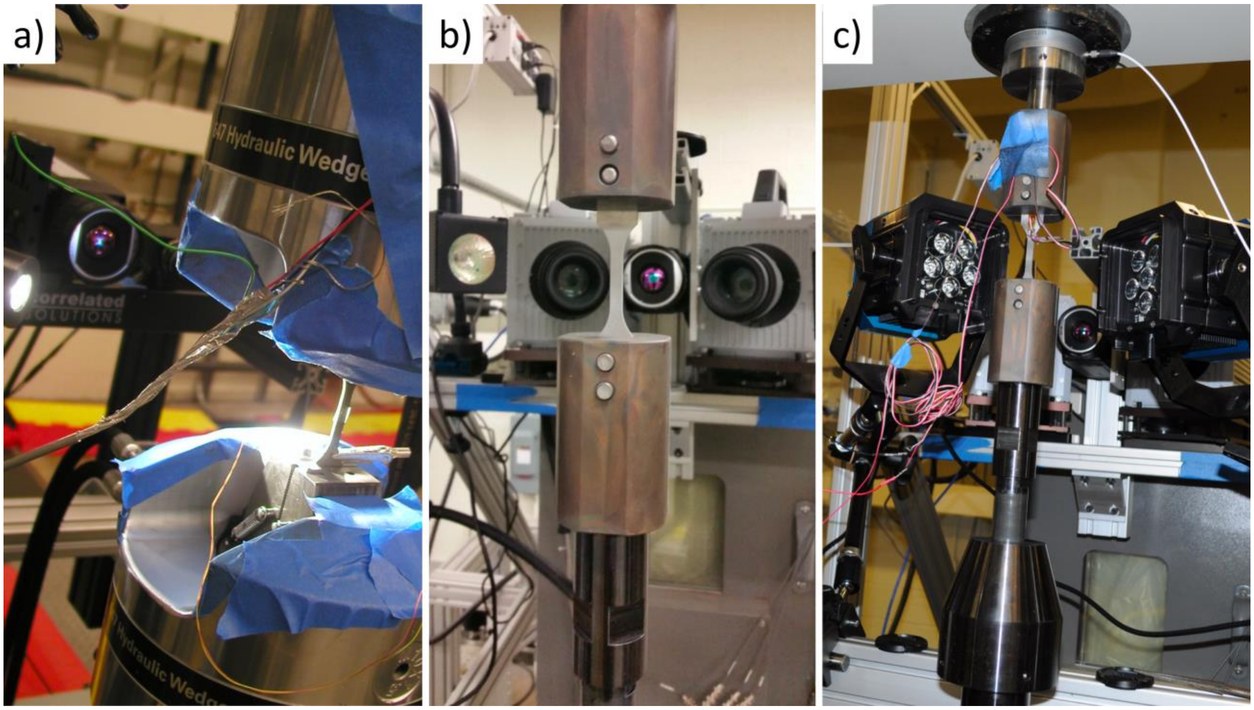

Figure 3-7: Mechanical testing setups for a) low rate tests from $\dot{\varepsilon} = 10^{-4}$ /s to $\dot{\varepsilon} = 10^{-2}$ /s, b) medium-rate tests at $\dot{\varepsilon} = 10^{1}$ /s and c) high-rate tests at $\dot{\varepsilon} = 10^{2}$ /s. Note the locations of the optical digital image correlation cameras and infrared thermal camera.

Figure 3-8: Tensile specimen pulled to failure at $\dot{\varepsilon} = 10^1$ /s (note the pin-loading holes). The image is used to show the size scale (ruler in inches) of the digital image correlation marks (black ink marks on a white background).

Figure 3-6 shows the specimen used in the servo-hydraulic tests involving the medium-Mn steel. Specimens used in low-rate tests on the Instron 8502 did not have pin-grip holes. Specimens were water-jet cut from the original sheets. Pin-loading holes were milled with a carbide tool while clamped in the vise of a milling machine. In general, the holes passed the loading pin without excessive force.

Tests at nominal strain rates of $\dot{\varepsilon} = 10^{-4}$ /s and $\dot{\varepsilon} = 10^{-2}$ /s took place on a 100 kN servo-hydraulic test machine with hydraulic grips (see Figure 3-7a). Strain measurement generally employed real-time digital image correlation (see Figure 3-8) using Correlated Solutions Vic-Gauge to virtually define a nominal G = 19.8 mm extensometer. This real-time processing sent a signal proportional to the strain directly to the test-machine software. In parallel, the software saved a subset of the images for post-test analysis (Correlated Solutions Vic-3d7). In several cases, these images were used to compute the strain, also by virtually defining a nominal G = 19.8 mm extensometer and computing engineering strain from the position of individual subsets in the test. Usual analysis parameters were approximately 30 pixel subset size, and 7 pixel step. The pattern for digital image correlation (DIC) was white paint sprayed on one face of the specimen, with black random pattern applied by an inked roller. Low-rate tests used Point Grey Gazelle 4 MP CMOS cameras

Tests at a nominal rate of $\dot{\varepsilon} = 10^1$ /s took place on the National Center for Automotive Lightweighting (NCAL) high-rate servohydraulic test machine (at the National Institute of Standards and Technology in Gaithersburg, MD) which uses a slack adapter and pin-loaded grips. Figure 3-7b shows a typical test setup. Forces were measured using a Kistler load washer. Cameras were 1 MP Photron SA5, windowed to 256x1024 and acquiring images at 21,000 frames per second. The DIC pattern was applied by white paint with black ink applied by an inked roller. Two halogen lamps positioned about 10 cm from the specimen provided lighting, but tended to heat the surface of the specimen about 10 °C before the test.

Tests at nominal rate $\dot{\varepsilon} = 10^2$ /s took place on the NCAL high-rate servohydraulic test machine, which uses a slack adapter and pin-loaded grips. Figure 3-7c shows a typical test setup that used large LED lights, which heated the specimen less than halogen lights and allowed shorter exposures. Images were acquired at 21,000 frames per second. All specimens were instrumented with two strain gauges (CEA-13-250UW-350) for force measurement, because the impact of the slack adapter produced unacceptable ringing in the load washer force signal (see Figure 3-7c). Before each test, these gauges were calibrated against the load washer up to $P = 1200$ N force in the testing machine. In these tests, the DIC pattern was white base and black overspray, which produced more optimal spot size.

3.2.4 Kolsky-Bar Tension of Medium-Mn Sheet Steel

Kolsy-Bar specimens were machined (see drawing in Figure 3-9) from the same medium-Mn steel sheets used for servo-hydraulic testing. These specimens were pin-loaded onto a 1 m striker bar (see Figure 3-10) and pressures of 70 psi were used to achieve failure of the specimens at approximately $\dot{\varepsilon} = 1 \times 10^3$ /s, while pressures of 40 psi were used to interrupt tests via a momentum trap, as recommended by the IISI [144]. Analysis of stress was carried out as described by Whitenton [169] and ultra-high frame rate digital image correlation was used to measure strain in the gauge length as described in section 3.2.3.

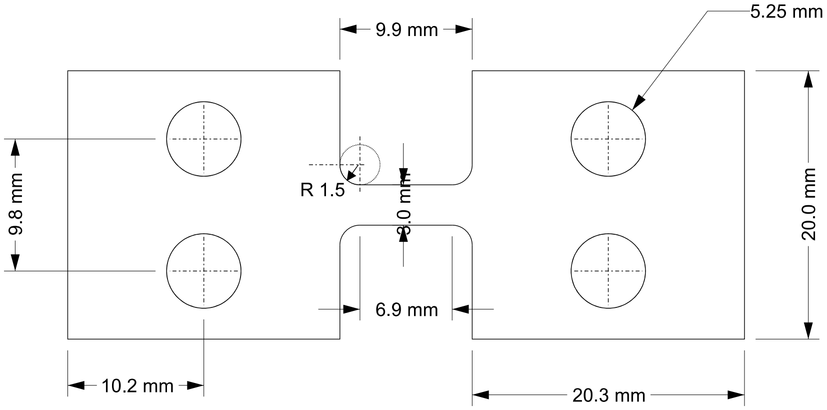

Figure 3-9: Drawing of pin-loaded sheet specimens for Kolsky-bar deformation

Figure 3-10: Kolsky-Bar setup at the National Institute of Standards and Technology in Gaithersburg, MD.

3.3 Non-Contact Temperature Measurements

Non-contact temperature measurements during servo-hydraulic testing of the high-Mn alloy were collected during all mechanical tests with an infrared thermal camera (FLIR® A655sc) at a frame rate of 200 Hz (5 ms between frames), to produce a matrix with 640 x 120-pixel resolution per frame. The calibration range of this device is -40 to 150 °C, and within this range the overall accuracy of absolute temperature measurement is ±3 °C. The maximum reading which could be displayed outside this calibrated range was 160.2 °C. To ensure consistent temperature measurements, the side of the gauge section without a strain gauge was coated with black spray paint [emissivity approximately equal to 1]. The camera had an unobstructed view of the specimen during testing as seen in Figure 3-5d. A large sheet of cardboard was placed behind the specimen during testing to achieve a uniform background. The absolute values of the non-contact temperature measurements were corroborated by measurements made with a thermocouple that was resistance-welded to the other side of a tensile specimen during a practice test. Non-contact temperature measurements during servo-hydraulic testing of the medium-Mn alloy were collected during all tests to capture a thermal history of the specimen using a FLIR® A655sc camera (640x480 pixels at 30 fps and windowed to 640x240 at 60 fps).

3.4 Data Acquisition at High Strain Rates

In the case of tests with the high-Mn alloy at $\dot{\varepsilon} = 2\text{x}10^2$ /s, measurement of load and strain was performed with multiple methods. The engineering strain rate was higher than expected based on the actual displacement rate and resulted in extrapolated total elongation values up to $\varepsilon_{eng.} = 0.25$ greater than total elongation measured on the fractured tensile specimen with calipers. Therefore, for $\dot{\varepsilon} = 2\text{x}10^2$ /s tests, actuator displacement rate was used instead to estimate strain after debonding of the strain gauge. For tests faster than $\dot{\varepsilon} = 2\text{x}10^1$ /s, the swift connection of the slack adapter generated mechanical resonance in the specimen and testing machine, which led to large oscillations in the load data, as seen in supplementary Figure A-1. The load-ringing amplitude could be minimized by reducing the mass between the gauge section and the load measuring device, which is why titanium grips were used [150][153]. Yang *et al.* suggest the use of two elastic strain gauges to reduce load oscillations (one on each side of the grip section seen in Figure 3-5c) during high strain-rate tensile testing on a servo-hydraulic testing machine [170]. The load data from both strain gauges is averaged and significantly reduces oscillation amplitude, as shown in supplementary Figure A-2. Although this was not an option for all pull-to-failure tests, this concept was implemented in one test to check agreement of the hardware-based method suggested by Yang *et al.* with the software-based smoothing methods described below. The data-reduction methods implemented in this work for the tests at $\dot{\varepsilon} = 2\text{x}10^2$ /s comprise a moving average using MATLAB® (three iterations of smoothing for each data set), and spline fitting of the linear-elastic region and necking-fracture regions using Grapher™ software, as shown in Figure A-3. Both the hardware and software-based smoothing methods provide satisfactory solutions to the problematic raw load-washer data, as shown in Figure A-4.

Low-rate tests of the medium-Mn alloy used the strain signal directly output from the Vic-gauge where possible. In some cases, where the real-time analysis failed during the test, the individual images were analyzed post-test, but always with a nominal G = 19.8 mm gauge length. Strains from medium-rate ($\dot{\varepsilon} = 2\text{x}10^1$ /s) tests were always computed post-test with the same nominal G = 19.8 mm gauge length. Forces and stresses were computed from the load-washer signal. The high-rate tests employed a more complicated analysis. The force and stress signals were computed as the average from the two strain gauges during the test. The tensile strength, S_u, was calculated from the force-time signal captured using a parallel, high speed data-acquisition unit running at 500 khz, instead of the unit that captured the images, which ran at 21 khz. Actual engineering strain rates were calculated from a linear regression of the engineering strain-time data, generally in a strain region after yield, and always before the ultimate tensile strength.

3.5 Optical Microscopy

Samples for optical microscopy were prepared from the high-Mn and medium-Mn steels by grinding through 400, 600, 800 & 1200 grit SiC paper, mechanical polishing through 3µm & 1µm diamond suspensions, plus a 50 nm silica suspension and then finally etched with a 10% nital solution, (10 % HNO_3 in 90 % CH_3OH by volume).

3.6 Micro-Hardness Testing

Micro-hardness measurements were made on 3 mm discs of every deformed sample of the high-Mn alloy (on samples prepared for optical microscopy) with 32 indents per sample and 400 µm spacing between indents, using an 800 g load on a Vickers micro-hardness machine.

3.7 Characterization of Planar Defects in the Single-Phase High-Mn Steel

To quantitatively characterize the effects of strain rate on changes in the distribution of planar defects in the high-Mn steel (especially twins and ε-martensite) both SEM and TEM-based characterization techniques have been utilized by others [171][58][59][174][61][176]. Such characterization techniques are used to quantify the thickness and spacing of planar defects (see Figure B-1 and Figure B-2) and include electron backscatter diffraction (EBSD), electron channeling contrast imaging (ECCI), and conventional dark-field transmission electron microscopy (DF-TEM). To minimize as many variables as possible in quantifying planar defects, the microscopy work discussed in this chapter is based on tensile specimens of the same sheet thickness (1.15 mm). Micro-hardness indents were placed in a grid on polished SEM samples to act as markers during imaging. EBSD was used to survey grains with <101> orientations parallel to the beam direction. For those properly oriented grains, ECCI was used to first survey for proper channeling conditions, then record at medium-high magnification a slow scan image revealing the planar defects. Figure B-1 shows example images recorded on the different microscopes. Suitable DF-TEM diffracting conditions were achieved with a TEM (FEI Tecnai Osiris) at 200 kV by first surveying grains with convergent beam electron diffraction (CBED) and orienting them to a <101> beam direction, followed by selecting the appropriate extra reflections (twinning or ε-martensite) in selected-area electron diffraction (SAED) patterns with a sufficiently small (10 µm) objective aperture to produce an unambiguous DF image (Figure B-2). An image-processing recipe [FFT filter, adaptive threshold, black-white inversion, feature rejection and watershed] was used to segment planar defects from a given image using MIPAR software [177]. Approximately 100 lines were drawn perpendicular to the segmented defects and used to count the thickness of and spacing between all planar defects in a given image.

3.7.1 Electron Backscatter Diffraction and Electron Channeling Contrast Imaging

For scanning electron microscopy (SEM) sample preparation of the high-Mn steel, 3 mm discs electro-discharge machined from gauge sections were mounted in conductive bakelite. To achieve the preparation quality needed for high-resolution measurements in the SEM, (which are discussed above), the bulk samples were mechanically polished with SiC paper (400 through 1200 grit) auto-polished with 3 µm and 1 µm diamond spray solution, etched for 20 s with 3 % nital to chemically remove mechanical polishing effects and auto-polished through a 50 nm oxide polishing suspension, before final cleaning. EBSD on a field-emission SEM (JEOL JSM 6500F) at 25 kV was used to survey grains with <101> orientations parallel to the beam direction. For those properly oriented grains, ECCI on a field-emission SEM (Zeiss Merlin) at 30 kV was used to first survey for proper channeling conditions, then record at medium-high magnification a slow scan image revealing the planar defects.

3.7.2 Transmission Electron Microscopy

For transmission electron microscopy (TEM) sample preparation from the gauge sections of interrupted and pulled-to-failure tensile specimens from the high-Mn steel, 3 mm discs were wire electro-discharge machined orthogonal to the thickness dimension. To achieve electron transparency, these discs were mechanically polished to ~100 µm with SiC paper and electro-polished with a Struers TenuPol-5 twin jet system (-30 °C, 15 V, 80 % CH_3OH, 20 % HNO_3 by volume). Conventional transmission electron microscopy techniques were completed with an FEI Tecnai Osiris TEM operated at 200 kV.

3.8 Characterization of Ultrafine-Grained Morphology, Alloy Partitioning and Deformation Mechanisms in the Multi-Phase Medium-Mn Steel

3.8.1 Electron Backscatter Diffraction

For electron backscatter diffraction (EBSD) sample preparation, sections of the intercritically annealed medium-Mn steel were mounted in conductive Bakelite and the rolling direction was noted. These samples were successively ground using 400, 600, 800, 1000 and 1200 grit SiC paper, auto-polished with a 1 µm diamond solution, etched for 5 s with 5 % Nital to chemically remove mechanical polishing effects, (5 % HNO_3 in 95 % CH_3OH by volume), hand-polished in a 50 nm OPS suspension, washed with a soapy cotton ball, rinsed with CH_3OH and blown dry. EBSD measurements were completed using a JEOL JSM-6500F FESEM with the following SEM and scan parameters: 15 kV accelerating voltage, 12 nA probe current, 18 mm working distance and a 30 nm step size. Data cleanup involved a grain confidence index standardization and data points with a confidence index lower than 0.1 were omitted from all figures.

3.8.2 Transmission Electron Microscopy and Energy Dispersive Spectroscopy

This work uses bright-field transmission electron microscopy (BF-TEM), convergent beam electron diffraction (CBED) and scanning TEM energy-dispersive X-ray spectroscopy (STEM-EDS) techniques to further characterize the UFG structure. TEM-based experiments were performed using an FEI Tecnai Osiris operated at 200 kV and equipped with a quad Super-X detector. Sections of the intercritically annealed medium-Mn steel were successively ground to 100 µm using 400, 600, 800, 1000 and 1200 grit SiC paper. Punched 3-mm discs viewed in the normal direction were electropolished to electron transparency with a Struers twin-jet system (5% $HClO_4$, 35% $[CH_3(CH_2)_3]$-O-C_2H_4OH, 60% CH_3OH by volume, -30°C, 15 V). Multiple methanol and ethanol cleaning baths were used during final dipping/cleaning. Other sections of the intercritically annealed material that were prepared for EBSD were used to extract focused ion beam (FIB) liftouts for TEM analysis [viewed in the rolling direction] using an FEI Helios NanoLab G3 CX FIB-SEM. Using Ga ions, a protective Pt layer was deposited, a trench was bulk milled at 21 nA/30 kV, intermediately milled at 2.5 nA/30kV, lifted out, attached to a grid, thinned at 0.79 nA/30 kV and cleaned at 0.07 nA/5kV. Bruker Esprit software was used to record 200 kV STEM-EDS hypermaps on electropolished samples and FIB liftouts with typically 40 µs dwell time per pixel, 1 nm pixels, 2 × 2 µm scanned area and 20 frames for approximately 600 s acquisition. Data processing included background subtraction, peak deconvolution and normalized wt% mapping for each hypermap.

3.8.3 Atom Probe Tomography

Atom probe tomography (APT) needles were created by first creating a FIB lift out sample (5 µm x 20 µm x 5 µm) from the intercritically annealed material. In the case of samples annealed for 0.5 h, when a low fraction of austenite was present, site-specific FIB lift outs were extracted using information from prior EBSD scans to capture all phases present. FIB liftouts were sectioned onto posts and concentrically milled at 2.5 nA/30 kV and then 0.79 nA/30kV to create a needle geometry. Final cleaning with the FIB at 5 kV and 0.07 nA was used to produce tips of approximately 25 nm radii and a 4 ° shank half angle. Such needles were subsequently loaded into a CAMECA LEAP 5000 XS APT system and ran until fracture, (Laser-pulse mode, 15 % field evaporation, 70 K environment temperature).

3.9 X-Ray Diffraction

3.9.1 High-Mn Steel

Sample preparation for XRD experiments of the high-Mn steel involved mechanical polishing through 1200 grit SiC paper and a final chemical polishing to remove the damaged surface layer (samples were dipped into baths of HF for ~ 300 s). The temperature-dependent XRD patterns were collected using an X-ray diffractometer (PANAlytical X’Pert MPD Pro) with Cu Kα radiation ($\lambda_{K\alpha1}$ = 1.54060 and $\lambda_{K\alpha2}$ = 1.54443 Å), equipped with an Anton Paar XRK-900 heating stage. Prior to each XRD measurement at each temperature, 3 minutes of waiting time was allowed for temperature equilibration. The 2θ scanning range, step size and scan rate for each measurement was 30-120°, 0.0167113° and 0.107815 deg/s, respectively. The XRD measurements which used the heating stage were performed in an Ar environment from 298 to

973 Kelvin and the first five allowable austenite peaks were identified for each XRD scan. Austenite lattice parameters were calculated using Bragg's law and the Nelson-Riley function to account for larger sensitivities of the lattice constant at higher diffraction angles [178]. Specifically, the angle of every k-alpha 1 diffraction peak was fit at full width half max using PANAlytical Data Viewer software and a linear regression of calculated lattice constants was used to find the intercept of all diffraction angles for a given alloy and temperature.

3.9.2 Medium-Mn Steel

Sections of the intercritically annealed medium-Mn steel used for X-ray diffraction (XRD) measurements were not mounted to minimize background noise. The sample surfaces [viewed in the normal direction] were ground with SiC paper from 400 through 1200 grit, auto-polished with 1-µm diamond solution, hand-polished with a 50-nm OPS suspension, electro-polished at 15 V for 45 s to chemically remove mechanical deformation, (10% $HCLO_4$ in 90% CH_3COOH by volume), rinsed with CH_3OH and blown dry. XRD patterns were collected using an X-ray diffractometer (Meteor0D) with Co Kα radiation ($\lambda K\alpha = 1.78897$ Å, 40 kV and 30 mA) in point focus mode and equipped with a Huber 4-circle + xyz goniometer. The 2θ scanning range, 2θ step size, count time and rate of sample rotation for each measurement were 20-130°, 0.03°, 20 s/step, and 1 turn/s, respectively. Bruker TOPAS v5.0 was used for Rietveld analysis and included calibration of instrumental broadening with a Si sample, a 4th order polynomial background subtraction and a preferred orientation (6th order).

CHAPTER 4

4. RESULTS AND DISCUSSION

4.1 Characterization of Planar Defects in a High-Mn TWIP-TRIP Steel Deformed by Uniaxial Ring Expansion

This work involves the investigation of deformed microstructures that exist after interruption of high strain-rate tests using Fe-25Mn-3Al-3Si wt% steel. The work by Grässel *et al.* [30] is of particular interest as the high strain-rate mechanical properties were previously measured with sub-sized tensile samples, but no high-strain rate tests were interrupted to investigate the evolution of the microstructure. Mechanical twinning was the only type of planar defect identified with TEM by Grässel *et al.* [30] in specimens from interrupted quasi-static tensile tests, but Pierce [31] identified both mechanical twins and hexagonal ε-martensite using TEM in specimens from interrupted quasi-static tensile tests. Therefore, section 4.1will present and discuss characterization results from tests of the Fe-25Mn-3Al-3Si wt% steel when interrupted at strain rates of $\dot{\varepsilon} = 1x10^3$ /s or greater.

4.1.1 Measurements of Strain Rate During Uniaxial Ring Expansion

The method of mechanical testing presented in this section, uniaxial ring expansion, uses a shock wave from a vaporized wire to provide strain rates from $\dot{\varepsilon} = 1x10^3$ /s to $\dot{\varepsilon} = 1x10^4$ /s. This expansion method uses a large bank capacitor to deliver kJ worth of energy in a few µs to vaporize an Al wire, which expands an elastomer cylinder and a ring of high-Mn steel that is positioned near the midpoint in height of the elastomer cylinder, (see Figure 3-2 for a detailed view of the experimental setup). A high frequency laser is mounted away from the point of vaporization and positioned orthogonally to the outer wall of the expanding ring. The change in frequency is used to calculate velocity and acceleration of the expanded ring via photonic Doppler velocimetry (pDv) [167]. The strain rate of the expanding ring is controlled by the ring diameter and the total strain by input energy. Figure 4-1 provides results of strain rate measurements with the high frequency laser during the expansion of a 25.4 mm diameter ring. Seen in Figure 4-1a is the frequency trace of the laser measured throughout the entire interrupted test, (expansion did not result in failure of the ring specimen). Using photonic Doppler velocimetry (pDv) [167], the Doppler effect is used to convert the change in frequency of the laser as a function of time to a change in velocity as a function of time (Figure 4-1b) and the diameter of the ring is used to calculate the strain rate as a function of true strain (Figure 4-1c) using the methods developed by Johnson [167], since the quotient of expansion rate and original diameter is proportional to strain rate. The ring is first expanded by the elastomer, then the elastomer contracts and the ring expands by its own inertia (termed a freely expanding ring). As the expansion in this case is an interruption (the ring was not pushed to failure) the strain rate is not constant throughout the entire test, as shown by the parabolic nature of velocity as a function of time. For simplicity, when describing interrupted uniaxial ring expansion tests, the highest strain rate measured by the laser during the free expansion of the ring will be specified in subsequent discussion, ($\dot{\varepsilon} = 3.5\text{x}10^3$ /s in the case of Figure 4-1c). Figure 4-1d provides a qualitative view of the interrupted test involving the expansion of a 25.4 mm diameter ring (before deformation) to 0.14 true strain (after expansion).

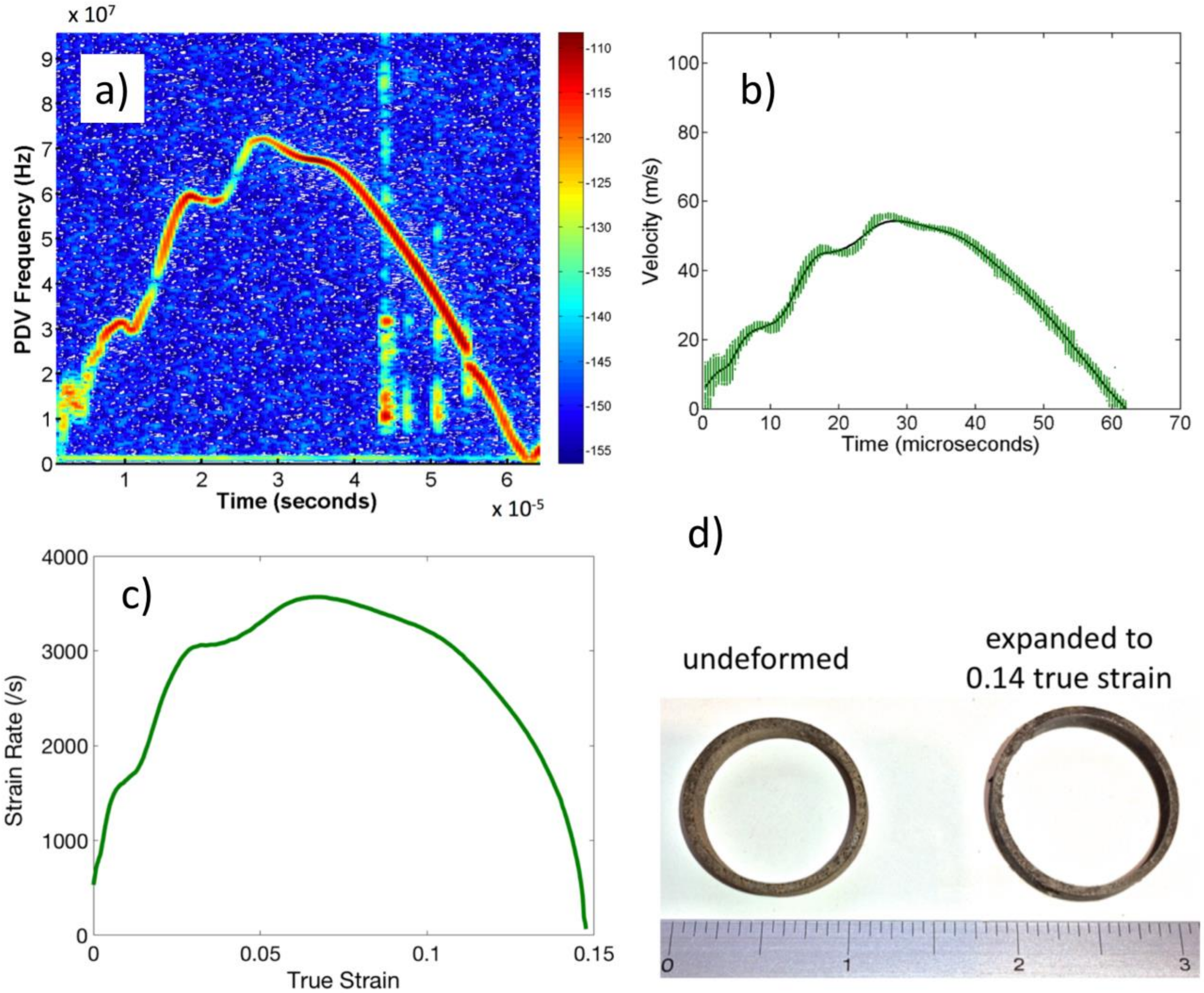

Figure 4-1: a) The trace of a high-frequency laser measured with photonic Doppler velocimetry [167], b) resulting velocity as a function of time and c) strain rate as a function of true strain. The results presented in parts a-c) are from the expansion of a 25.4 mm (1 in) ring that was interrupted at 0.14 true strain and the d) optical view of an undeformed and expanded ring (ruler in inches).

4.1.2 Optical Microscopy of Deformed Microstructures

Multiple sets of concentric rings were machined from a 5 mm thick plate of Fe-25Mn-3Al-3Si, (drawing of the concentric rings shown in Figure 3-1a). With radius-to-wall-thickness ratios held constant, inner ring diameters of 16, 25 & 51 mm resulted in strain rates of $\dot{\varepsilon}$ = 9.1 x10^3 /s, $\dot{\varepsilon}$ = 3.5x10^3 /s & $\dot{\varepsilon}$ = 1.1x10^3 /s and input energies of 2, 4 & 8 kJ produced total true strains of 0.12, 0.14 & 0.18, respectively, for all inner ring sizes. Figure 4-2a provides an optical view of the undeformed microstructure, which consists of equiaxed grains of approximately 20 μm in size and annealing twins within some of the undeformed grains annealing twins, which are produced during the homogenization step. Figure 4-2b-d shows optical micrographs of resulting microstructures from the interrupted ring expansion tests mentioned. Even though TEM is required to differentiate between mechanical twins and/or martensite plates, Figure 4-2b-d provides discernible examples of thin strain-induced planar defects within grains and in some cases, multiple variants (indicated by white arrows). After interruption at ε_{true} = 0.12 (Figure 4-2b), planar defects are apparent in a minority of the grains whereas interruption at ε_{true} = 0.18 (Figure 4-2d) at a strain rate approximately an order of magnitude smaller than that during the interruption at ε_{true} = 0.12, planar defects are clearly visible in the majority of grains. The micrographs in Figure 4-2 originate from areas within deformed rings that are viewed in the same direction the laser measures strain rate (orthogonal to the outer wall of the expanding ring).

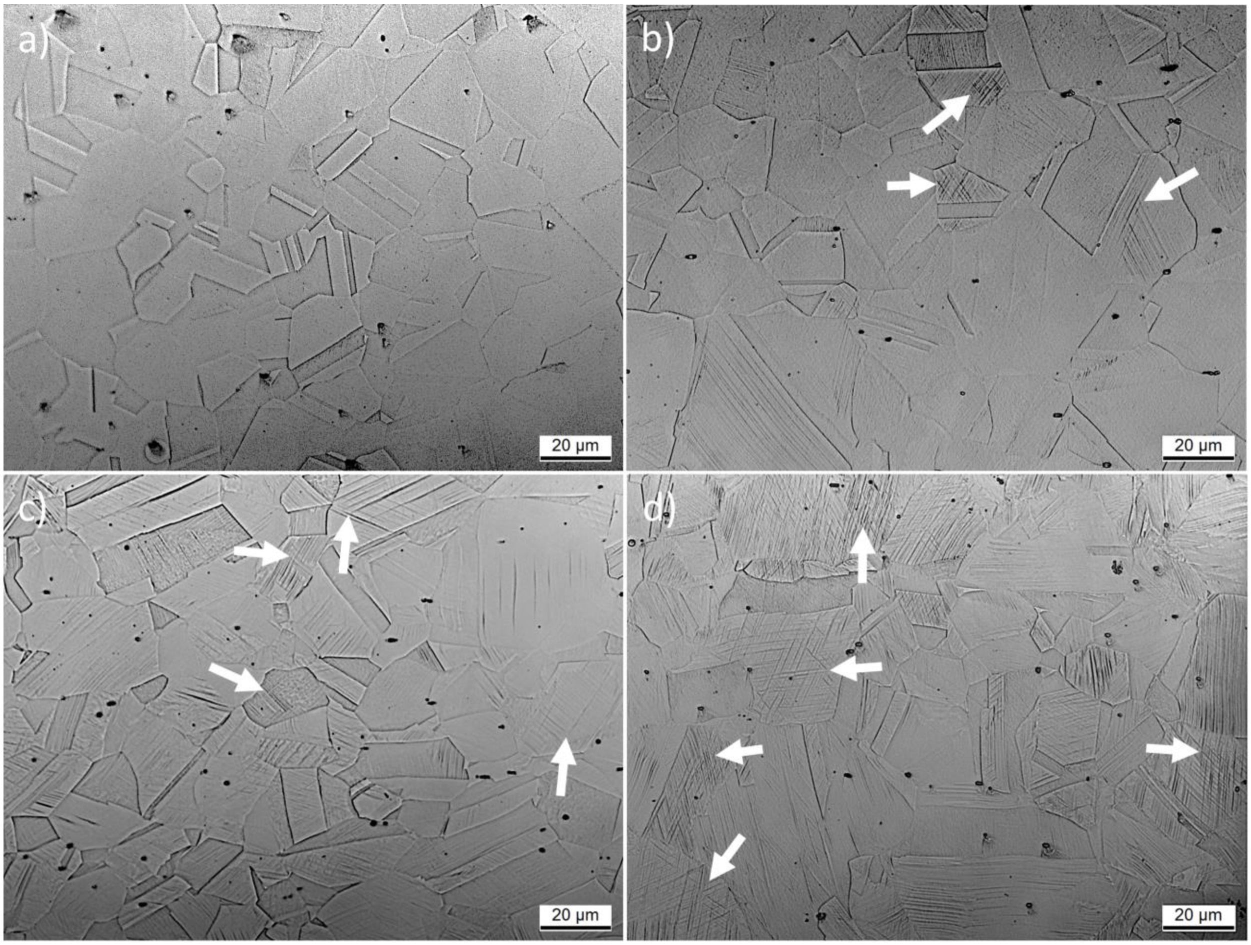

Figure 4-2: Optical micrographs of the Fe-25Mn-3Al-3Si alloy deformed using uniaxial ring expansion: a) undeformed material, b) small ring tested at $\dot{\varepsilon} = 9\text{x}10^3$ /s and expanded to $\varepsilon_{\text{true}} = 0.12$, c) medium ring tested at $\dot{\varepsilon} = 3.5\text{x}10^3$ /s and expanded to $\varepsilon_{\text{true}} = 0.14$ and d) large ring tested at $\dot{\varepsilon} = 1\text{x}10^3$ /s and expanded to $\varepsilon_{\text{true}} = 0.18$. Multiple variants of mechanical twins and/or hexagonal epsilon martensite laths are indicated by arrows. All samples etched for 20 s with 10% nital and the current view is orthogonal to the expanding direction.

4.1.3 BF-TEM Surveying Prior to HR-STEM

Bright-field TEM (BF-TEM) micrographs shown in Figure 4-3 provide higher resolution images (as compared to optical microscopy) of the deformed microstructures created during high strain-rate ring expansion of Fe-25Mn-3Al-3Si steel. The planar features in Figure 4-3a are planar defects, which are mixed in between widely separated partial dislocations and extended stacking faults, (image recorded within a single grain of a small ring sample deformed at at $\dot{\varepsilon} = 9x10^3$ /s and expanded to $\varepsilon_{true} = 0.12$). Figure 4-3b shows an image from a ring sample deformed to $\varepsilon_{true} = 0.18$ at $\dot{\varepsilon} = 1x10^3$ /s, where there are planar defects and a high density of stacking faults and tangled partial dislocations. Other BF-TEM observations in a medium ring sample deformed at at $\dot{\varepsilon} = 3.5x10^3$ /s and expanded to $\varepsilon_{true} = 0.14$ include multiple variants of stacking faults (see Figure 4-3c) and planar defects that appear to both impede (black arrows in Figure 4-3d) and allow transmission of (white arrows in Figure 4-3d) subsequent partial dislocation motion on non-coplanar slip systems. This behavior is quite interesting as the high magnification BF-TEM image in Figure 4-3d shows no obvious indications as to why a relatively thick planar defect can both impede and transmit partial dislocation motion on non-coplanar glide planes. Higher-resolution techniques, such as probe-corrected high-angle-annular-dark-field (HAADF) STEM imaging, are needed to characterize and understand planar defects in deformed high-Mn steel.

A crucial aspect of acquiring atomic-resolution images of defects in metals with advanced electron microscopes involves surveying grains in BF-TEM prior to high-resolution scanning. Not only is meticulous planning required to find a previously identified area of interest that is a few microns wide, but there are specific experimental challenges involved with high resolution imaging of planar defects in electropolished samples of high-Mn steel. One challenge is that electropolished samples are thick (> 25 nm) and often have poor edge retention (curling and cracking). In the case of BF-TEM images in Figure 4-4a and Figure 4-4b, the edges of the grains are thin (noted by the gradual increase in electron transparency) and are not curled or cracked. Also, electropolished samples have local bending and the deformed materials have subtle changes in local crystallographic orientation across the area of interest. The grains observed in Figure 4-4a and Figure 4-4b are flat, which is confirmed by the absence of significant bend contours (most of the grain is dark because it is flat and tilted to a zone axis). Finally, the correct <110> zone axis with the twin/martensite {111} habit plane must be parallel to the beam direction must be chosen (note the extra reflections in the inset diffraction patterns of Figure 4-4a and Figure 4-4b), with minimum sample tilt so as to minimize the effective thickness and beam scattering within the tilted thin foil.

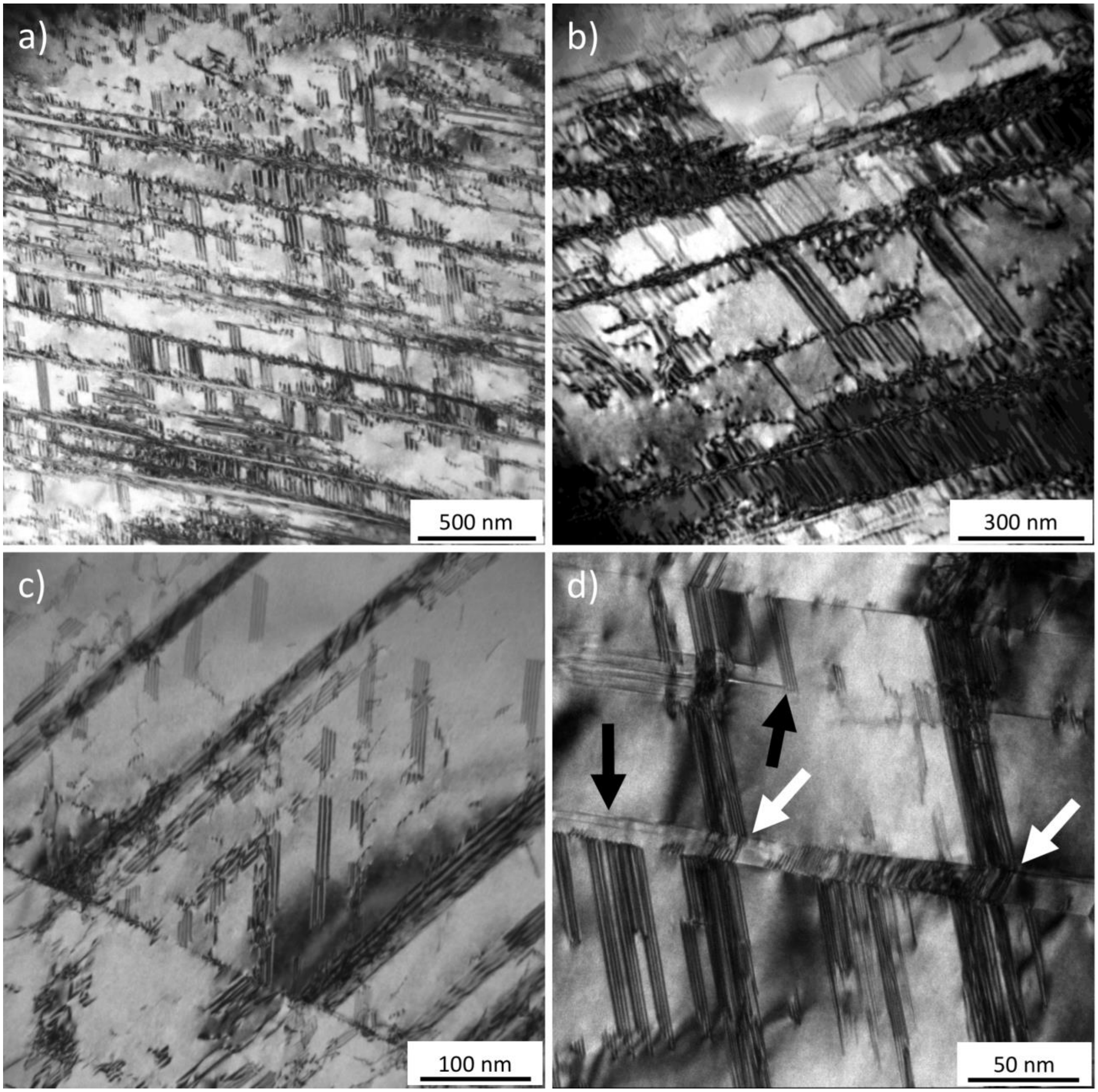

Figure 4-3: BF-TEM micrographs of the Fe-25Mn-3Al-3Si alloy deformed using uniaxial ring expansion: a) small ring tested at $\dot{\varepsilon} = 9\text{x}10^3$ /s and expanded to $\varepsilon_{true} = 0.12$, b) large ring tested at $\dot{\varepsilon} = 1\text{x}10^3$ /s and expanded to $\varepsilon_{true} = 0.18$ and c) medium ring tested at $\dot{\varepsilon} = 3.5\text{x}10^3$ /s and expanded to $\varepsilon_{true} = 0.14$. d) Planar defects found in specimens from the medium ring expanded to $\varepsilon_{true} = 0.14$ can in some cases impede the motion of subsequent partial dislocations on non-coplanar slip systems (black arrows) and in other cases allow transmission of partial dislocations (white arrows).

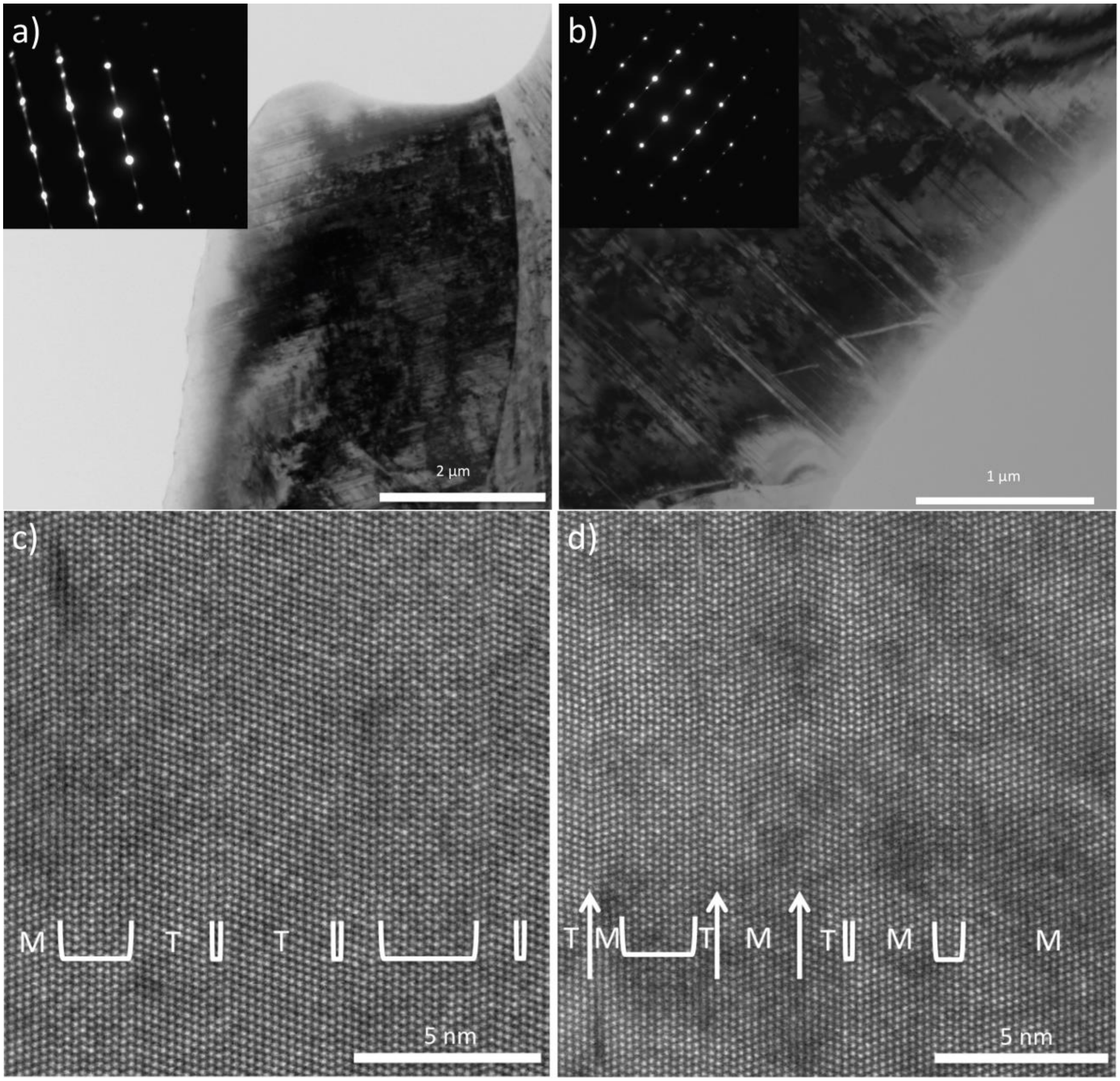

Figure 4-4: BF TEM images of separate grains in a ring sample deformed to $\varepsilon_{true} = 0.18$ strain at $\dot{\varepsilon} = 1\text{x}10^3$ /s. The inset SAED patterns, recorded at <110> zones, indicate two types of planar defects: a) hexagonal ε-martensite and b) mechanical twinning. High-resolution HAADF-STEM images recorded using a 300 kV probe-corrected FEI Titan3 G2 at the Center for Electron Microscopy and AnalysiS from the respective grains above (part c corresponds to the grain in part a and part d corresponds to the grain in part b), where regions of FCC matrix (M), hexagonal ε-martensite (white bracket), twinning with respect to matrix (T) and twin boundaries (white arrow) are marked.

Figure 4-4a shows a BF-TEM image of a deformed grain with numerous planar defects and is part of a sample extracted and electropolished from a ring specimen deformed to

ε_{true} = 0.18 strain at $\dot{\varepsilon} = 1 \times 10^3$ /s. The inset selected area electron diffraction (SAED) pattern recorded at a <110> zone axis provides evidence of hexagonal reflections in between the larger and more intense FCC reflections and are characteristic of ε-martensite plates [99]. Therefore, the SAED pattern in Figure 4-4a indicates that the planar defects viewed parallel to the direction of the electron beam in the bright field image are hexagonal ε-martensite plates. Figure 4-4b shows a BF-TEM image of another grain in the same electropolished sample that has been tilted to the <110> zone axis as noted by the dark contrast surrounding the planar defects. The inset SAED pattern indicates the planar defects viewed parallel to the beam direction are mechanical twins, as indicated by the smaller (less intense) reflections that give the appearance of a rotated reciprocal lattice [171]. However, when the grains are viewed at higher magnification with a probe-corrected STEM, (the image is recorded from a HAADF detector), stacking sequences of the resolved atomic columns indicate that mechanical twins and ε-martensite plates exist in both grains, regardless of which dominantes in the SAED pattern. This behavior is consistent with dark-field TEM measurements by Pierce [22]. Furthermore, the defects are as small as a few atomic columns in width. The main limitation of this imaging technique is the limited field of view, which is outweighed by the atomic-resolution performance. Although in-situ heating was not measured during ring expansion testing, the results in Figure 4-4 confirm that mechanical twins and ε-martensite are still active deformation mechanisms during high strain-rate deformation ($\dot{\varepsilon} = 1 \times 10^3$ /s) and may co-exist within the same grain, regardless of dominant reflections in the SAED pattern. Finally, an advantage of imaging with HAADF-STEM is that the amplitude contrast is less susceptible to local sample tilt compared to phase contrast imaging in HR-TEM [171], but requires removal of artifacts from slow scan noise before quantitative measurements can be completed.

4.1.4 Slow-Scan Noise Removal in Atomic-Resolution HR-STEM Images and Quantitative Strain Mapping

Additional high-resolution HAADF-STEM imaging was performed on the same areas shown in Figure 4-4a/b viewed in the <110> zone axis and carried out with a double-corrected TEAM 0.5 FEI Titan operated at 300 kV in the National Center for Electron Microscopy (now part of the Molecular Foundry, LBNL), using a method which combines orthogonal STEM scans to correct for slow-scan noise [179]. After a real-space reference lattice is defined, images from the 0 and 90° scans, with respect to the slow scan direction are combined. Each pixel along the fast-scan direction of the 0° image is used to locate the position of each atomic column, which is then cross-referenced with the same atomic column position in the 90° scan. Therefore, the atomic column position has been identified using the fast-scan and slow-scan directions. Moreover, artifact removal and noise reduction is best achieved when atomic planes are angled slightly away from parallel, with respect to the slow-scan direction. These images were further analyzed with a principal component analysis (PCA) technique, which can cluster atomic-column positions into categories based on local distance and angle [180]. An example of a relatively low magnification atomic-resolution image recorded from the grain with twinning reflections in the SAED pattern (Figure 4-4b) is shown in Figure 4-5a, where the slow scan noise has already been removed by the method developed by Ophus *et al*. [179]. In Figure 4-5b, the results of the PCA technique confirms the observations in Figure 4-4d, but for a much larger field of view. Mainly, in the grain that yields a SAED pattern with only twin reflections, both twins and very thin hexagonal ε-martensite plates are present, in many cases existing on neighboring glide planes and/or being mixed together.

Next, real-space strain analysis, was completed on high-magnification images (after slow-scan noise removal). First, planar defects in the grain with twin reflections in the SAED pattern were analyzed. Figure 4-6b shows the PCA analysis, which reveals two twins with a matrix plane separating the two, including an extra AB stacking layer neighboring the twin boundary of the bottom twin from the real-space strain-analysis results in Figure 4-6d-f, there is one clear observation. Between the lower twin boundary of the top twin and the upper boundaries of the lower twin, (which includes a single matrix layer, one layer of AB stacking and a trapped partial dislocation), there is a consistent grouping of compressive strain perpendicular to the basal planes as well as compressive shear strain. These results indicate that either the number of twin boundaries/AB layers contributes to the compressive strains or that the proximity of planar defects, (in this case only separated by one plane of FCC matrix), contributes to the compressive strains that may have trapped the partial dislocation in the bottom left corner of the image. In-situ TEM analysis by Brooks et al. [52] [53] on epsilon martensite plates in austenite measured an approximate 1-2% contraction of the spacing perpendicular to the fault plane by comparing TEM electron micrographs of overlapping stacking-faults to computed micrographs of the same stacking-faults. The authors observed that ε-martensite usually forms on the operating slip plane and nucleated from the conglomeration of irregularly spaced stacking faults which gradually (with more deformation) become thicker. Other authors have reported that coherency strain energy arises from the contraction of the fault plane within the FCC matrix [51][57].

To corroborate the first set of real-space strain-analysis results, real-space strain analysis was completed on high-magnification scans of an area from the grain shown in Figure 4-4a, which exhobits ε-martensite reflections in the SAED pattern. PCA analysis (see Figure 4-

7b) reveals a thick layer of ε-martensite plates in the middle of the image and thin layers of the plates near the bottom of the image, although a two-layer epsilon martensite plate is also considered an extrinsic stacking fault [99]. Again, there is a compressive shear strain present in the matrix that separates ε-martensite plates (see Figure 4-7f), but the other real-space measurements of the strain perpendicular and parallel to the basal planes (see Figure 4-7d/e) are less conclusive. However, it is possible that the low amount of strain measured parallel to the planes in the matrix is indicative of relief by thin film preparation and should not necessarily be considered a result of adiabatic heating during deformation at high strain rates.

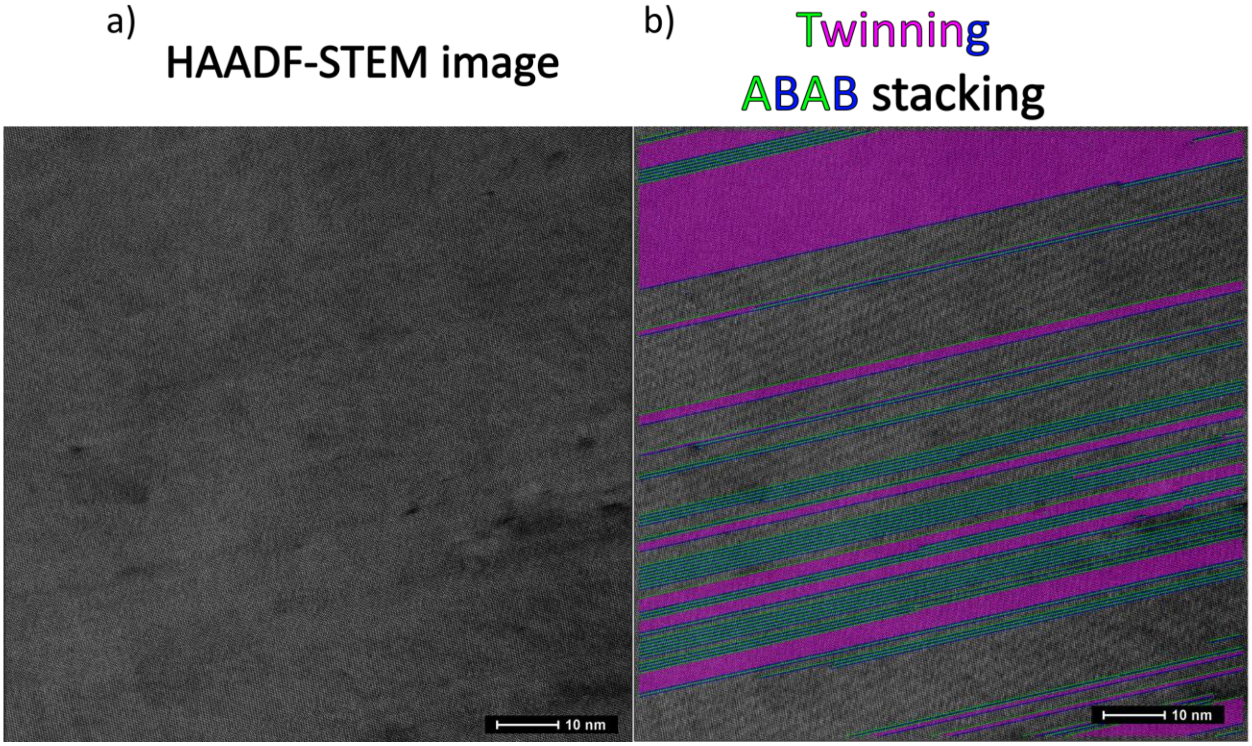

Figure 4-5: a) High resolution HAADF-STEM image recorded from the same grain shown in Figure 4-4b that has only twin reflections in the SAED pattern. This image was recorded on a 300 kV double-corrected TEAM 0.5 FEI Titan and the slow scan noise has already been removed by combining orthogonal scans of the same area [179]. b) Principal component analysis results indicate both twinning and hexagonal ε-martensite (ABAB stacking) on neighboring slip planes.

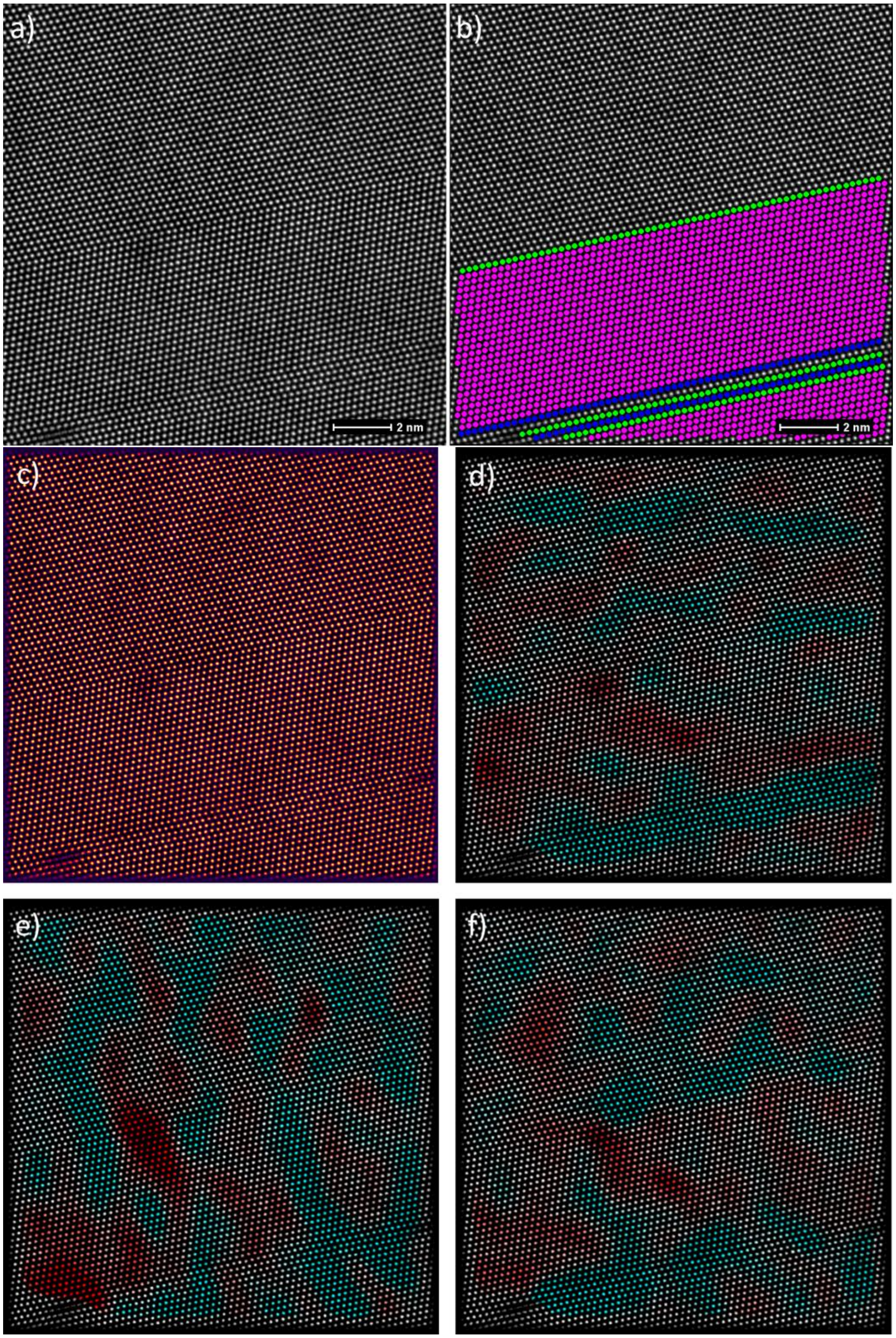

Figure 4-6: a) High-magnification HR-STEM image recorded from the same grain shown in Figure 4-4b with slow-scan noise removed. b) PCA analysis of planar defects (two twins and a thin layer of epsilon martensite) present in the image. c) Location of atomic-column positions in the [1-10] zone axis with real-space strain analysis of d) strain perpendicular to the basal planes in the [111] direction, e) strain parallel to the basal planes in the [112] direction and f) shear strains. Blue represents -1% compressive strain and red represents +1% tensile strain.

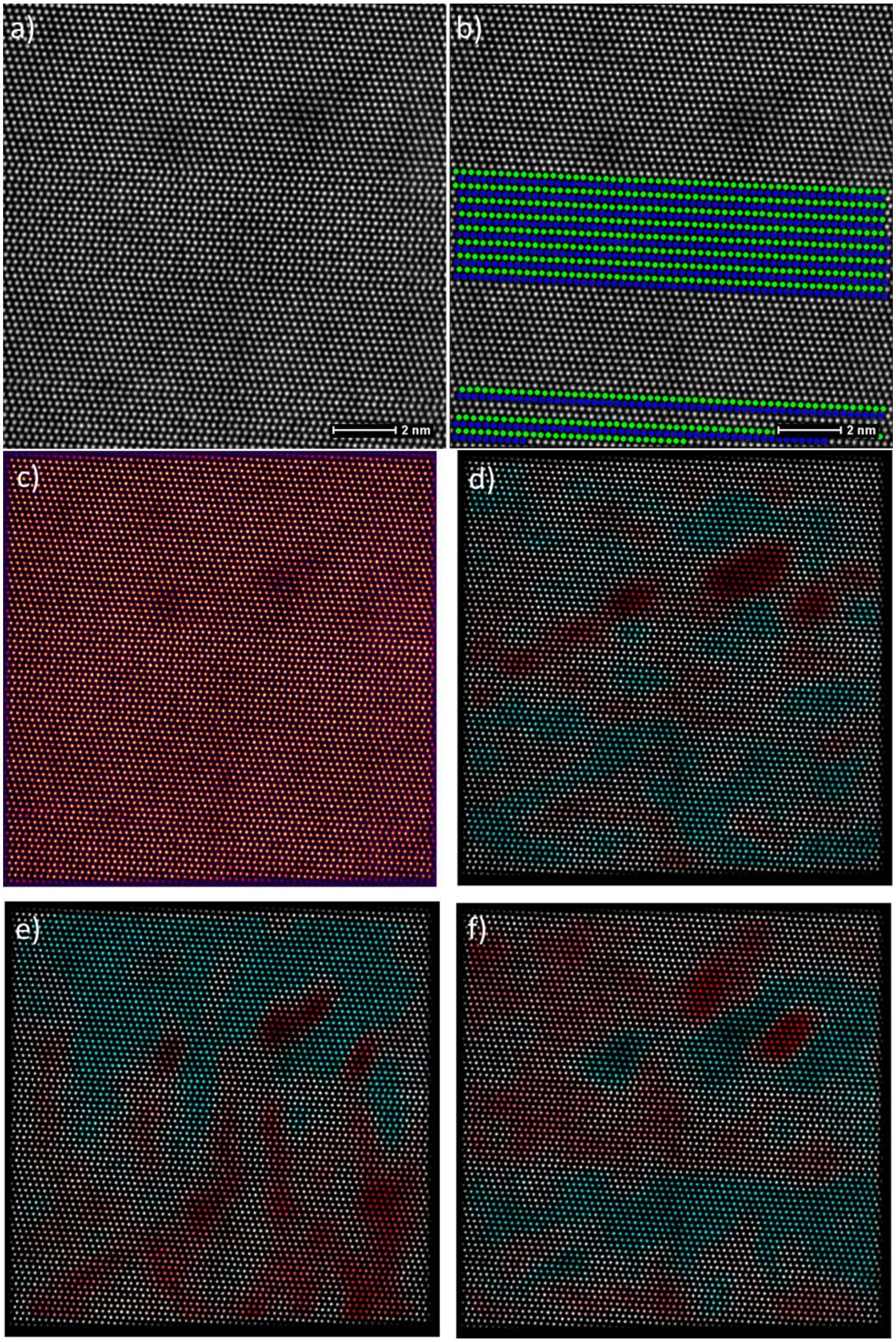

Figure 4-7: a) High-magnification HR-STEM image recorded from the same grain shown in Figure 4-4a with slow scan-noise removed. b) PCA analysis of planar defects (only ε-martensite in this case) present in the image. c) Location of atomic-column positions in the [1-10] zone axis with real-space strain-analysis of d) strain perpendicular to the basal planes in the [111] direction, e) strain parallel to the basal planes in the [112] direction and f) shear strains. Blue represents -1% compressive strain and red represents +1% tensile strain.

4.1.5 Conclusions

- Uniaxial ring expansion is a useful technique to deform steel rings at strain rates on the order of 10^3 /s, and enables the investigation of microstructural evolution after interruption at high strain rates.
- Planar defects in the Fe-25Mn-3Al-3Si steel can allow transmission of partial dislocations on non-coplanar glide planes and also effectively impede/trap partial dislocation motion on non-coplanar glide planes.
- Although <110> SAED patterns may indicate the presence of only deformation twinning or only ε-martensite plates parallel to the beam direction in a given grain, high-resolution imaging reveals that both types of planar defects exist in the same grain, regardless of the extra reflections present in the SAED patterns. These results also confirm that both types of secondary deformation mechanisms are possible after deformation at high strain rates.
- PCA analysis of HR-STEM images that have undergone slow-scan noise removal, shows that mechanical twinning and ε-martensite exist not only in the same grain, but in some cases on neighboring planes and/or are inter-mixed together. When viewed on-edge, these planar defects can be as wide as a few tens of nanometers or as thin as a few atomic planes.
- Real-space strain analysis shows that in some cases, compressive strains perpendicular to the basal plane and compressive shear strains may provide insight into why partial dislocations may be trapped at thin interfaces between the FCC matrix and defect boundaries.

4.2 Influences of Strain Rate on Mechanical Properties and Deformation Mechanisms of a High-Mn TWIP-TRIP Steel

Continued research involving the Fe-25Mn-3Al-3Si wt% steel focused on measuring high strain-rate mechanical properties and investigating the effects of adiabatic heating on stacking fault energy and the resulting deformation mechanisms. This section expands on the work of Pierce [22] (who identified that TWIP and TRIP mechanisms are present during quasi-static strain rates) by investigating the influences of strain rate on the deformation mechanisms. This section also compares the mechanical properties of full-sized tensile specimens measured on the same servo-hydraulic tensile machine, including two specimen thicknesses, to the work by Grässel *et al.* [30] which measured high strain-rate mechanical properties with multiple sample geometries and mechanical-testing methods for a steel with the same nominal composition. This section also includes detailed discussion of the effect of strain-rate on the thermal and athermal contributions to flow stress.

4.2.1 Optical Microscopy of Deformed Microstructures

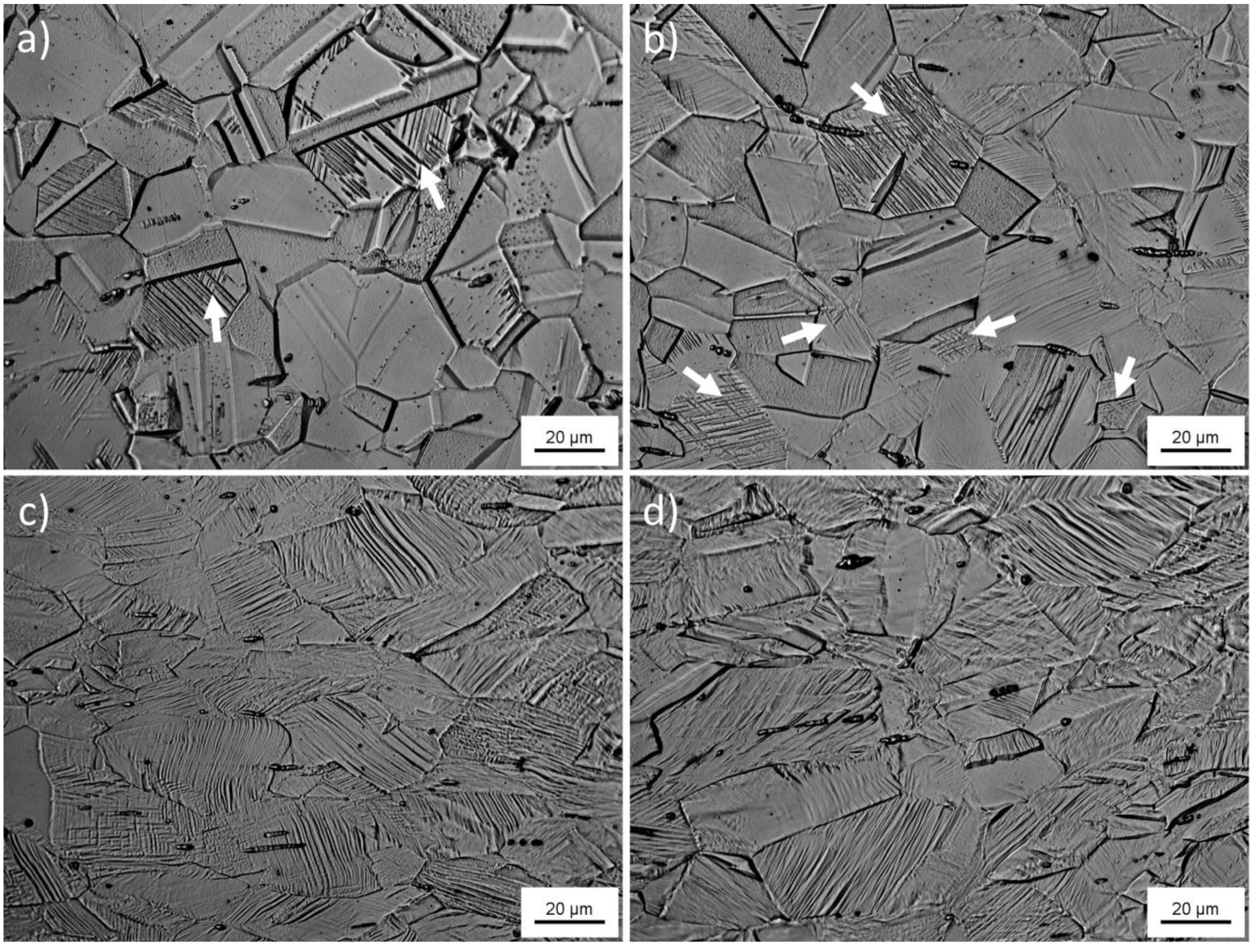

Figure 4-8: Optical micrographs of the Fe-25Mn-3Al-3Si alloy a) tested at $\dot{\varepsilon} = 2x10^2$ /s and interrupted at $\varepsilon_{eng.} = 0.07$, b) tested at $\dot{\varepsilon} = 2x10^2$ /s and interrupted at $\varepsilon_{eng.} = 0.2$, c) deformed to failure ($\varepsilon_{eng.} = 0.62$) at $\dot{\varepsilon} = 2x10^{-4}$ /s and d) deformed to failure ($\varepsilon_{eng.} = 0.60$) at $\dot{\varepsilon} = 2x10^2$ /s. In parts a) and b) grains with multiple variants of mechanical twins and/or hexagonal ε-martensite laths are indicated by arrows. All samples etched for 20 s with 10% nital. The tensile axis is in the horizontal direction.

Figure 4-8 shows optical micrographs of the deformed microstructure for interrupted and pulled-to-failure tensile tests at various strain rates. For Figure 4-8a, the tensile test at $\dot{\varepsilon}$ = $2x10^2$ /s was interrupted at $\varepsilon_{eng.} = 0.07$. Although TEM is required to differentiate between mechanical twins and/or ε-martensite laths, Figure 4-8a clearly reveals planar defects in a few grains and in some instances, multiple variants (as indicated by arrows). After interruption at $\varepsilon_{eng.}$ = 0.2 at the same strain rate, ($\dot{\varepsilon} = 2x10^2$/s), planar defects are apparent in most grains (as seen in

Figure 4-8b) in conjunction with more frequent instances of multiple variants (as indicated by arrows). The micrographs in Figure 4-8c-d originate from areas in the uniformly elongated region of the gauge section that are far from the fracture surfaces of tensile samples that were pulled to failure. The optical micrographs of microstructures in specimens deformed to failure at $\dot{\varepsilon} = 2x10^{-4}$ /s and $\dot{\varepsilon} = 2x10^{2}$ /s (Figure 4-8c-d, respectively) are qualitatively the same. In general, most grains show evidence of planar defects (mechanical twins and/or ε-martensite laths) distributed throughout the entire grain in at least one variant. The accommodation of large amounts of engineering strain by multiple slip systems is highlighted by substantial curvature of planar features and shearing within each elongated grain.

4.2.2 Influence of Strain Rate and Specimen Thickness on Mechanical Properties

An important criterion for AHSS design involves maximizing the strain at instability, i.e. the amount of uniform strain. This instability is derived from the Considère criterion and is defined as the true strain at which the strain-hardening rate is equal to the true stress [36][33]. Figure 4-9a shows the representative engineering stress-strain curves for the 0.95 mm sheet thickness at strain rates in the range of $\dot{\varepsilon} = 2x10^{-2}$ to $\dot{\varepsilon} = 2x10^{2}$ /s and Figure 4-9b shows the representative engineering stress-strain curves for the 1.15 mm sheet thickness at strain rates in the range of $\dot{\varepsilon} = 2x10^{-4}$ to $\dot{\varepsilon} = 2x10^{2}$ /s. All engineering stress-strain curves can be found in Appendix A (see Figure A-1). Representative true stress-strain curves and corresponding strain-hardening rates were calculated from engineering stress-strain values up to the point of instability and are shown in Figure 4-10a for the 0.95 mm sheet thickness and in Figure 4-10b for the 1.15 mm thick sheet. The true stress-strain values which satisfy the instability condition are converted to engineering stress-strain values of ultimate tensile strength (UTS) and uniform elongation (UE) and summarized in Figure 4-11 as a function of strain rate.

Values of the 0.2 % offset yield strength (YS) and total elongation (TE) from the representative engineering stress-strain curves in Figure 4-9 are also summarized in Figure 4-11 as a function of strain rate. Figure 4-11a illustrates the behavior of the YS and UTS for the 0.95 mm sheet thickness as a function of strain rate, while Figure 4-11c displays the change in YS and UTS as a function of strain rate for the 1.15 mm sheet thickness. Figure 4-11b shows the effect of strain rate on UE and TE values for the 0.95 mm sheet thickness, while Figure 4-11d demonstrates the effect of strain rate on UE and TE for the 1.15 mm sheet thickness.

The 0.2 % offset yield strength of the 1.15 mm thick sheet rose continuously from 306 ± 10 MPa to 503 MPa (a 64 % increase) with increasing the strain rate by 6 orders of magnitude from $\dot{\varepsilon} = 2\text{x}10^{-4}$ to $\dot{\varepsilon} = 2\text{x}10^{2}$ /s, (see Figure 4-9b and Figure 4-11c). As for the 0.95 mm thick sheet, increasing strain rate by 4 orders of magnitude from $\dot{\varepsilon} = 2\text{x}10^{-2}$ to $\dot{\varepsilon} = 2\text{x}10^{2}$ /s resulted in an increase of the 0.2 % offset yield strength from 394 ± 18 MPa to 502 ± 10 MPa (a 27 % increase), as seen in Figure 4-9a and Figure 4-11a. For comparison, the 0.2 % offset yield strength of the 1.15 mm thick sheet specimen deformed at $\dot{\varepsilon} = 2\text{x}10^{-2}$ /s was 395 MPa, which also increased by 27 % from $\dot{\varepsilon} = 2\text{x}10^{-2}$ to $\dot{\varepsilon} = 2\text{x}10^{2}$ /s. Therefore, the different sheet thicknesses had no influence on the magnitude of the 0.2 % offset yield strength or the strain rate sensitivity of the yield strength.

The instantaneous engineering stress at any given strain is >100 MPa higher at a strain rate of $\dot{\varepsilon} = 2\text{x}10^{-2}$ than at a strain rate of $\dot{\varepsilon} = 2\text{x}10^{2}$ /s, regardless of sheet thickness (see Figure 4-9a-b). Truly quasi-static strain rate tests ($\dot{\varepsilon} = 2\text{x}10^{-4}$ /s in this case) were only conducted with the 1.15 mm thick sheet, as seen in Figure 4-9b, and the results show greater work-hardening, plus a higher UTS and TE as compared to the $\dot{\varepsilon} = 2\text{x}10^{-2}$ /s test of the same sheet thickness. The product of strength and elongation (PSE) of the 0.95 mm thick sheet increased from 33,000 MPa·% to 44,000 MPa·% with increasing the strain rate from $\dot{\varepsilon} = 2x10^{-2}$ to $\dot{\varepsilon} = 2x10^{2}$ /s. The same increase in strain rate for the 1.15 mm thick sheet yielded an increase in PSE from 44,000 MPa·% to 58,000 MPa·%. As a baseline measurement for PSE comparisons, the quasi-static PSE of the 1.15 mm thick sheet is 48,000 MPa·%. Thus, increasing the strain rate from $\dot{\varepsilon} = 2x10^{-2}$ to $\dot{\varepsilon} = 2x10^{2}$ /s increases the PSE and increasing sheet thickness increases the PSE of the Fe-25Mn-3Al-3Si alloy.

In the case of the 1.15 mm sheet thickness, Figure 4-9b shows that the flow stress of the $\dot{\varepsilon} = 2x10^{-2}$ /s test, for strain values below approximately $\varepsilon_{eng.} = 0.2$, was greater than for the quasi-static test ($\dot{\varepsilon} = 2x10^{-4}$ /s). Differences in the strain-hardening rate (shown in Figure 4-10b) lead to a slightly smaller TE and UE (by approximately $\varepsilon_{eng.} = 0.03$) for the test at $\dot{\varepsilon} = 2x10^{-2}$ /s and to a slightly larger UTS (by approximately 50 MPa) for the quasi-static tests ($\dot{\varepsilon} = 2x10^{-4}$ /s). These observations equate to a slight decrease in PSE between $\dot{\varepsilon} = 2x10^{-4}$ /s and $\dot{\varepsilon} = 2x10^{-2}$ /s. Within the context of the strain-hardening behavior in Figure 4-10, the lowest value of strain-hardening rate below $\varepsilon_{true} = 0.15$ is observed for the tests at $\dot{\varepsilon} = 2x10^{-2}$ /s, regardless of sheet thickness. The [quasi-static] test at $\dot{\varepsilon} = 2x10^{-4}$ /s of the 1.15 mm thick sheet has a greater strain-hardening rate than the test at $\dot{\varepsilon} = 2x10^{-2}$ /s, but a lower yield strength. As strain rate is increased from $\dot{\varepsilon} = 2x10^{-2}$ /s to $2x10^{2}$ /s, the strain-hardening rate between $\varepsilon_{true.} = 0.07$ and 0.15 increases slightly by >200 MPa. However, given the limited number of tensile tests conducted with the 1.15 mm sheet thickness, strict conclusions should not be drawn from these observations.

The average TE increases by less than 10% engineering strain across the entire range of strain rates for the 0.95 mm sheet thickness, as shown in Figure 4-11b. There is little change in UE with increasing strain rate up to $\dot{\varepsilon} = 2x10^{1}$ /s, and UE decreases between $\dot{\varepsilon} = 2x10^{1}$ /s and $\dot{\varepsilon} = 2x10^{2}$ /s, (see Figure 4-11b). The data for the 1.15 mm thick sheet show that an increase in strain rate from $\dot{\varepsilon} = 2x10^{-4}$ to $\dot{\varepsilon} = 2x10^{2}$ /s increases YS significantly and UTS slightly, (see Figure 4-11c), whereas UE decreases, (see Figure 4-11d). Between $\dot{\varepsilon} = 2x10^{-4}$ and $\dot{\varepsilon} = 2x10^{-2}$ /s, TE decreases slightly and then increases by nearly 10% strain between $\dot{\varepsilon} = 2x10^{-2}$ and $\dot{\varepsilon} = 2x10^{2}$ /s for the 1.15 mm sheet thickness. As seen in Figure 4-11, the average UE and average UTS is slightly greater for the 1.15 mm sheet thickness (for tests deformed at the same strain rate: $\dot{\varepsilon} = 2x10^{-2}$ /s and $\dot{\varepsilon} = 2x10^{2}$ /s). However, when one standard deviation is taken into account for the multiple tests with 0.95 mm sheet thickness and compared to the 1.15 mm sheet thickness results, (which are based on only one tensile test each at $\dot{\varepsilon} = 2x10^{-2}$ /s and $\dot{\varepsilon} = 2x10^{2}$ /s), it is concluded that UE and UTS do not differ significantly in a statistical manner between the studied sheet thicknesses.

Figure 4-11b and Figure 4-11d also show that an increase in sample thickness (of approximately 10%) increased total elongation by approximately 10% (for tests deformed at the same strain rate, $\dot{\varepsilon} = 2x10^{-2}$ /s and $\dot{\varepsilon} = 2x10^{2}$ /s). Reduction-in-area was also considered and measured at the smallest region of the neck of the fracture point with calipers. Figure 4-12 shows reduction-in-area measurements on all tensile samples for both thicknesses. The 1.15 mm thick sheet specimens had slightly higher reduction-in-area than the 0.95 mm thick sheet specimens, but reduction-in-area measurements on sheet specimens are more difficult than on cylindrical samples and can lead to large inaccuracies. In summary of Figure 4-12, quasi-static strain rates showed the highest reduction-in-area, but reduction-in-area values for strain rates of $\dot{\varepsilon} = 2x10^{-2}$ /s to $\dot{\varepsilon} = 2x10^{2}$ /s do not show any significant difference for the same sheet thickness. Therefore, the TE, UE and reduction-in-area values suggest that post-uniform elongation and/or more diffuse necking (longer necks and/or multiple necks) is more prevalent at higher strain rates.

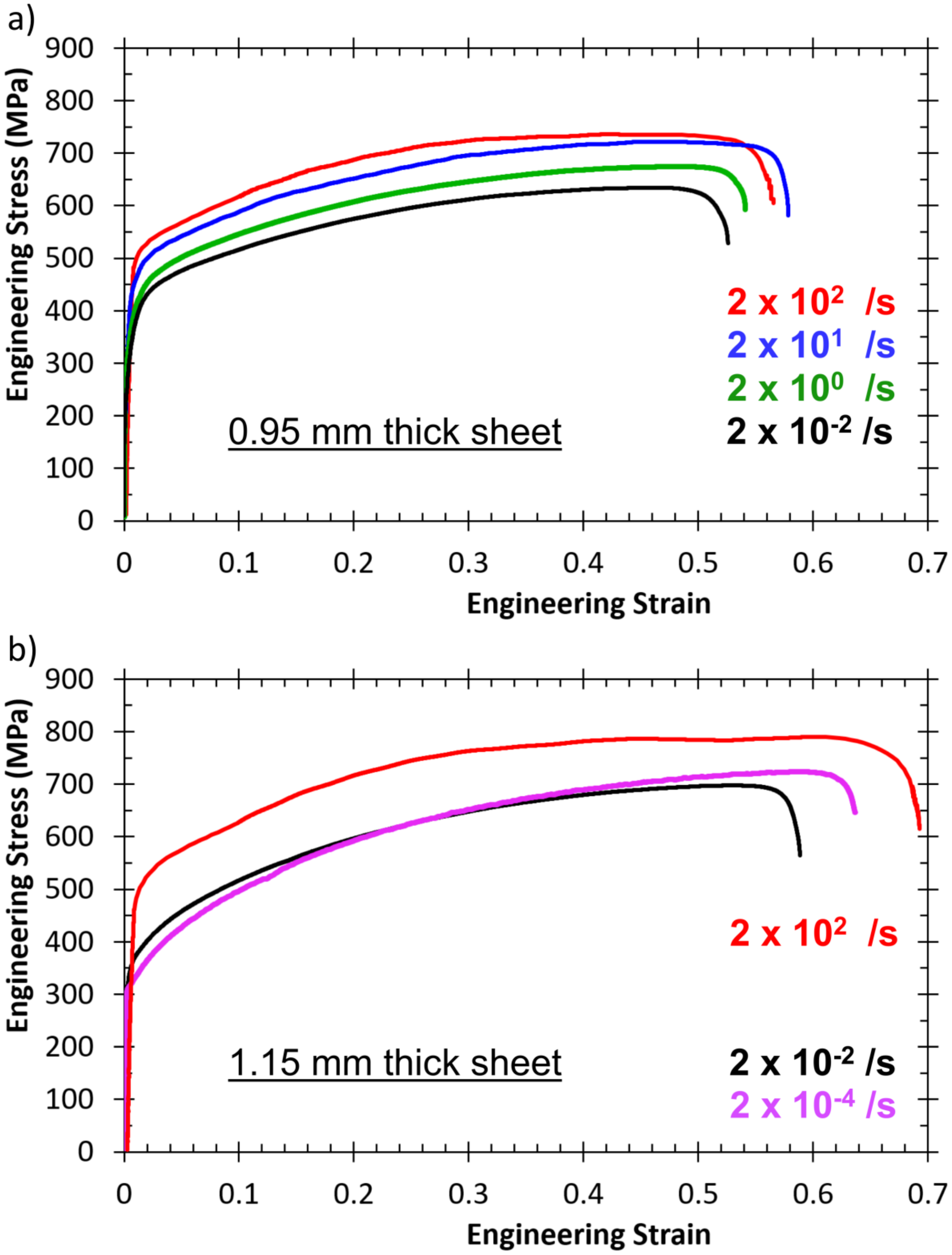

Figure 4-9: Representative engineering stress (MPa) vs. engineering strain curves for the Fe-25Mn-3Al-3Si alloy when pulled-to-failure at strain rates from $\dot{\varepsilon} = 2x10^{-4}$ /s to $\dot{\varepsilon} = 2x10^{2}$ /s, based on: a) specimens from the 0.95 mm thick sheet and b) specimens from the 1.15 mm thick sheet.

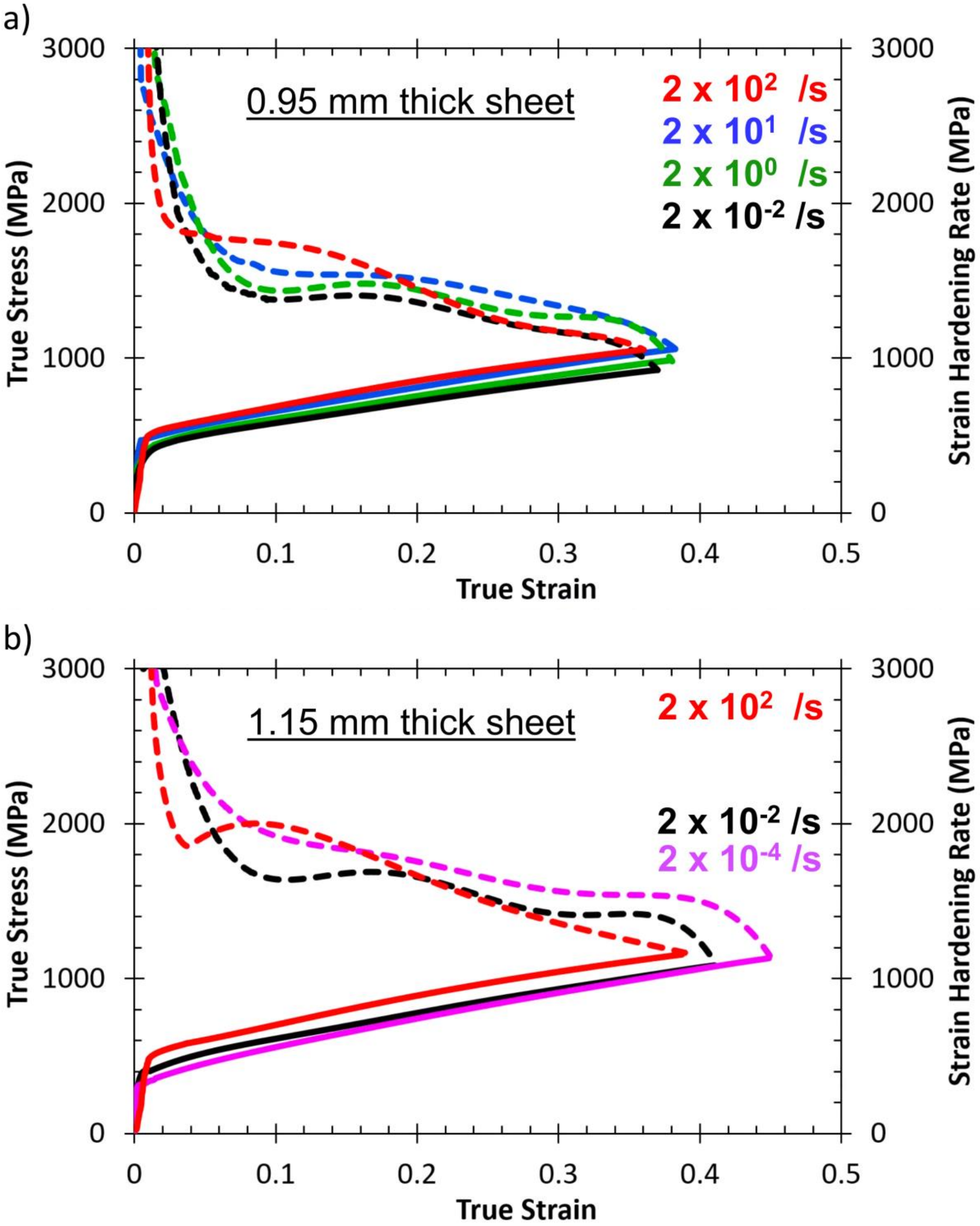

Figure 4-10: Representative true stress (MPa) and strain-hardening rate (MPa) vs. true strain for the Fe-25Mn-3Al-3Si alloy when pulled-to-failure at strain rates from $\dot{\varepsilon} = 2\text{x}10^{-4}$ /s to $\dot{\varepsilon} = 2\text{x}10^{2}$ /s, based on: a) specimens from the 0.95 mm thick sheet and b) specimens from the 1.15 mm thick sheet. The Considère criterion was used to determine the instability condition, such that these true stress-strain curves end at the point where the strain-hardening rate curve intersects the true stress-strain curve.

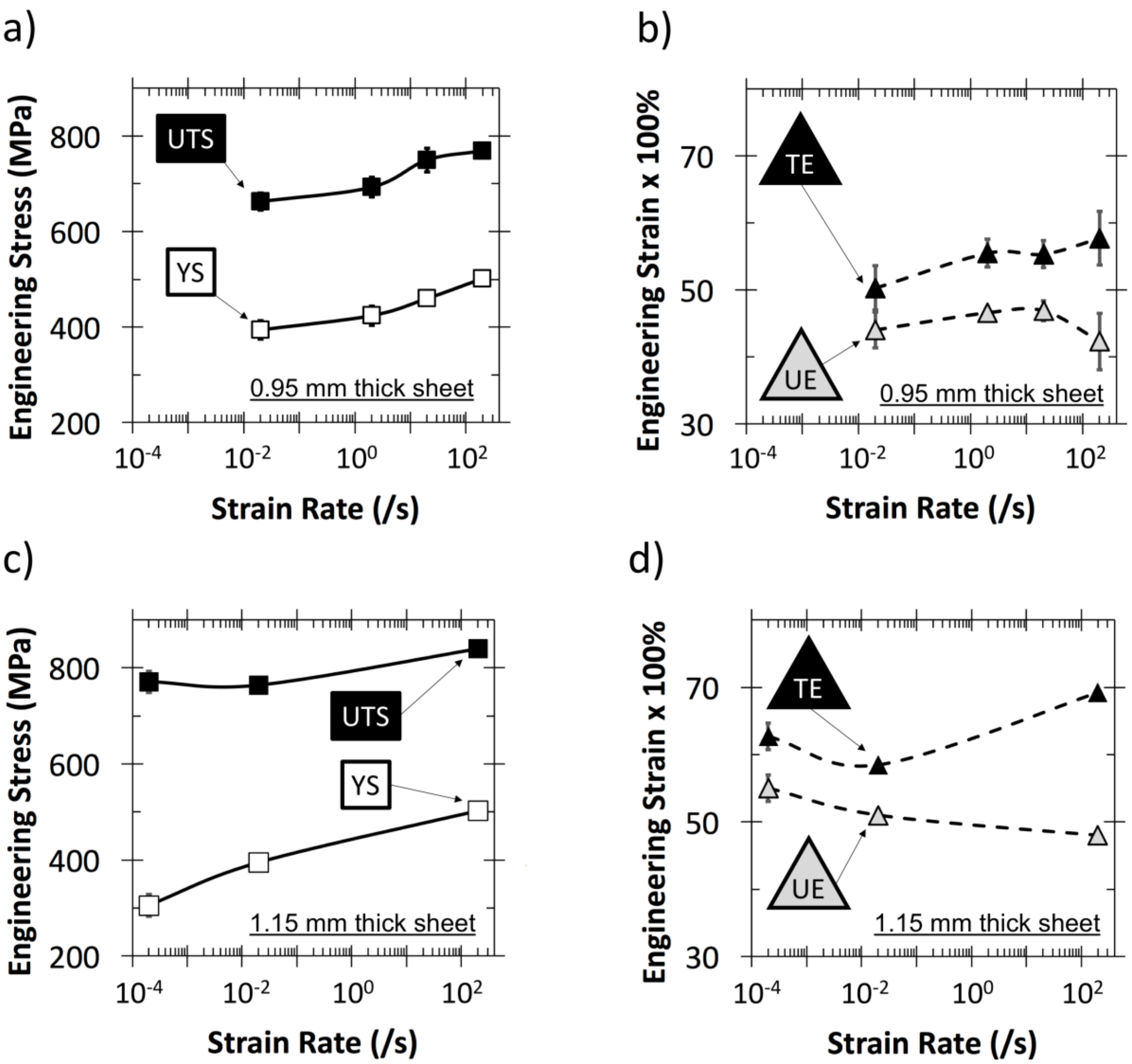

Figure 4-11: a) and c) Ultimate tensile strength (UTS) and 0.2 % offset yield-strength (YS) values, along with b) and d) total elongation (TE) and uniform elongation (UE) values are summarized as a function of strain rate for a-b) 12 specimens from the 0.95 mm thick sheet and c-d) 4 specimens from the 1.15 mm thick sheet. Error bars represent one standard deviation. Data points without error bars are based on only one pull-to-failure test for that strain rate and sheet thickness.

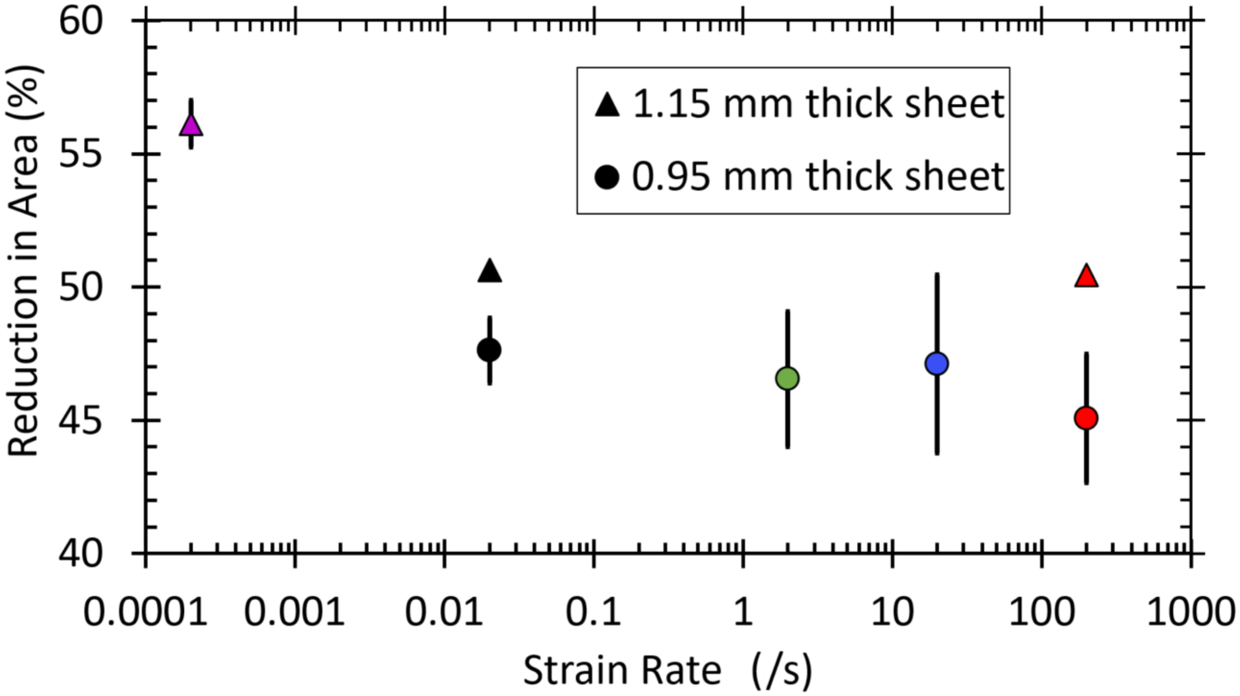

Figure 4-12: Reduction-in-area for both sheet thicknesses of all pull-to-failure tests. Error bars represent one standard deviation and data points without error bars are based on one pull-to-failure test.

4.2.3 Micro-Hardness Measurements of Deformed Microstructures

The micro-hardness was measured for specimens in the as-recrystallized state and following both interrupted and pull-to-failure tests to determine if any significant differences exist in the material hardness after deformation at different strain rates for the same nominal strain. Any differences in the micro-hardness with respect to a change in strain and/or strain rate might be attributed to changes in the microstructure, including differences in dislocation density, dislocation sub-structure, and the type, spacing, and amount of planar secondary deformation activity. The grain size is 21 µm for both sheet thicknesses (1.15 mm and 0.95 mm). The hardness of the as-recrystallized 0.95 mm and 1.15 mm thick sheets were 151 ± 15 HV and 160 ± 19 HV, respectively. As no statistically significant difference in micro-hardness for the as-received microstructures existed, the measurements on both steel sheets are plotted together.

Figure 4-13 clearly shows an increase in Vickers micro-hardness with increasing engineering strain from approximately 155 HV in the as-received condition to approximately 350 HV after pull-to-failure. However, Vickers measurements of all interrupted and pull-to-failure samples do not indicate a significant difference in micro-hardness with respect to a difference in strain rate at the same nominal level of strain. This could indicate that 1) no significant differences in the microstructure exist at different strain rates for the same nominal strain, or 2) that any microstructural differences that exist do not significantly influence the hardness.

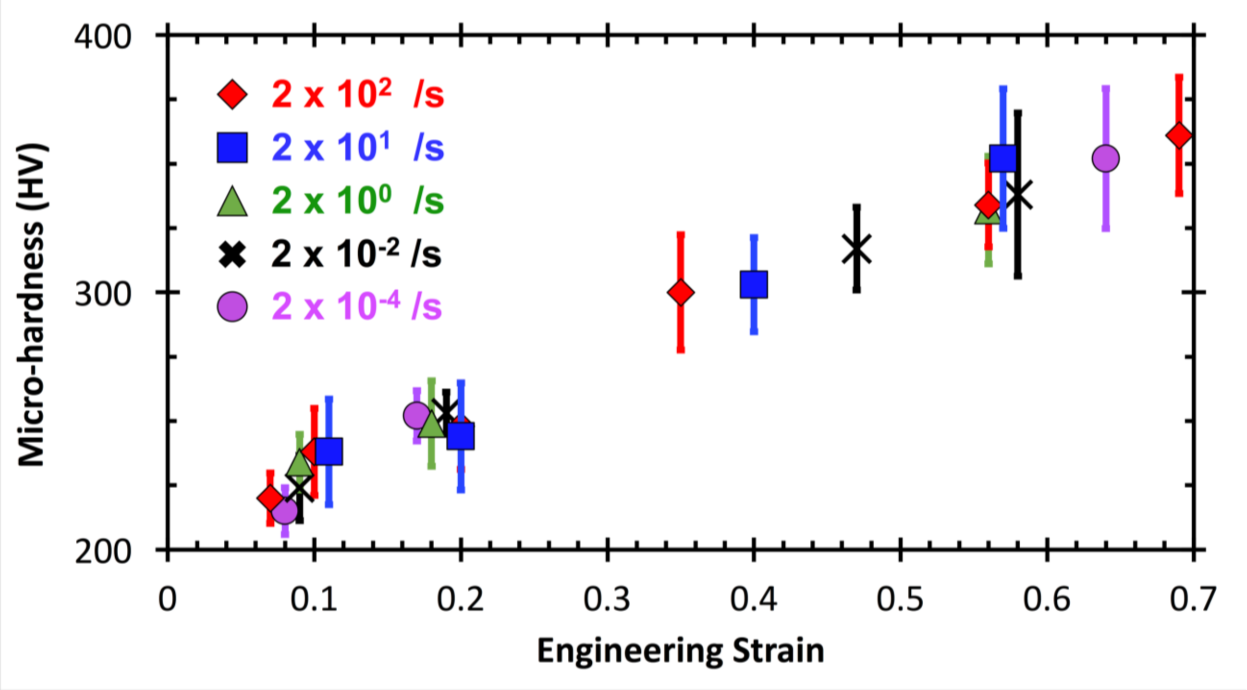

Figure 4-13: Micro-hardness measurements completed for all interrupted and pull-to-failure samples and plotted as a function of engineering strain, for all strain rates. Error bars represent one standard deviation based on an average of all hardness indents made for a given strain rate and strain.

4.2.4 Non-Contact Temperature Measurements During Deformation

Figure 4-14a-b depicts thermal images recorded using a calibrated thermal camera at specific time/strain intervals during tensile tests conducted at engineering strain rates of a) $\dot{\varepsilon} = 2 \times 10^{-2}$ /s and b) $\dot{\varepsilon} = 2 \times 10^{1}$ /s. At both strain rates the temperature distribution in the gauge section was approximately uniform at 0.21 strain. However, the images immediately following fracture show that localized heating on the order of 110 °C occurred in a single neck location for $\dot{\varepsilon} = 2 \times 10^{-2}$ /s. In comparison, the temperature distribution of the $\dot{\varepsilon} = 2 \times 10^{1}$ /s sample shows several areas of locally higher temperature as compared to the rest of the gauge section, which suggests multiple areas of strain localization. The appearance of multiple regions of strain localization was observed in several instances for the $\dot{\varepsilon} = 2\text{x}10^{1}$ /s and $\dot{\varepsilon} = 2\text{x}10^{2}$ /s tests, (another example is provided in Figure C-1). The average temperature of the localized heat patterns registered 26 °C higher as compared to the rest of the uniformly deformed gauge section. The appearance of multiple strain localizations at the higher strain rate supports the increase in post-uniform necking at higher strain rates, whereas reduction-in-area (at the smallest region of a neck) is constant with an increase in strain rate from $\dot{\varepsilon} = 2\text{x}10^{-2}$ /s to $\dot{\varepsilon} = 2\text{x}10^{2}$ /s. The fracture area of a given test was observed to be significantly hotter than the uniformly elongated gauge, as expected for the large energy release associated with the creation of the free surfaces (the strain rate in the neck increases because of the localization of strain). A maximum spot temperature near the fracture surface was measured to be approximately 160 °C for a tensile specimen deformed at $\dot{\varepsilon} = 2\text{x}10^{1}$ /s. The temperature of such locations most likely exceeded this value in some of the tests, but the camera could not accurately record temperature too far outside the calibration range of -40 to 150 °C. After fracture, the average sample temperature continued to rise slightly by approximately 5 °C. This post-fracture temperature rise may be attributed to thermal equilibration of the sample. More heat is likely generated at the mid-thickness of the sample than at the free surface during plastic deformation, resulting in conductive heat transfer to the free surface during the test. Consequently, the data obtained from the thermal camera may slightly underestimate the average temperature of the specimen at any specific strain/time interval during the test, especially for higher strain rates tests.

ResearchIR™ software was used to calculate the average surface temperature across the entire area of the gauge length, neglecting the necked region and fracture surface, for every mechanical test. As sample thickness did not influence temperatures by more than 2 °C for a given strain rate, the average temperatures from representative pull-to-failure tests for the 0.95 mm and 1.15 mm thick sheets are plotted together in Figure 4-14c. Fluctuations in temperature measurement after fracture of samples deformed at $\dot{\varepsilon} = 2x10^1$ and $\dot{\varepsilon} = 2x10^2$ /s are due to the sample moving laterally with the load train outside of the defined area of the stationary thermal camera. The sharp increase in specimen temperature at 0.005 s for the tests at $\dot{\varepsilon} = 2x10^2$ /s is because the thermal camera could only record up to 200 fps (a frame captured every 5 ms) so only one image was recorded before fracture for the $\dot{\varepsilon} = 2x10^2$ /s tests as seen in Figure C-1. After fracture of the tensile specimen, the average surface temperature along the gauge length, neglecting the necked region and fracture surface, was approximately 91±5 °C for the tests at $\dot{\varepsilon} = 2x10^2$ /s, representing an increase in temperature of approximately 65 °C. The increase in strain rate from $\dot{\varepsilon} = 2x10^1$ to $\dot{\varepsilon} = 2x10^2$ /s resulted in an increase in average temperature of only 6°C, which should be proportional to the difference in work put into the sample minus the heat dissipated by the grips and surrounding air at the two different strain rates [77]. For the $\dot{\varepsilon} = 2x10^0$ /s, $\dot{\varepsilon} = 2x10^1$ /s , and $\dot{\varepsilon} = 2x10^2$ /s tests the average temperatures after fracture were 82, 85, and 91 °C, respectively. Under adiabatic heating conditions, the amount of heating is proportional to the amount of plastic work [181][77]. As shown in Table 4-1, the area under the engineering stress-strain curve, based on results in Figure 4-9, increases with increasing strain rate (not including quasi-static strain rates where heating is negligible). The expected temperature rise under fully adiabatic conditions was calculated using an accepted formula for estimating temperature rise during measured plastic work including a 90 % efficiency in conversion of mechanical energy to heat energy and a heat capacity of 0.46 kJ/(kg K) [15][56]. The mass density used in the calculations for the Fe-25Mn-3Al-3Si steel is 7.4 g/cm^3 [22]. The trend in calculated results is consistent with the trend in experimental observations (described in more detail with reference to Figure 4-14d) such that the average temperature in the uniformly elongated area increases with increasing strain rate. Lastly, the $\dot{\varepsilon}$ = 2x10^2 /s and $\dot{\varepsilon}$ = 2x10^1 /s tests seemed to exhibit a wider spread in maximum average temperature across the elongated gauge section (neglecting the fracture surface) as compared to the lower strain rate tests.

The average surface temperature in the area of uniform elongation is plotted as a function of strain for representative curves in Figure 4-14d. The 200/s data is not included in the plot, because only one image was recorded before fracture. Figure 4-14d confirms that as strain accumulates and strain rate increases, (from $\dot{\varepsilon}$ = 2x10^{-2} to $\dot{\varepsilon}$ = 2x10^1 /s), the average surface temperature of the gauge length (where it deforms uniformly) increases. The calculated results in Table 4-1, (based on measured plastic work under the assumption of adiabatic heating conditions), predict a temperature of 80 °C for the $\dot{\varepsilon}$ = 2x10^0 /s tests, which is consistent with the temperature measured right before fracture during the $\dot{\varepsilon}$ = 2x10^0 /s tests, seen in Figure 4-14d. Also seen in Figure 4-14d, the specimen temperature curves at $\dot{\varepsilon}$ = 2x10^0 and $\dot{\varepsilon}$ = 2x10^1 /s exhibit some overlap, suggesting that near-adiabatic heating conditions are reached for strain rates at or greater than $\dot{\varepsilon}$ = 2x10^0 /s.

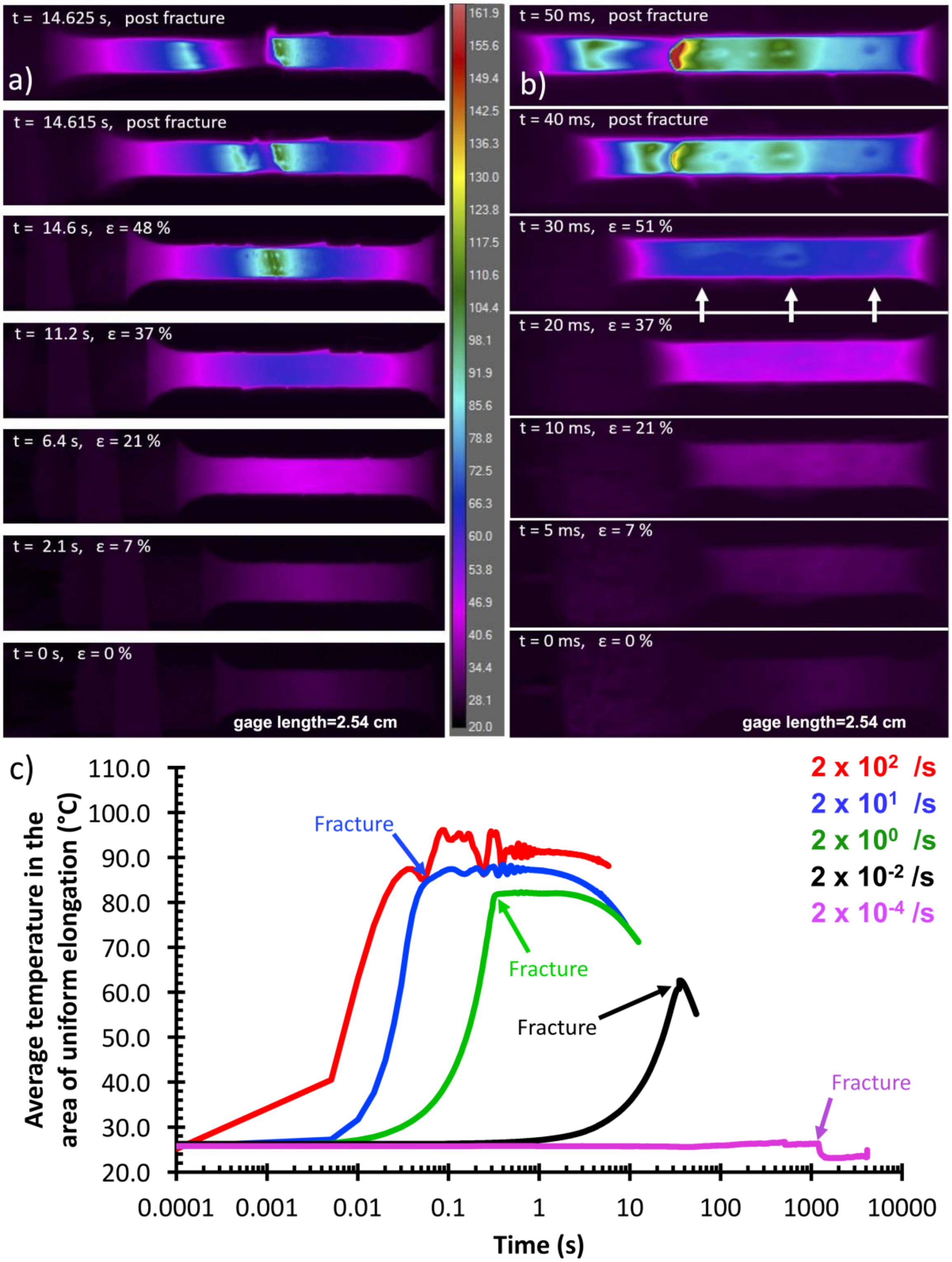
a)
t = 14.625 s, post fracture
t = 14.615 s, post fracture
t = 14.6 s, ε = 48 %
t = 11.2 s, ε = 37 %
t = 6.4 s, ε = 21 %
t = 2.1 s, ε = 7 %
t = 0 s, ε = 0 %
gage length=2.54 cm
161.9
155.6
149.4
142.5
136.3
130.0
123.8
117.5
110.6
104.4
98.1
91.9
85.6
78.8
72.5
66.3
60.0
53.8
46.9
40.6
34.4
28.1
20.0
b)
t = 50 ms, post fracture
t = 40 ms, post fracture
t = 30 ms, ε = 51 %
t = 20 ms, ε = 37 %
t = 10 ms, ε = 21 %
t = 5 ms, ε = 7 %
t = 0 ms, ε = 0 %
gage length=2.54 cm
c)
Average temperature in the area of uniform elongation (°C)
110.0
100.0
90.0
80.0
70.0
60.0
50.0
40.0
30.0
20.0
0.0001
0.001
0.01
0.1
1
10
100
1000
10000
Time (s)
Fracture
Fracture
Fracture
Fracture
2 x 10² /s
2 x 10¹ /s
2 x 10⁰ /s
2 x 10⁻² /s
2 x 10⁻⁴ /s

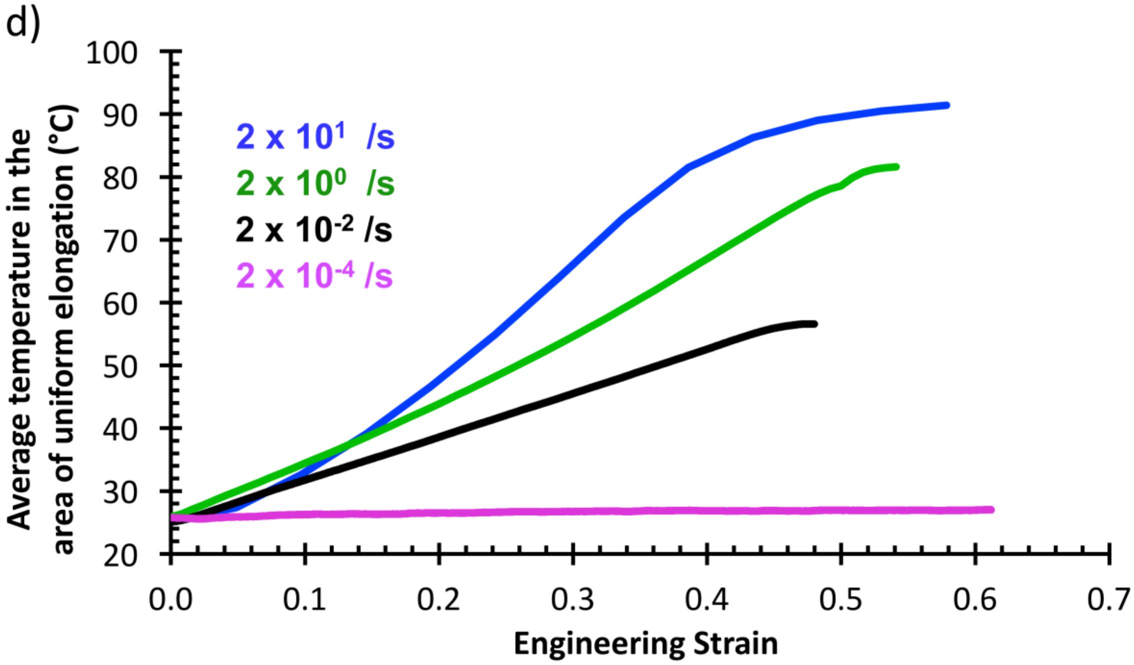

Figure 4-14: a,b) Thermal images recorded at 200 fps by an infrared camera as a function of strain, with indicated time stamps corresponding to different strain rates: a) $\dot{\varepsilon} = 2x10^{-2}$ /s and b) $\dot{\varepsilon} = 2x10^{1}$ /s. The arrows in b) indicate localized hot-spots (multiple necking initiation points) with the left-most being the eventual fracture surface. c) Non-contact measurements of the average surface temperature along the gauge length are plotted as a function of time for the different strain rates for representative pull-to-failure tests. d) Average surface temperature of uniformly elongated regions during representative pull-to-failure tensile tests of the Fe-25Mn-3Al-3Si alloy.

Table 4-1: Average area under engineering stress strain curves from Figure 4-9 (numerically-integrated) and predicted [15][56] increase in temperature.

Strain rate (/s)	0.95 mm thick sheets Average (area under engineering stress-strain curve) and the [predicted temperature] under the assumption of adiabatic conditions. (mJ/mm^3) / [°C]	1.15 mm thick sheets Average (area under engineering stress-strain curve) and the [predicted temperature] under the assumption of adiabatic conditions. (mJ/mm^3) / [°C]
2 x 10^2	388 / 94	501 / 122
2 x 10^1	354 / 86	--
2 x 10^0	330 / 80	--
2 x 10^{-2}	283 / 69	358 / 87

4.2.5 Thermodynamic Modeling of Stacking Fault Energy

A composition- and temperature-dependent thermodynamic model was previously developed to predict the SFE of Fe-Mn-Al-Si steels [23]. This model was used in the current work to assess the increase in SFE as a function of strain and temperature and the results are reported in Table 4-2 and Table 4-3, respectively. The model calculates the SFE on the basis of the difference in Gibbs free energy of the face-centered cubic (FCC) and hexagonal close-packed (HCP) phases, the interfacial energy between the FCC and HCP phases, as well as the strain energy that arises due to a contraction in molar volume of the HCP phase [23]. The exact temperature dependence of the FCC/HCP interfacial energy is unknown and for the purposes of this calculation, the FCC/HCP interfacial energy of 8.6 mJ/m^2 determined at RT for a Fe-25Mn-3Al-3Si steel of nearly the same actual composition is assumed. However, Cotes *et al.* [182] reported that the FCC/HCP interfacial energy decreases with increasing temperature in binary Fe-Mn steels. In addition, the strain-energy term, calculated to be 2.3 mJ/m^2 at room temperature is also assumed to be independent of temperature in the calculation of the SFE. However, the dependence of the strain-energy term on shear modulus, which is reported to decrease with increasing temperature in high Mn steels [183], suggests the strain energy term might also decrease with increasing temperature. Therefore, the calculated SFEs may slightly overestimate the actual SFEs of the material at elevated temperatures. Table 4-2 shows the predicted SFE for samples deformed at $\dot{\varepsilon} = 2x10^1$ /s to various amounts of strain based on three interruption tests and one pull-to-failure test. The model predicts that the SFE increases from a RT value of approximately 21 [23] to 35.3 mJ/m^2 at maximum uniform elongation of a test at $\dot{\varepsilon} = 2x10^1$ /s corresponding to a temperature of 91 °C. Table 4-3 shows the predicted SFE for samples interrupted at $\varepsilon_{eng.} = 0.2$ in the strain-rate range of $\dot{\varepsilon} = 2x10^{-4}$ to $\dot{\varepsilon} = 2x10^2$ /s. An increase of 6 orders of magnitude in strain rate from $\dot{\varepsilon} = 2\text{x}10^{-4}$ to $\dot{\varepsilon} = 2\text{x}10^{2}$ /s increases the average specimen temperature by only 17 °C and the SFE by only 3 mJ/m^2 for two samples interrupted at $\varepsilon_{eng.} = 0.2$ and is not expected to significantly change the deformation mechanisms.

Table 4-2: Predicted stacking fault energy with respect to an increase in temperature due to adiabatic heating for three interrupted tests & an average temperature of the four pulled-to-failure tests (average total strain of 0.58) when deformed at the same strain rate.

Total strain ($\varepsilon_{eng.}$)	Average temperature in the uniformly elongated area when deformed at $\dot{\varepsilon} = 2 \text{ x } 10^1$ /s (°C)	Predicted SFE (mJ/m^2)
0.58	91.1	35.3
0.40	59.9	30.1
0.18	41.8	27.2
0.11	37.8	26.6

Table 4-3: Predicted stacking fault energy with respect to an increase in temperature due to adiabatic heating when interrupted to $\varepsilon_{eng.} = 0.2$ at different strain rates.

Strain rate (/s)	Average temperature in the uniformly elongated area interrupted to $\varepsilon_{eng} = 0.18$ (°C)	Predicted SFE (mJ/m^2)
$2 \text{ x } 10^{2}$	43.9	27.6
$2 \text{ x } 10^{1}$	41.8	27.2
$2 \text{ x } 10^{0}$	39.1	26.8
$2 \text{ x } 10^{-2}$	36.3	26.4
$2 \text{ x } 10^{-4}$	26.7	25.1

4.2.6 TEM for Characterizing Planar Defects in Interrupted Samples

The onset of strain-induced mechanical twinning and/or ε-martensite is often manifested by the appearance of a change in shape, usually between ε_{true}= 0.1 and 0.2, of the strain-hardening rate versus true strain curve at quasi-static strain rates [12]. Therefore, changes in the strain-hardening rate at high strain rates may indicate a difference in twin volume fraction or a change in the strain at which mechanical twinning begins [77] relative to quasi-static strain rates. In previous work on this high-Mn alloy using different tensile geometries [30][29][12], characterization of the evolution of dislocation structures during deformation at quasi-static strain rates indicated a TWIP-dominated behavior, with some evidence of TRIP in the form of hexagonal ε-martensite. As shown in the bright-field TEM micrograph in Figure 4-15, a specimen interrupted at $\varepsilon_{eng.} = 0.1$ tested at $\dot{\varepsilon} = 2x10^2$ /s in the present work exhibits mechanical twinning. The mechanical twins are clearly impeding the glide of other partial dislocations on non-coplanar slip systems. Twins and ε-martensite have been reported to form at around $\varepsilon_{eng.} = 0.1$ for this alloy at quasi-static strain rates [12], so it is no surprise that the planar defects present at $\varepsilon_{eng.} = 0.1$ are observed to impede motion of leading partial dislocations [99] on different slip systems. More importantly, an increase in strain hardening may also arise from a decrease in dislocation mean-free-path by an increase in forest dislocation density or decrease in the average spacing between planar defects. After interruption at $\varepsilon_{eng.} = 0.2$ for a specimen tested at $\dot{\varepsilon} = 2x10^2$ ε/s, (see Figure 4-16), both TWIP and TRIP effects are observed on parallel {111} slip systems. This observation indicates hexagonal ε-martensite can still form at high strain rates, despite an increase in the SFE due to adiabatic heating. Moreover, the overall message gathered from Figure 4-15 and Figure 4-16 is that there are no significant changes in the underlying TWIP-TRIP mechanisms between $\dot{\varepsilon} = 2x10^{-4}$ /s and $\dot{\varepsilon} = 2x10^2$ /s because the microstructural evolution is similar (TWIP-dominated behavior with some evidence of TRIP in the form of hexagonal ε-martensite). These observations will be quantified and discussed in the next section with the implication that slight differences in strain-hardening rate for the Fe-25Mn-3Al-3Si (wt%) alloy are not associated with a transition from TRIP-dominated to TWIP-dominated behavior, but rather due to slight changes in dislocation mean free path.

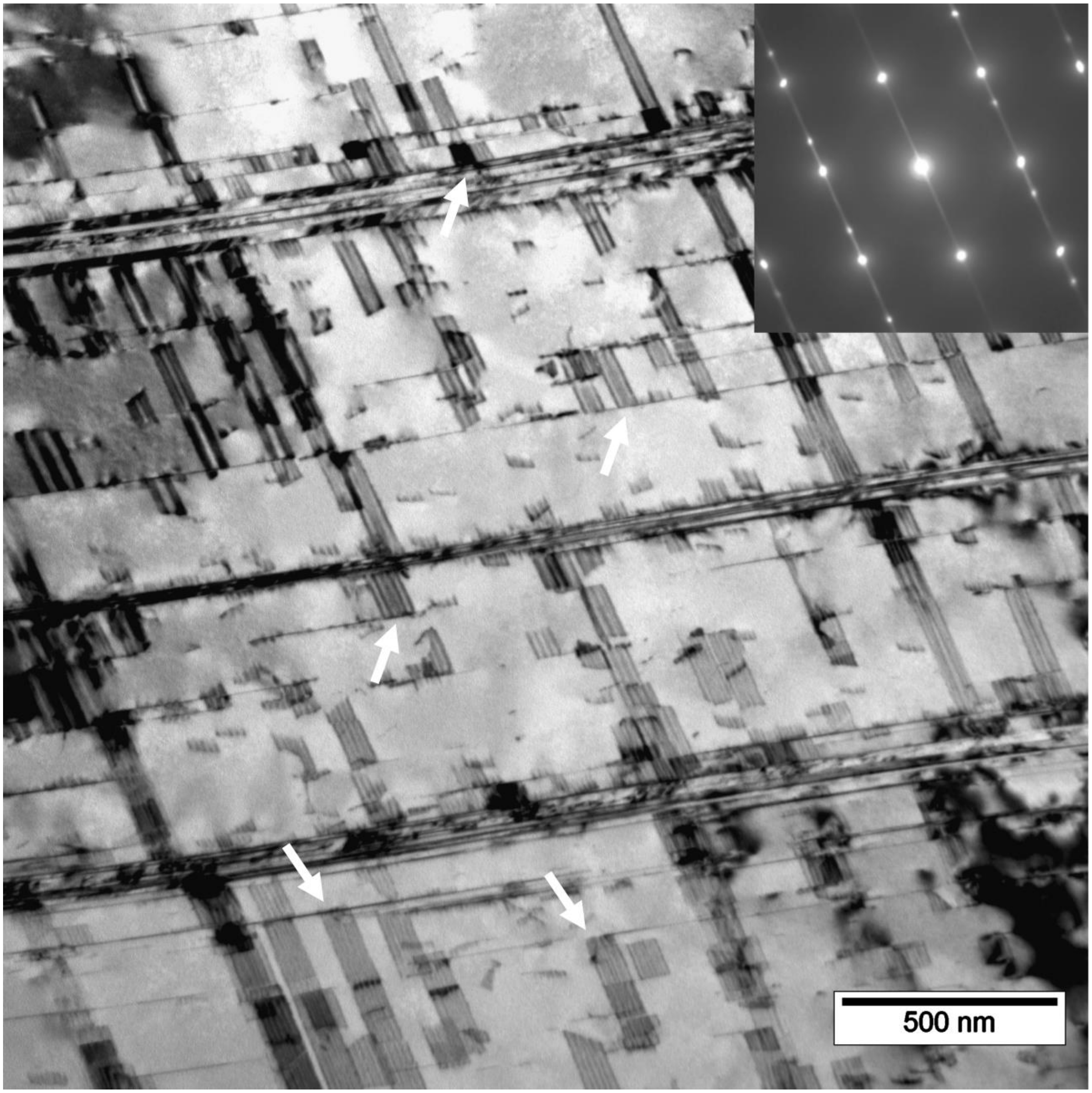

Figure 4-15: The inset selected area electron diffraction pattern (SAEDP) was recorded at the [110] zone axis to identify the edge-on planar defects (in this case: deformation twinning) in a 0.95 mm sheet specimen interrupted at $\varepsilon_{eng.} = 0.1$ and tested at $\dot{\varepsilon} = 2x10^2$ /s. By tilting the sample slightly off the zone axis, a two-beam condition using a 1 -1 -1 diffracting (g)-vector to provide greater defect contrast was created for the bright field image, which highlights the ability of some planar defects to impede subsequent partial dislocation motion along other {111}/<110> slip systems, as indicated by white arrows.

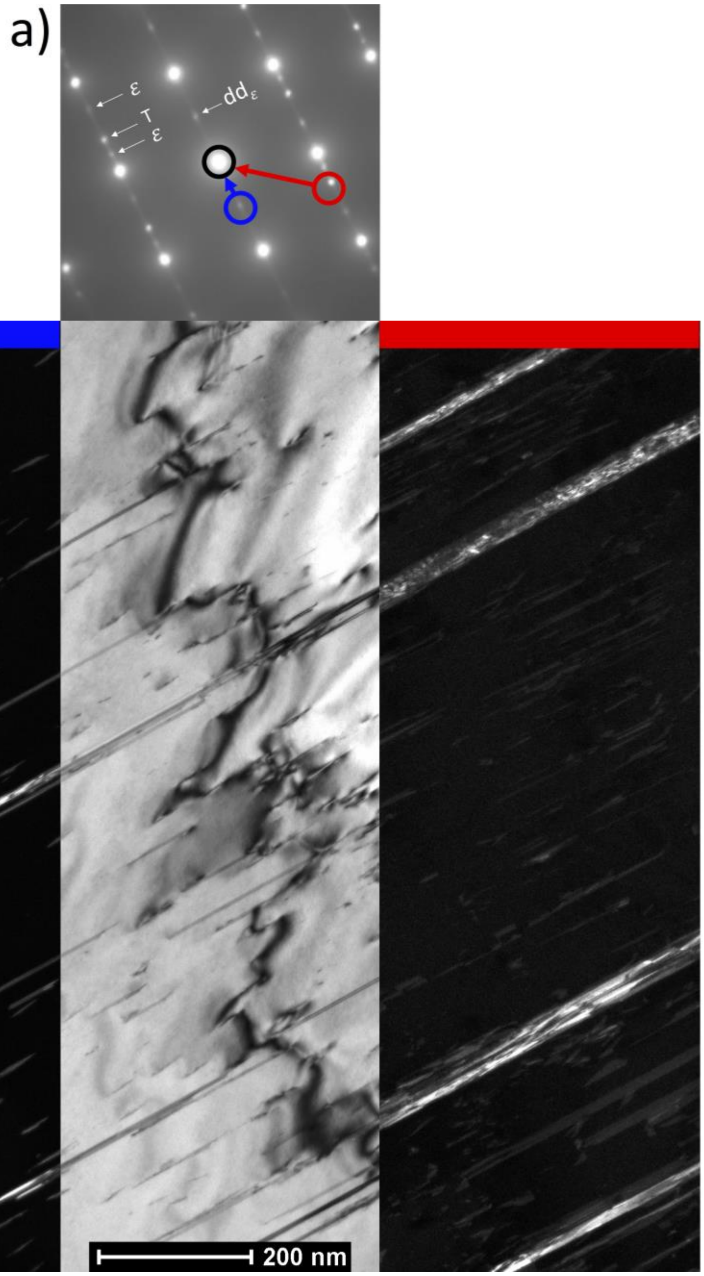

Figure 4-16: In a sample interrupted at $\varepsilon_{eng.} = 0.2$ at $\dot{\varepsilon} = 2\text{x}10^{2}$ /s with the 0.95 mm sheet, a) non-matrix diffraction spots in the [110] austenite SAED pattern (ε-martensite is “ε”, deformation twinning is “T” and dd$_{\varepsilon}$ is double diffraction contributed from the {0-11-1} and {01-10} hexagonal epsilon martensite reflections [12]). A centered objective aperture was used to form b) respective dark-field images and the bright-field image for continuity. Diffraction analysis indicates ε-martensite platelets (left) and deformation twinning (right) are observed after interruption at high strain rates.

4.2.7 Quantification of Planar Defects

SEM- and TEM-based characterization techniques were used to quantify the thickness and spacing of planar defects in specimens from interrupted tensile tests at different strain rates. Although some surveyed grains contained a higher number of planar defects and other grains contained fewer planar defects, representative images are shown in Figure 4-17. DF-TEM measurements of ε-martensite thickness revealed 94% of the population is grouped at 10 nm and smaller. Kernel fitting of planar defect thickness distributions acquired by ECCI and DF-TEM, seen in Figure 4-18, shows that distributions acquired by ECCI measurements tend to miss most of the planar defects that are less than 10 nm in thickness for this alloy. It should be noted that ECCI doesn't differentiate between twins and ε-martensite. As the distributions are non-Gaussian, both the average thickness and median thickness for a given distribution are reported in Figure 4-19. Table 4-4 indicates an approximately 50% chance of surveying a grain which also contained planar defects. The percentage of grains for which mechanical twinning and ε-martensite reflections were observed in <101> SAED patterns is also reported in Table 4-4 and indicates that an increased strain rate results in a modest increase in the fraction of grains with twins, but a slight decrease in the fraction of grains containing ε-martensite. A slight decrease (265 nm to 211 nm) in the spacing between twins was observed for higher strain rates, as seen in Figure 4-20. However, ECCI and DF-TEM distributions shown in Figure 4-19 and Figure 4-20 do not reveal significant trends in the effect of strain rate ($\dot{\varepsilon} = 2\text{x}10^{-4}$ to $\dot{\varepsilon} = 2\text{x}10^{0}$ /s) on the thickness and spacing of planar defects in samples interrupted at $\varepsilon_{eng.} = 0.18$ and 0.17 engineering strain.

Table 4-4: Comparison of SEM- and TEM-based techniques used to survey grains in samples interrupted to nominally the same level of engineering strain at different strain rates ($\dot{\varepsilon} = 2\text{x}10^{-4}$ /s and $\dot{\varepsilon} = 2\text{x}10^{0}$ /s). Both tensile specimens were machined from the same 1.15 mm thick sheet. *some grains contained both twins and hexagonal ε-martensite platelets.

	Characterization techniques to measure # of grains with planar defects	
Engineering strain and strain rate (/s)	Bulk samples: EBSD + ECCI	Thin foil samples: DF-TEM
$\varepsilon_{eng.} = 0.18$ at $\dot{\varepsilon} = 2 \text{ x } 10^{0}$ /s	51 % of 37 surveyed grains (with <110> orientation and optimal channeling conditions) contained planar defects	52 % of 23 surveyed grains contained planer defects*
		52 % of 23 surveyed grains contained twinning
		17 % of 23 surveyed grains contained epsilon martensite
$\varepsilon_{eng.} = 0.17$ at $\dot{\varepsilon} = 2 \text{ x } 10^{-4}$ /s	47 % of 34 surveyed grains (with <110> orientation and optimal channeling conditions) contained planar defects	42 % of 24 surveyed grains contained planar defects*
		38 % of 24 surveyed grains contained twinning
		33 % of 24 surveyed grains contained epsilon martensite

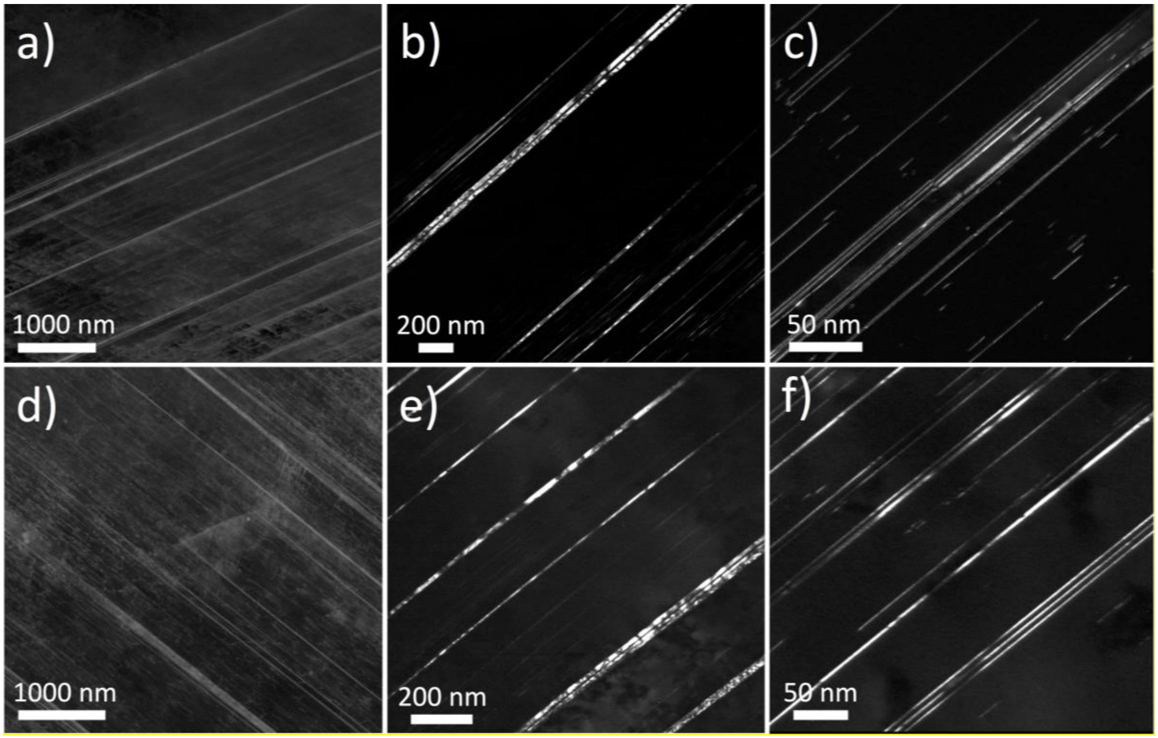

Figure 4-17: Representative images of planar defects characterized in specimens of the same sheet thickness (1.15 mm) tested at (a-c) $\dot{\varepsilon} = 2\text{x}10^{0}$ /s and interrupted at $\varepsilon_{eng.} = 0.18$ and (d-f) tested at $\dot{\varepsilon} = 2\text{x}10^{-4}$ /s and interrupted at $\varepsilon_{eng.} = 0.17$. Characterization techniques shown are (a,d) ECCI, (b,e) twin reflections selected to form a DF-TEM image and (c,f) ε-martensite reflections selected to form a DF-TEM image. Twin and martensite reflections were selected from the same SAED pattern and thus the same grain of interest. The differentiation of twinning from ε-martensite by DF-TEM is also described in detail in the caption of Figure 4-16.

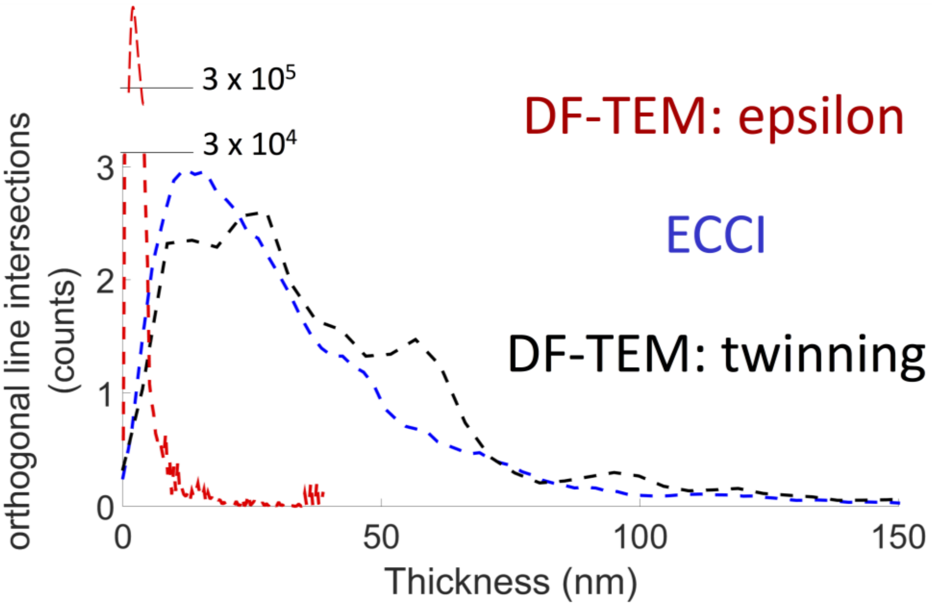

Figure 4-18: Kernel fitting of separate thickness distributions were used to illustrate the difference in deviation of a given distribution acquired by multiple imaging techniques for a sample interrupted at $\varepsilon_{eng.} = 0.17$ during a $\dot{\varepsilon} = 2\text{x}10^{-4}$ /s test (1.15 mm thick sheet).

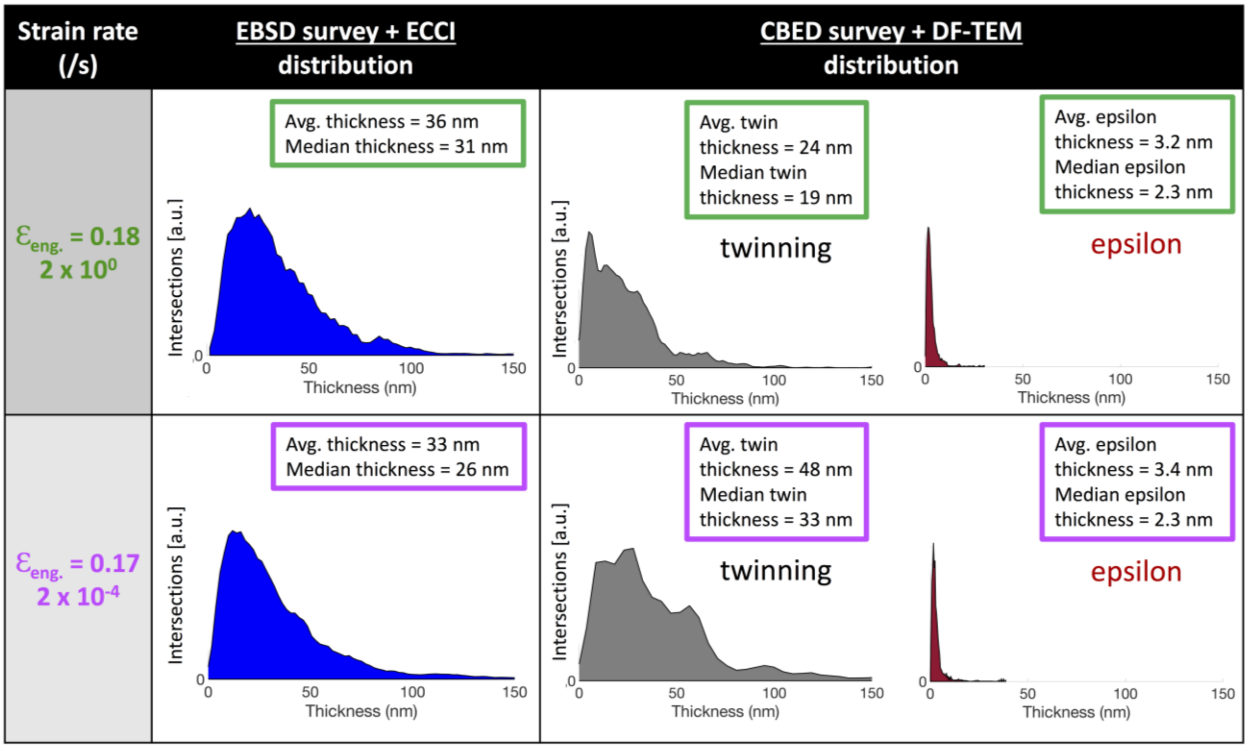

Figure 4-19: Quantitative thickness measurements from SEM & TEM techniques based on tensile specimens from the same sheet thickness (1.15 mm) interrupted at $\varepsilon_{eng.} = 0.18$ tested at $\dot{\varepsilon} = 2\text{x}10^{0}$ /s and $\varepsilon_{eng.} = 0.17$ tested at $\dot{\varepsilon} = 2\text{x}10^{-4}$ /s.

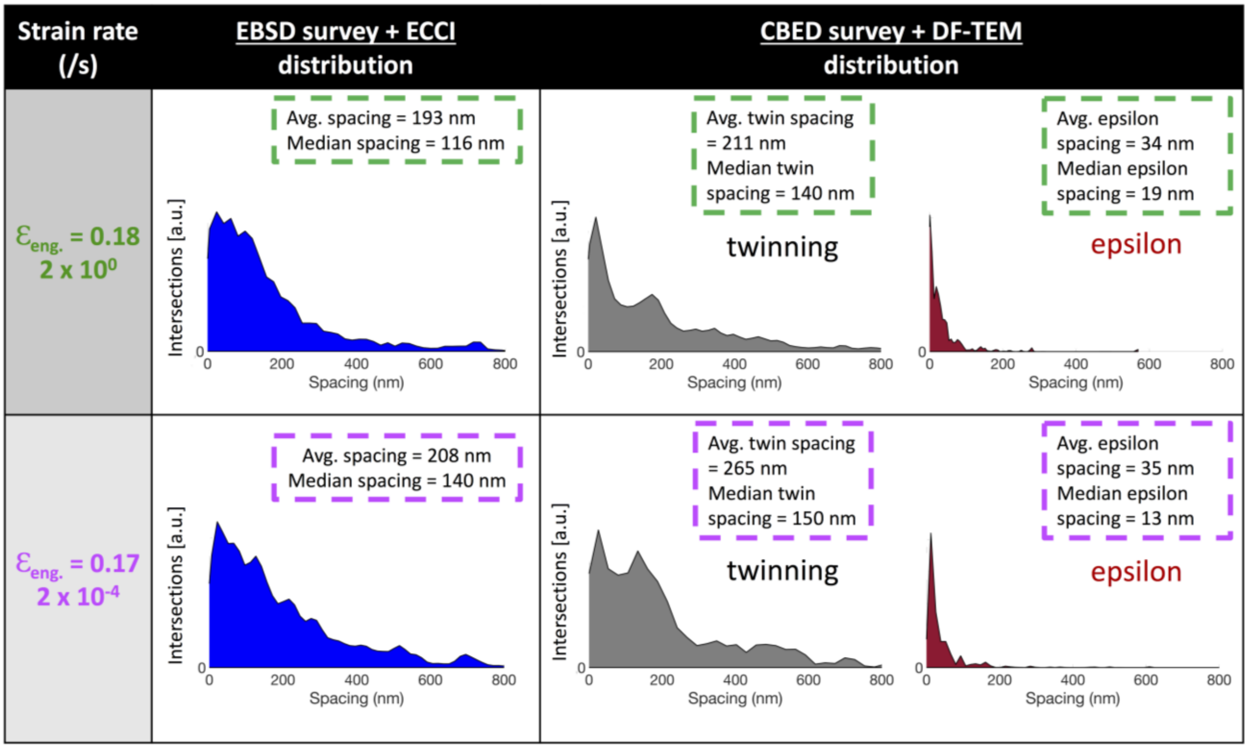

Figure 4-20: Quantitative spacing measurements from SEM & TEM techniques based on tensile specimens from the same sheet thickness (1.15 mm), interrupted at $\varepsilon_{eng.}$ = 0.18 tested at $\dot{\varepsilon}$ = 2x10^0 /s and $\varepsilon_{eng.}$ = 0.17 tested at $\dot{\varepsilon}$ = 2x10^{-4} /s.

4.2.8 Techniques for Measuring High Strain-Rate Servo-Hydraulic Tensile Properties

As strain rate is increased from quasi-static and low strain rates ($\dot{\varepsilon} = 10^{-5}$ /s to $\dot{\varepsilon} = 10^{0}$ /s) to dynamic-low strain rates ($\dot{\varepsilon} = 10^{0}$ /s to $\dot{\varepsilon} = 10^{3}$ /s), dynamic considerations of the mechanical resonance in the test specimen and tensile-testing machine become more important [150]. Consistent with Meyers' [150] recommendations on common testing methods, the International Iron and Steel Institute [184] also recommends the use of servo-hydraulics to evaluate mechanical properties of sheet steels within the strain rate range of $\dot{\varepsilon} = 10^{-1}$ /s to $\dot{\varepsilon} = 10^{2}$ /s. Between $\dot{\varepsilon} = 10^{1}$ /s and $\dot{\varepsilon} = 10^{3}$ /s, oscillations in the load data are purely due to mechanical resonance in the testing setup, for materials which do not exhibit dynamic strain-aging effects.

Inertial effects of plastic-wave, shear-wave and shock-wave propagation are only considered at strain rates of $\dot{\varepsilon} = 10^3$ /s and greater [150].

As detailed in section 2.4, the load-ringing amplitude can be minimized by reducing the mass between the gauge section and the load measuring device [150][153] or using two elastic strain gauges on each side of the grip section [170]. Avoiding the use of extensometers for strain measurement and implementing load oscillation reduction procedures are necessary steps to evaluate the dynamic tensile properties of next generation AHSS [184]. The present work uses titanium grips to reduce mass (between the tensile specimen and load washer) and strain gauges to minimize non-linearity in strain measurement, the limitations of which are outlined in chapter 3.4. Figure A-4 compares the use of two different methods to minimize ringing in stress-strain measurements, but the techniques are not foolproof. Rather, the software-based method implemented in this work likely underestimates the yield strength and initial strain-hardening rates during tests at $\dot{\varepsilon} = 2x10^2$ /s. Large amplitudes of load ringing during tests at $\dot{\varepsilon} = 2x10^2$ /s and the maximum frame rate of the thermal camera (5 ms per frame) significantly reduces the ability to accurately measure stress, strain and adiabatic heating. Simply put, mechanical resonance at high strain rates inherently affects data quality, specifically in the initial values of strain when the oscillation amplitude from the actuator's engagement with the test specimen is greatest [184]. Therefore, interpretation of any changes in tensile behavior or strain-hardening rate during low values of strain should be carefully considered during high strain-rate tests.

4.2.9 Influence of Strain Rate and Adiabatic Heating on Deformation Mechanisms

High strain-rate testing does not allow sufficient time for heat to diffuse from the interior of a tensile specimen to the free surfaces and subsequently be lost to the environment, which leads to adiabatic heating [150]. As specimen thickness increases, adiabatic heating may also occur at even lower strain rates [150][185]. The evolution of the temperature increase during deformation is important since different temperature-dependent deformation modes may be activated during a single test. Furthermore, the significant adiabatic heating that may occur at high strain rates, along with the effect of strain rate on the thermal component of flow stress, can lead to complicated mechanical behavior of TWIP steels.

In the current work, a high-speed thermal camera was used to measure the increase in specimen temperature as a function of time and thus strain for these tests. The rise in specimen temperature from room temperature (23 °C) to 83 °C (average temperature at maximum uniform elongation for all tests at $\dot{\varepsilon} = 2\text{x}10^1$) was input into a thermodynamic model which predicted a rise in SFE from 21 to 35 mJ/m^2 for the Fe-25Mn-3Al-3Si (wt%) alloy. In previous work, the influence of SFE on the microstructural evolution and mechanical properties of a Fe-25Mn-3Al-3Si and a Fe-28Mn-3Al-3Si alloy were evaluated during RT tensile deformation at quasi-static strain rates (where adiabatic heating was insignificant) [12]. The measured RT SFE of the Fe-25Mn-3Al-3Si and Fe-28Mn-3Al-3Si alloys are 21 and 39 mJ/m^2, respectively [23]. The Fe-25Mn-3Al-3Si alloy exhibited both planar and wavy deformation characteristics along with the formation of both mechanical twins and ε-martensite. In contrast, the Fe-28Mn-3Al-3Si alloy exhibited a greater propensity for cross slip, a more wavy dislocation structure, and mechanical twinning was the dominant secondary deformation mechanism with no significant observations of ε-martensite formation. It is also notable that in that work, increasing the SFE from 21 to 39

mJ/m^2 by increasing Mn content reduced strength and ductility only slightly during RT deformation [12]. In summary, the largest predicted rise in SFE from adiabatic heating is at high strain rates and in the present work is expected to have only a small effect on UTS and UE, based on studies of similar Fe-Mn-Al-Si steels with different SFE values.

The combined effects of strain rate on dislocation slip and continued refinement of the dislocation substructure by planar defects, referred to as the dynamic Hall-Petch effect, are important considerations in this work when discerning differences in substructure spacing and dislocation mean free paths [78][135]. Micro-hardness measurements were completed on samples interrupted and pulled to failure at all strain rates in the present work, but did not show any statistically significant difference in micro-hardness at any given strain rate for the same nominal strain. Rather, the micro-hardness measurements showed only a statistically significant increase in hardness with increasing engineering strain. These results may indicate that the microstructure evolution at different strain rates is similar or that any microstructural differences that exist do not significantly influence the hardness.

Although deformation twinning has been previously confirmed with DF-TEM, formation of ε-martensite was not observed as a deformation mechanism in the Fe-25Mn-3Al-3Si alloy (using XRD and DF-TEM) by Grässel *et al.,* regardless of strain rate. However, recent work by Pierce *et al.* [23], which was conducted at quasi-static strain rates, identified ε-martensite with DF-TEM. The present work reports the first observation of both deformation twinning and ε-martensite in the same grain taken from samples of the Fe-25Mn-3Al-3Si alloy deformed at high strain rates. These results are a strong indicator that the microstructure is similar at quasi-static and high strain rates. As has been reported previously, the critical resolved shear stress required for a leading partial dislocation to break away from the trailing dislocation is more sensitive to temperature and SFE than strain rate in the context of producing a large effect on the twin volume fraction [15][19]. More importantly, the sensitivity of the flow stress to thermally-activated short-range barriers indicates that any change in the volume fraction or onset of mechanical twinning caused by high strain rates may not be the main contributor to observable changes in work-hardening. The sensitivity of the strain-hardening behavior may suggest the main contributing factor to the increased flow stress in the current work at high strain rates is related to the dislocation mean free path [19][34] and an increase in flow stress for dislocation glide to overcome short-range barriers with increasing strain rate. This explanation is more likely than a significant change in the dynamics of mechanical twinning or ε-martensite formation, as both planar defects are still observed at low and high strain rates for this alloy. The strain-hardening rate for the tests at $\dot{\varepsilon} = 2 \times 10^{-2}$ /s possess the lowest value at initial stages of accumulated strain as compared to all other strain rates, which is consistent with observations by Grässel et al. [30]. Lee et al. reported a minimum strain-hardening rate for a strain rate of $\dot{\varepsilon} = 10^{-3}$ /s at which the critical resolved shear stress (CRSS) of the strain-induced martensite and dislocation slip was lower [and favored] as compared to twinning [20]. In the present study, the real reason for the low values of strain-hardening rate of the $\dot{\varepsilon} = 2 \times 10^{-2}$ /s as compared to those at higher strain rates is likely quite complex and most likely dependent on multiple mechanisms related to dislocation mobility and planar defect generation.

Christian and Mahajan have stated that an increase in strain-rate generally leads to an increase in twinning activity [186]. Other researchers have observed twinning after shock loading in FCC materials that do not twin under quasi-static deformation conditions, such as aluminum alloys [186]. In another study, microstructural evaluation of an Fe-18Mn-1.22Al-0.56C alloy showed adiabatic shear banding and twinning after ballistic testing at $\dot{\varepsilon} = 10^{5}$ /s

[187]. As Steinmetz et al. [77] pointed out, quantifying twin volume fractions is difficult due to the heterogeneous nature of grains and the observation that twins may not completely cross the full diameter in each grain. Therefore, in the present work careful image processing techniques were utilized to quantify all observable features in a given field of view for each imaging technique. The drawbacks of comparing ECCI and DF-TEM techniques are evident due to the point-to-point resolution limit of ECCI techniques (~8-10 nm) [176], the characterization of only one variant of planar defects in the SAED pattern for a given grain and the limited number of observable grains in electro-polished TEM samples. Further, the slight decrease in frequency of observed martensite reflections in SAED patterns at higher strain rates (see Table 4-4) could be due to either the rise in SFE [23][188][80], (in this case from adiabatic heating) or simply because the ε-martensite platelets are too thin to contribute clearly to the SAED pattern [99]. A slight decrease in twin spacing with increased strain rate is observed and is consistent with observations of an increase in twin volume fraction by others [30][11][54]. In contrast, Steinmetz et al. also pointed out that an increase in twinning volume fraction at higher strain rates was observed in simulation and experiment, but the contribution to strain-hardening was not significant [77]. An important observation in the current work is that TWIP and TRIP effects are observed by DF-TEM at all strain rates for the Fe-25Mn-3Al-3Si alloy, which has a room temperature SFE of 21 mJ/m^2. Thus, there is most likely not a significant change in the dominant mechanism within the range of strain rates investigated (from $\dot{\varepsilon} = 10^{-4}$ /s to $\dot{\varepsilon} = 10^{2}$ /s).

4.2.10 Effects of Strain Rate and Specimen Thickness on Tensile Properties

High strain-rate deformation reduces the time for dislocations to overcome short-range dislocation barriers, which causes an increase in flow stress [68]. Allain et al. reported that the short-range barriers in austenitic steels responsible for the thermal- and strain-rate dependence of the yield strength are the sum of contributions from solid-solution and thermally-activated contributions from a viscoplastic potential [65][190]. As in the present work on Fe-25Mn-3Al-3Si (wt%), there is a notable strain rate sensitivity of the yield strength. Surprisingly, Allain et al. reported that large amounts of Mn [20-30 wt %] and Al [0-3 wt%] contents do not play significant roles on the activation volume of thermally dependent barriers to dislocation mobility. However, Allain et al. specifically noted that approximately 3 wt % Si has a remarkable effect on dislocation mobility by significantly reducing the apparent activation volume and mean free path. The activation volume of thermally dependent short-range barriers and dislocation mean free path respectively influence the yield strength and work-hardening. Previous research on Si-containing TWIP steels revealed a distinct sensitivity in yield strength and work hardening at strain rates lower than predicted from work on Fe-Mn-C alloys (steel systems not containing silicon) [65][30]. In summary, the increase in flow stress necessary for partial dislocations to overcome thermally dependent short-range barriers during dislocation glide with increasing strain rate explains the positive strain-rate sensitivity of the yield strength in the present work on the Fe-25Mn-3Al-3Si (wt%) steel and is consistent with previous work [29][148][65].

A previous study on a Fe-25Mn-3Al-3Si (wt%) steel by Grässel et al. [30] shows similar trends in mechanical properties as a function of strain rate, as compared to the present study on a steel alloy with the same nominal composition. Specifically, the trends show that with increasing strain rate, YS increases significantly, UTS increases modestly and UE decreases modestly, as seen in Figure 4-11. Curtze and Kuokkala's work [68] on a high-Mn TWIP steel also showed a positive strain-rate sensitivity for YS and UTS within the same range of strain rates. Lichtenfeld et al. [16] also found increases in YS and UTS and a decrease in UE with increasing strain rate for type 309 stainless steel consisting of stable austenite. In the present work, an increase in strain rate also increased the PSE, which is consistent with other TWIP steel research [30][148][191][145][20][189][21]. Furthermore, PSE values at strain rates of $\dot{\varepsilon} = 2x10^{-2}$ and $\dot{\varepsilon} = 2x10^{2}$ /s are greater for the 1.15 mm sheet thickness than for the 0.95 mm sheet thickness in the present work. Previous research corroborates the present work in that the yield strength and uniform elongation are independent of sheet thickness [158][156][155][192][193][159]. However, post-uniform elongation depends on the stress distribution of the necked region, which itself is dependent on specimen thickness for specimens with rectangular cross sections [158]. More specifically, Yuan et al. reported that increasing the thickness of specimens with rectangular cross sections resulted in longer regions of the neck being exposed to stress levels greater than the yield point of the material (X80 steel), ultimately resulting in more diffuse necking and greater post uniform elongation [158]. These observations are consistent with current work as post-uniform elongation is greater for the 1.15 mm thick sheet as compared to the 0.95 mm sheet for samples deformed at the same strain rates ($\dot{\varepsilon} = 2x10^{-2}$ and $\dot{\varepsilon} = 2x10^{2}$ /s). However, observations of all fracture surfaces for both sheet thickness reveal that the fracture mechanism is micro-void coalescence (see Figure C-2 and Figure C-3), which indicates ductile failure [194].

As seen in Figure 4-11, the YS and UTS strain-rate sensitivities are very similar between $\dot{\varepsilon} = 2x10^{-2}$ and $\dot{\varepsilon} = 2x10^{2}$ /s, whereas the UTS strain-rate sensitivity is lower than the YS strain rate sensitivity from $\dot{\varepsilon} = 2x10^{-4}$ to $\dot{\varepsilon} = 2x10^{-2}$ /s. Mechanical twins and ε-martensite laths develop before $\varepsilon_{eng.} = 0.1$. The planar defects act as obstacles to partial dislocation motion during slip on other glide planes, which increases the work-hardening capacity by reducing the mean free path of dislocations and leads to a higher UTS [12]. As strain increases, the dislocation density increases and eventually planar defects develop, which are barriers to dislocation motion on non-coplanar slip systems [21][32][80]. As no significant differences in micro-hardness were measured with an increase in strain rate for the same nominal strain and both twins and ε-martensite are observed at the lowest and highest strain rates, the cause of the increase in UTS with increasing strain rate is most likely due to a modest decrease of spacing between twins or simply because the reduced time for dislocations to overcome short-range dislocation barriers causes an increase in flow stress [68].

However, as strain rate increases, UE decreases and TE increases, indicating an increased likelihood of strain localizations at lower strains at higher strain rates [196]. Early work on the Fe-25Mn-3Al-3Si alloy by Frommeyer [30][62] also measured a decrease in UE with an increase in strain rate, which was attributed to specimen softening from adiabatic heating, but the heating was not experimentally measured. Further, a significant decrease in YS, UTS, UE and TE with increasing environment testing temperature has been observed in work on alloys of nominally the same composition [30][22]. With increasing strain rate from $\dot{\varepsilon} = 2x10^{-2}$ /s to $\dot{\varepsilon} = 2x10^{2}$ /s, reduction in area remains approximately constant but post-uniform elongation increases. In the present work, the mechanical test results, in combination with thermal imaging that revealed multiple localized regions of greater temperature at strain rates of $\dot{\varepsilon} = 2x10^{1}$ /s and $\dot{\varepsilon} = 2x10^{2}$ /s (see Figure 5 and S 8), suggest that multiple areas of strain localization are occurring at the higher strain rates and are contributing to the post uniform elongation. The wider difference in temperature for tests at the same strain rate as well as the observation of localized heating, which corresponds to strain localizations [77], is consistent with observations by other researchers [197][196]. Grässel *et al.* also observed a large difference in TE and UE (increased post-uniform elongation) at strain rates above $\dot{\varepsilon} = 10^{-1}$ /s for the Fe-25Mn-3Al-3Si alloy [30]. Moreover, multiple strain localizations at larger levels of strain and increased adiabatic heating are likely the cause of a decrease in uniform elongation with respect to an increase in strain rate.

4.2.11 Conclusions

- The 0.2 % offset yield strength of the Fe-25Mn-3Al-3Si (wt%) alloy increased by approximately 64% in the strain-rate range of $\dot{\varepsilon} = 2x10^{-4}$ to $\dot{\varepsilon} = 2x10^{2}$ /s. The positive yield-strength strain-rate sensitivity is likely due to an increase in flow stress necessary for partial dislocations to overcome thermally dependent short-range barriers during dislocation glide with increasing strain rate.
- The product of [ultimate tensile] strength and [total] elongation (PSE) increases with increasing strain rate and sheet thickness. Sheet thickness did not affect the magnitude of the yield strength, yield-strength strain-rate sensitivity, or uniform elongation.
- Increasing strain rate from $\dot{\varepsilon} = 2x10^{-2}$ /s to $\dot{\varepsilon} = 2x10^{2}$ /s increased the amount of post-uniform elongation. As reduction-in-area measurements on the necked regions did not change significantly for this range of strain rates, multi-site strain localization is the likely mechanism, a conjecture which is supported by localized regions of higher temperatures observed by thermal imaging during tests at $\dot{\varepsilon} = 2x10^{1}$ and $\dot{\varepsilon} = 2x10^{2}$ /s. An increase in sheet thickness also increased the post-uniform elongation.
- The average tensile specimen temperature increased with increasing strain and strain rate at rates from $\dot{\varepsilon} = 10^{-2}$ /s to $\dot{\varepsilon} = 10^{2}$ /s. The thermodynamic model used to correlate specimen temperature with SFE predicts an increase from 21 mJ/m^2 at room temperature

(23 °C) to ~34 mJ/m^2 at 83 °C. An increase in SFE of this magnitude is expected to have only a small effect on tensile properties.

- Deformation twinning and ε-martensite are observed in tensile specimens interrupted from quasi-static ($\dot{\varepsilon}$ = 2x10^{-4} /s) through low-dynamic ($\dot{\varepsilon}$ = 2x10^2 /s) strain rates. ECCI and DF-TEM measurements do not reveal a statistically significant effect of strain rate on the thickness and spacing of mechanical twins or ε-martensite laths in the Fe-25Mn-3Al-3Si (wt%) steel.

4.3 Characterization of Microstructure Evolution in a Multi-Phase Medium-Mn Steel

A major aspect of this dissertation focuses on designing an industrially relevant multi-phase medium-Mn (Fe-12Mn-3Al-0.05C wt%) steel alloy, based on a prior understanding of deformation mechanisms in single-phase high-Mn steels and resulting high strain-rate behavior. The single-phase high-Mn steel has an austenitic stacking fault energy (SFE) of 21±3 mJ/m^2, which promotes a combination of deformation mechanisms at quasi-static strain rates. The primary mechanism is dislocation glide, but secondary mechanisms such as twinning-induced plasticity (TWIP) and transformation-induced plasticity (TRIP), in the form of ε-martensite formation, contribute to strength by impeding dislocation motion. A medium-Mn steel was designed such that the austenite phase, now a minor microstructural constituent, possessed a SFE similar to that of the single-phase high-Mn austenitic steel (~ 21 mJ/m^2). Alloy design inherently focused on reducing alloying content to decrease cost and increase weldability, but still maintain an appropriate combination of strength and ductility, useful for forming complex automotive parts. As intercritical annealing is one of the most important steps in the medium-Mn alloy design process, the effect of annealing time (at the same annealing temperature) on microstructure, mechanical properties and deformation mechanisms was investigated. The characterization of a multi-phase medium-Mn steel is particularly challenging as the austenite is ultrafine in size (<500 nm) and the majority of the microstructure is martensite and ferrite, which is ferromagnetic and thus increases the difficulty of TEM analysis. As the room-temperature SFE of the austenite depends on its local phase composition, energy dispersive spectroscopy (STEM-EDS) and atom probe tomography (APT) were used to quantify the compositions of the ultrafine-grained (UFG) austenite after intercritical annealing.

4.3.1 Considerations in Alloy Design

As detailed in section 2.3, the types of third generation AHSS capable of achieving desired mechanical properties with significantly less alloy content than second generation AHSS include medium-Mn steels, lightweight steels and quenched & partitioned TRIP steels [1][2]. A steel with a multi-phase microstructure produced with Mn contents between 3 and 15% can balance both cost and desired mechanical properties. Medium-Mn steels generally exhibit a martensitic microstructure after hot and cold rolling, but intercritical annealing in the $\alpha+\gamma$ phase field produces ultrafine-grained (UFG) reverted austenite and ferrite, with an equilibrium volume fraction of reverted austenite that ranges between 20 and 50% [39]. Multiple annealing times were used to investigate the microstructural evolution in the context of phase fraction and equilibrium phase composition.

The medium-Mn steel was cold-rolled to produce a fully deformed martensitic microstructure (see Figure D-1) and the average Vickers micro-hardness value was 390 HV, (average of 7 indents measured with a load of 2 kg). By means of dilatometry (10 °C/s heating rate and sample dimensions of 9 x 4 x 1.7 mm3) the Ac1 and Ac3 temperatures (lower and upper temperature bounds of the austenite+ferrite phase field) were determined to be 512 °C and 792 °C, respectively. Following intercritical annealing of the fully deformed martensitic microstructure at 585 °C, Thermo-Calc® software predicts an equilibrium austenite volume fraction of 0.44 and an austenitic SFE of 21 mJ/m^2 at room temperature (see Figure 4-21) with an equilibrium austenite composition of Fe-20.8Mn-2.1Al-0.11C (wt%) (see Figure D-2) and an equilibrium ferrite composition of Fe-4.9Mn-3.7Al-0.001C (wt%).

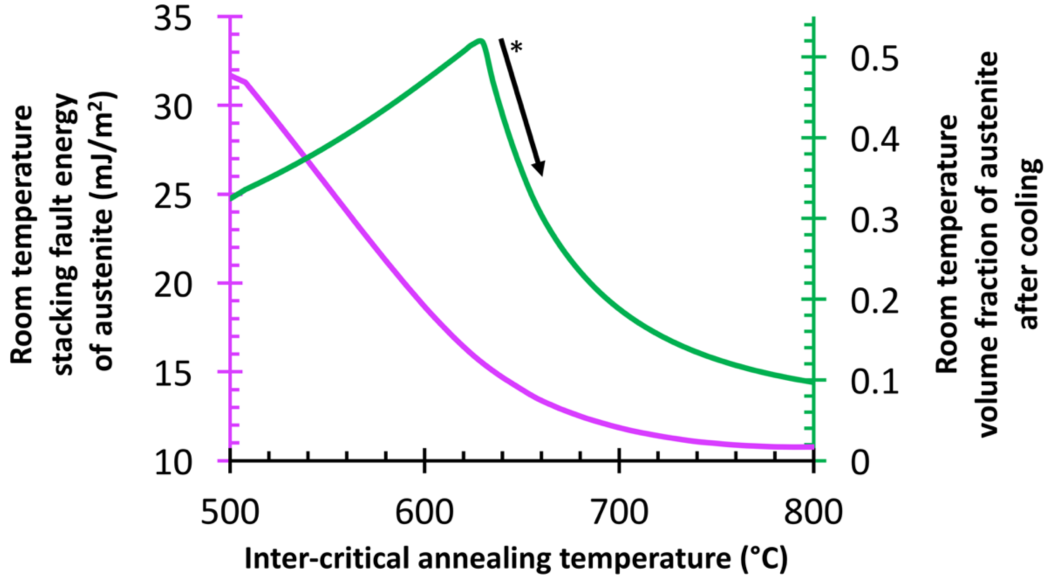

Figure 4-21: Thermo-Calc® predictions of austenitic SFE and volume fraction of austenite at room temperature plotted as a function of intercritical annealing temperature for a Fe-12Mn-3Al-0.05C (wt%) alloy. * Corrections to Thermo-Calc® predictions were introduced to compensate for the formation of fresh athermal martensite during cooling as described in [39], i.e. the inflection point in austenite volume fraction occurs when the M_s temperature becomes greater than room temperature.

4.3.2 Effects of Intercritical Annealing Time on Phase Fractions and Grain-Size Areas

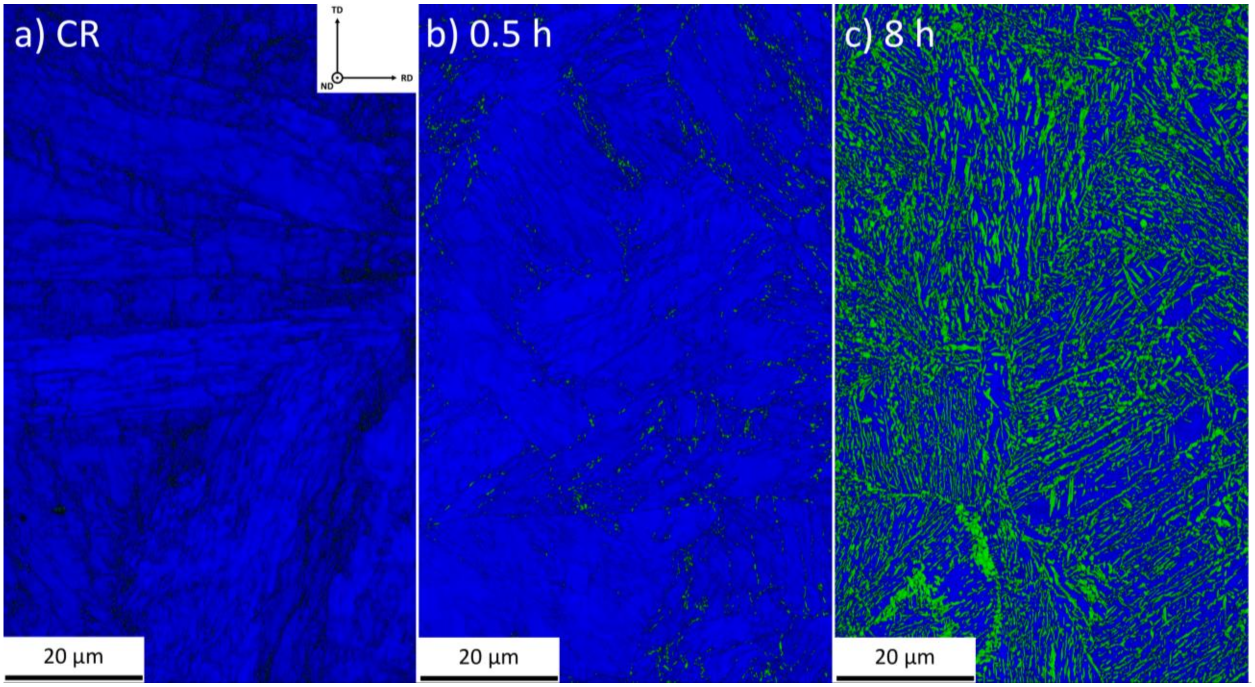

Figure 4-22: EBSD maps of image quality and phase, (blue is α-Fe and green is γ-Fe), of the Fe-12Mn-3Al-0.05C (wt%) alloy presented in the following conditions: a) cold-rolled, b) annealed for 0.5 h at 585 °C and c) annealed for 8 h at 585 °C.

In Figure 4-22a, a fully deformed martensitic microstructure is observed after cold-rolling as indicated by the lath-shaped grains (elongated in the rolling direction) and dark image quality (high dislocation density). After intercritical annealing the cold-rolled material for 0.5 h at 585 °C, a small decoration of austenite [γ-Fe] is observed (as seen in Figure 4-22b) which provides insight into initial stages of the austenite reversion process. After increasing annealing time to 8 h, a significant amount of γ-Fe is present throughout the microstructure, seen in Figure 4-22c, and is ultrafine in grain size. Figure D-3 provides another comparison of the microstructures produced with 0.5 h and 8 h of annealing time. Based on variations in the location of austenite observed in Figure 4-22b, not all nucleation sites have completely developed after 0.5 h of annealing time at 585 °C.

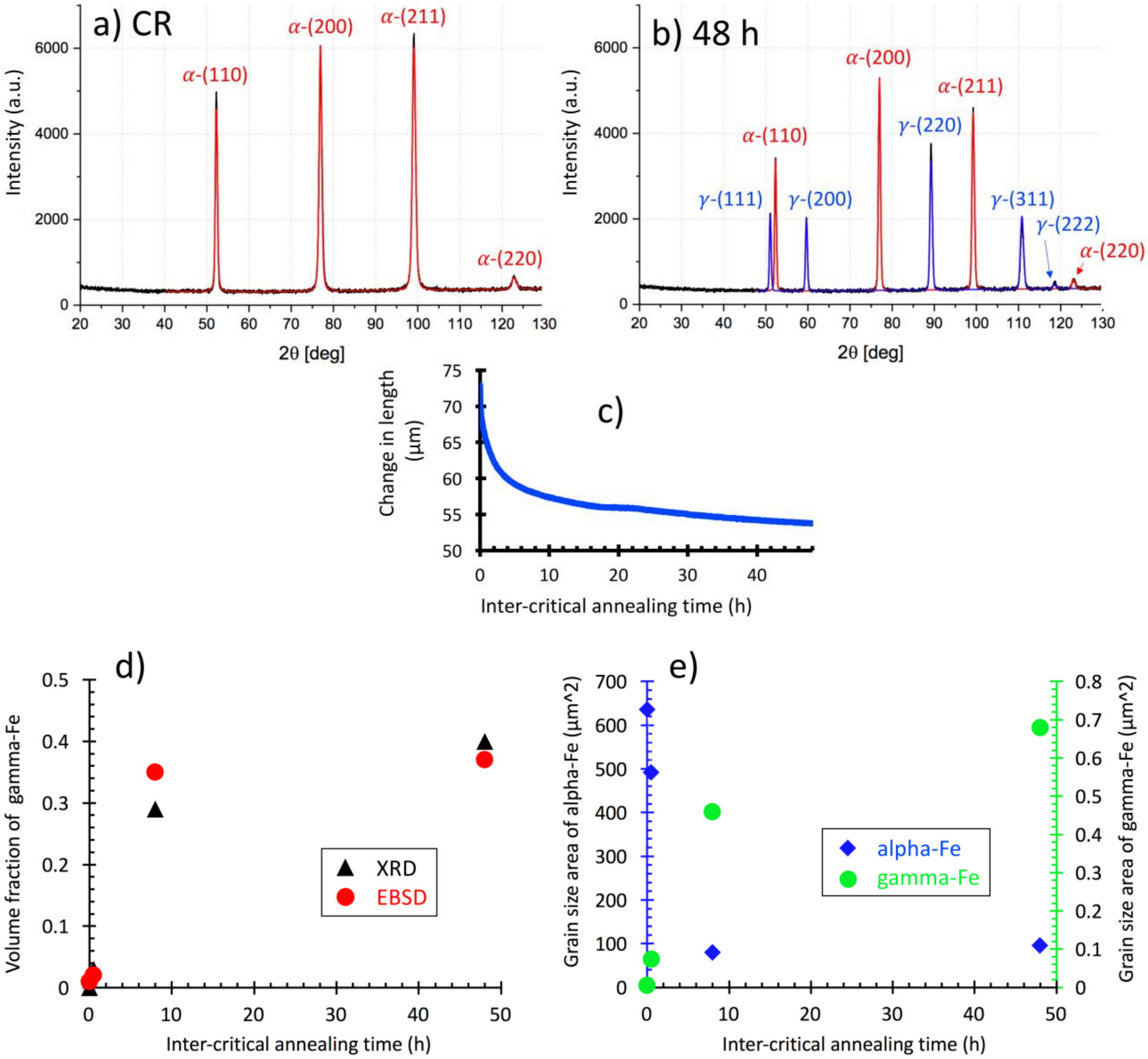

Figure 4-23: XRD measurements [with a Cobalt x-ray source] of the a) cold-rolled condition and b) after intercritical annealing for 48 h at 585 °C. c) Dilatometer measurements of the Fe-12Mn-3Al-0.05C (wt%) alloy intercritically annealed at 585°C for 48 h. d) γ volume fraction measured with XRD and EBSD and e) α and γ average grain-size areas, measured with EBSD, are plotted as functions of intercritical annealing time at the intercritical annealing temperature (585 °C).

As seen in Figure 4-23a, the XRD profile of the cold-rolled material indicates a strongly textured martensitic microstructure, which is expected for a fully deformed material prior to annealing steps. Typically, alpha-Fe powder-XRD samples show the highest intensity in the peaks corresponding to (110) planes. The multiplicity of (110) planes is twelve, while the multiplicity of (200) planes is six. Besides multiplicity, structure factor contributes to differences in peak intensity ratios for powder-XRD samples and depends on atomic scattering factor for allowable diffraction peaks. The scattering amplitude from a neutral atom also depends on the Bragg angle (assuming the same atomic number). In powder-XRD measurements, the (200) planes have a peak intensity of 11% (compared to (110) planes deemed as 100%) when measured for pure alpha-Fe [198]. However, in the fully deformed martensitic microstructure, the (211) and (200) peak intensities were approximately 15% greater than the (110) peak intensities, therefore confirming a strong texture in the microstructure. After intercritical annealing for 48 h at 585 °C, austenite peaks appear with strong intensity (see Figure 4-23b) but ferrite/martensite peaks still possess the higher intensities. Also after annealing for 48 h at 585 °C, a decrease in sample length as measured via dilatometry (see Figure 4-23c) is observed and is attributed to the denser packing fraction of austenite as compared to that of ferrite/martensite. As the (211) and (200) peak intensities of the alpha phase are still greater than the (110) ferrite/martensite peak intensities after annealing for 48 h at 585 °C (Figure 4-23b) it can be inferred that most of the alpha microstructure that remains is still relatively textured. XRD measurements of all annealing times (0.5 h, 8 h and 48 h) show the presence of ferrite/martensite and austenite peaks, but no evidence of hexagonal ε-martensite peaks. An increase in annealing time from 0.5 h to 48 h increases the austenite volume fraction from 3 to 40 % and average grain-size area of reverted austenite from 0.06 μm^2 to 0.68 μm^2, as shown in Figure 4-23d-e. Grain-size area rather than grain size diameter, measured with EBSD using a 30 nm step size, is used in this case because diameter is a better choice for equiaxed grains, but not for elongated or plate-like grains. The grain size area of alpha-Fe decreases with increasing annealing time from 0.5 h to 8 h, indicating some of the parent martensite has not only reverted to austenite, but has partially recrystallized to create UFG ferrite. However, the average grain-size area of alpha-Fe increases slightly from 79 to 95 μm^2 when increasing annealing time from 8 to 48 h. This is a likely indication that after 8 h of annealing time, nucleation processes of UFG ferrite and UFG austenite are near completion and growth processes dominate. However, average grain-size area does not tell the full story. The distributions of each grain-size area for each phase at a given annealing time give more insight into the reversion process.

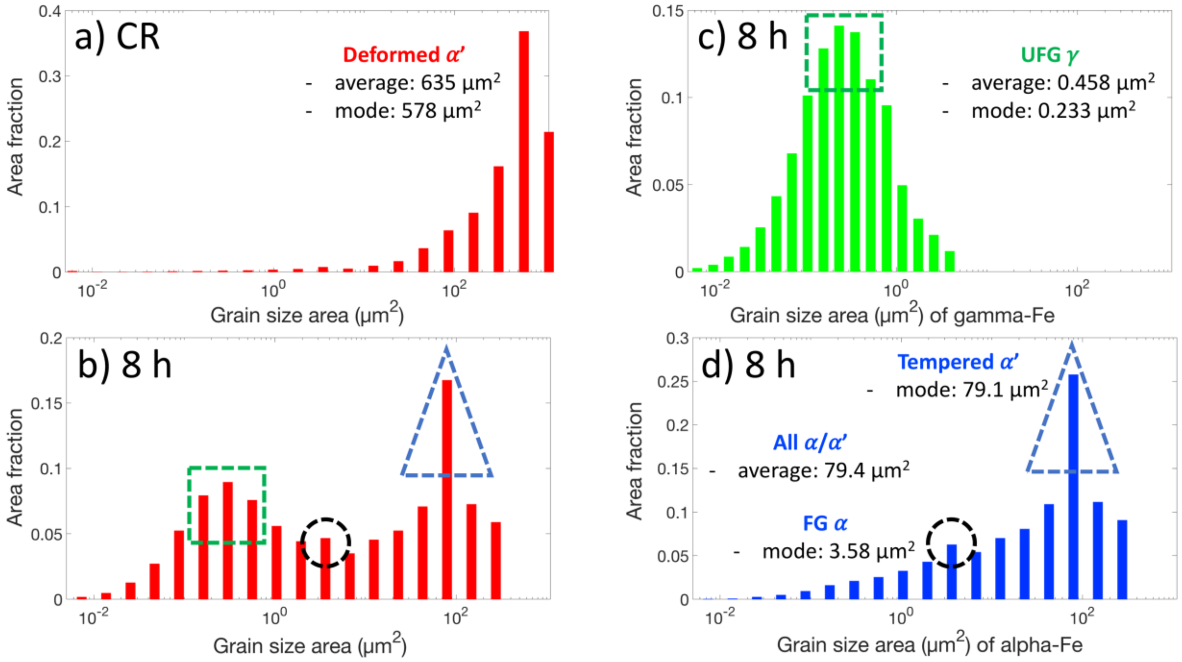

Figure 4-24: Corresponding grain-size area distributions, (x-axis plotted in log scale), of a) the fully deformed martensitic microstructure produced by cold-rolling, b) all phases present after intercritical annealing for 8 h at 585 °C and the differentiated grain size areas for given phase fractions of c) γ-Fe and d) α-Fe.

The cold-rolled material (composed of deformed martensite) exhibits a singular distribution in grain size area (see Figure 4-24a) with a sharp peak at 577 μm^2 and an average of 635 μm^2. After intercritical annealing for 8 h at 585 °C, the same sharp peak in grain size area shifts from 577 to 79 μm^2 (see Figure 4-24b of grain size area for all phases) but other grain size area peaks also appear. Specifically, for the distribution of only ferrite/martensite (see Figure 4-24d) a smaller peak at 3.6 μm^2 indicates the nucleation and growth of UFG ferrite. Also, the austenite distribution after 8 h of annealing time has an average grain-size area of 0.46 μm^2, with the mode of that distribution/peak being 0.3 μm^2, as seen in Figure 4-24c.

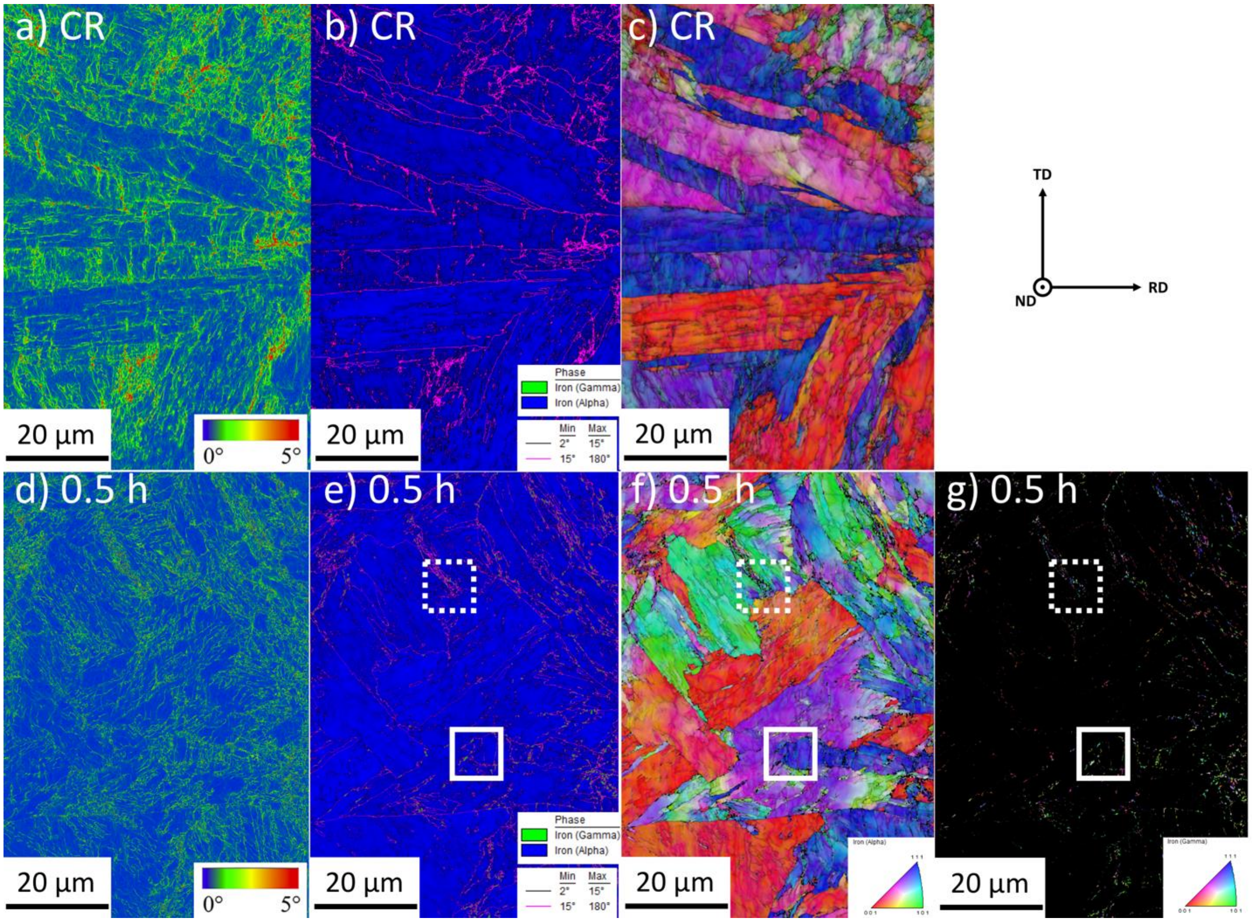

Figure 4-25: EBSD maps are provided for the a/b/c) cold-rolled condition and d/e/f/g) after annealing for 0.5 h at 585 °C. Separate maps are shown for a/d) kernel average misorientation, b/e) image quality, phase and grain boundaries, c/f) image quality and ferrite/martensite IPF and g) image quality and austenite IPF.

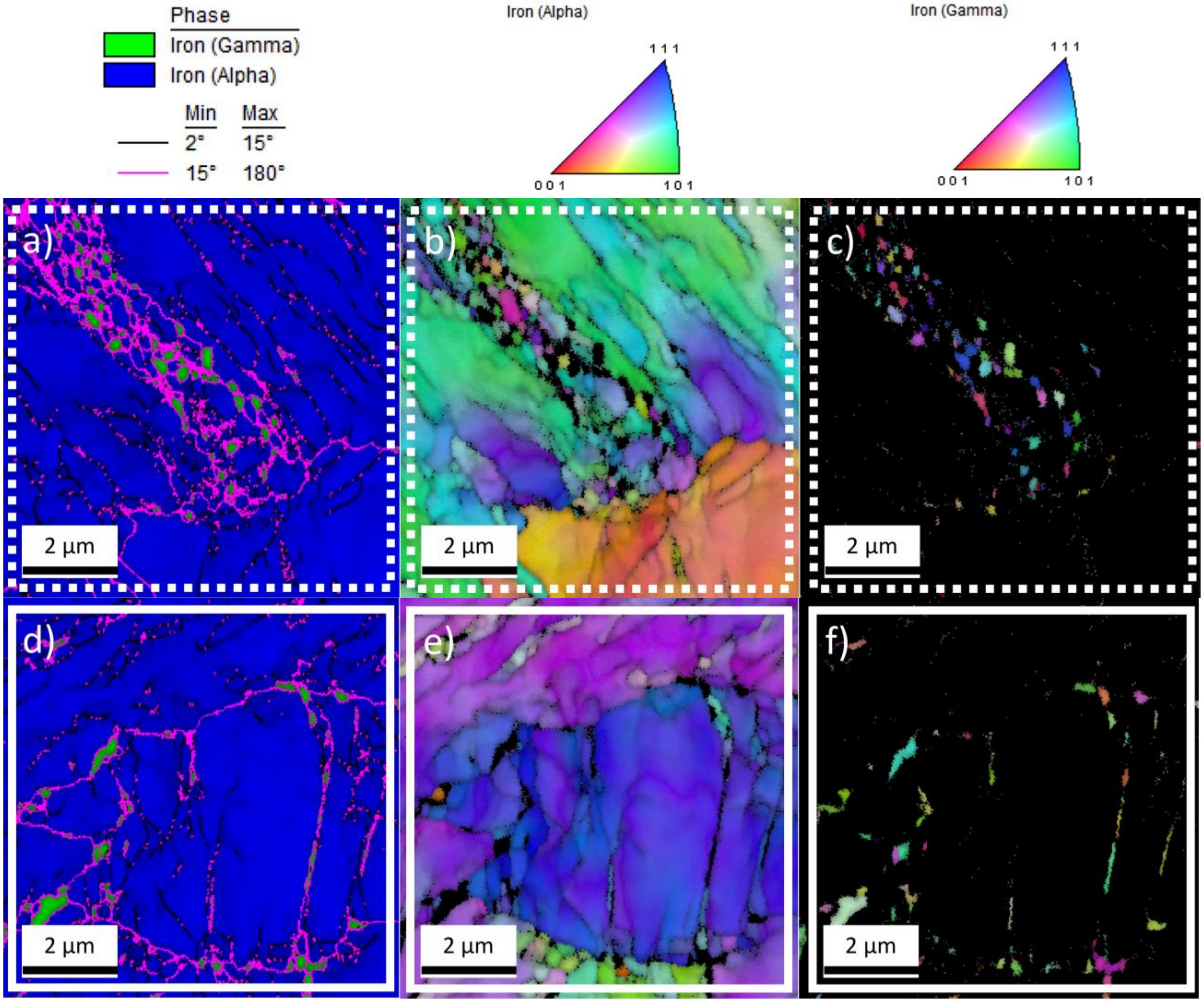

Figure 4-26: Outlined regions in Figure 4-25 (dashed and solid box outlines), are respectively magnified. Separate maps are shown for a/d) image quality, phase and grain boundaries, b/e) image quality and ferrite/martensite IPF and c/f) image quality and austenite IPF.

Figure 4-25 highlights the early stages of indirect competition between martensite recovery, UFG ferrite recrystallization and UFG austenite reversion. When comparing Figure 4-25a and Figure 4-25d, the kernel average misorientation (KAM) intensity is clearly greater in the cold-rolled condition (Figure 4-25a) compared to the annealed-for-0.5 h condition (Figure 4-25d). The KAM intensity is directly related to the location and localized misorientation distribution of high angle grain boundaries in the microstructure (purple lines in Figure 4-25b and Figure 4-25e). Figure 4-25c and Figure 4-25f compare the inverse pole figure (IPF) orientation maps of ferrite/martensite before and after annealing for 0.5 h and indicates that the textured parent martensitic microstructure (coarse in size) remains. Further, the image quality is clearly improved after annealing for 0.5 h (the image quality is darker in the cold-rolled condition and is easier to compare them in Figure 4-22a-b) which indicates recovery of the martensite, synonymous with a decreased dislocation density. Outlined regions in Figure 4-25f, respectively shown in Figure 4-26b and Figure 4-26e, reveal the presence of ultrafine ferrite grains, which provides evidence to support that in some cases the martensite not only recovers, but also recrystallizes to form UFG ferrite. Finally, in the same outlined regions, Figure 4-26c and Figure 4-26f, reveals ultrafine grains of austenite, notably in locations neighboring the UFG ferrite grains, which confirms the reversion process of UFG austenite has begun after annealing for only 0.5 h. Figure D-4 provides another comparison of nucleation sites of austenite (along prior-austenite grain boundaries and parent-martensite lath boundaries).

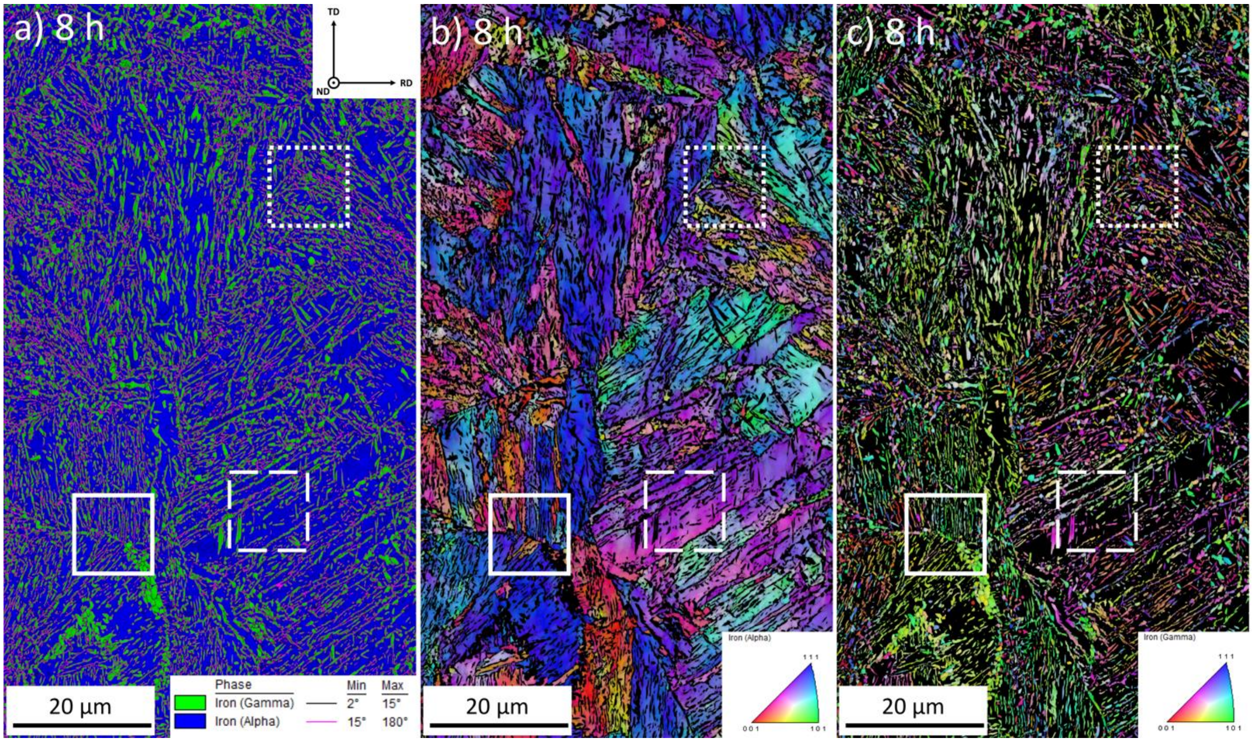

Figure 4-27: Fe-12Mn-3Al-0.05C (wt%) annealed for 8 h at 585 °C. EBSD maps with a) image quality, phase and grain boundaries, b) image quality and ferrite/martensite IPF and c) image quality and austenite IPF.

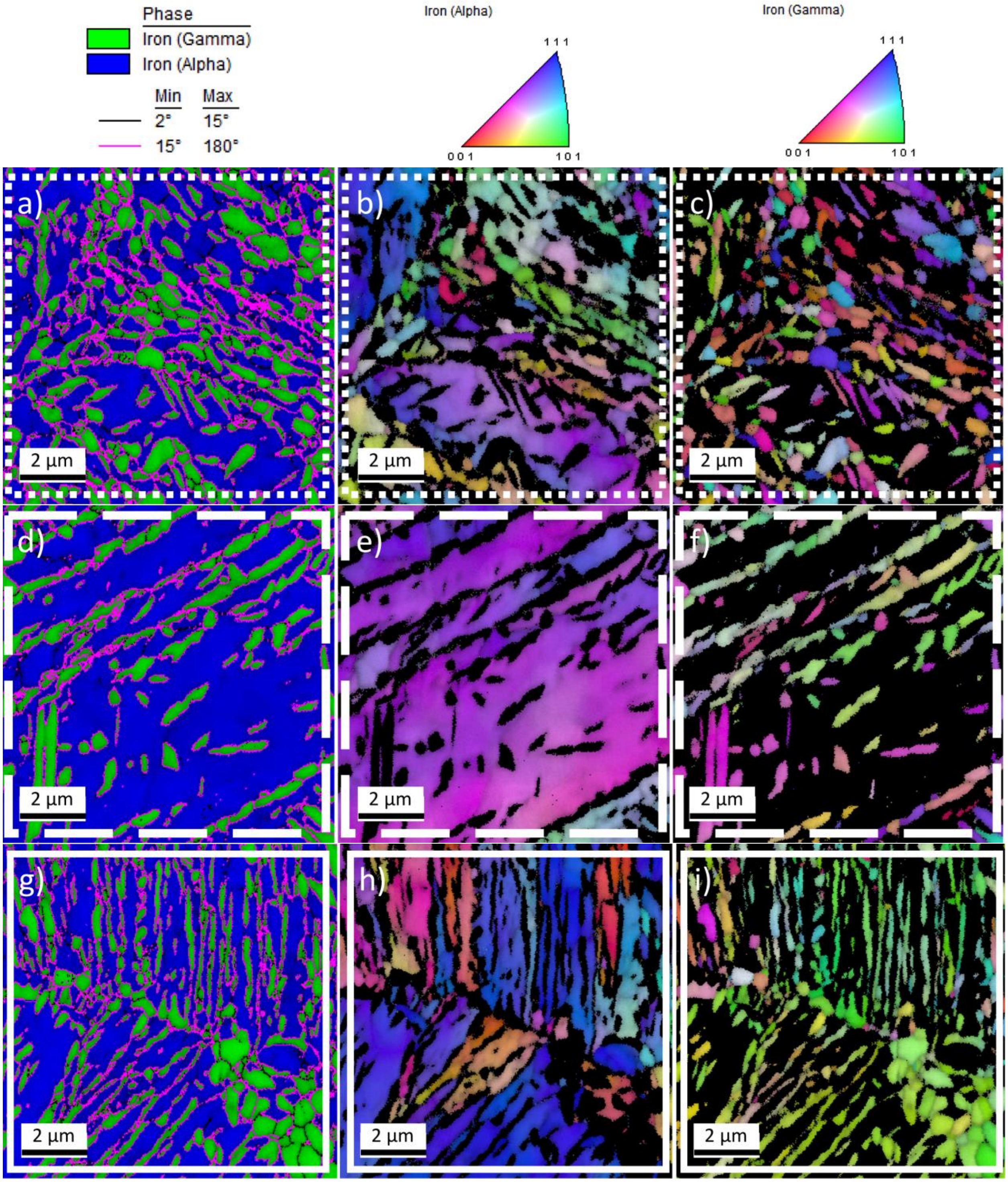

Figure 4-28: Outlined regions in Figure 4-27 (dashed and solid box outlines), are respectively magnified. Separate maps are shown for a/d/g) image quality, phase and grain boundaries, b/e/h) image quality and alpha-Fe IPF and c/f/i) image quality and gamma-Fe IPF.

As seen in Figure 4-27a-c, after 8 h at 585 °C the austenite reversion process has proceeded much closer to equilibrium since all of the coarse-sized parent martensite grains show evidence of UFG austenite reversion. The outlined area near the top of Figure 4-27a-c (seen in Figure 4-28a-c) is likely a triple-point of prior-austenite grains created during the early homogenization step of the thermo-mechanical processing. More importantly, this area (Figure 4-28a-c) shows that austenite grains reverted near a triple-point of the prior austenite, are randomly oriented since the IPF map in Figure 4-28c shows UFG austenite manifested by a nearly random distribution of IPF orientations. Prior-austenite is the austenite stable at high temperatures during homogenization and the cold-rolled martensite is termed the parent. Also, Figure 4-28c shows that most of the UFG austenite is relatively equiaxed and more notably, Figure 4-28a-c provides evidence that UFG ferrite is present near the equiaxed and randomly oriented UFG austenite. Figure 4-28f shows the austenite reverted in the middle of a parent martensite grain, specifically in a parent lath. The austenite morphology appears less equiaxed in shape and far less randomly oriented compared to that in Figure 4-28c. Figure 4-28f shows rod-like or plate-like austenite grains that stand alone whereas most austenite grains are elongated grains strung together, both of which can be distinguished by the location of high- and low-angle grain boundaries in Figure 4-28. Further, Figure 4-28g-i highlights an area of a parent-parent grain boundary, which reveals an extremely textured austenite orientation as evident by similar IPF color (near <110>). There are many austenite rods oriented in the same direction, but also a group of relatively equiaxed austenite grains with the same orientation and low angle austenite-austenite grain boundaries. An overall observation noted in Figure 4-27 and Figure 4-28 is that the vast majority of dissimilar phase boundaries (austenite-ferrite or austenite-martensite) are high angle in nature (15° misorientation or greater). However, boundaries between the same phase (austenite-austenite) vary between low-angle (x < 15°) and high-angle (x > 15°) boundaries which is, of course, dependent on relative orientation differences, but also depends on the location in the parent microstructure.

4.3.3 Measurements of Chemical Compositions After 0.5 h of Intercritical Annealing

In the case of samples annealed for 0.5 h (only ~ 3% austenite present) a site-specific FIB lift out (Figure 4-29a) was necessary for APT sample preparation in order to capture the early stages of austenite reversion. Figure 4-29b shows an EBSD phase- and grain-boundary map that identified a row of locations containing UFG austenite, which is ideal for a rectangular FIB liftout. Figure 4-29c-d confirms that in some locations, UFG ferrite neighbors the UFG austenite. The rectangular FIB liftout was sectioned onto posts and each sectioned chunk of material was concentrically milled to create a needle geometry, taking care to mill away the protective Pt layer so that the top of the needle is closest to the surface viewed in the EBSD scan. Three successful APT measurements collected 150, 360 & 370 million ions (respectively labeled with star-1, star-2 and star-3 in Figure 4-29b) the results of which are shown in Figure 4-30, Figure 4-31 and Figure 4-32. Figure 4-30a shows a decoration of 14 at.% Mn iso-surfaces that appear to be linear defects and lead one to infer that this area is from the recovered martensite, as is consistent with the needle location denoted in Figure 4-29b (star-1). Figure 4-30b-c reveals interesting results such that the locations of Mn and C ions are the mostly the same, indicating co-segregation, plus some boundaries in the triple point are carbon-rich whereas others are carbon depleted. Further, Figure 4-30b-c indicates that the austenite reversion process in the ultrafine Mn-enriched grain is not equilibrated as seen in the variation of concentration in normalized at.% maps. Figure 4-31a depicts a Mn-rich austenite grain near the top of the APT needle with many unique features.

Mainly, the overall Mn composition (Figure 4-31b) is close to the equilibrium predicted for austenite by Thermo-Calc® for this annealing temperature (22.5 at.% Mn is approxiamtely 22 wt% Mn), but there is still some variablility in Mn content throughout the grain. Quantitative C concentration maps of the bent boundary at the bottom of the austenite grain (Figure 4-31c) shows evidence of a capillary effect in that the bent boundary is carbon enriched while the top boundary is carbon poor. Other variability in C content is attributed to crystallographic effects (poles) on the right side of the austenite grain, seen in the APT reconstruction. Figure 4-31d reveals two C-enriched regions (about 9 nm in diameter) located near a decoration of Mn-rich linear defects with C and Mn concentrations (Figure 4-31e) far above the values predicted by thermodynamic calculations for the local equilibrium (LE) between ferrite and austenite. The origin of these austenite embryos will be discussed later in the context of the early stages of Mn and C co-segregation. The final APT reconstruction from the sample annealed for 0.5 h at 585 °C (Figure 4-32) contains an austenite grain with a composition similar to the equilibrium predicted by Thermo-Calc® and less variability in Mn content, (only the bottom boundary of the grain is carbon enriched). The position of the austenite grain (top of the needle) is consistent with the location from which the milled FIB post originated (UFG austenite grains near the center of the star-3 box). Finally, given the orientation of the low angle boundaries farther down the needle and the decoration of Mn-enriched linear defects, the rest of the needle likely contains two neighboring recovered martensite laths (from top to bottom the APT needle contains UFG austenite, UFG ferrite, martensite lath and another martensite lath).

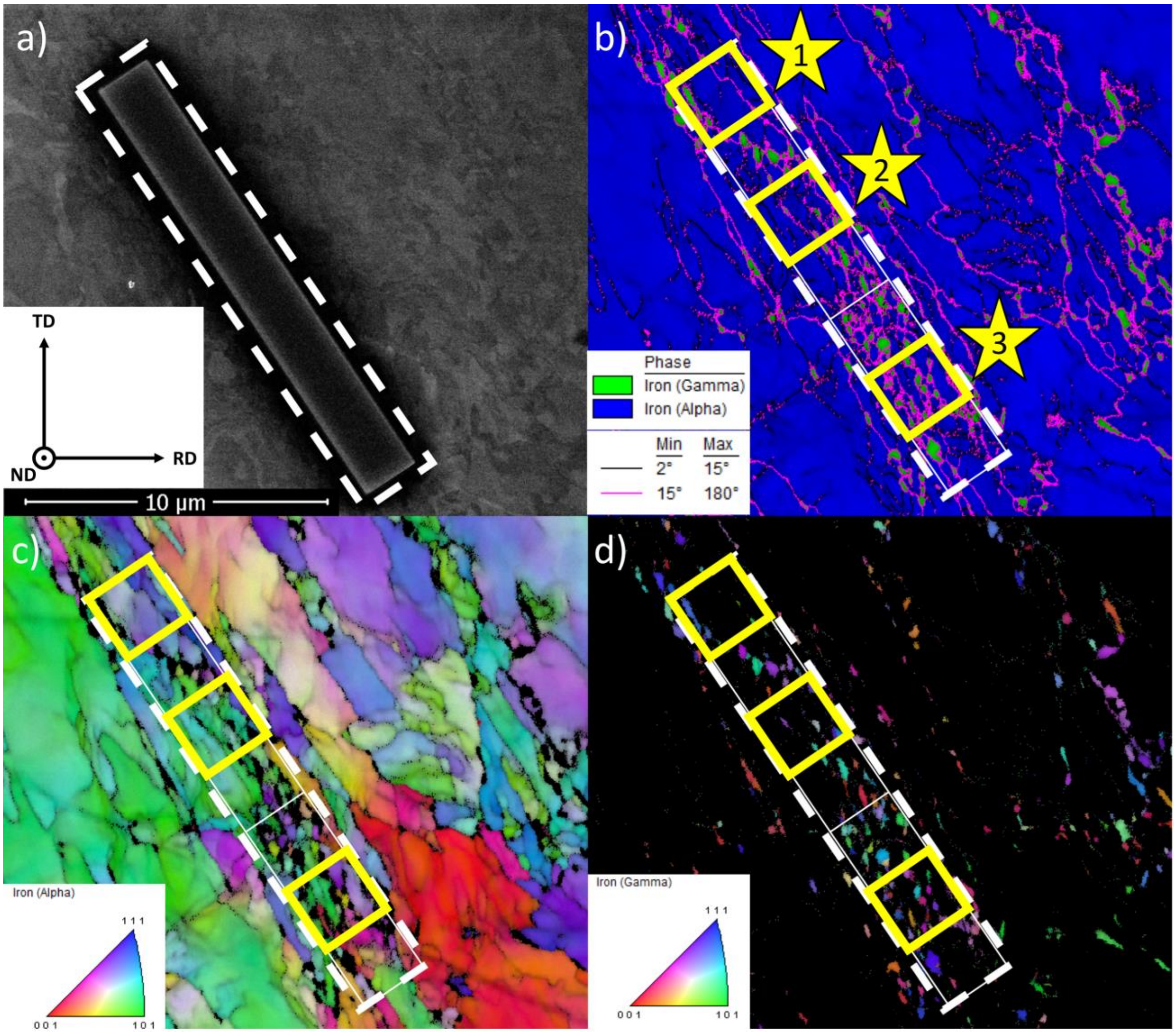

Figure 4-29: a) Secondary electron image shows the protective Pt layer for site-specific liftouts. Such a region was based on a prior EBSD scan and the respective maps of: b) image quality, phase and grain boundaries, c) image quality and ferrite/martensite IPF and d) image quality and austenite IPF indicate the presence of both UFG ferrite and UFG austenite. Stars labeled 1, 2, & 3 in b) are used to identify the original locations of APT needles, with data presented respectively in Figure 4-30, Figure 4-31 and Figure 4-32.

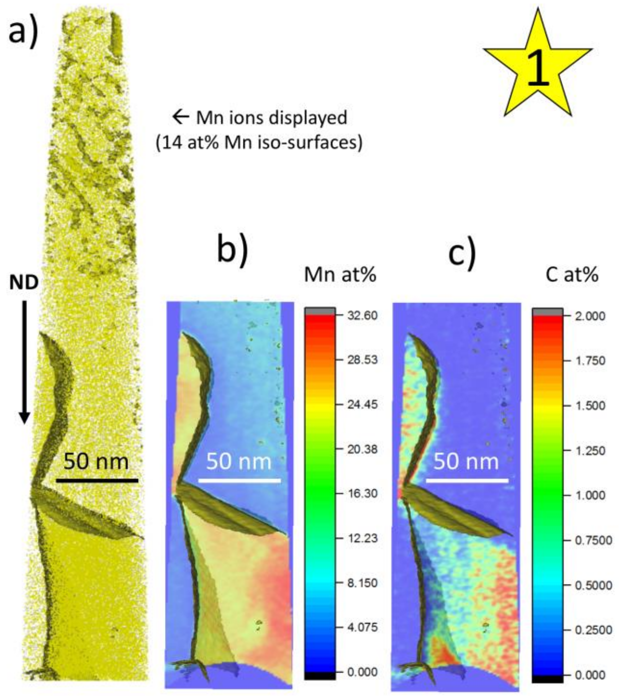

Figure 4-30: a) Mn ions displayed from an APT run of 1.5 x 10^8 ions from a sample annealed for 0.5 h at 585 °C. The quantitative maps b) Mn and c) C of the triple-point boundary provide evidence of co-segregation within a given ultra-fine austenite grain.

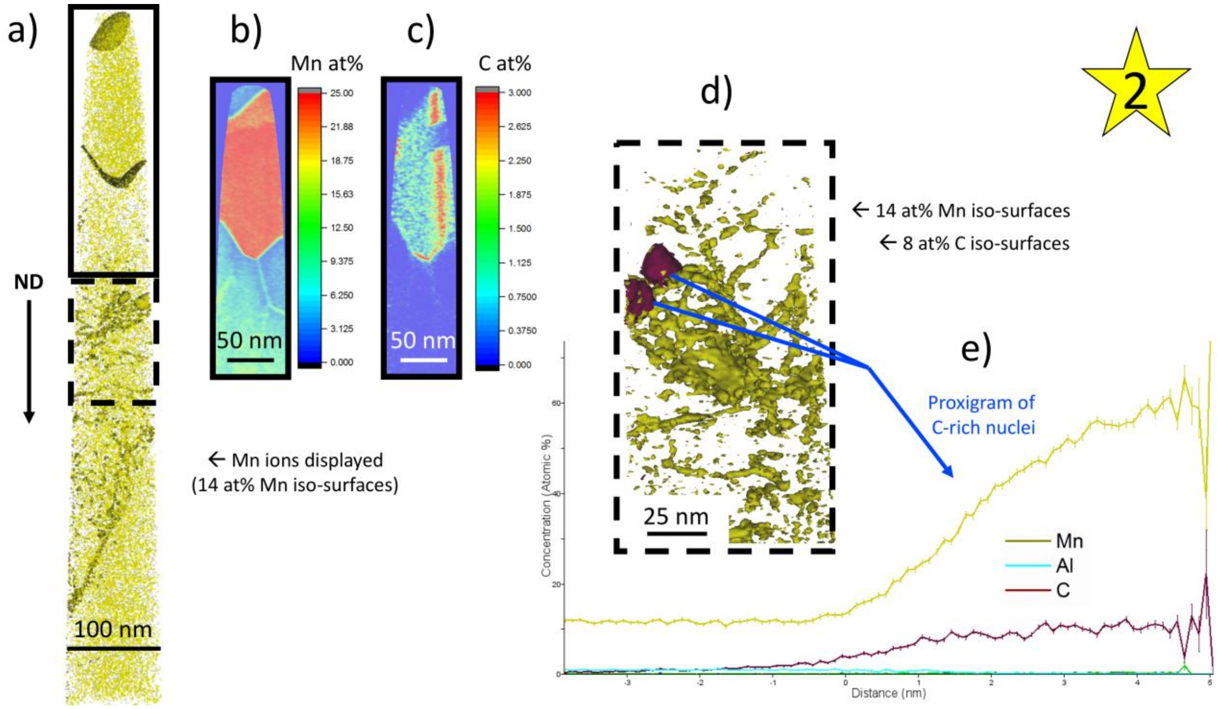

Figure 4-31: a) Mn ions displayed from an APT run of 3.6 x 10^8 ions from a sample annealed for 0.5 h at 585 °C. The quantitative maps b) Mn and c) C of the bent boundary at the bottom of the austenite grain show evidence of a capillary effect. d) The highlighted region does not display

ions, only iso-surfaces of Mn and C, and reveals the presence of austenite embryos about 9 nm in diameter, which are extremely rich in C and Mn as seen in the e) proxigram profile.

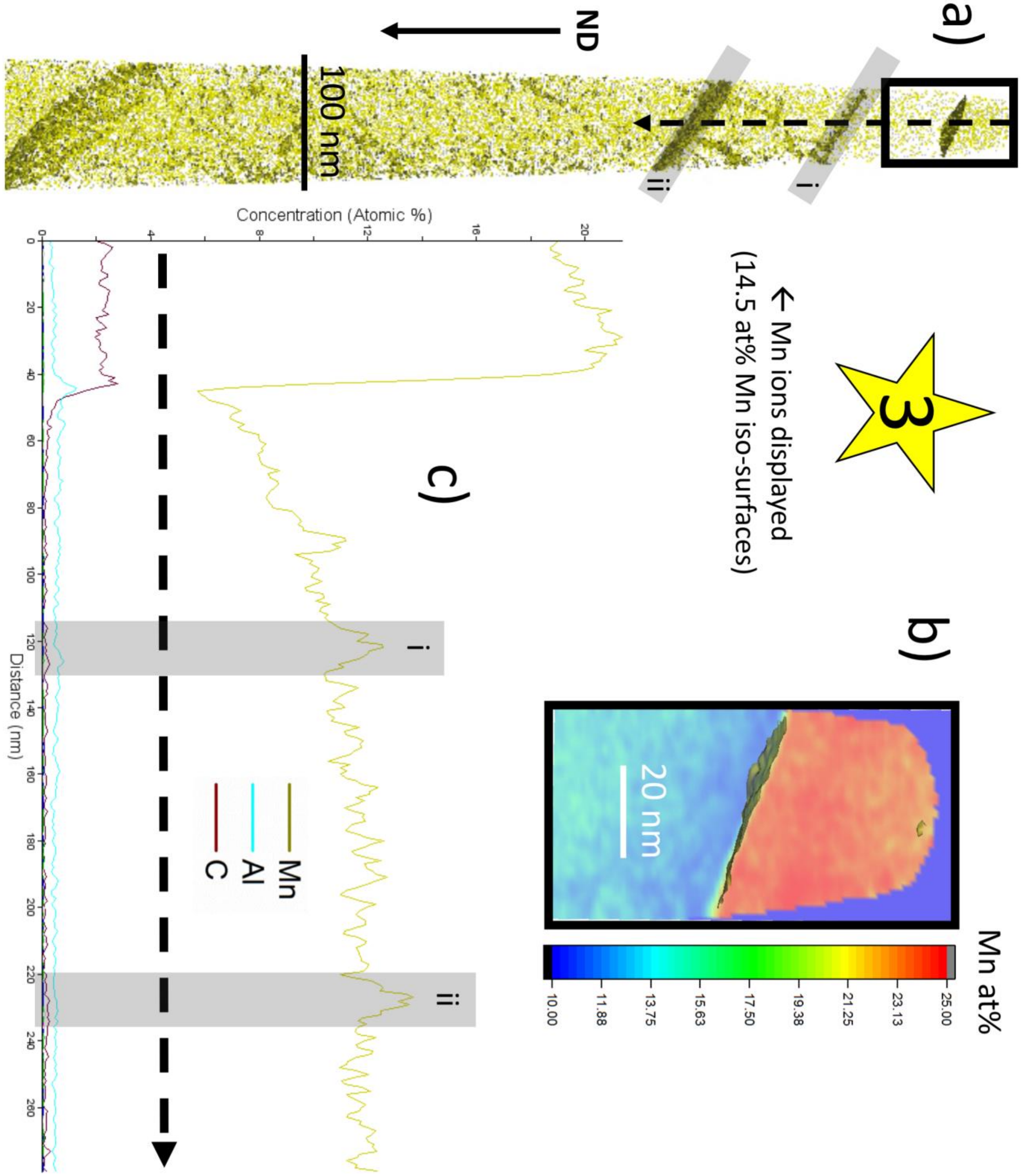

Figure 4-32: a) Mn ions displayed from an APT run of 3.7 x 10^8 ions from a sample annealed for 0.5 h at 585 °C. The quantitative map of b) Mn of the APT tip reveals an austenite grain with a Mn content consistent with equilibrated values as predicted by Thermo-Calc®. The c) line

profile through the upper half of the APT needle indicates a ferritic region strongly depleted in Mn near the austenite grain and i/ii) spikes in Mn concentrations at given ferrite-martensite boundaries.

To further investigate compositions in samples annealed for 0.5 h at 585 °C, a FIB liftout sample (Figure 4-33) was analyzed using STEM. Bruker Esprit software was used to record energy dispersive spectroscopy (EDS) hypermaps in STEM mode operating at 200 kV. It should be noted that in the context of Thermo-Calc® predictions, (Fe-12Mn-3Al-0.05C wt% bulk composition and annealed at 585 °C), equilibrated Mn concentrations in austenite should be ~ 22 wt% Mn, which is synonymous with the green color of the rainbow scale in a quantitative Mn hypermap that ranges from 0-40 wt%. Figure 4-33b-e indicates many instances of austenite grains with near equilibrium concentrations of Mn. However, there is still some variability in some of the observed austenite embryos (as high as 34.1 wt% Mn) as well as differences in the Mn content of the surrounding matrix (as low as 8.5 wt% Mn near the austenite grains and as high as 12.6 wt% Mn far from the austenite grains), which is a trend consistent with the line profile of the APT reconstruction in Figure 4-32, (a gradient from low to medium Mn concentrations).

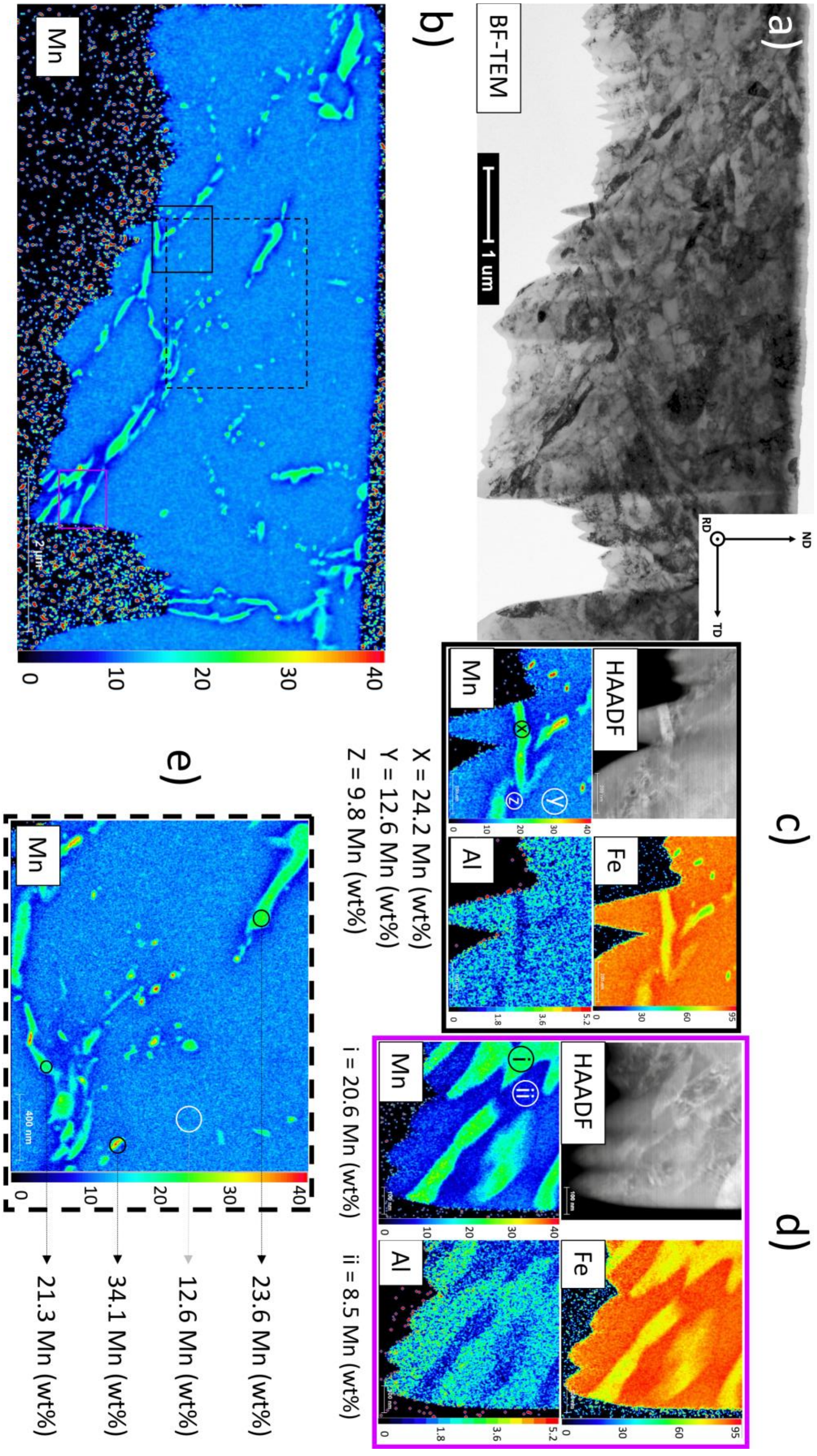
a)
BF-TEM
1 um
ND
TD
RD
b)
Mn
2 µm
0
10
20
30
40
c)
HAADF
Fe
Mn
Al
X
Y
Z
X = 24.2 Mn (wt%)
Y = 12.6 Mn (wt%)
Z = 9.8 Mn (wt%)
d)
HAADF
Fe
Mn
Al
i
ii
i = 20.6 Mn (wt%)
ii = 8.5 Mn (wt%)
e)
Mn
400 nm
23.6 Mn (wt%)
12.6 Mn (wt%)
34.1 Mn (wt%)
21.3 Mn (wt%)

Figure 4-33: FIB liftout of a sample annealed for 0.5 h at 585 °C, viewed in the rolling direction, as indicated in a) the BF-TEM image. b) The quantitative Mn hypermap indicates a decoration of a Mn-enriched UFG phase (austenite). Outlined regions (solid boxes) are magnified in c) and d) and include quantitative hypermaps of 0-95 wt% Fe, 0-40 wt% Mn, and 0-5.2 wt% Al, with spot analysis results of Mn contents indicated. c) and e) indicate a large variability in Mn concentration of the γ and α/α' and phases.

4.3.4 Measurements of Chemical Compositions After 8 h of Intercritical Annealing

The distribution of austenite grains is widespread throughout samples annealed for 8 h at 585 °C (see Figure 4-27) so the FIB liftout was randomly selected in terms of location. A consistent trend observed in APT needles from the 8 h heat treatment is an equilibrated Mn content in the constituent phases (no observed gradients). Also, Al contents are consistently lower in both phases, as compared to Thermo-Calc predictions, but the relative comparison between the austenite and ferrite is consistent with the theory, i.e. Al depletion in austenite and Al enrichment in ferrite during the reversion process [199]. Further, a study by Dmitrieva et al. [200] mentioned ions that are field evaporated between voltage/laser pulses may lead to errors in composition measurement due to preferential field evaporation of some elements and is specifically dependent on laser energy. As depicted in Figure 4-34, the 150-million-ion APT-run consists of an ultrafine austenite grain with an equilibrated Mn concentration that matches Thermo-Calc® predictions and the neighboring phase matches the Mn concentration predicted for ferrite. Furthermore, carbon-enriched and carbon-depleted interfaces are still observed at the two austenite-ferrite boundaries, indicating the local C content may play a significant role in the local equilibrium model of a moving interface between austenite and ferrite even after 8 h of annealing time at 585 °C. Figure 4-35 shows another APT reconstruction from a sample annealed for 8 h, which again reveals equilibrated Mn concentrations that match Thermo-Calc®

predictions and also the presence of carbon-enriched and carbon-depleted interfaces (in this case at a triple-point junction).

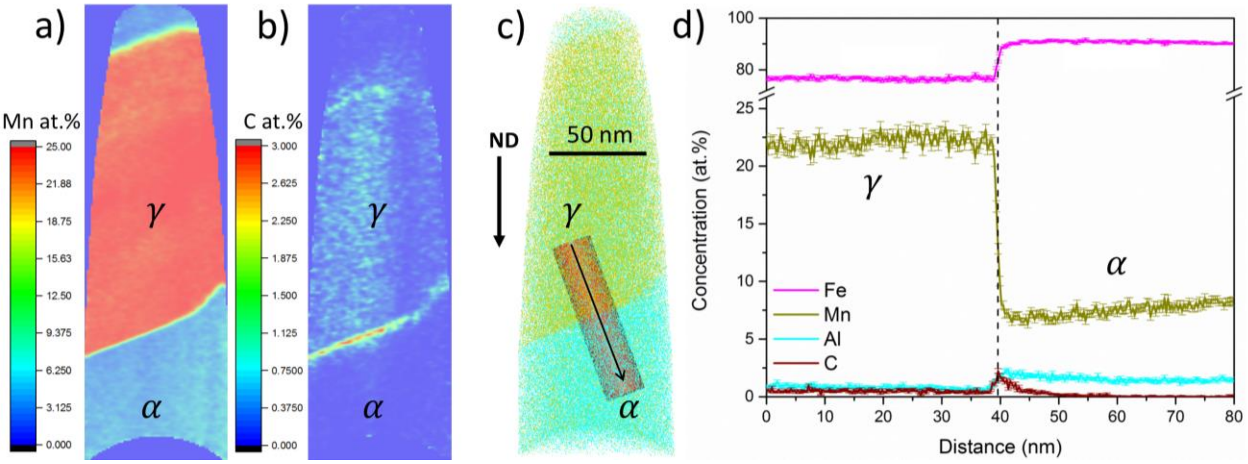

Figure 4-34: Quantitative maps of a) Mn ions and b) C ions from an APT run of 1.5 x 10^8 ions from a sample annealed for 8 h at 585 °C. The c) Mn & Al ions displayed and cylinder profile marked in c) provides quantitative compositional measurements across a d) γ-α boundary. The composition of α was determined to be Fe-7.4Mn-1.6Al-0.19C (at.%)/Fe-7.4Mn-0.77Al-0.04C (wt %) and for γ is Fe-22Mn-0.83Al-0.49C (at.%)/Fe-22Mn-0.4Al-0.11C (wt%).

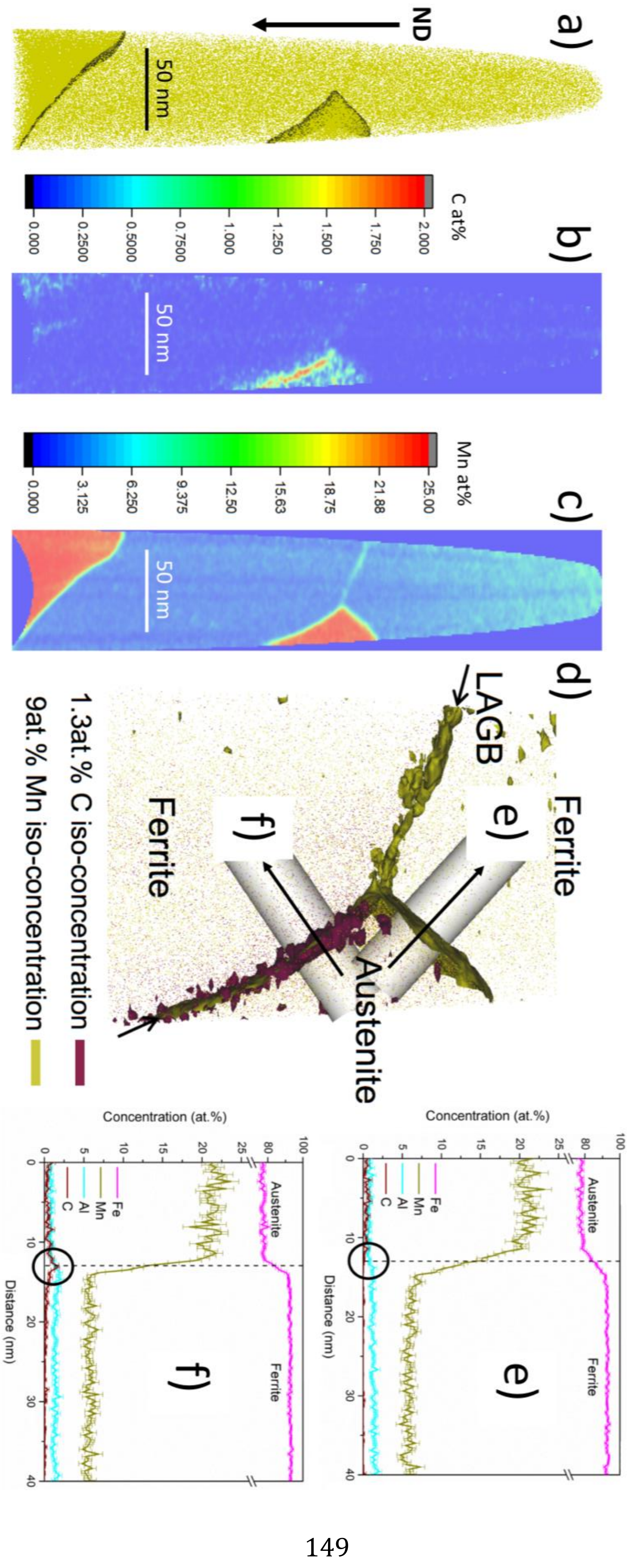
a)
ND
50 nm
b)
C at%
0.000
0.2500
0.5000
0.7500
1.000
1.250
1.500
1.750
2.000
50 nm
c)
Mn at%
0.000
3.125
6.250
9.375
12.50
15.63
18.75
21.88
25.00
50 nm
d)
LAGB
Ferrite
e)
f)
Austenite
Ferrite
1.3at.% C iso-concentration
9at.% Mn iso-concentration
Concentration (at.%)
Distance (nm)
Austenite
Ferrite
Fe
Mn
Al
C
e)
f)
0
5
10
15
20
25
80
100
0
10
20
30
40

Figure 4-35: a) Mn ions displayed from an APT run of 2.7 x 10^8 ions from a sample annealed for 8 h at 585 °C. The quantitative maps of b) C and c) Mn are provided for the entire APT tip. d) Location of cylinder profiles near the triple point GB reveal e) and f) γ-α boundaries of differing characteristics (enrichment and depletion of carbon).

Convergent beam electron diffraction (CBED) analysis in the TEM was successful for electropolished disc samples annealed for 8 h at 585 °C, as seen in Figure 4-36a-c, which confirms the presence of UFG ferrite in close proximity to UFG austenite. Line-scan results across ferrite and austenite grains (Figure 4-36d) yields Mn and C contents nearly identical to Thermo-Calc® predictions for austenite and ferrite. The Al contents for both the ferrite and austenite grains are lower than predicted, but the relative comparison between the two ultrafine grains is consistent with the theory that austenite becomes depleted in Al and ferrite becomes enriched with Al during the reversion process. However, because of the absorption of Al X-rays, the absolute values of Al content can be underestimated and vary with the elevation angle of EDS detectors and path length in the sample towards the detector [201][202]. As austenite grains were preferentially electropolished (see Figure 4-37b) Mn/Fe K_α peak ratios from spot analyses (displayed in Figure 4-37a) were useful for phase identification to negate thickness effects. Mn/Fe K_α peak ratios are ~3 times greater in the γ phase as compared to the α phase. Similar to observations in EBSD scans (see Figure 4-27), various morphologies of austenite (equiaxed and rod-shaped) are observed in electropolished TEM samples viewed in the normal direction (see Figure 4-37 and Figure 4-38). To understand the morphology viewed in the rolling direction, a FIB was used to liftout a specimen orthogonal to the normal direction and thinned so that the viewing direction is orthogonal to the rolling direction (Figure 4-39). The BF-TEM image in Figure 4-39a complements the observations from EBSD measurements (Figure 4-27), such that austenite grains appear to be equiaxed, strung together and also rod-like/plate-like. FIB liftouts also mitigate the limitations imposed by selective electropolishing and reduce the ferromagnetic mass, compared to self-supporting discs. STEM-EDS maps from a FIB liftout yielded area fractions of 35% austenite in a sample annealed for 8 h at 585 °C (viewed in the rolling direction) which matches EBSD measurements of phase fraction for that annealing time. FIB liftouts also allow composition profiles to be obtained at near edge-on phase boundaries in flat samples, as shown in Figure 4-40d. Such profiles are nearly identical to APT results (see Figure 4-34d and Figure 4-35e/f) in that equilibrated compositions are observed at a distance of 6 nm or less from the interface. While STEM-EDS offers high-resolution mapping of tens of grains at a time in a given FIB liftout specimen, 3D APT offers improved spatial resolution for measurements of composition profiles across UFG austenite-ferrite boundaries.

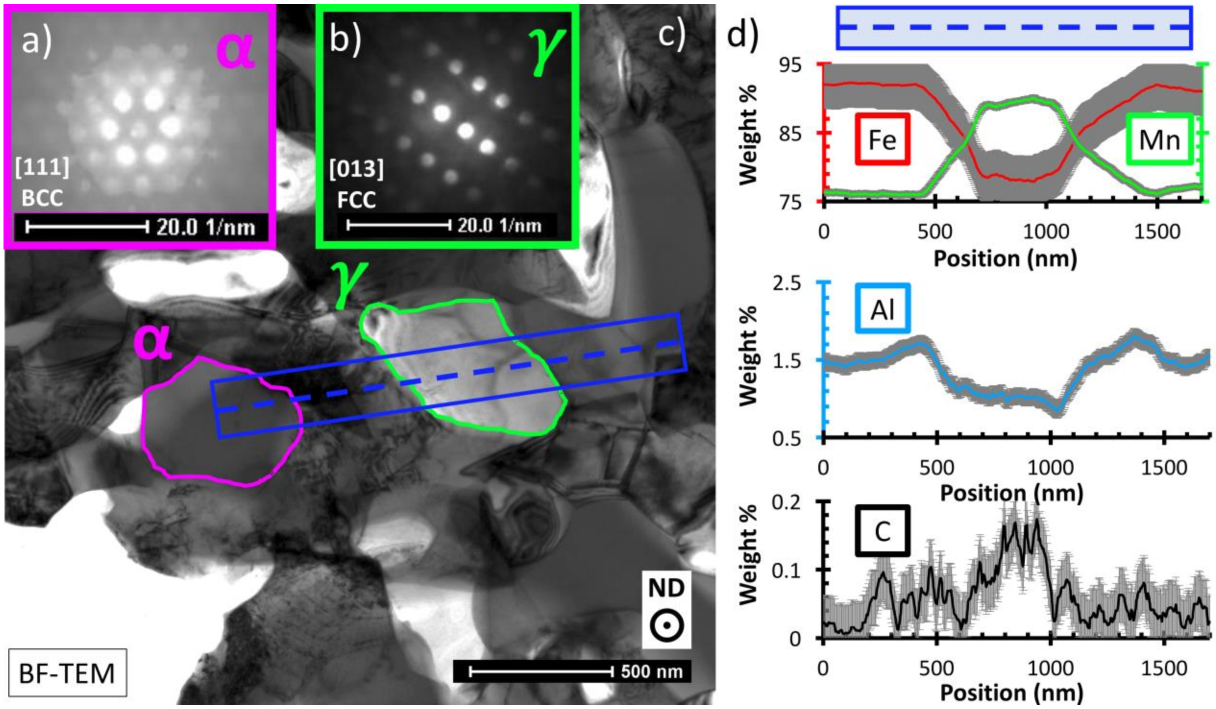

Figure 4-36: 200 kV CBED patterns were used to identify a) ferritic [α] and b) austenitic [γ] grains shown in c) the BF-TEM image of a sample annealed for 8 h at 585 °C. d) A line scan across γ and α grains highlights normalized differences in Fe, Mn & Al (wt%). Error bars are based on 3 sigma values reported in the Esprit software for this specific spectrum deconvolution.

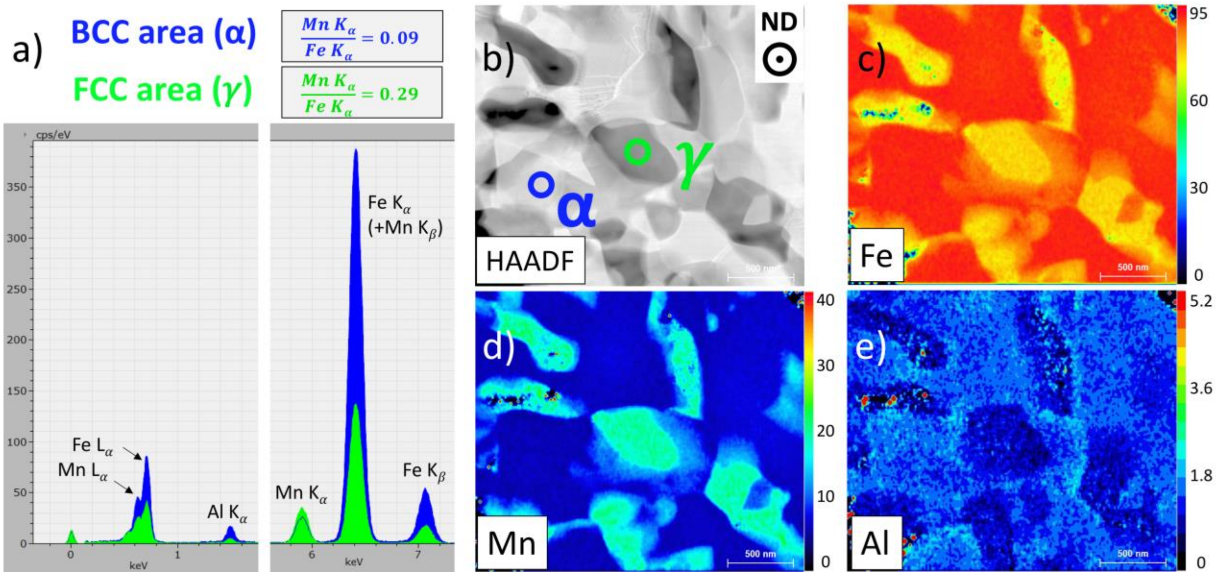

Figure 4-37: a) spectra from spot-EDS marked in b) the STEM-HAADF image, which distinguishes between γ and α phases via Mn/Fe Kα peak ratios. The quantitative hypermaps of a sample annealed for 8 h at 585 °C c) 0-95 wt% Fe, d) 0-40 wt% Mn, and e) 0-5.2 wt% Al, indicates a γ phase [Fe-20.8Mn-1.2Al (wt%)] enriched in Mn and depleted in Fe and Al.

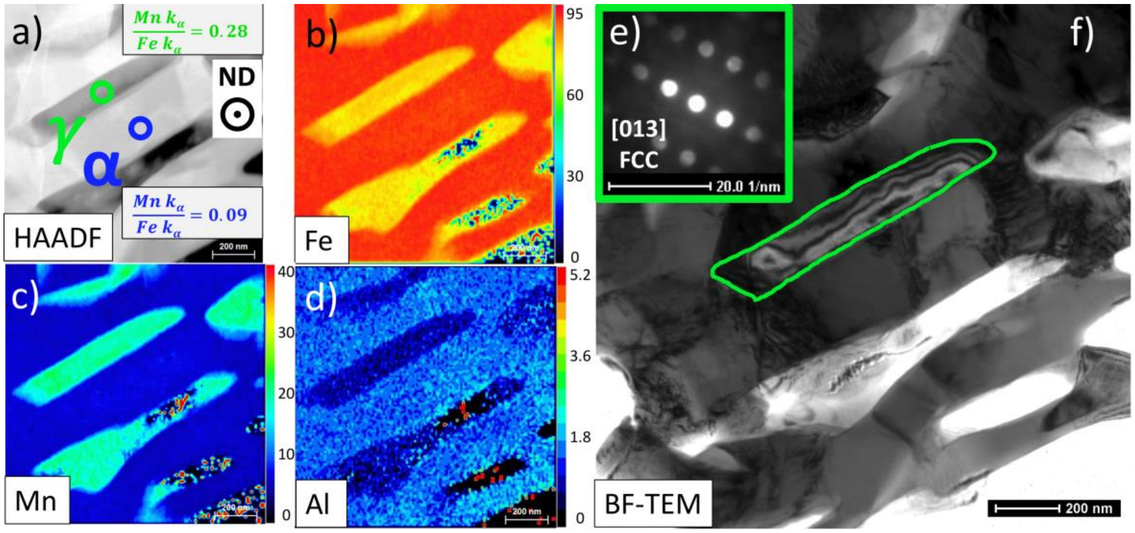

Figure 4-38: Mn/Fe Kα peak ratios from spot-EDS marked in a) the STEM-HAADF image of a sample annealed for 8 h at 585 °C. The quantitative hypermaps b) 0-95 wt% Fe, c) 0-40 wt% Mn, and d) 0-5.2 wt% Al, indicates a γ phase [Fe-19.9Mn-0.9Al (wt%)] enriched in Mn and depleted in Fe and Al, compared to the α phase [Fe-7.4Mn-1.5Al (wt%)]. e) 200 kV CBED patterns were used to identify an austenite grain shown in f) the BF-TEM image.

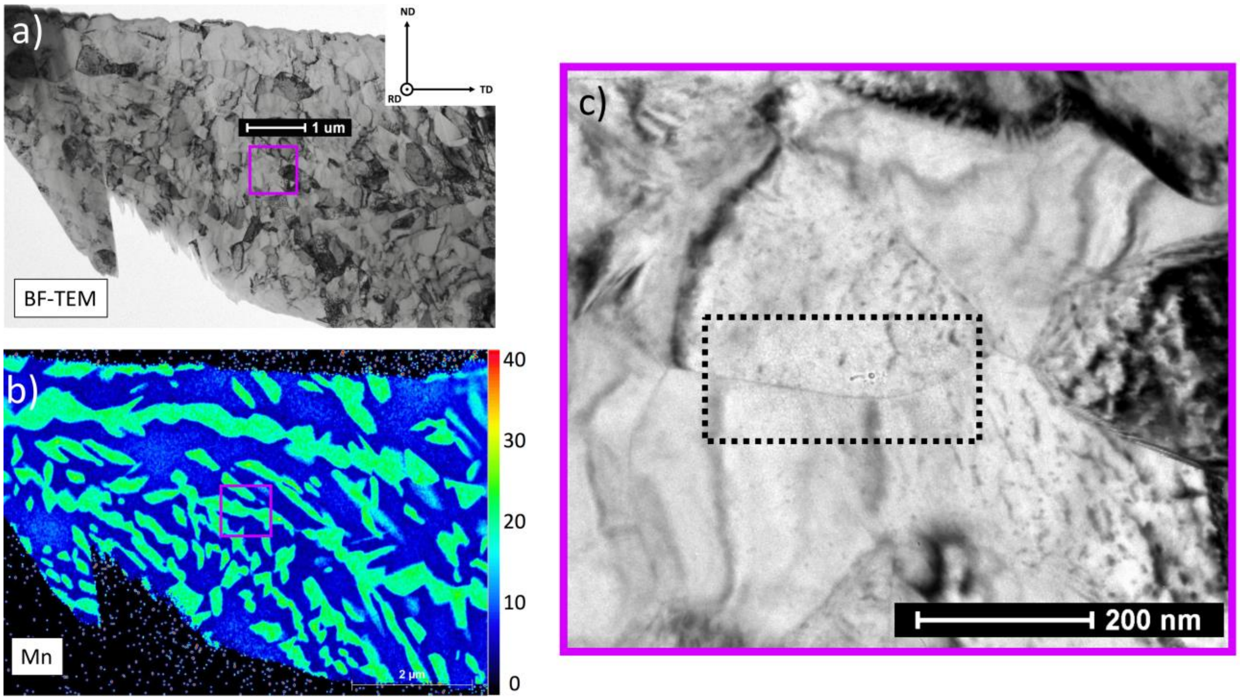

Figure 4-39: FIB liftout of a sample annealed for 8 h at 585 °C viewed in the rolling direction as indicated in the a) BF-TEM image. b) The quantitative Mn hypermap indicates UFG austenite (green grains with ~ 21 wt% Mn) that either are rod-like or equiaxed and strung together. The purple highlighted square region is viewed in c) the inset BF-TEM image, which shows a near edge-on boundary between austenite and ferrite (determined in part b).

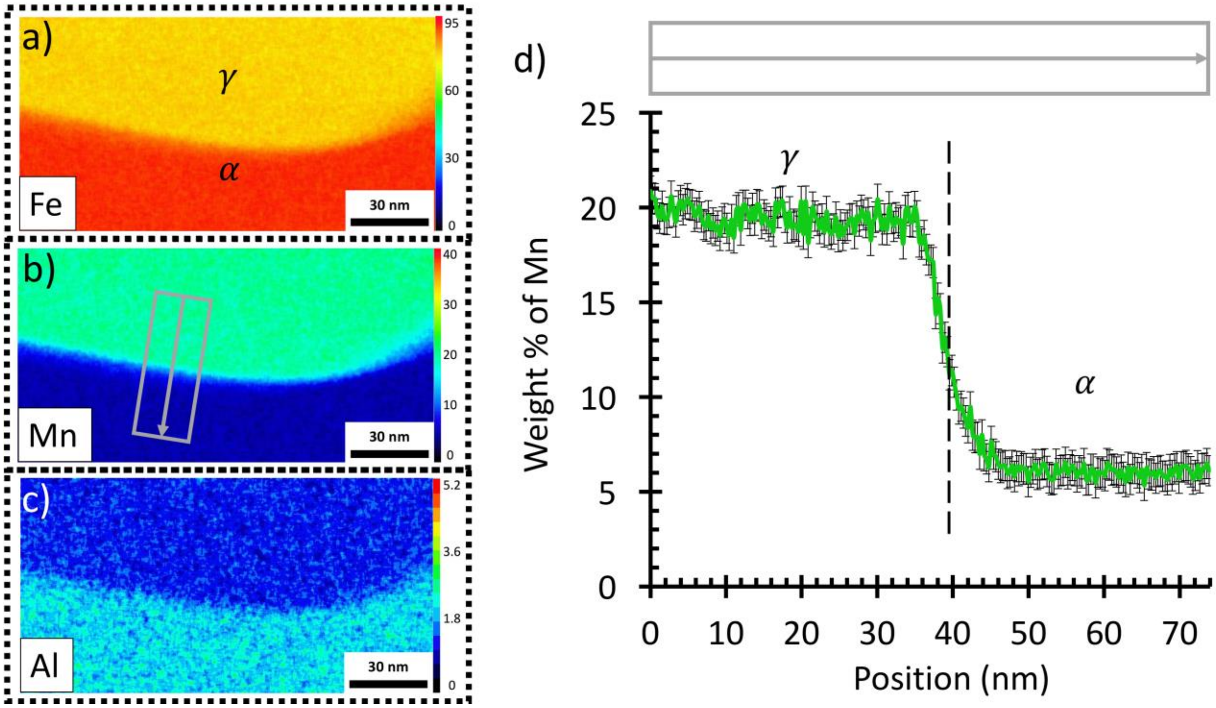

Figure 4-40: The near edge-on boundary marked by the dashed box in Figure 4-39c was further analyzed by STEM-EDS. Quantitative hypermaps of a) 0-95 wt% Fe, b) 0-40 wt% Mn, and c) 0-5.2 wt% Al. A d) linescan (location denoted in part b) indicates equilibrated concentrations (lack of significant gradients) approximately 6 nm away from the interface. Error bars are based on 3 sigma values reported in the Esprit software for this specific spectrum deconvolution.

4.3.5 Competing Factors During Evolution of a Multi-Phase Microstructure

In the present work on a Fe-12Mn-3Al-0.05C (wt%) steel, the low carbon content (< 0.05 weight%) does not provide a high chemical driving force for the formation of cementite. Specifically, Thermo-Calc® predicts a cementite mole fraction of 0.001 with an equilibrium composition of Fe-70Mn-6C (wt%) for an intercritical annealing temperature of 500 °C, but no cementite stability above 500 °C. During intercritical annealing at 585 °C, the first austenite nuclei identified with APT (see Figure 4-31) in samples annealed for 0.5 h possess C and Mn concentration (Fe-60Mn-10C at.% / Fe-64Mn-2.3C wt%) far above the values predicted by thermodynamic calculations for the local equilibrium (LE) between ferrite and austenite. Further, a consistent observation from APT results in the present work is the identification of carbon-enriched austenite-ferrite boundaries, which Luo et al. [107] and Seo et al. [203] also observed in time- and space-dependent simulations using a Thermo-Calc® module (DICTRA). Seo et al. [203] observed carbon-rich austenite-martensite interfaces in APT measurements of quenched-and-partitioned FeMnC steels. STEM-EDS results from samples annealed for 0.5 h (see Figure 4-33) reveal an inhomogeneous distribution of UFG austenite and Mn-enriched austenite nuclei (a range from 21 to 34 wt% Mn). Figure D-5 and Figure D-6 provide SEM and TEM observations of austenite grains and nearby particles that are not etched or electropolished. Upon additional interrogation with STEM-EDS (see Figure D-7) it appears that some of these particles are a type of Mn-rich carbide, some of which have already transformed to embryonic austenite, or at least some of the particle compositions match Thermo-Calc® predictions of austenite composition. These results indicate that the parent martensite may be supersaturated with Mn (Mn is an austenite stabilizer) and upon quenching and cold-rolling, the excess Mn produces Mn-rich carbides that later form some of the austenite embryos. Recent DICTRA simulations show that the initial austenite during early stages of nucleation has a much higher Mn content compared to equilibrium predictions with Thermo-Calc® [204]. Further, the simulations show that as annealing time increases (which moves the austenite-ferrite interface) the C content becomes diluted in the austenite and the Mn content also decreases. These results are exacerbated when the simulations are required to decompose an FCC $Mn_{23}C_6$ carbide into austenite. At later stages, (between 0.5 h and 8 h), the growth of austenite follows the LE model for the moving interface [204]. The following sequence of reversion is proposed: (i) C and Mn co-segregation; (ii) formation of Mn- and C-enriched face-centered-cubic critical nuclei and (iii) growth of austenite controlled by LE mode. The compositions of UFG phases observed in the STEM-EDS linescan of Figure 4-40d near the edge-on boundary is equilibrated approximately 6 nm away from the boundary, which is relatively consistent with APT results (equilibration approximately 2-4 nm away from boundaries) in Figure 4-34d and Figure 4-35e-f. These concentration profiles are consistent with recent DICTRA results [204], confirming that austenite growth is controlled by local equilibrium, as observed after 8 h of annealing.

The determination of the intercritical annealing temperature which produces the maximum amount of reverted austenite (Tγ-max) is important because temperatures below Tγ-max should not produce new α' martensite after quenching to room temperature, due to a lowering of the martensite-start temperature below room temperature [39][54]. Typically, thermodynamic predictions tend to underestimate the Tγ-max, as compared to experimental measurements of austenite fraction vs. annealing temperature, due to effects by dislocation density and thus solute mobility [122]. In this work, the Tγ-max is predicted to be 630 °C (see Figure 4-21) which is greater than the chosen intercritical annealing temperature (585 °C). Further, the microstructure present after annealing for 8 h at 585°C consists of mostly coarse grained recovered/tempered α' martensite with approximately 35 vol % UFG austenite and less than 10 vol % of UFG α ferrite. However, the coarse grained martensite is not new α' martensite (formed during quenching to room temperature from the intercritical annealing temperature), but rather is a product of incomplete recrystallization of the cold-rolled α' martensite during intercritical annealing. Although C diffusion in medium-Mn steels is faster than Mn, there is clearly competition during annealing between the driving forces of martensite recrystallization and the reversion of UFG austenite. Arlazarov et al. proposed that variations in dislocation density and Mn content in a hot-rolled medium-Mn steel were coupled to the presence of polygonal ferrite and can aid in martensite recrystallization [50]. Zhang et al.’s work [59] on a medium-Mn steel (Fe-7.14Mn-0.14C-0.23Si wt%) that was hot-rolled, intercritically batch-annealed, cold-rolled and intercritically annealed again for various times showed a pronounced change in morphology based on annealing time. For continuous casting conditions, (a final intercritical annealing time of 3 min), the relatively low temperature and short annealing time produced an elongated and still slightly deformed microstructure. Observations of elongated UFG ferrite and elongated UFG austenite were attributed to a dependence on the prior martensitic microstructure since final annealing times of 12 h and greater (classified as batch-annealed) produced a completely equiaxed microstructure of ferrite and austenite [59]. Notably, the UFG ferrite was always larger than UFG austenite, regardless of annealing time [59].

A study by Han et. al [52] on the improvement of impact toughness in medium-Mn steels reports that cold-rolling medium-Mn steels prior to intercritical annealing is a necessary step in producing globular austenite. Specifically, Han et al. observed the nucleation of lamellar austenite without recrystallization of martensite along high-angle boundaries, (prior austenite boundaries and martensite packet/block boundaries), and low-angle boundaries (martensite lath boundaries) in hot-rolled samples. On the other hand, cold-rolled samples produced microstructures containing UFG globular austenite and UFG globular ferrite, meaning the martensite matrix was actively recrystallized [52]. In contrast, Chen et al. [205] observed block-form and lath-like austenite morphologies in a hot-rolled Fe-3.3Mn-1.4 Ni-0.23Si-0.05C (wt%) steel annealed at 650 °C for 2 h. Chen et al. specifically noted that the presence of block-form ferrite always neighbored block-form austenite, whereas lath-like austenite always formed in between tempered martensite laths. However, it was determined that both block-form and lath-form austenite had the same Kurdjumov-Sachs (K-S) orientation relationship with the parent martensitic microstructure [205]. Arlazarov et al. [50] observed both lath-like and polygonal austenite, tempered martensite and polygonal ferrite in a cold-rolled Fe-4.6Mn-0.09C wt% steel that was subjected to a double annealing heat treatment. The nature of the dual morphology of the UFG grains (lath-like and polygonal) was attributed to Mn micro-segregation (Mn-enriched and Mn-depleted bands in the bulk microstructure) such that Mn-rich bands tended to form lath-like austenite whereas Mn-depleted bands were the likely origin of polygonal austenite and polygonal ferrite, since the martensite is more actively recrystallized when there is less competition from chemical/diffusive driving forces. The present work shows UFG block-like and plate-like austenite, which are respectively observed near prior austenite grain boundaries and within parent martensite laths. Further yet, in the present work, block-like UFG ferrite is nearly always observed next to UFG block-like austenite, indicating a competition between recrystallization (martensite to ferrite) and reversion (martensite to austenite). This competition could be possible if the driving force of the recrystallization (typically proportional to dislocation density) is out-weighed by diffusion kinetics. Even after 48 h of annealing, the texture of the originally cold-rolled microstructure is still observed, meaning the microstructure is not fully recrystallized nor equiaxed (see Figure D-8). Finally, a cold-rolled sample from the present work was cold-rolled even more from 50% to 65% and subjected to a heat treatment of 8 h at 585 °C, which produced nearly the same amount of austenite (32% measured by XRD) as compared in the original work on 50% cold-rolled samples annealed for 8 h at 585 °C (29% austenite measured with XRD and 35% austenite measured with EBSD, as seen in Figure 4-23). Such results indicate that the differences between 50 % and 65 % cold-rolled reductions are insufficient to produce changes in the annealed microstructure or that the chemical driving force of the austenite reversion and sluggish diffusion of Mn for a relatively high content of Mn (for a medium-Mn steel) tend to determine the rate of the austenite reversion kinetics.

4.3.6 Summary and Conclusions

- XRD and EBSD measurements yield an increase in volume fraction and grain-size area of reverted austenite with increasing annealing time for an intercritical annealing temperature of 585 °C using a Fe-12Mn-3Al-0.05C wt% steel.
- EBSD and TEM/CBED results reveal that relatively equiaxed ultrafine ferrite grains and rod-like and plate-like ultrafine austenite grains are dispersed throughout the parent microstructure of recovered martensite.
- Variation in morphology and orientation distribution of the austenite is attributed to the location of nucleation within the parent martensitic microstructure and local defect content. Rod-like and plate-like austenite is observed in between low-angle laths of the parent martensitic microstructure. Ultrafine austenite that is relatively more equiaxed in nature is always observed near equiaxed ultrafine ferrite, which was typically observed near high-angle grain boundaries of the parent martensite and/or grandparent prior austenite microstructures.
- STEM-EDS confirms that austenite is enriched in Mn and depleted in Fe and Al compared to the parent martensitic microstructure. Although Mn/Fe K-alpha peak ratios are useful for identifying austenite grains, some variability in Mn content is observed for an annealing time of 0.5 h and is attributed to prior existence of Mn-rich carbides in the parent microstructure. The Mn content of austenite is equilibrated after 8 h of annealing time at 585 °C and also matches Thermo-Calc® predictions.
- Quantitative 3D measurements of compositions for all phases with APT follow trends that are consistent with STEM-EDS results, (some variability in composition for an annealing time of 0.5 h, but equilibrated compositions after 8 h of annealing). The added

benefit of APT (accurate carbon content measurements) provides a consistent observation that both carbon-enriched and carbon-depleted interfaces with austenite are present, regardless of annealing time, indicating the chemical driving force in austenite reversion of this medium-Mn steel is primarily steered by sluggish Mn diffusion, since C diffusion is faster.

4.4 Influences of Strain Rate on Mechanical Properties and Deformations of a Multi-Phase Medium-Mn TWIP-TRIP Steel

Given the detailed analysis of microstructures annealed for 0.5 h and 8 h at 585 °C, novel in-situ measurement techniques were used to quantify differences in strain and temperature during high rate testing of the medium-Mn steel annealed for 0.5 h and 8 h at 585 °C. Mechanical properties are measured with servo-hydraulic tension and Kolsky-bar deformation (strain rates from $\dot{\varepsilon} = 10^{-4}$ /s to $\dot{\varepsilon} = 10^{3}$ /s). Conventional characterization techniques such as BF-TEM, DF-TEM, SAED and XRD are used to quantify observed deformation mechanisms, which in turn were used to develop a constitutive model that captures the mechanical behavior of the multi-phase microstructure annealed for 8 h. The constitutive model aided in explanation of the complex mechanical behavior of the multi-phase steel.

4.4.1 Effects of Intercritical Annealing Time and Strain Rate on Mechanical Properties

Figure 4-41 shows the representative engineering stress-strain curves from servo-hydraulic tensile tests of the medium-Mn steel annealed for 0.5 h (Figure 4-41a) and 8 h (Figure 4-41b). The Young’s modulus of the medium-Mn steel measured during quasi-static strain rates was the same for both annealing times (approximately 180 GPa). Mechanical properties are summarized as a function of strain rate in Figure 4-42. The 0.2% offset yield strength (YS) of the medium-Mn steel annealed for 0.5 h rose from 769 ± 11 MPa to 876 ± 21 MPa with increasing strain rate from $\dot{\varepsilon} = 2x10^{-4}$ /s to $\dot{\varepsilon} = 2x10^{1}$ /s (see Figure 4-42a) and the YS of the medium-Mn steel annealed for 8 h rose from 669 ± 1 MPa to 758 ± 1 MPa with the same increase in strain rate from $\dot{\varepsilon} = 2x10^{-4}$ /s to $\dot{\varepsilon} = 2x10^{1}$ /s (see Figure 4-42b). Yield strengths of $\dot{\varepsilon} = 2x10^{2}$ /s tests were not computed due to excessive ringing in the load washer and elastic gauges (see Figure A-5) and a low data acquisition rate. The ultimate tensile strength (UTS) of the 0.5 h heat treatment increased from 825 ± 11 MPa to 997 ± 23 MPa by increasing the strain rate by 6 orders of magnitude from $\dot{\varepsilon} = 2x10^{-4}$ /s to $\dot{\varepsilon} = 2x10^{2}$ /s (see Figure 4-42a) and the UTS of the 8 h heat treatment increased from 780 ± 3 to 911 MPa by increasing strain rate from $\dot{\varepsilon} = 2x10^{-4}$ /s to $\dot{\varepsilon} = 2x10^{2}$ /s (see Figure 4-42b). Therefore, both heat treatments of the medium-Mn steel show positive strain-rate sensitivity of yield and ultimate tensile strengths (from $\dot{\varepsilon} = 2x10^{-4}$ /s to $\dot{\varepsilon} = 2x10^{2}$ /s) and a decrease in annealing time (from 8 h to 0.5 h) increased the yield and ultimate tensile strengths (when compared at the same strain rate).

As shown in Figure 4-42c and Figure 4-42d, the medium-Mn steels annealed for 0.5 h and 8 h show no large differences in uniform elongation (UE) with increasing strain rate from $\dot{\varepsilon} = 2x10^{-4}$ /s to $\dot{\varepsilon} = 2x10^{2}$ /s. Slight increases in total elongation (TE) for both heat treatments are noted at $\dot{\varepsilon} = 2x10^{2}$ /s, as compared to those at $\dot{\varepsilon} = 2x10^{-2}$ /s (see Figure 4-42c and Figure 4-42d). However, an increase in annealing time from 0.5 h to 8 h clearly increases both the UE and TE of the medium-Mn steel (when compared at the same strain rate). Specifically, increasing annealing time from 0.5 h to 8 h increases UE from 0.1 to 0.14 and TE from 0.17 to 0.25, when deformed at $\dot{\varepsilon} = 2x10^{-4}$ /s. The product of ultimate tensile strength and total elongation (PSE) of the 0.5 h heat treatment increases from 14,200 MPa% to 22,300 MPa% when increasing strain rate from $\dot{\varepsilon} = 2x10^{-4}$ /s to $\dot{\varepsilon} = 2x10^{2}$ /s. For the 8 h heat treatment, the PSE at $\dot{\varepsilon} = 2x10^{-4}$ /s is 19,200 MPa% and drops slightly to 17,400 at $\dot{\varepsilon} = 2x10^{-2}$ /s, but then increases to 24,600 MPa% at $\dot{\varepsilon} = 2x10^{2}$ /s. When comparing values at the same strain rate, the 8 h heat treatment always has a higher PSE than the 0.5 h heat treatment.

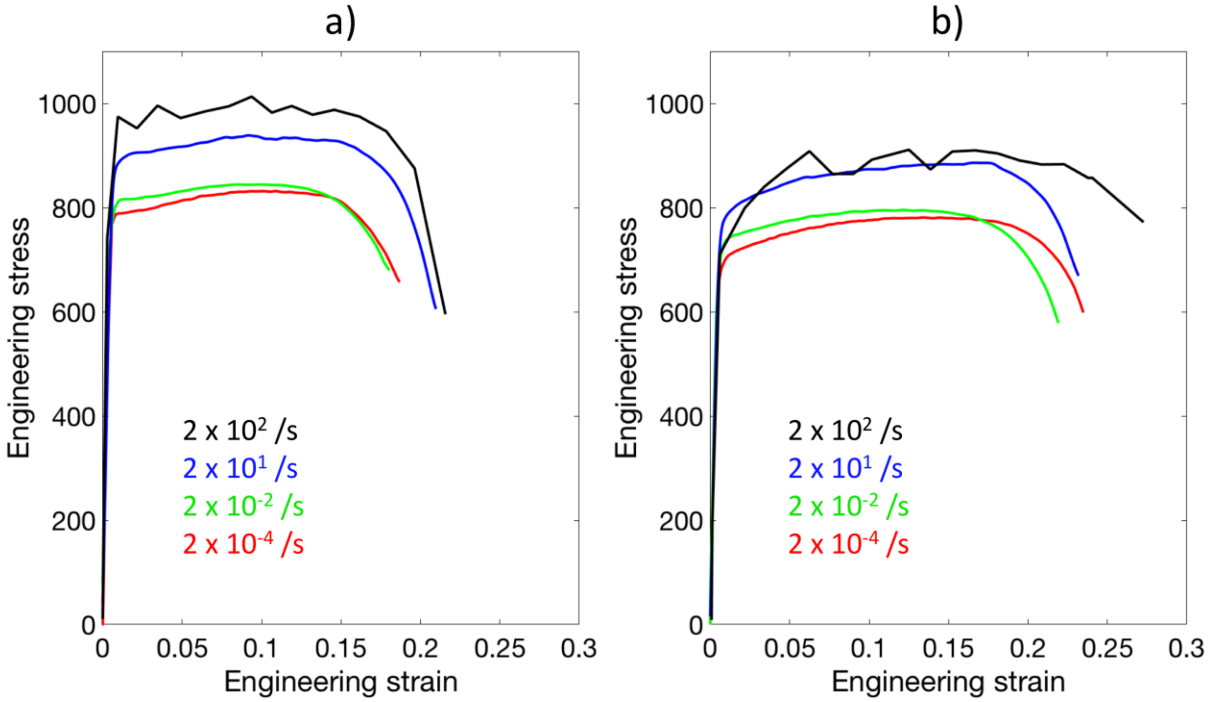

Figure 4-41: Representative engineering stress-strain curves of the Fe-12Mn-3Al-0.05C (wt%) alloy a) annealed for 0.5 h at 585°C and b) annealed for 8 h at 585 °C. Servo-hydraulic tensile tests were performed at strain rates from $\dot{\varepsilon} = 2x10^{-4}$ ε/s to $\dot{\varepsilon} = 2x10^{2}$ ε/s.

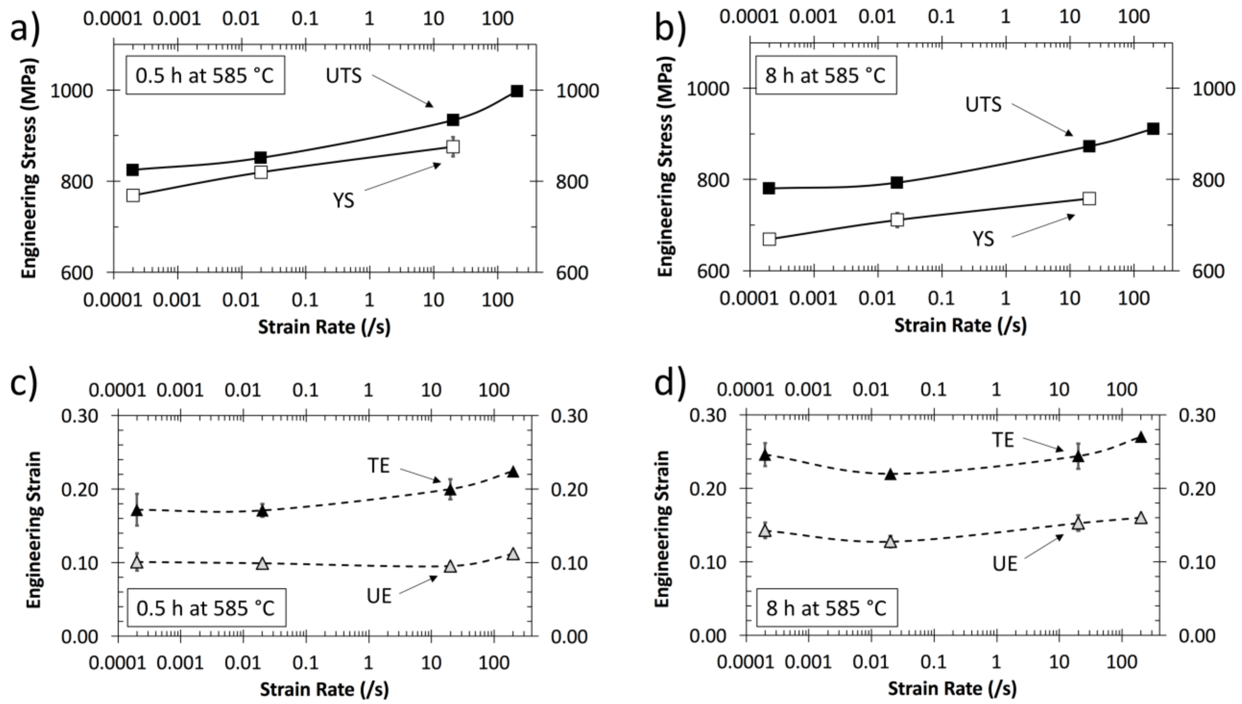

Figure 4-42: a) and b) ultimate tensile strength (UTS) and 0.2% offset yield strength (YS) values, plus c) and d) total elongation (TE) and uniform elongation (UE) values are shown as a function of strain rate for the Fe-12Mn-3Al-0.05C (wt%) steel annealed for a/c) 0.5 h at 585 °C and b/d) 8 h at 585 °C. Error bars are based on deviation between two tensile tests, which in some cases is smaller than the size of the data marker.

Mechanical properties from Kolsky-bar testing of the medium-Mn sheet steel were obtained for sub-sized samples, (machined from the same sheets as the servo-hydraulic tensile tests), that were deformed to failure using a 1 m striker bar and a pressure of 70 psi. As seen in Figure 4-43, samples from each annealing condition were deformed to failure at approximately the same strain rate ($\dot{\varepsilon}_{\text{true max}} = 1\text{x}10^3\ \varepsilon/\text{s}$) with respect to true strain. The true stress-strain curves are plotted up to the point of instability (maximum uniform strain). Figure 4-44 shows the true stress-strain curves of both heat treatments deformed to failure at the strain rates designated in Figure 4-43. The YS and UTS of the medium-Mn steel annealed for 0.5 h are greater than those specimens with the 8 h heat treatment, whereas the UE of specimens with the 8 h heat treatment are significantly greater than the UE of the 0.5 h heat treatment. The product of true ultimate tensile strength and true uniform strain for the 8 h heat treatment (16,000 MPa%) is approximately 60 % greater than the equivalent value for the 0.5 h heat treatment (10,000 MPa%), which is consistent with mechanical properties of full-sized tensile specimens measured by servo-hydraulic tension.

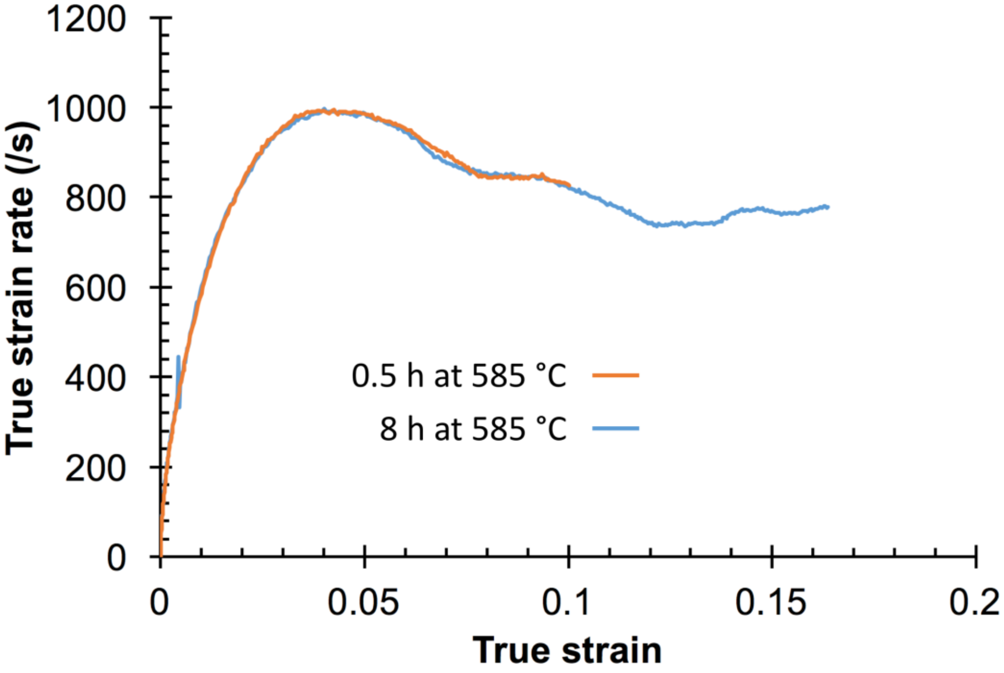

Figure 4-43: True strain rate measured during pull-to-failure Kolsky-bar testing of the Fe-12Mn-3Al-0.05C (wt%) sheet steel.

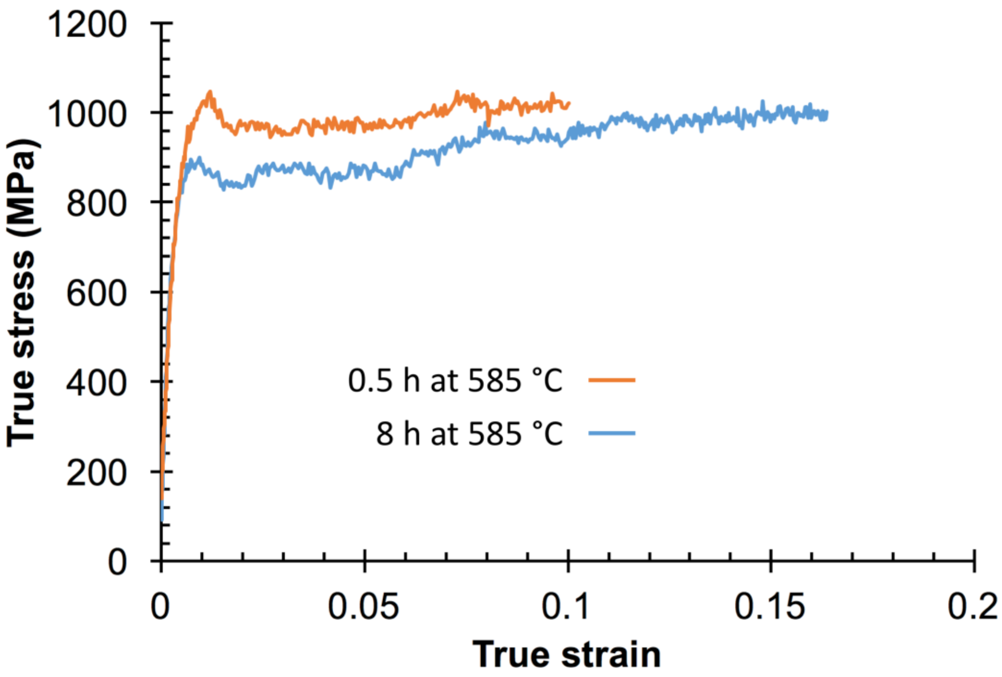

Figure 4-44: True stress-strain curves measured for sub-sized samples pulled-to-failure with Kolsky-bar testing at the same strain rate.

4.4.2 Non-Contact Measurements of Strain and Temperature

Digital image correlation (DIC) was used to measure strain during all servo-hydraulic and Kolsky-bar tensile tests using methods described previously in section 3.2.3. The use of non-contact methods with sufficient data acquisition rates is not only recommended [184], but also allows for in-situ measurements of strain localizations during tensile testing. Figure 4-45 shows an engineering stress-strain curve of the Fe-12Mn-3Al-0.05C (wt%) alloy annealed for 0.5 h and deformed at $\dot{\varepsilon} = 2\text{x}10^{-2}$ ε/s. DIC results show that strain remains relatively uniform (as represented by of a constant color) throughout the parallel length of the gauge section of the tensile sample, up until the point of necking. Figure 4-46 provides a similarly annotated stress-strain curve of the medium-Mn steel annealed for 8 h at 585 °C and deformed at $\dot{\varepsilon} = 2\text{x}10^{-2}$ ε/s. The DIC images in Figure 4-46 use the same engineering strain scale bar as in Figure 4-45. In a simple comparison of the mechanical properties, the longer heat treatment (8 h vs 0.5 h) produces larger amounts of uniform and total elongation with the trade-off of a moderate decrease in yield and ultimate tensile strengths. The increase in uniform elongation is clear when comparing images at approximately 0.16 engineering strain. In Figure 4-45, at 0.16 engineering strain, the part of the gauge section that has accommodated 0.16 engineering strain (the color green) is only just over half the length of the region seen in Figure 4-46. Finally, right before fracture in Figure 4-46, the region of necking has comparatively accommodated more total engineering strain (red – 0.25 eyy) as compared to the necked region in Figure 4-45 (orange – 0.2 eyy). Ductile failure by micro-void coalescence was observed on fracture surfaces of samples deformed from $\dot{\varepsilon} = 2x10^{-4}$ ε/s to $\dot{\varepsilon} = 2x10^{1}$ ε/s. The comparison of engineering stress-strain curves deformed at $\dot{\varepsilon} = 2x10^{-2}$ ε/s was chosen since adiabatic heating likely occurs at that strain rate and corresponding thermal images of the same tests are compared.

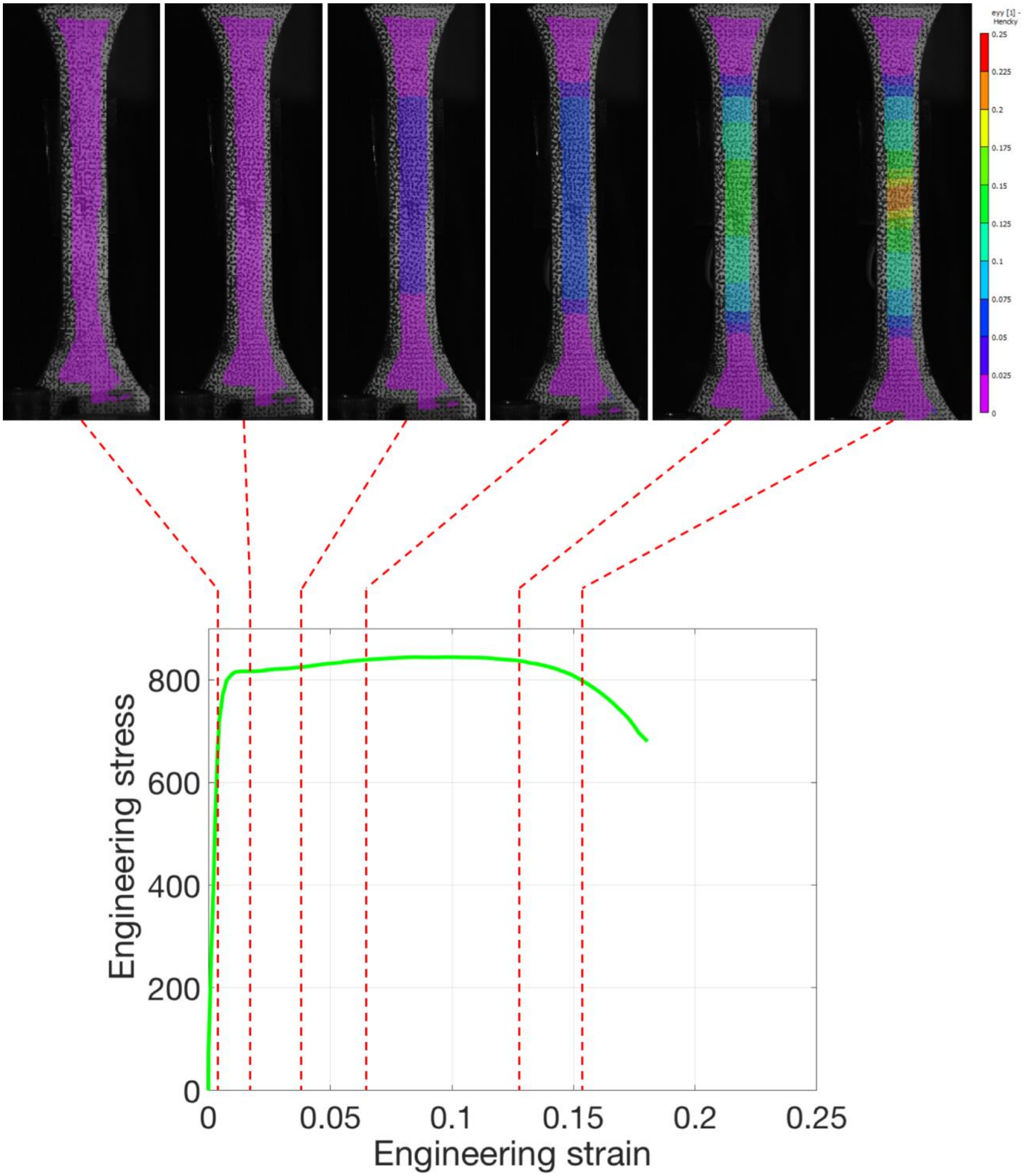

Figure 4-45: Engineering stress-strain curve annotated with optical images and an overlay of digital image correlation used to measure virtual engineering strain with respect to the tensile direction (e_{yy}), where red is 0.25 strain. The sample was annealed for 0.5 h at 585 °C and deformed at $\dot{\varepsilon} = 2\text{x}10^{-2}$ ε/s.

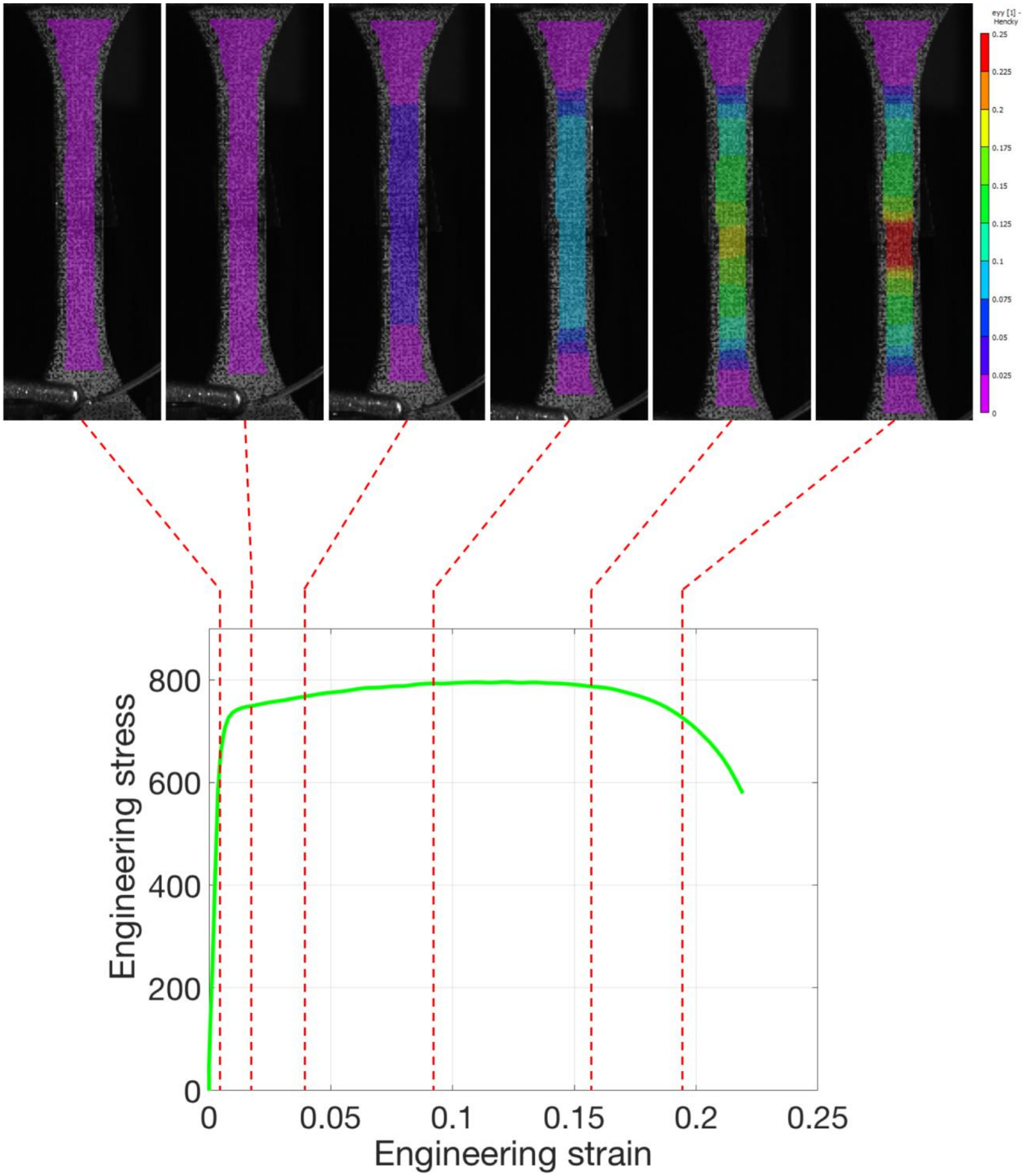

Figure 4-46: Engineering stress-strain curve annotated with optical images and an overlay of digital image correlation used to measure virtual engineering strain with respect to the tensile direction (e_{yy}), where red is 0.25 strain. The sample was annealed for 8 h at 585 °C and deformed at $\dot{\varepsilon} = 2x10^{-2}\ \varepsilon/s$.

To directly compare thermal imaging during tests performed at nominally the same strain rate of $\dot{\varepsilon} = 2x10^{-2}$ ε/s for different annealing condtions, thermal images of the sample annealed for 0.5 h (Figure 4-45) and the sample annealed for 8 h (Figure 4-46) are shown side-by-side in (Figure 4-47a and Figure 4-47b). Thermal images recorded at the same total engineering strain of 0.171 (Figure 4-47a and Figure 4-47b) show that the sample annealed for 0.5 h has already begun to neck and localized heat is generated in the center of the tensile sample, whereas the sample annealed for 8 h does not show signs of significant necking or strong localization of heat. Figure 4-47c and Figure 4-47d provide plots of the temperature profile along the centerline of the gauge section for various time steps, while Figure 4-47e and Figure 4-47f show the maximum, mean and minimum temperatures for various centerline profiles, plotted as a function of time. When comparing the same times (3.1 s and 5.4 s) the sample annealed for 0.5 h and deformed at $\dot{\varepsilon} = 2x10^{-2}$ ε/s is hotter than the sample annealed for 8 h and deformed at $\dot{\varepsilon} = 2x10^{-2}$ ε/s. At 5.4 s the average temperature along the centerline of the gauge length for the sample annealed for 0.5 h is 8 °C warmer than the sample annealed for 8 h and the difference in maximum temperature is greater than 20 °C indicating heat and strain localization (as shown in Figure 4-47e and Figure 4-47f). When comparing temperature profiles (see Figure 4-47c and Figure 4-47d) where the maximum temperature along the centerline of the gauge section is nominally the same (approximately 92 °C), the sample annealed for 0.5 h and deformed at $\dot{\varepsilon} = 2x10^{-2}$ ε/s had been deforming for 7.014 s, whereas the sample annealed for 8 h and deformed at $\dot{\varepsilon} = 2x10^{-2}$ ε/s had been deforming for 10.9 s. Just before fracture, the area of the necked region of the sample annealed for 8 h is much hotter (max temp of 129 °C in Figure 4-47b) than the necked region of the sample annealed for 0.5 h (max temp of 110 °C in Figure 4-47a) indicating that more strain has been accommodated in the neck of the 8 h samples, which is consistent with DIC results in Figure 4-46 and Figure 4-45.

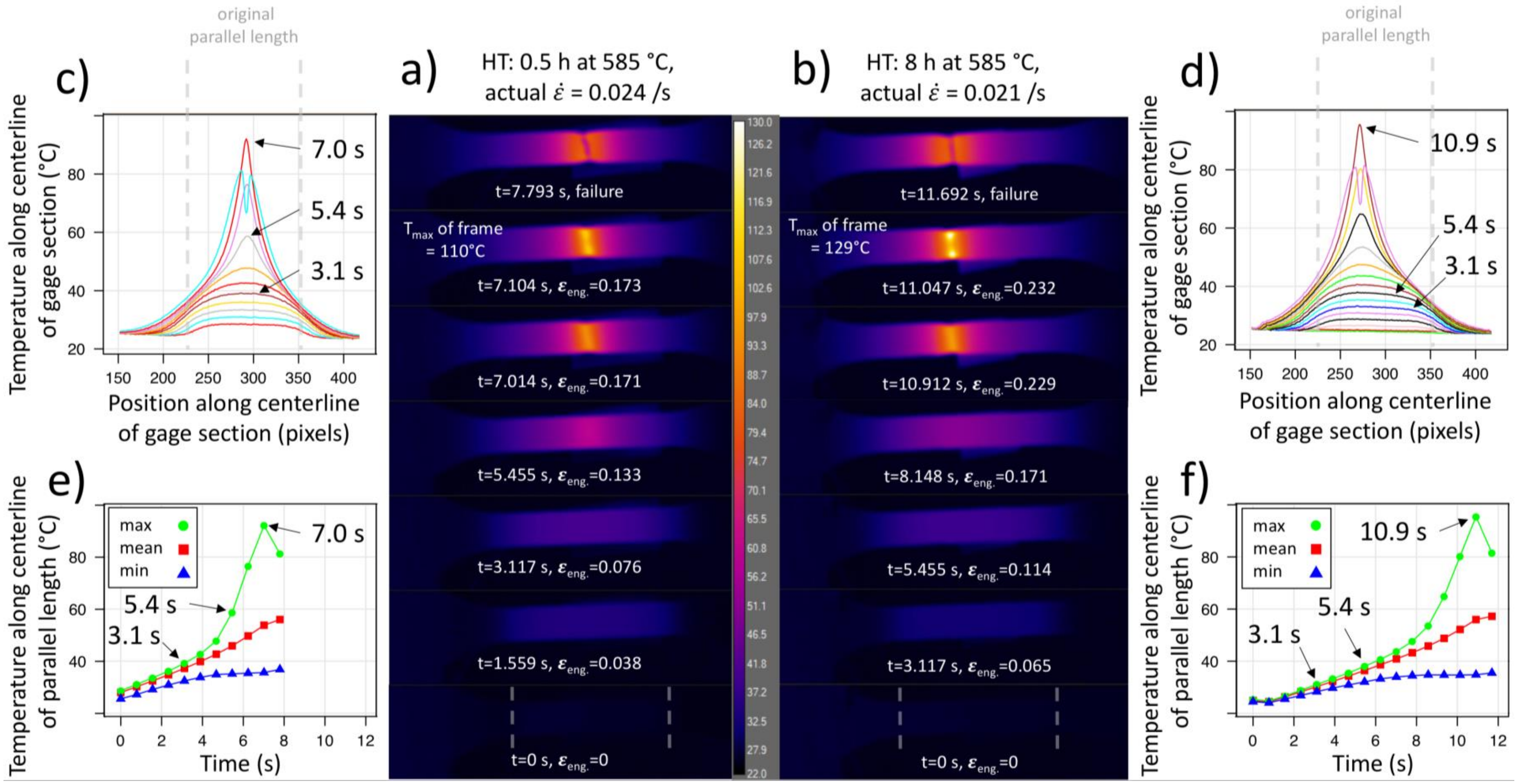
c)
original parallel length
Temperature along centerline of gage section (°C)
Position along centerline of gage section (pixels)
7.0 s
5.4 s
3.1 s
20
40
60
80
150
200
250
300
350
400
a)
HT: 0.5 h at 585 °C, actual $\dot{\varepsilon}$ = 0.024 /s
t=7.793 s, failure
T_{max} of frame = 110°C
t=7.104 s, $\varepsilon_{eng.}$=0.173
t=7.014 s, $\varepsilon_{eng.}$=0.171
t=5.455 s, $\varepsilon_{eng.}$=0.133
t=3.117 s, $\varepsilon_{eng.}$=0.076
t=1.559 s, $\varepsilon_{eng.}$=0.038
t=0 s, $\varepsilon_{eng.}$=0
130.0
126.2
121.6
116.9
112.3
107.6
102.6
97.9
93.3
88.7
84.0
79.4
74.7
70.1
65.5
60.8
56.2
51.1
46.5
41.8
37.2
32.5
27.9
22.0
b)
HT: 8 h at 585 °C, actual $\dot{\varepsilon}$ = 0.021 /s
t=11.692 s, failure
T_{max} of frame = 129°C
t=11.047 s, $\varepsilon_{eng.}$=0.232
t=10.912 s, $\varepsilon_{eng.}$=0.229
t=8.148 s, $\varepsilon_{eng.}$=0.171
t=5.455 s, $\varepsilon_{eng.}$=0.114
t=3.117 s, $\varepsilon_{eng.}$=0.065
t=0 s, $\varepsilon_{eng.}$=0
d)
original parallel length
Temperature along centerline of gage section (°C)
Position along centerline of gage section (pixels)
10.9 s
5.4 s
3.1 s
20
40
60
80
150
200
250
300
350
400
e)
Temperature along centerline of parallel length (°C)
Time (s)
max ●
mean ■
min ▲
7.0 s
5.4 s
3.1 s
40
60
80
0
2
4
6
8
10
12
f)
Temperature along centerline of parallel length (°C)
Time (s)
max ●
mean ■
min ▲
10.9 s
5.4 s
3.1 s
40
60
80
0
2
4
6
8
10
12

Figure 4-47: Thermal images captured during servo-hydraulic tensile tests at $\dot{\varepsilon} = 2x10^{-2}$ ε/s for the medium-Mn steel annealed for a/c/e) 0.5 h and b/d/f) 8 h at 585 °C. Non-contact temperature measurements using a line drawn across the center of the gauge section are shown as profile plots for various time steps in c) and d) with the original length of the parallel gauge section marked. The maximum, mean and minimum temperatures across the centerlines of the gauge section are plotted as functions of time in e) and f).

Temperatures in Figure 4-47c-f were measured along a line positioned in the center of the gauge section. ResearchIR^{TM} software was used to calculate the average surface temperature across the entire area of the reduced parallel length, excluding the necked region and fracture surface, for all mechanical tests. Representative temperature plots as a function of engineering strain for strain rates from $\dot{\varepsilon} = 2x10^{-4}$ ε/s to $\dot{\varepsilon} = 2x10^{1}$ ε/s are shown in Figure 4-48a for the medium-Mn steel annealed for 0.5 h and in Figure 4-48b for the medium-Mn steel annealed for 8 h. Results from strain rates of $\dot{\varepsilon} = 2x10^{2}$ ε/s were not included due to insufficient data acquisition rates of the thermal imaging. As expected, quasi-static strain rates ($\dot{\varepsilon} = 2x10^{-4}$ ε/s) showed no signs of tensile specimen heating. Consistent with Figure 4-47, the average temperature of samples deformed at $\dot{\varepsilon} = 2x10^{-2}$ ε/s was 6 °C greater for the sample annealed for 8 h (Figure 4-48b) as compared to the sample annealed for 0.5 h (Figure 4-48a). In the case of the $\dot{\varepsilon} = 2x10^{1}$ ε/s tests, the initial tensile-specimen temperature was higher because of the high intensity of the LED lights (necessary for illumination), which were turned on 30 s before each $\dot{\varepsilon} = 2x10^{1}$ ε/s test. Nevertheless, the final average temperature in the area of the reduced gauge length after deformation at $\dot{\varepsilon} = 2x10^{1}$ ε/s is only 3 °C greater for the specimen annealed for 8 h compared to the specimen annealed for 0.5 h and is directly proportional to the numerically-integrated areas under the engineering stress-strain curves (19,400 MPa% vs. 18,500 MPa%). Numerically-integrated areas under engineering stress-strain curves are directly proportional to PSE values, but should not be interchanged as PSE values are simply the product of two values

(UTS and TE). Based on previous thermodynamic calculations outlined in section 4.2, an increase in temperature from 22 to 46 °C should not significantly raise the SFE of the austenite.

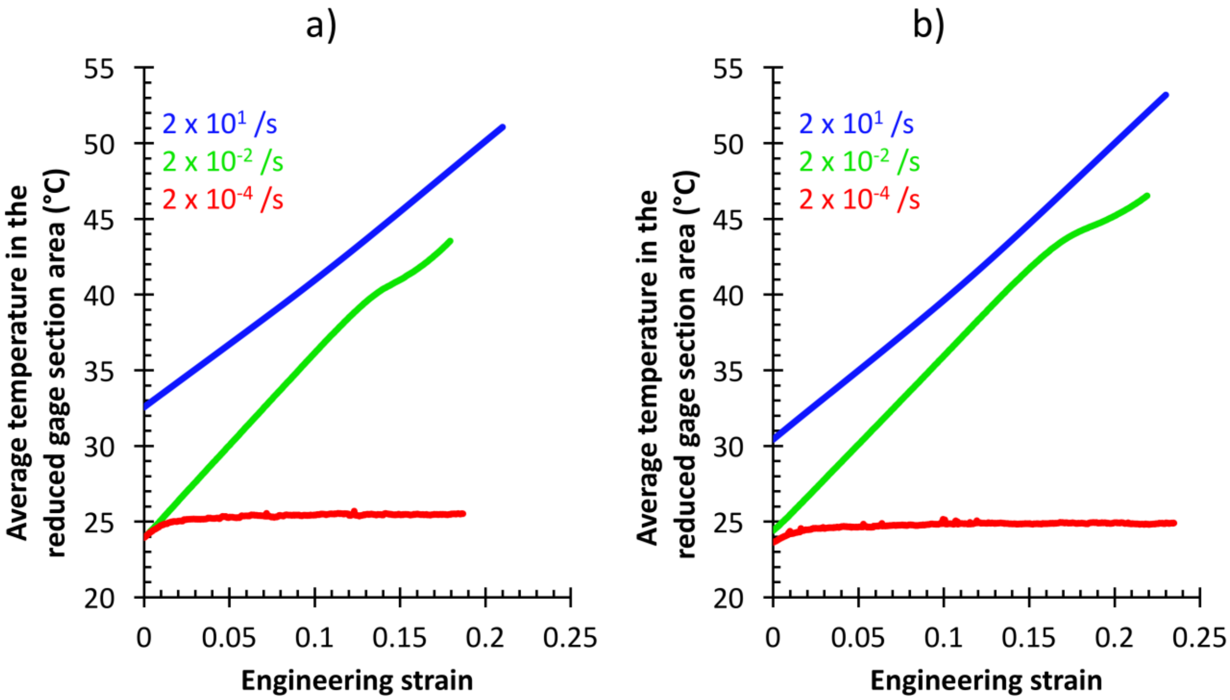

Figure 4-48: Average surface temperatures of areas in the reduced section of the parallel gauge length measured at various strain rates for Fe-12Mn-3Al-0.05C (wt%) steel specimens annealed for a) 0.5 h at 585 °C and b) 8 h at 585 °C.

4.4.3 Deformation Mechanisms

A key characteristic of medium-Mn steels is the UFG microstructure that is produced during intercritical annealing, after hot and/or cold-working. Through a Hall-Petch relationship, the ultrafine grain size is one of the main contributors to the high YS and UTS values. Figure 4-49 shows BF-TEM images of some of the ultrafine grains (approximately 500 nm or less in diameter) recorded from an electropolished sample of the steel annealed for 0.5 h and deformed to failure at quasi-static strain rates. Coarse-grained recovered martensite, UFG ferrite and UFG austenite, (estimated to be only 3% volume fraction for this heat treatment), accommodate the strain in this multi-phase medium-Mn steel. Seen in Figure 4-49c and Figure 4-49d, austenite grains of approximately 300 to 500 nm in size show planar defects, consistent with the predicted SFE value and measured compositions as presented in section 4.3. Furthermore, the medium-Mn steel annealed for 8 h contains nearly a 35 % volume fraction of austenite and has more equilibrated compositions. Figure 4-50b shows BF-TEM images of a samples annealed for 8 h and deformed to 0.08 engineering strain (interrupted at quasi-static strain rates) where strain-induced planar defects are visible. Figure 4-50a provides evidence that UFG ferrite grains also have begun to deform.

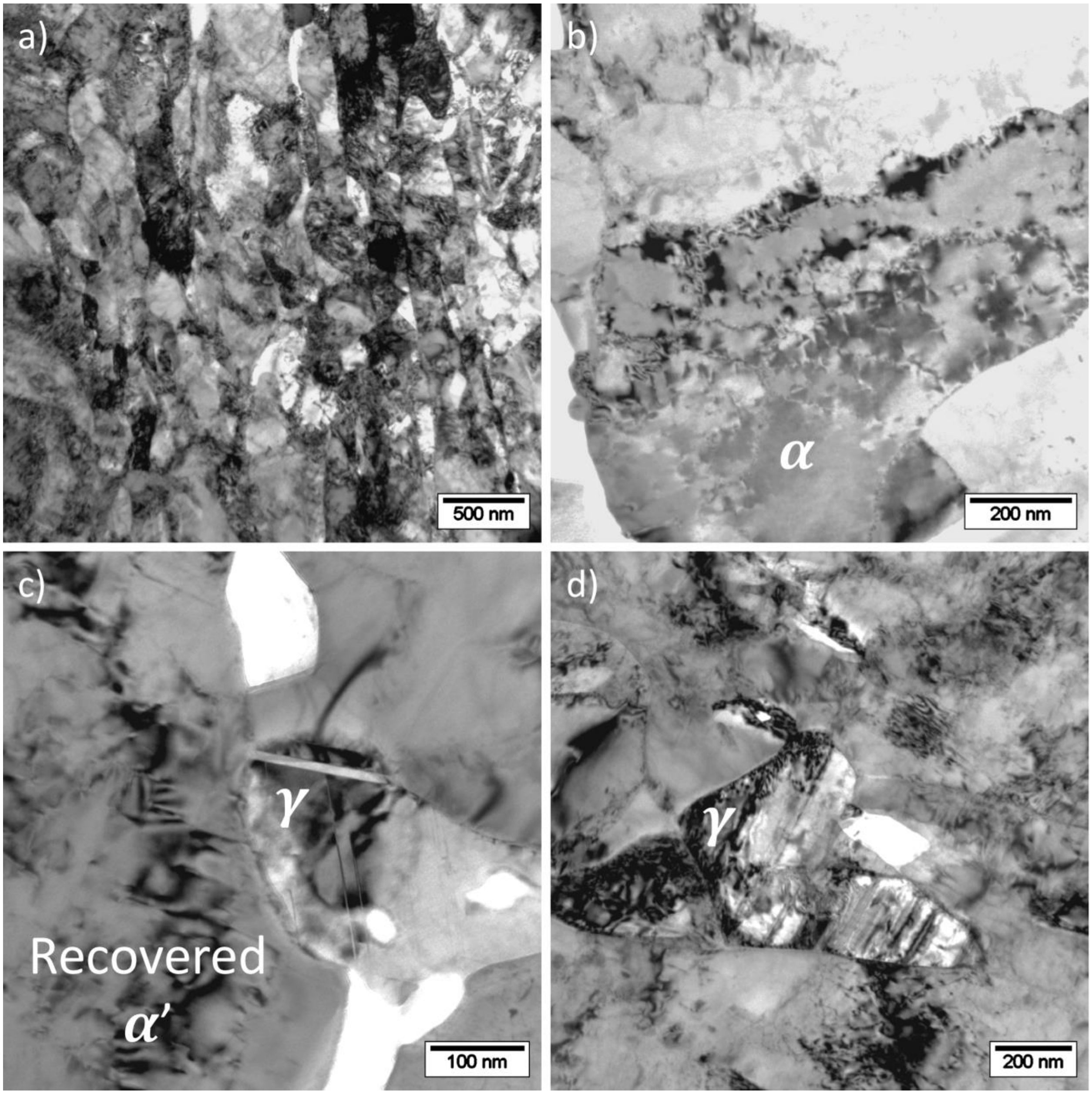

Figure 4-49: BF-TEM images of a sample annealed for 0.5 h and pulled to failure at $\dot{\varepsilon} = 2x10^{-4}$ ε/s: a) image of the deformed microstructure in an areas consisting of some ultrafine grains, b) and UFG ferrite grains with evidence of dislocation tangles, c/d) coarse-grained recovered martensite and UFG austenite with evidence of planar defect formation. The horizontal planar defect in the UFG austenite grain in part c) is probably an annealing twin whereas the vertical planar defects are strain-induced.

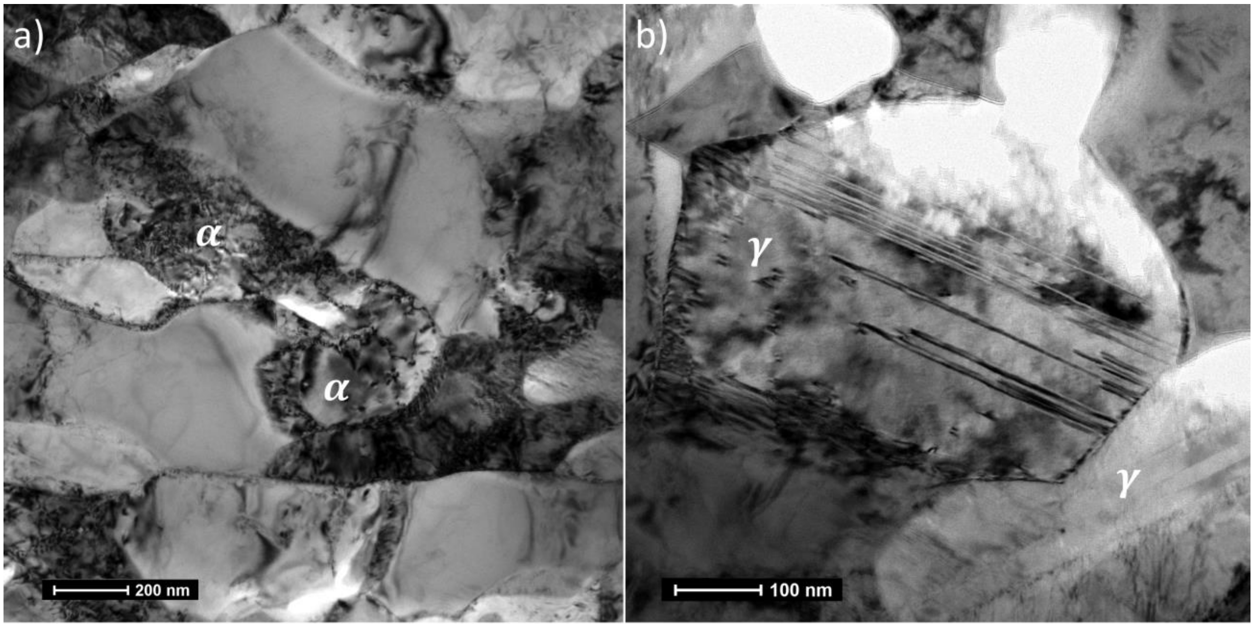

Figure 4-50: BF-TEM images of a sample annealed for 8 h and interrupted at $\varepsilon_{eng.} = 0.08$ (tested at $\dot{\varepsilon} = 2x10^{-4}$ /s). a) UFG ferrite grains shows signs of deformation with dislocation tangles and b) UFG austenite grains have already begun to develop planar defects (stacking faults and possibly mechanical twins).

The XRD measurement of the as-received material (bottom of Figure 4-51a), which indicates a textured martensitic microstructure with a minor constituent of austenite, is consistent with results in Figure 4-27 and has already been discussed, the martensite and ferrite present after annealing for 48 h is still textured. Austenite peaks do not indicate much texture, with the exception of the (311) peak intensities as typically the (220) and then (222) peaks have the lowest intensity, indicating that the austenite reversion depends on the textured parent microstructure (usually characterized as a K-S orientation relationship). After deformation to failure at quasi-static strain rates, XRD shows an increase in intensity of the (200), (211) and (220) alpha-Fe peaks, plus a relative decrease in (111) peak intensity of gamma-Fe, (see top of Figure 4-51a). However, a significant amount of gamma-Fe (austenite) is still present after deformation to failure. Such results may indicate that dislocation glide and/or TWIP processes are dominant mechanisms in the austenite as opposed to a TRIP effect to ε- and/or α'-

martensite. The Olson-Cohen model is typically the prime model for understanding the transformation rate of retained austenite in conventional TRIP steels, where the SFE is usually below 10 mJ/m^2 meaning ε- and α'-martensite transformations are readily activated. Further, XRD measurements do not reveal the presence of ε-martensite peaks, but perhaps this is not unexpected because of the small volume fractions and peak broadening from the very thin ε-martensite platelets observed by TEM. EBSD results of the as-received and deformed microstructures indicate that the austenite volume fraction decreases from 35 to 18 % after deformation to failure at quasi-static strain rates and also reveals a small volume fraction of ε-martensite (4%) within the austenite grains. A comparison of the kernel average misorientation maps (synonymous with quantitative strain) between as-received and pulled-to-failure microstructures (see Figure 4-51b) shows a significant increase of local misorientation within the microstructure for all phases present, which is expected for a microstructure deformed to failure. Dark-field TEM results in Figure 4-52 confirm the presence of mechanical twins and hexagonal ε-martensite in the ultrafine austenite grains, which is consistent with SFE predictions. Figure 4-53 also reveals that mechanical twins can still develop in the ultrafine-grained austenite during deformation at high strain rates. In comparison to KAM maps in Figure 4-51b, DF-TEM results in Figure 4-52 and Figure 4-53 demonstrate that the recovered martensitic matrix and ultrafine ferrite also accommodate large amounts of the deformation as indicated by the numerous dislocation tangles.

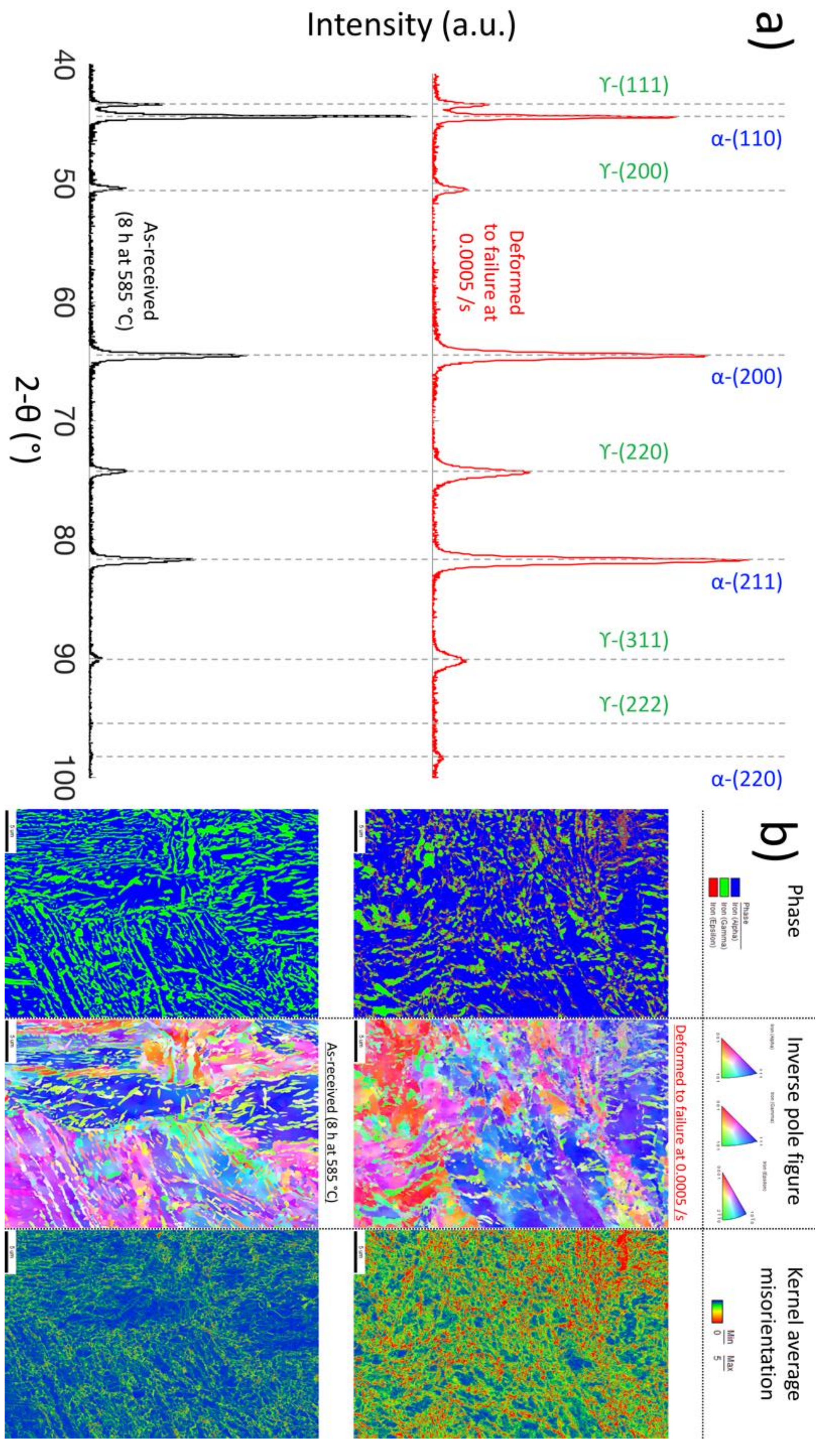
a)
Intensity (a.u.)
2-θ (°)
40
50
60
70
80
90
100
Υ-(111)
α-(110)
Υ-(200)
α-(200)
Υ-(220)
α-(211)
Υ-(311)
Υ-(222)
α-(220)
Deformed to failure at 0.0005 /s
As-received (8 h at 585 °C)
b)
Phase
Phase
Iron (Alpha)
Iron (Gamma)
Iron (Epsilon)
Inverse pole figure
Iron (Alpha)
Iron (Gamma)
Iron (Epsilon)
Kernel average misorientation
Min Max
0 5
Deformed to failure at 0.0005 /s
As-received (8 h at 585 °C)
5 µm

Figure 4-51: a) XRD and b) EBSD comparison of as-received specimen and specimen deformed to failure at quasi-static strain rates

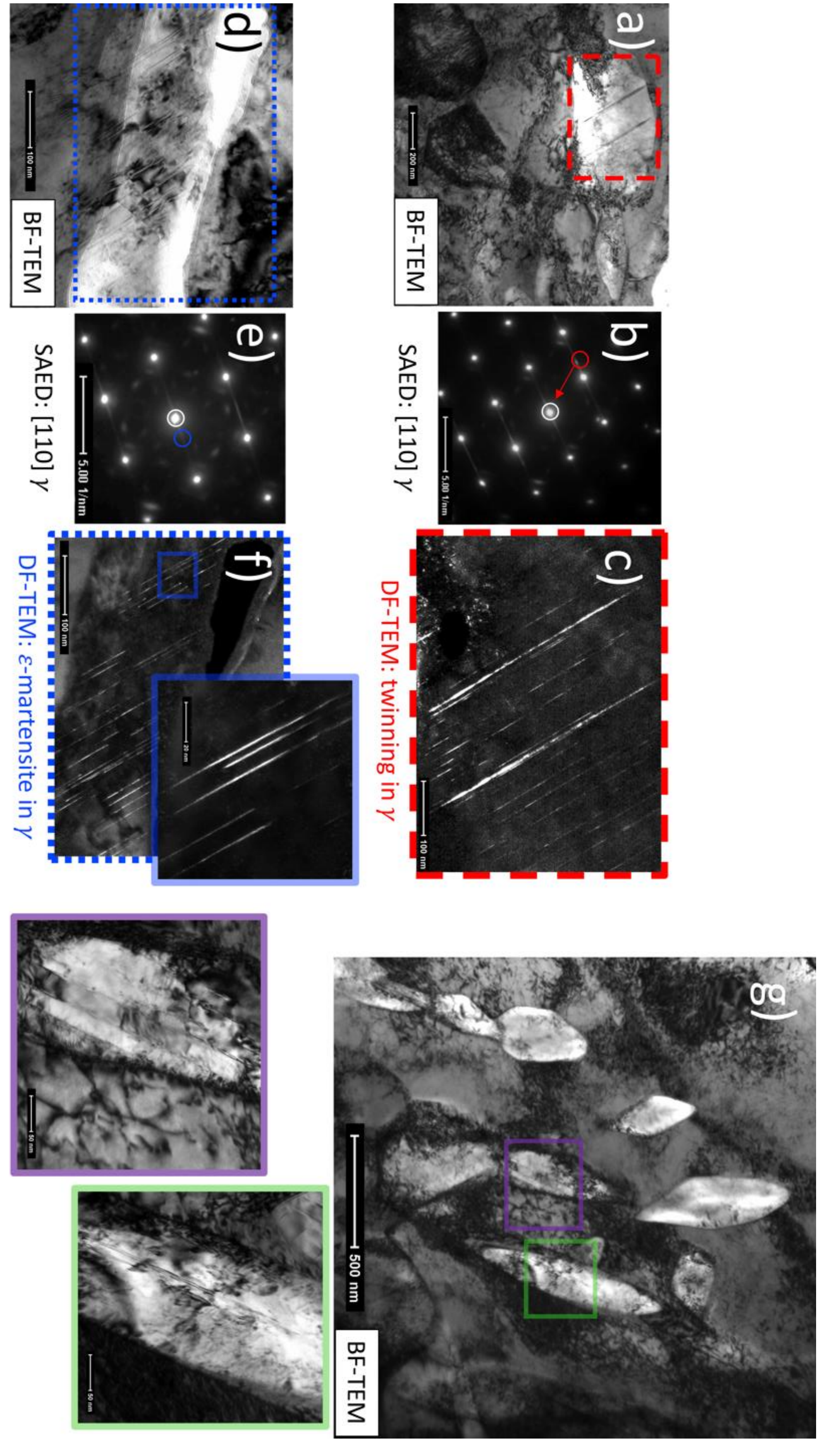
a)
BF-TEM
200 nm
b)
SAED: [110] γ
5.00 1/nm
c)
DF-TEM: twinning in γ
100 nm
d)
BF-TEM
100 nm
e)
SAED: [110] γ
5.00 1/nm
f)
DF-TEM: ε-martensite in γ
100 nm
20 nm
g)
BF-TEM
500 nm
50 nm
50 nm

Figure 4-52: a/d/g) Bright field and c/f) dark field TEM images of planar defects visible in specimens deformed to failure at quasi-static rates. b/e) Selected area electron diffraction results indicate two types of planar defects present in the ultrafine-grained austenite: mechanical twinning and hexagonal epsilon martensite.

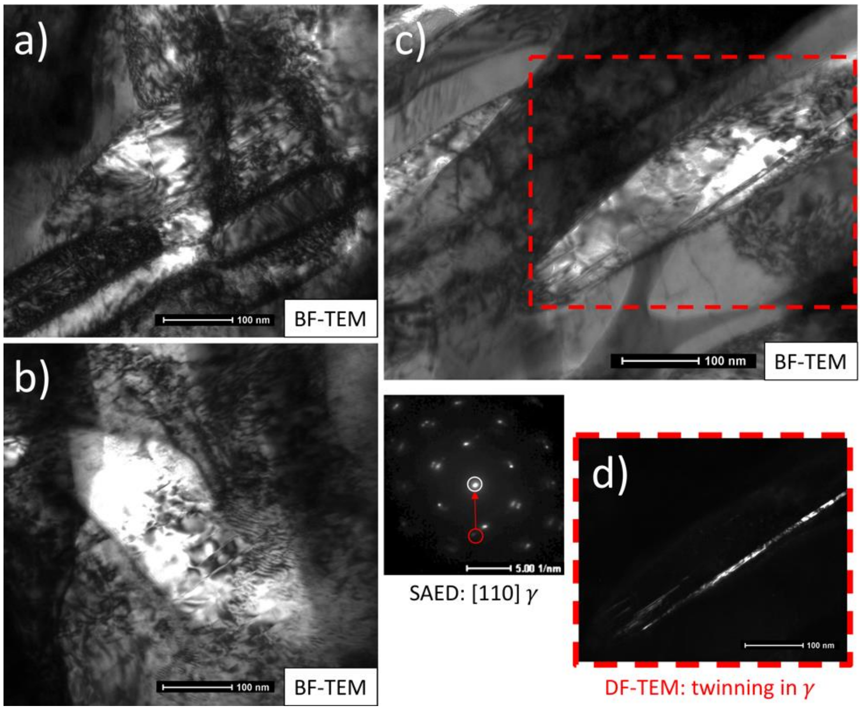

Figure 4-53: Bright-field and dark-field TEM results of specimens deformed to failure at 2x10^1 /s indicate mechanical twinning is still observed in ultrafine austenite grains.

Tensile properties show a positive strain-rate sensitivity of the yield- and ultimate tensile strengths, which is a strong indication that thermally-activated and time-dependent short-range barriers dominate the flow stress [149][136][150]. For BCC metals, the primary short range dislocation barrier is the frictional-based Peierls Nabarro stress, whereas dislocation forests and solute atoms are dominating short-range barriers in FCC metals and are predominantly thermally-activated [148][19]. Notably, when only crystal structure is considered, the Peirels barrier (in energy per unit length [206]) is more difficult to overcome in the BCC lattice as compared to short-range barriers in the FCC lattice [149], which indicates that the predominant strain-rate sensitivity effect on flow stress in this multi-phase medium-Mn steel is related to the ferritic and martensitic microstructural constituents. However, previous high strain-rate work [207] on a high-Mn TWIP-TRIP austenitic steel with nominally the same austenitic stacking fault energy as the steel in the present work (21 mJ/m^2) showed a large strain-rate sensitivity of the yield strength, which was attributed to thermally-activated short-range dislocation barriers, rather than a change in TWIP or TRIP mechanisms.

The partitioning of Mn and C from α'/α to form γ and partitioning of Al from γ to α during intercritical annealing in the $\gamma + \alpha$ phase field controls the amount, size and stacking fault energy of the reverted γ. Specifically, recent work [54][131] has shown that an increase of the intercritical annealing temperature decreases the Mn content in austenite and also decreases the SFE of the austenite. The SFE is important for controlling TWIP and TRIP effects in the γ phase during deformation [39][132][55][133][56][134]. Studies investigating deformation mechanisms and mechanical properties of medium-Mn steels have reported the effects of intercritical annealing temperature and phase fractions/sizes [36][39]. Other researchers of medium-Mn steels and TWIP steels have observed static and dynamic strain-aging effects, (respectively termed Lüders bands and PLC bands), which can lead to plastic instabilities during deformation. These static and dynamic strain-aging effects, which are influenced by microstructure, composition, dislocation mobility, temperature and strain rate [40][41][42][43][44][45][46], are not observed in this work. The absence of Lüders bands is attributed to a low volume fraction of UFG ferrite and the absence of DSA/PLC bands is attributed to the low carbon content of the austenite and to the morphology of most of the UFG austenite grains which vary among plate-like, rod-like and strings of equiaxed grains. As this work contains various morphologies of ultrafine-grained constitutents, it is important to note that Davut et al. provided experimental and computational evidence to support the observations of higher stresses developing in more elongated grains that transform earlier [47]. Stout *et al.* [208] wer able to correlate transformation kinetics using the von Mises effective strain criterion for strain-induced TRIP in 304 stainless steels. Crystal plasticity modeling is used in the next section to decipher the complicated mechanical behavior of this multi-phase medium-Mn TWIP-TRIP steel.

4.4.4 Constitutive Modeling of Strain Hardening Behavior in a Multi-Phase Medium-Mn Steel

Based on the experimentally-determined results of the medium-Mn steel annealed for 8 h, a two-level finite-element model was developed to further understand and quantify the plasticity mechanisms involved during deformation. Specifically, the model allows for a better understanding of the individual contributions to plasticity for a given microstructural constituent and provides the ability to tune microstructural parameters to predict structure-property relationships beyond the experimental regime. The first level of the model focuses on macro-scale tensile properties using the Taylor algorithm [209], which does not consider grain morphology or grain interactions, but rather focuses on size-dependent slip resistance. Anisotropic elastic properties used in this work are found in Table 4-5 and based on the literature database, while relative orientations of the as-received microstructure are based on EBSD measurements. Crystal plasticity has been proven to be an effective way to model the microstructure-based mechanical behavior of metals. In this work, the dislocation density based crystal plasticity model is implemented in an FE-based strain framework. Twinning, as well as phase transformation, is incorporated into the model and allows for tuning of physical parameters to capture the plastic behavior of the TWIP-TRIP steel. The constitutive formula are presented in numerical order, based on the sequence of hierarchy in the general crystal plasticity model.

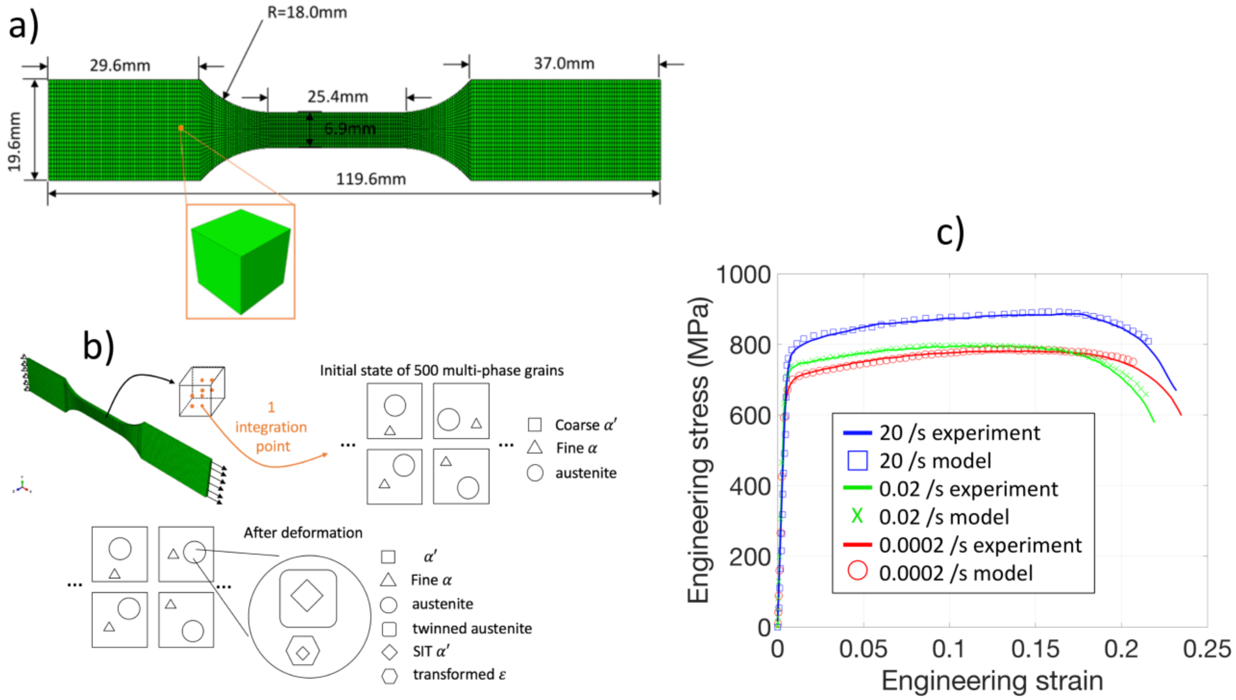

Figure 4-54: a) Taylor-based finite element model of the tensile sample used in this work with the b) boundary conditions applied and the generalized plasticity model explained for each finite element, integration point and multi-phase grain where SIT indicates a strain-induced transformation. The c) resulting tensile properties are compared to the experimental results (strain rates from $\dot{\varepsilon} = 2x10^{-4}$ /s to $\dot{\varepsilon} = 2x10^{1}$ /s).

The Taylor model, in this case considers the macro-scale contributions of 10,000 finite elements, which are arranged to create a 3D model of the tensile drawing (including thickness) from Figure 3-6. The final 10,000 finite-element model is shown in see Figure 4-54a. Each finite element includes 8 integration points and each integration point consists of 500 multi-phase grains. In the case of the model, a multi-phase grain is simply a coarse tempered martensite grain that contains an ultrafine austenite grain and an ultrafine ferrite grain (see Figure 4-54b). Each of the phases within the multi-phase grain contain one orientation and one grain size. Since there are 500 multi-phase grains per integration point, the orientations, grain sizes and phase fractions are assigned to match the respective statistical distributions acquired from the

EBSD data. In the undeformed microstructure, where k is used to count each multi-phase grain, each multi-phase grain begins with the same initial fraction of ultrafine austenite (0.35), fine ferrite (0.10) and coarse tempered martensite (0.55), where the fraction of each multi-phase grain is set equal to one as shown in equation 4-1. As deformation takes place, the initial austenite can be decomposed into twins, epsilon martensite, a strain-induced transformation to martensite and the remaining austenite that has only deformed by slip, as shown in equation 4-2. Substituting equation 4-2 into 4-1 yields equation 4-3, meaning that the initial ferrite and martensite does not transform (the volume fraction does not change and only deforms by slip) whereas the austenite can both slip and transform. In order to obtain physically meaningful material parameters, the volume fraction constraints are applied at the beginning of each time increment.

$$f_{ini}^{A(k)} + f_{ini,c}^{\alpha'(k)} + f_{ini,f}^{\alpha\,(\mathrm{k})} = 1 \qquad \text{(equation 4-1)}$$

$$f_{ini}^{A(k)} = f^{A\,(k)} + f^{\varepsilon\,(k)} + f^{tw\,(k)} + f_{sit}^{\alpha'(k)} = \text{constant} \qquad \text{(equation 4-2)}$$

$$f^{A\,(k)} + f^{\varepsilon\,(k)} + f^{tw\,(k)} + f_{sit}^{\alpha'(k)} + f_{ini,c}^{\alpha'(k)} + f_{ini,f}^{\alpha\,(\mathrm{k})} = 1 \qquad \text{(equation 4-3)}$$

Previous in-situ work on this medium-Mn steel has shown that cold-rolled and annealed specimens have begun to transform around 8% engineering strain (failure occurs at 25 % engineering strain) and TEM analysis in the present work shows mechanical twins are observed as early as 8% engineering strain (s=0.08). EBSD results in the present work show that the initial austenite fraction of 0.35 is reduced to 0.18 in a tensile specimen deformed to failure at engineering strain of 25% (s=0.25). This evolution of the volume fraction of austenite (transformation rate) is calibrated from FE results and when the sum of all k-th multi-phase grains reaches an austenite fraction of 0.18, the transformation is halted. This means that some austenite grains will completely transform, while others will not. The initial fraction is 0.35 and the final fraction is 0.18 (determined by volume θ and fraction f^A. The experimental controls introduced in this constitutive model are schematically described in equation 4-4.

$$f^A = \begin{cases} f^A_{ini} = 35.2\% & s = 0.08 \\ f^A_{ini} - f^{\varepsilon} - f^{tw} - f^{\alpha'}_{sit} & s \in (0.08, 0.25) \\ f^A_{min} = 18.2\% & s = 0.25 \end{cases} \qquad f^A \sum\nolimits_k f^{A(k)} \cdot \frac{|\theta^k|}{\theta} \qquad \text{(equation 4-4)}$$

The volume-averaged stress in a given integration point and thus in the k-th multi-phase grain is described by equation 4-10.

$$\bar{\sigma} = \frac{1}{N} \sum_{k=1}^{N} \sigma^{(k)} \cdot \frac{|\theta^k|}{\theta} \quad \text{such that:}$$

$$\sigma^{(k)} = \left(f^{A(k)} + f^{tw(k)}\right)\sigma^{A(k)} + \left(f^{\varepsilon(k)}\right)\sigma^{\varepsilon(k)} + \left(f^{\alpha(k)}_{ini,f}\right)\sigma^{\alpha(k)} + \left(f^{\alpha'(k)}_{sit} + f^{\alpha'(k)}_{ini,c}\right)\sigma^{\alpha'(k)}$$

(equation 4-5)

From here on (equations 4-6 through 4-31), the plasticity enhancing mechanisms in each a given k-th multi-phase grain are provided and therefore the (k) counter and volume average will not be listed in each proceeding equation for clarity, but all counters and volume fractions are included in the crystal plasticity simulation. When considering the plasticity enhancing mechanisms, work by Bouaziz et al. [210] described the kinetics of twinning by a phenomenological law in equation 4-6, where $\alpha_{tw} = 3$ and m=2 are dimensionless parameters extrapolated from the literature, f^{tw}_{max}=0.2 is the saturation fraction of twinning and γ_{tot} is the total shear strain. When the total shear strain is greater than a critical value γ_c that linearly depends on grain size, a twin is formed (f^{tw} increases). Twin fraction increases with strain (after a given strain value) even though the local fraction can decrease near a twin-twin intersection that creates α' martensite, which is consistent with work by others [141][55][54].

$$\mathrm{f}^{\mathrm{tw}} = \mathrm{f}^{\mathrm{A}}\mathrm{f}^{\mathrm{tw}}_{\mathrm{max}}(1 - \exp(-\alpha^{\mathrm{tw}}(\gamma_{\mathrm{tot}} - \gamma^{\mathrm{c}}_{\mathrm{tot}})))^{\mathrm{m}} \qquad \text{(equation 4-6)}$$

As described in Chapter 2.2, there is debate in the literature as to what exact mechanism controls mechanical twinning and the formation of epsilon martensite. The assumption used in this constitutive model is that the mechanisms share a relationship through the movement of partial dislocations. Therefore, the kinetics of epsilon martensite generation are described by a similar phenomenological law as compared to the twinning mechanism and shown in equation 4-7.

$$\mathrm{f}^{\varepsilon} = \mathrm{f}^{\mathrm{A}}\mathrm{f}^{\varepsilon}_{\mathrm{max}}(1 - \exp(-\alpha^{\varepsilon}(\gamma_{\mathrm{tot}} - \gamma^{\mathrm{c}}_{\mathrm{tot}})))^{\widehat{m}} \qquad \text{(equation 4-7)}$$

For transformation kinetics from austenite to α' martensite through twinning intersections, the general Olson-Cohen model [98] is employed, where $f^{\alpha'}_{sit,tw}$ is the volume fraction of strain-induced martensite from twin intersections, but similar to the work by Lee and De Cooman [54] (see equation 4-8), the f^{A} term is included because the austenite in this material does not completely transform. The martensite evolution in this equation is considered solely dependent on the twinning activity rather than shear-banding [98]. $\beta^{\alpha'}$ is a parameter related to the probability that twin intersections nucleate martensite and the exponent n is a fixed term that relates to the number of intersections in the austenite based on the morphology and orientation distribution of the austenite [19].

$$f^{\alpha'}_{sit,tw} = \mathrm{f}^{\mathrm{A}}(1 - \exp(-\beta^{\alpha'}\mathrm{f}^{\mathrm{tw}}))^{\mathrm{n}} \qquad \text{(equation 4-8)}$$

However, for lower SFE materials, the strain-induced α' martensite is usually dependent on the volume fraction of ε-martensite. The Olson-Cohen model could be employed for epsilon-epsilon intersections, but another driving force is considered in this case. For phase transformation from austenite to ε-martensite [211], equation 4-9 is considered, where p^{c} stands for the critical value of the transformation driving force. A $\dot{\mathrm{f}}^{\mathrm{t}}_{\mathrm{max}}$ is the maximum transformation rate, υ is the viscosity-like parameter and p^{t} is the athermal transformation driving force (transformation shear stress) as defined in equation 4-10. λ_T is the latent heat, Θ_T is the transformation temperature, ρ_0 is mass density and $b^t \cdot m^t$ is the phase transformation system.

$$\dot{\mathrm{f}}^{\mathrm{t}} = \begin{cases} \dot{\mathrm{f}}^{\mathrm{t}}_{\mathrm{max}} \tanh\left(\frac{1}{\upsilon} \cdot \frac{\mathrm{p}^{\mathrm{t}}-\mathrm{p}^{\mathrm{c}}}{\mathrm{p}^{\mathrm{c}}}\right) & \text{if } \mathrm{p}^{\mathrm{t}} > \mathrm{p}^{\mathrm{c}} \\ 0 & \text{otherwise} \end{cases} \qquad f^{\alpha'}_{sit,\varepsilon} \sum_{t=1}^{N_{tr}} f^t \qquad \text{(equation 4-9)}$$

$$\mathrm{p}^{\mathrm{t}} = b^t \cdot (\mathbf{F}^{\mathrm{e}} \cdot \boldsymbol{\sigma} \cdot \mathbf{F}^{\mathrm{e}} \cdot \boldsymbol{\sigma}) \cdot m^t - \rho_0 \frac{\lambda_T}{\Theta_T} (\Theta - \Theta_T) \qquad \text{(equation 4-10)}$$

The total deformation gradient (F) can be decomposed into three components including elastic, plastic and transformation gradients for each integration point in the computational field (see equation 4-12). Ferrite and martensite do not include a transformation gradient, but austenite does (see equation 4-13).

$$\mathbf{F} = \mathbf{F}^{\mathrm{e}}\mathbf{F}^{\mathrm{p}}\mathbf{F}^{\mathrm{tr}} \qquad \text{(equation 4-12)}$$

$$\mathbf{F}^{\mathrm{tr}} = \mathbf{I} + \sum_{\mathrm{t}=1}^{\mathrm{N_{trans}}} \mathrm{f}^{\mathrm{t}} \mathbf{b}^{\mathrm{t}}_{\mathrm{trans}} \otimes \mathbf{m}^{\mathrm{t}}_{\mathrm{trans}} = \mathbf{I} + \sum_{\mathrm{t}=1}^{\mathrm{N_{trans}}} \mathrm{f}^{\mathrm{t}} \mathbf{P}^{\mathrm{t}}_{\mathrm{trans}} \qquad \text{(equation 4-13)}$$

Here in equation 4-14, f^{t} is the volume fraction of phase transformation on the $\mathbf{t^{th}}$ transformation system. $\mathrm{N_{trans}}$ is the number of phase transformation systems from austenite to ε-martensite. $\mathbf{b}^{\mathbf{t}}_{\mathbf{trans}}$ is the average transformation direction and $\mathbf{m}^{\mathbf{t}}_{\mathbf{trans}}$ is the habit plane normal

[212]. $\mathbf{P}_{\mathrm{trans}}^{\mathrm{t}}$ is the Schmid factor of the t transformation system. **I** represents the two dimensional identity matrix in equation 4-14, where A is the expansion coefficient, θ_0 is the reference temperature point and θ is the absolute temperature.

$$\mathbf{F}^{\theta} = [1 + \mathrm{A}(\theta - \theta_0)]\mathbf{I} \qquad \text{(equation 4-14)}$$

The elastic stress-strain relationship is represented by equation 4-15, where, the Green strain is defined in equation 4-16 and the 2nd Piola-Kirchhoff stress is defined by equation 4-17.

$$\mathbf{T}^{e} = \mathbf{C}{:}\,\mathbf{E}^{e} \qquad \text{(equation 4-15)}$$

$$\mathbf{E}^{\mathrm{e}} = \frac{1}{2}(\mathbf{F}^{\mathrm{e}^{\mathrm{T}}} \cdot \mathbf{F}^{\mathrm{e}} - \mathbf{I}) \qquad \text{(equation 4-16)}$$

$$\mathbf{T}^{\mathrm{e}} = \mathbf{F}^{\mathrm{e}^{-1}}[\det(\mathbf{F}^{\mathrm{e}}) \cdot \boldsymbol{\sigma}]\mathbf{F}^{\mathrm{e}^{-\mathrm{T}}} \qquad \text{(equation 4-17)}$$

The material derivative of plastic deformation gradient (F^{p}) results in the plastic velocity gradient $\mathbf{L}^{\mathrm{p}}$ [211]. It is described by both mechanisms of dislocation slip and mechanical twinning in the austenite phase as seen in equation 4-18. Whereas for the martensite phase, F^{p} is described only by dislocation slip as shown in equation 4-19. $\mathrm{N}_{\mathrm{slip}}$ and $\mathrm{N}_{\mathrm{twin}}$ are the number of slip and twin systems, respectively. $\dot{\gamma}^{\alpha}(\alpha \in [1, \mathrm{N}_{\mathrm{slip}}])$ and $\dot{\gamma}^{\beta}(\beta \in [1, \mathrm{N}_{\mathrm{twin}}])$ are the shear strain rate on slip and twin systems, respectively. $\mathbf{P}_{\mathrm{slip}}$ and $\mathbf{P}_{\mathrm{twin}}$ are the Schmid factor in dislocation slip and twin systems. f^{A} and f^{M} are the volume fraction of the austenite and corresponding martensite phases.

$$\mathbf{L}^{\mathrm{p}} = \dot{\mathbf{F}}^{\mathrm{p}} \cdot \mathbf{F}^{\mathrm{p}^{-1}} = \mathrm{f}^{\mathrm{A}} \sum_{\alpha=1}^{\mathrm{N}_{\mathrm{slip}}} \dot{\gamma}^{\alpha}\mathbf{P}_{\mathrm{slip}}^{\alpha} + \mathrm{f}^{\mathrm{tw}} \sum_{\beta=1}^{\mathrm{N}_{\mathrm{twin}}} \dot{\gamma}^{\beta}\mathbf{P}_{\mathrm{twin}}^{\beta} \qquad \text{(equation 4-18)}$$

$$\mathbf{L}^{\mathrm{p}} = \dot{\mathbf{F}}^{\mathrm{p}} \cdot \mathbf{F}^{\mathrm{p}^{-1}} = \mathrm{f}^{\mathrm{M}} \sum_{\alpha=1}^{\mathrm{N}_{\mathrm{slip}}} \dot{\gamma}^{\alpha}\mathbf{P}_{\mathrm{slip}}^{\alpha} \qquad \text{(equation 4-19)}$$

The thermal activation is inserted to consider the effect of strain rate. Based on the present understanding of Fe-Mn-Al-C systems, a SFE from 0 to ~20 $\mathrm{mJ/m^2}$ could induce the transformation from γ phase to ε-martensite phase, along with dislocation slip. Whereas, a SFE from 20 to ~50 $\mathrm{mJ/m^2}$ means mechanical twinning can occur in γ, in addition to primary dislocation glide. If SFE exceeds 50 $\mathrm{mJ/m^2}$, the planar defects or mobile partial dislocations are not observed in the material, but rather only full dislocations that glide. The shear strain rate of dislocation slip, or twinning is affected by the SFE. Here, the thermally activated shear strain is defined by equation 4-20, where ΔF is the Helmholtz free energy, or the effective activation energy barrier. ρ_m is the average mobile dislocation density, ν_{id} the dislocation vibration frequency, b the magnitude of Burgers vector, k the Boltzmann constant, ΔV the thermal activation volume. τ^α and s^α are the resolved shear stress and the dislocation slip resistance in αth slip system, respectively.

$$\dot{\gamma}^\alpha = \frac{\rho_m \upsilon_{id} b^{\alpha^2}}{2} \exp\left(\frac{-\Delta F}{k\theta}\right) \exp\left(\frac{(\tau^\alpha - s^\alpha)\Delta V}{k\theta}\right) \mathrm{sgn}(\tau^\alpha) \qquad \text{(equation 4-20)}$$

A similar formula is provided for the mechanism of mechanical twinning in equation 4-21, where, τ^β and s^β represent the resolved shear stress and the twin resistance on the βth twin system, respectively. The critical twinning stress is known to be significantly influenced by grain size for grains less than 0.5 µm [20]. The stress constraint in Eqn. (13) indicate the twinning deformation is directional and the twin volume fraction is always positive, since full transformation does not occur in this material. The sum of the twinned volumes does not exceed the grain volume and the twinned region must stay as such unless a transformation occurs. The shear resistance is decomposed to four terms corresponding to the initial temperature associated s_0^α, Hall-Petch-associated s_{HP}^α, forest dislocation density related s_{for}^α and debris dislocation density related s_{deb}^α, respectively [213] and described by equation 4-22 and equation 4-23, where χ is the dislocation interaction constant, taken to be 0.31 for Fe-Mn-C steel. Where μ is the elastic shear modulus evolving linearly with temperature and ρ_{for}^α is the forest dislocation density in one grain. Here only the self-hardening is considered and the latent hardening is neglected.

$$\dot{\gamma}^\beta = \begin{cases} \frac{\rho_m \upsilon_{id} {b^\beta}^2}{2} \exp\left(\frac{-\Delta F}{k\theta}\right) \exp\left(\frac{(\tau^\beta - s^\beta)\Delta V}{k\theta}\right) & \text{if } \tau^\beta > 0 \\ 0 & \text{otherwise} \end{cases} \qquad \text{(equation 4-21)}$$

$$s^\alpha(\dot{\gamma}^\alpha) = s_0^\alpha + s_{HP}^\alpha + s_{for}^\alpha(\dot{\gamma}^\alpha) + s_{deb}^\alpha(\dot{\gamma}^\alpha) \qquad \text{(equation 4-22)}$$

$$s_{for}^\alpha = b^\alpha \chi \mu \sqrt{\rho_{for}^\alpha} \qquad \text{(equation 4-23)}$$

Stage IV hardening is represented by substructure hardening (s_{deb}^α) represents for the substructure strengthening in the stage IV hardening and k_{deb} is a material-independent constant defined as 0.1 for both FCC and BCC crystal structures and as 0.086 for hcp crystals [214], and finally ρ_{deb} is the total debris dislocation density for one grain as shown in equation 4-24.

$$s_{deb}^\alpha = k_{deb} \mu b^\alpha \sqrt{\rho_{deb}} \ln\left(\frac{1}{b^\alpha \sqrt{\rho_{deb}}}\right) \qquad \text{(equation 4-24)}$$

HP^α is the Hall-Petch-like coefficient and d_g^α is the grain size of corresponding phase. The critical propagation resistance s_{tw}^β for βth twin system consists two components [213] as shown in equation 4-25 and equation 4-26. Since the effect of slip dislocation on twinning is already considered in volume fraction evolution in Eq. (12), the interaction between twinning and forest dislocation is neglected here. The dislocation interaction between twinning and debris dislocation are found to be negligible [213]. s_0^β is the initial propagation resistance and s_{HP}^β is the Hall-Petch-like strength related to the twin boundaries as shown in equation 4-27. Here, d_{MTF}^β is the width of mean free path, which is approximated as the grain size of newly transformed α'. In dislocation density based theory, the forest dislocation density evolution is related to two part the generation and recovery dislocation densities [213].

$$s_{HP}^{\alpha} = \mu HP^\alpha \sqrt{\frac{b^\alpha}{d_g^\alpha}} \qquad \text{(equation 4-25)}$$

$$s_{tw}^\beta = s_0^\beta + s_{HP}^\beta \qquad \text{(equation 4-26)}$$

$$s_{HP}^\beta = \mu HP^\beta \sqrt{\frac{b^\beta}{d_{MTF}^\beta}} \qquad \text{(equation 4-27)}$$

The partial recovery component is strengthened and transformed into a debris dislocation and the other dislocation component is annihilated as shown in equation 4-28, equation 4-29 and equation 4-30.

$$\frac{\partial \rho_{for}^\alpha}{\partial \gamma^\alpha} = \frac{\partial \rho_{gen}^\alpha}{\partial \gamma^\alpha} - \frac{\partial \rho_{rev}^\alpha}{\partial \gamma^\alpha} = \frac{\partial \rho_{gen}^\alpha}{\partial \gamma^\alpha} - \left(\frac{\partial \rho_{deb}}{\partial \gamma^\alpha} + \frac{\partial \rho_{ann}^\alpha}{\partial \gamma^\alpha}\right) \qquad \text{(equation 4-28)}$$

$$\frac{\partial \rho_{for}^\alpha}{\partial \gamma^\alpha} = \frac{\partial \rho_{gen}^\alpha}{\partial \gamma^\alpha} - \frac{\partial \rho_{rev}^\alpha}{\partial \gamma^\alpha} = k_1 \sqrt{\rho_{for}^\alpha} - k_2(\dot{\gamma}, \theta)\rho_{for}^\alpha \qquad \text{(equation 4-29)}$$

$$k_2^\alpha(\dot{\gamma}^\alpha, \theta) = \frac{k_1 b^\alpha \chi}{g^\alpha}\left[1 - \frac{k\theta}{D^\alpha b^{\alpha^3}} \ln\left(\frac{\dot{\gamma}^\alpha}{\dot{\gamma}_0^\alpha}\right)\right] \qquad \text{(equation 4-30)}$$

The debris dislocation density evolution is defined on the sum of effects from multiple slip systems for one grain, where q^α is a rate coefficient related with thermal-activated energy and volume, describing how point defects can grow into debris by local thermal activation (see equation 4-31).

$$d\rho_{\mathrm{deb}} = \sum_{\alpha} \frac{\partial \rho_{\mathrm{deb}}}{\partial \gamma^{\alpha}} d\gamma^{\alpha} = \sum_{\alpha} q^{\alpha} b^{\alpha} \sqrt{\rho_{\mathrm{deb}}} k_2^{\alpha}(\dot{\gamma}^{\alpha}, \theta) \rho_{\mathrm{for}}^{\alpha} \quad \text{(equation 4-31)}$$

Table 4-5: Elastic properties from [22][25] used in the appropriate constitutive equations

Phase	C_{11} (GPa)	C_{12} (GPa)	C_{44} (GPa)	C_{13} (GPa)	C_{33} (GPa)
Austenite (γ)	174	85	99		
Martensite (α')	169	82	96		
Ferrite (α)	175	82	97		
Martensite (ε)	420	30	320	120	570

The calibrated 3D Taylor model (see Figure 4-54) shows strong agreement with the mechanical properties of the medium-Mn steel annealed for 8 h at 585 °C and deformed at strain rates from $\dot{\varepsilon} = 2\text{x}10^{-4}$ /s to $\dot{\varepsilon} = 2\text{x}10^{1}$ /s. The instantaneous strain-rate sensitivity is captured in the thermal activation volume and thermal activation energy barrier of FCC and BCC crystals and is thus directly incorporated in this model and calibrated for each value of accumulated strain [215][216]. Consequently, one single set of physical-based parameters could be identified to capture the mechanical behavior at different strain rates. Results in Table 4-6, based on fits of the model to the engineering stress-strain curves in Figure 4-54d show that the thermal activation energy barrier (ΔF^{α} in Joules) is higher for BCC than for FCC, which is consistent with the prediction that short-range barriers in BCC (Peirels barriers) play a larger role in the positive strain rate sensitivity of yield strength as the majority of the microstructure is BCC-based. Dislocation forest densities in FCC are greater than BCC, which is consistent with a prediction that the short range barriers contributing to the positive strain rate sensitivity of this multi-phase medium-Mn steel might also depend slightly on the FCC short-range barriers.

Figure 4-55 shows results from a crystal plasticity finite element simulation which takes into account the interaction between neighboring grains (as opposed to the Taylor model). The stress concentration occupies the martensite phase whereas strain localization occurs mostly within the austenite. After further deformation, some of the austenite eventually transforms and locally reveals a high concentration of stress, but a low concentration of strain (since that particular finite element is now considered a different phase). The abrupt increase in strength slightly increases the strain hardening rate of the material. The dislocation activation resistance is elevated in the newly formed martensite. Furthermore, once transformation occurs in the austenite, stress localizations begin to increase in magnitude within the parent microstructure, ultimately causing failure.

Based on results from this work with a two-level finite-element model, a parametric analysis (see Figure 4-56) was completed to predict properties for future AHSS design, with the basis beginning with the medium-Mn steel investigated in this work. Physical parameters that are relevant for alloy design are tuned. Phase fraction (a composite effect on mechanical properties [36]) can be controlled experimentally by annealing temperature and annealing time [39]. Generally speaking, increasing the volume fraction of austenite increases overall ductility and decreases ultimate tensile strength of the medium-Mn steel in this work (see Figure 4-56). Grain size (Hall-Petch effect [213]) can be controlled experimentally by annealing temperature and annealing time [59]. When the martensite volume fraction is less than 29%, the grain refinement of austenite leads to an increase in ductility in the macroscopic material. In the dislocation-density based model, the smaller grain size of polycrystalline austenite requires more dislocation activation to achieve a given magnitude of plastic strain. The grain size reduction in austenite results in higher deform resistance and thus the loss of ductility. The ratio of twinning to epsilon martensite in austenite (strain hardening rate effect from a change in stacking fault energy [12]), can also be controlled experimentally by tuning the SFE with composition, but also depends on annealing temperature and inherently affects phase fraction [206].

Table 4-6: Resulting plastic properties from calibration of tensile curves during deformation of the Taylor-based model using ABAQUS.

Parameters	BCC(α,α')	HCP (ε)	FCC (γ)
ΔF^{α} (J)	$4.45\text{x}10^{-20}$	$5.36\text{x}10^{-20}$	$6.39\text{x}10^{-21}$
ΔV^{α} (m^3)	$7.68\text{x}10^{-29}$	$4.19\text{x}10^{-29}$	$6.25\text{x}10^{-28}$
b^{α} (μm)	$2.50\text{x}10^{-4}$	$2.48\text{x}10^{-4}$	$2.56\text{x}10^{-4}$
s_0^{α} (MPa)	247	550	110
s_0^{β} (MPa)	N/A	N/A	160
$HP^{\alpha\beta}$ (MPa)	130	120	100
k_1 (m^{-1})	$4.29\text{x}10^{7}$	$1.08\text{x}10^{10}$	$2.49\text{x}10^{8}$
g^{α}	$1.21\text{x}10^{-2}$	$3.44\text{x}10^{-2}$	$4.65\text{x}10^{-2}$
D^{α} (MPa)	348	785	295

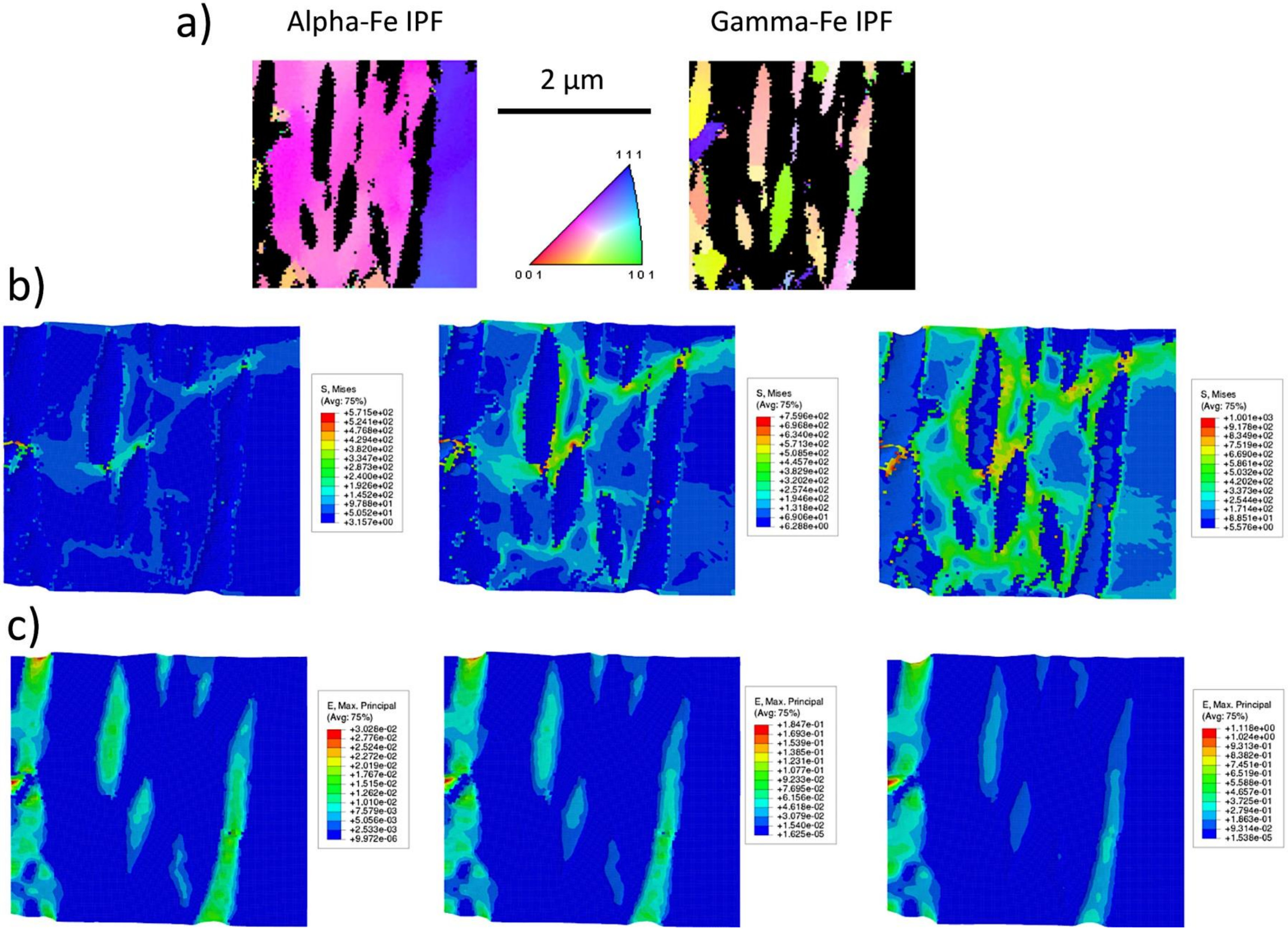
a)
Alpha-Fe IPF
2 µm
1 1 1
0 0 1
1 0 1
Gamma-Fe IPF
b)
S, Mises
(Avg: 75%)
+5.715e+02
+5.241e+02
+4.768e+02
+4.294e+02
+3.820e+02
+3.347e+02
+2.873e+02
+2.400e+02
+1.926e+02
+1.452e+02
+9.788e+01
+5.052e+01
+3.157e+00
S, Mises
(Avg: 75%)
+7.596e+02
+6.968e+02
+6.340e+02
+5.713e+02
+5.085e+02
+4.457e+02
+3.829e+02
+3.202e+02
+2.574e+02
+1.946e+02
+1.318e+02
+6.906e+01
+6.288e+00
S, Mises
(Avg: 75%)
+1.001e+03
+9.178e+02
+8.349e+02
+7.519e+02
+6.690e+02
+5.861e+02
+5.032e+02
+4.202e+02
+3.373e+02
+2.544e+02
+1.714e+02
+8.851e+01
+5.576e+00
c)
E, Max. Principal
(Avg: 75%)
+3.028e-02
+2.776e-02
+2.524e-02
+2.272e-02
+2.019e-02
+1.767e-02
+1.515e-02
+1.262e-02
+1.010e-02
+7.579e-03
+5.056e-03
+2.533e-03
+9.972e-06
E, Max. Principal
(Avg: 75%)
+1.847e-01
+1.693e-01
+1.539e-01
+1.385e-01
+1.231e-01
+1.077e-01
+9.233e-02
+7.695e-02
+6.156e-02
+4.618e-02
+3.079e-02
+1.540e-02
+1.625e-05
E, Max. Principal
(Avg: 75%)
+1.118e+00
+1.024e+00
+9.313e-01
+8.382e-01
+7.451e-01
+6.519e-01
+5.588e-01
+4.657e-01
+3.725e-01
+2.794e-01
+1.863e-01
+9.314e-02
+1.538e-05

Figure 4-55: a) 2D EBSD scan with experimental scale bar and b/c) crystal plasticity finite element simulation of the fully resolved micrsotructure. The b) Von Mises stress and c) principal strain are shown with varying scale bars to highlight significant fluctuations in the microstructure (tension is applied in the horizontal direction with the left side being the stationary boundary condition).

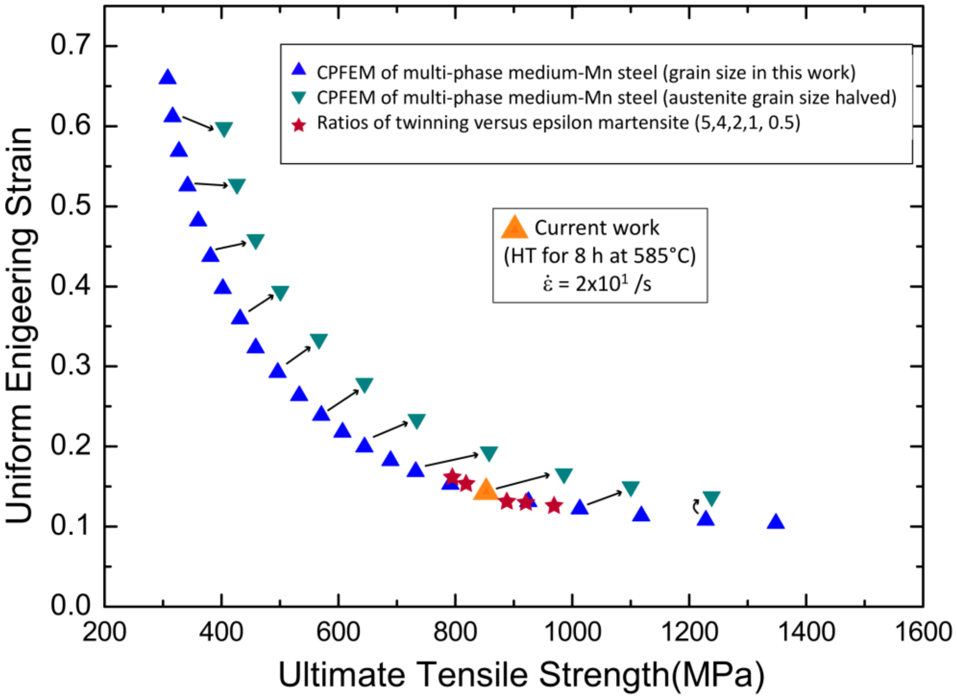

Figure 4-56: Parametric analysis of a change in volume fraction of austenite (blue triangles) and reduction in grain size of austenite (upside down green triangle), based on results from the current work on a multi-phase medium-Mn TWIP-TRIP steel, i.e. the triangles connected by an arrow. have the same volume fraction, but a different grain size of austeniteThe ratio of twinning versus epsilon martensite was also varied (red stars) showing more twinning led to more elongation and decreased strength.

The finite element results from a study [141] on a Fe-6Mn-3Al-1.5Si-0.15C TWIP-TRIP steel revealed an alternating behavior of strain localization. Mainly, the strain partitioning models that Latypov et al. implemented [142][143] showed that the initially softer austenite deformed at low levels of strain until TWIP & TRIP effects were activated, which then led to accommodation of strain in the ferrite phase. Due to the low strain-hardening capacity of ferrite, failure occurred once all strain had transitioned to ferrite. Therefore, the delay in transition from the local flow stress of austenite (through TWIP & TRIP effects) to ferrite is the main explanation of the unusual delayed strain hardening behavior of that multi-phase steel. Latypov et al. concluded, with a comparison to iso-work models which don't include initial microstructural inputs, that a microstructure-based model is better suited in explaining the strain-hardening behavior of a medium-Mn TWIP-TRIP steel. Further, work by Lee et al. on a Fe-12Mn-3Al-0.3C (wt%) TWIP+TRIP steel using a Mecking-Kocks-Estrin type constitutive model showed that the yield strength of austenite was lower than that of ferrite, but the strain hardening rate of austenite was greater and the combined TWIP and TRIP effects contributed as effective plasticity-enhancing mechanisms in the ultrafine constituents [55].

4.4.5 Summary and Conclusions

- Both heat treatments of the medium-Mn steel showed positive strain rate sensitivity of yield and ultimate tensile strengths from $\dot{\varepsilon} = 2x10^{-4}$ /s to $\dot{\varepsilon} = 2x10^{2}$ /s. A decrease in annealing time (from 8 h to 0.5 h) increased the yield and ultimate tensile strengths (when compared at the same strain rate).
- No significant differences in the strain-rate sensitivity of uniform elongation were noted for either heat treatment, whereas total elongation increased at higher strain rates. However, an increase in annealing time from 0.5 h to 8 h clearly increased both the UE and TE of the medium-Mn steel (when compared at the same strain rate) as well as PSE.
- The final average temperature in the area of the reduced gauge length after deformation from $\dot{\varepsilon} = 2x10^{-4}$ /s to $\dot{\varepsilon} = 2x10^{1}$ /s is greater for the specimen annealed for 8 h compared to the specimen annealed for 0.5 h and is directly proportional to the numerically-

integrated areas under the engineering stress-strain curves. Increases in austenitic SFE from adiabatic heating are not expected to influence the deformation mechanisms.

- TEM results confirm the presence of mechanical twinning and hexagonal ε-martensite after quasi-static deformation, which is consistent with the predicted RT SFE value of 21 mJ/m^2. Planar defects are observed as early as 0.08 engineering strain in the austenite and even after deformation to failure at the highest strain rates.
- The two-level finite element model developed from empirical data provided key insight into how the multi-phase microstructure behaves at high strain rates. The Taylor-based model showed that the strain-rate sensitivity of the material depends on the dislocation forest density in austenite and thermal-activation barriers in ferrite. Crystal-plasticity finite-element simulations of the fully resolved microstructure shows that austenite accommodates most of the localized strain-induced deformation, which eventually transfers most of the stress to the major component of the microstructure (recovered martensite) and results in premature failure.

CHAPTER 5

5. SUMMARY AND CONCLUSIONS

The effect of strain rate on the mechanical properties and deformation mechanisms of a single-phase high-Mn steel and a multi-phase medium-Mn steel was investigated by mechanical testing at strain rates from $\dot{\varepsilon} = 2x10^{-4}$ /s to $\dot{\varepsilon} = 2x10^{3}$ /s. Servo-hydraulic tension, uniaxial ring expansion and Kolsky-bar testing provided the desired range of strain rates. Advanced imaging and diffraction-based techniques (such as HR-STEM, DF-TEM, SAED, CBED, XRD, EBSD and ECCI) were used to characterize deformation mechanisms in interrupted and pulled-to-failure tensile tests, with a focus on TWIP and TRIP effects. A high-speed thermal camera was used to measure the increase in specimen temperature as a function of strain, which enabled the use of a thermodynamic model to predict the increase in SFE. Thermal imaging and digital image correlation techniques were used identify strain localizations in tensile specimens. To further characterize the medium-Mn alloy design process, the effect of annealing time on microstructure evolution and austenite composition in a multi-phase medium-Mn steel was also examined using STEM-EDS, APT, CBED, EBSD and XRD. Finally, a two-level finite-element model derived from empirical results was developed to help elucidate differences in high strain rate mechanical behavior of a multi-phase medium-Mn steel. A common philosophy behind this work was to use multiple techniques to quantify a given measurement. Complementary techniques provide different perspectives on the significance of results and impart further insight into the limitations of a given measurement method.

The significant positive yield-strength strain-rate sensitivity of the single-phase Fe-25Mn-3Al-3Si (wt%) steel is due to an increase in flow stress that is necessary for partial dislocations in austenite to overcome time-dependent thermally activated short-range barriers during dislocation glide with increasing strain rate. For both annealing times (0.5 h and 8 h) the multi-phase Fe-12Mn-3Al-0.05C (wt%) steel also shows positive strain-rate sensitivity of the yield strength, which predominantly depends on time-dependent thermally-activated short-range barriers in ferrite/martensite (lattice resistances known as the Peirels barriers) since austenite is a minor microstructural constituent.

The Fe-25Mn-3Al-3Si (wt%) steel and Fe-12Mn-3Al-0.05C (wt%) steels slightly differ in strain-rate sensitivity of ultimate tensile strengths, mainly due to differences in adiabatic heating and uniform elongation. The UTS of the Fe-25Mn-3Al-3Si (wt%) steel decreases slightly when increasing the strain rate from $\dot{\varepsilon}$ = 2x10^{-4} /s to $\dot{\varepsilon}$ = 2x10^{-2} /s and is attributed to the onset of adiabatic heating, slight changes in strain hardening rate and a decrease in uniform elongation, meaning the adiabatic heating from large amounts of accumulated strain has enough time to cause a softening effect. When increasing strain rate from $\dot{\varepsilon}$ = 2x10^{-2} /s to $\dot{\varepsilon}$ = 2x10^{2} /s, the UTS of the Fe-25Mn-3Al-3Si (wt%) steel shows a positive strain-rate sensitivity, meaning there is less time for adiabatic heating to assist dislocations across thermally-activated barriers, causing an increase in flow stress. For both annealing times, (0.5 h and 8 h), the multi-phase Fe-12Mn-3Al-0.05C (wt%) steel shows positive UTS strain rate sensitivity, indicating that the adiabatic heating generated during relatively low amounts of uniform elongation (compared to high-Mn steels) does not allow for the onset of thermal softening and therefore the thermally-activated barriers dominate the flow stress.

A moderate decrease in uniform elongation is noted between the lowest and highest strain rates for the Fe-25Mn-3Al-3Si (wt%) steel. Increasing the strain rate from $\dot{\varepsilon}$ = 2x10^{-2} /s to $\dot{\varepsilon}$ = 2x10^{2} /s increased the amount of post-uniform elongation significantly. As reduction-in-area measurements on the necked regions did not change significantly for the same sheet thickness in this range of strain rates, strain localization is the likely mechanism. This conclusion is supported by localized regions of higher temperatures observed in thermal imaging during tests at $\dot{\varepsilon}$ = 2x10^1 and $\dot{\varepsilon}$ = 2x10^2 /s. The product of ultimate tensile strength and total elongation of the Fe-25Mn-3Al-3Si (wt%) steel increases with increasing strain rate and sheet thickness. No significant differences in the strain-rate sensitivity of uniform elongation are noted for either heat treatment (0.5 h and 8 h) for the Fe-12Mn-3Al-0.05C (wt%) steel, but post-uniform elongation increases at higher strain rates and is again attributed to strain localizations.

Increasing the sheet thickness of the Fe-25Mn-3Al-3Si (wt%) steel increased the post-uniform elongation and thus the reduction-in-area (when compared at the same strain rate). However, sheet thickness does not significantly affect the magnitude of the yield strength, yield strength strain-rate sensitivity, or uniform elongation.

An increase in annealing time from 0.5 h to 8 h decreased the yield and ultimate tensile strengths of the Fe-12Mn-3Al-0.05C (wt%) steel when comparisons are made at the same strain rate and is credited to an increase in grain size of the UFG phases (the Hall-Petch effect). An increase in annealing time from 0.5 h to 8 h increases the UE, TE and PSE of the Fe-12Mn-3Al-0.05C (wt%) steel (when compared at the same strain rate) which is associated with an increase in the volume fraction of austenite.

With increasing strain rate, the average temperature of the tensile specimens deformed to failure for the Fe-25Mn-3Al-3Si (wt%) steel increased (from 26 °C to 53 °C at $\dot{\varepsilon}$ = 10^{-2} /s and from 26 °C to 95 °C at $\dot{\varepsilon}$ = 10^2 /s). Adiabatic conditions were reached as early as $\dot{\varepsilon}$ = 10^{-1} /s for the Fe-25Mn-3Al-3Si (wt%) steel. The thermodynamic model used to correlate specimen temperature with SFE predicts an increase from 21 mJ/m^2 at room temperature (23 °C) to ~34 mJ/m^2 at 83 °C, but such increases were noted at higher levels of engineering strain (0.4 or greater). When comparing temperature measurements at 0.18 engineering strain, increasing the strain rate from at $\dot{\varepsilon} = 10^{-2}$ /s to at $\dot{\varepsilon} = 10^{2}$ /s only increased the relative temperature from 36 °C to 44 °C. An increase in SFE of this magnitude is expected to have only a small effect on tensile properties. Therefore, only later levels of accumulated strain that generate large amounts of heat are expected to change the dominant deformation mechanism, assuming there is time for the heat to assist thermally-activated barriers. For the Fe-12Mn-3Al-0.05C (wt%) steel, increasing the strain rate only caused a maximum change in temperature of only ΔT=24 °C after deformation to failure, which is consistent with shorter uniform elongations than for the high-Mn steel. An increase in annealing time was observed to have only a small effect on the increase in specimen temperature during high strain-rate testing, which is expected to have only a minor effect on the SFE and dominant deformation mechanism in the austenite.

Although <110> SAED patterns may indicate the presence of only deformation twinning or only ε-martensite plates parallel to the beam direction in a given grain, high-resolution imaging reveals that both types of planar defects exist in the same grain, regardless of the extra reflections present in the SAED patterns. These results also confirm that both types of secondary deformation mechanisms are possible after deformation at high strain rates. Deformation twinning and ε-martensite are observed in tensile specimens of the Fe-25Mn-3Al-3Si (wt%) steel interrupted from quasi-static ($\dot{\varepsilon} = 2\text{x}10^{-4}$ /s) through low-dynamic ($\dot{\varepsilon} = 2\text{x}10^{2}$ /s) strain rates. ECCI and DF-TEM measurements do not reveal a statistically significant effect of strain rate on the thickness and spacing of mechanical twins or ε-martensite plates in the Fe-25Mn-3Al-3Si (wt%) steel. DF-TEM confirms the presence of mechanical twinning and hexagonal ε-martensite after quasi-static deformation of the Fe-12Mn-3Al-0.05C (wt%) steel, which is consistent with the predicted RT SFE value of 21 mJ/m^2. However, the planar defect density in the UFG austenite of the multi-phase medium-Mn steel is clearly lower than that observed in the coarse-grained single-phase high-Mn steel and is directly proportional to the measured uniform elongations.

EBSD and TEM/CBED results reveal ultrafine ferrite grains, plus rod-like and plate-like ultrafine austenite grains dispersed throughout the parent microstructure of tempered martensite in the Fe-12Mn-3Al-0.05C (wt%) steel. The low-carbon cold-rolled α'-martensite is inherited from the parent cold-rolled microstructure and is not fully recrystallized into ferrite and the measured volume fraction of reverted austenite is less than that predicted by simulations. STEM-EDS confirms that the austenite is enriched in Mn and depleted in Fe and Al as compared to the parent martensitic microstructure. An inhomogeneous distribution of UFG austenite and Mn-enriched austenite nuclei are observed for an annealing time of 0.5 h. The Mn content of austenite is equilibrated after 8 h of annealing time at 585 °C and also matches Thermo-Calc® predictions of composition and austenite SFE. Quantitative 3D measurements of compositions for all phases with APT follow trends consistent with the STEM-EDS results, (some variability in composition for the annealing time of 0.5 h, but equilibrated compositions after 8 h of annealing). The added benefit of APT (accurate carbon content measurements and improved spatial resolution) provides a consistent observation that both carbon-enriched and carbon-depleted austenite boundaries are present, regardless of annealing time. Carbon is a key austenite stabilizer (besides Mn) and provides a high chemical driving force during austenite reversion. The observation of interfaces that are either enriched or depleted in carbon provides clues as to why reverted austenite is UFG in size for medium-Mn steels as some interfaces between austenite and the matrix have differing local composition and thus mobility.

The two-level finite element model developed for the Fe-12Mn-3Al-0.05C (wt%) steel and based on empirical data provided key insights into how the multi-phase microstructure behaves at high strain rates and translates to changes in mechanical properties. The Taylor-based model, which does not consider microstructural morphology, showed that forest dislocation density is higher in FCC (because of short-range barriers in austenite) and that the thermal activation-energy barrier of ferrite (similar to a Periels barrier) was greater than that of austenite. Therefore, an increase in strain rate did not show a significant dependence on long-range barriers (athermal barriers), but rather a strong dependence on thermally-activated short-range barriers. When including morphology of the UFG austenite, crystal-plasticity finite-element simulations of the microstructure show that austenite accommodates most of the strain-induced deformation and premature failure occurs when stress localizes at boundaries between austenite and ferrite/martensite.

CHAPTER 6

6. FUTURE WORK

Mechanical properties of Fe-Mn-Al-Si austenitic steels depend on temperature and composition, so alloy design requires accurate predictions of SFE since this parameter is dependent on temperature and composition and controls the deformation mechanisms [100]. Traditionally, thermodynamic descriptions do not consider the stacking fault character and use constant values for FCC/HCP interfacial and strain-energy parameters because the variation with respect to temperature isn't well understood. In reality, the interfacial energy likely decreases with increasing temperature [102]. The FCC Néel temperature was calculated as 282 K for the Fe-25Mn-3Al-3Si steel [23], meaning all magnetism above room temperature (approximately 298 K) is described as paramagnetic (PM). This is an important point because SFE has been shown to depend on magnetic contributions, in addition to the already described chemical and interfacial contributions [68]. Unlike most austenitic steels, Fe-Mn based alloys undergo an anti-ferromagnetic (AFM) to PM transition at Néel temperatures above 200K [60]. The future work on Fe-Mn-Al-Si steels should include detailed microstructural characterization at temperatures below the Néel temperature as well as temperatures above RT to investigate changes in deformation mechanisms. Possible findings could include the absence of planar defects when deformed at higher temperatures. These findings would help decipher how planar defects and dislocations contribute to plasticity for a given temperature and magnetic state. Differences in planar defect content and strain hardening rate likely depend on the critical stress to initiate mechanical twinning [77]. This type of future work at high temperatures will aid in design of hot-forming/hot-pressing processes used in automotive stamping.

For medium-Mn steels, future work could focus on investigating how the 3D morphology of each microstructural constituent accommodates stress and strain, which could be investigated with 3D-EBSD and 3D-CPFE. Comparing the austenite stability of the same bulk steel composition intercritically annealed at the same temperature and time would be interesting for two extreme differences in cold rolling reductions (10% vs 90% for example) because hot-rolled vs. cold-rolled samples tend to produce completely different yielding and strain hardening behavior. Also, in-situ tensile testing and digital image correlation in an SEM (including EBSD scans at interrupted strains) could give more insight into how Schmid factors of a given phase contribute to the strain partitioning and overall plasticity of the multi-phase microstructure. FIB liftouts of deformed areas with known orientations could help confirm the effect of Schmid factor on the activity of mechanical twinning and transformation within a given ultrafine austenite grain. These types of in-situ analysis could be useful to the modeling community since transformation rates and twin fractions are typically calibrated between upper and lower bounds provided by other empirical measurements of the microstructure.

APPENDIX

A. Ringing at High Strain Rates

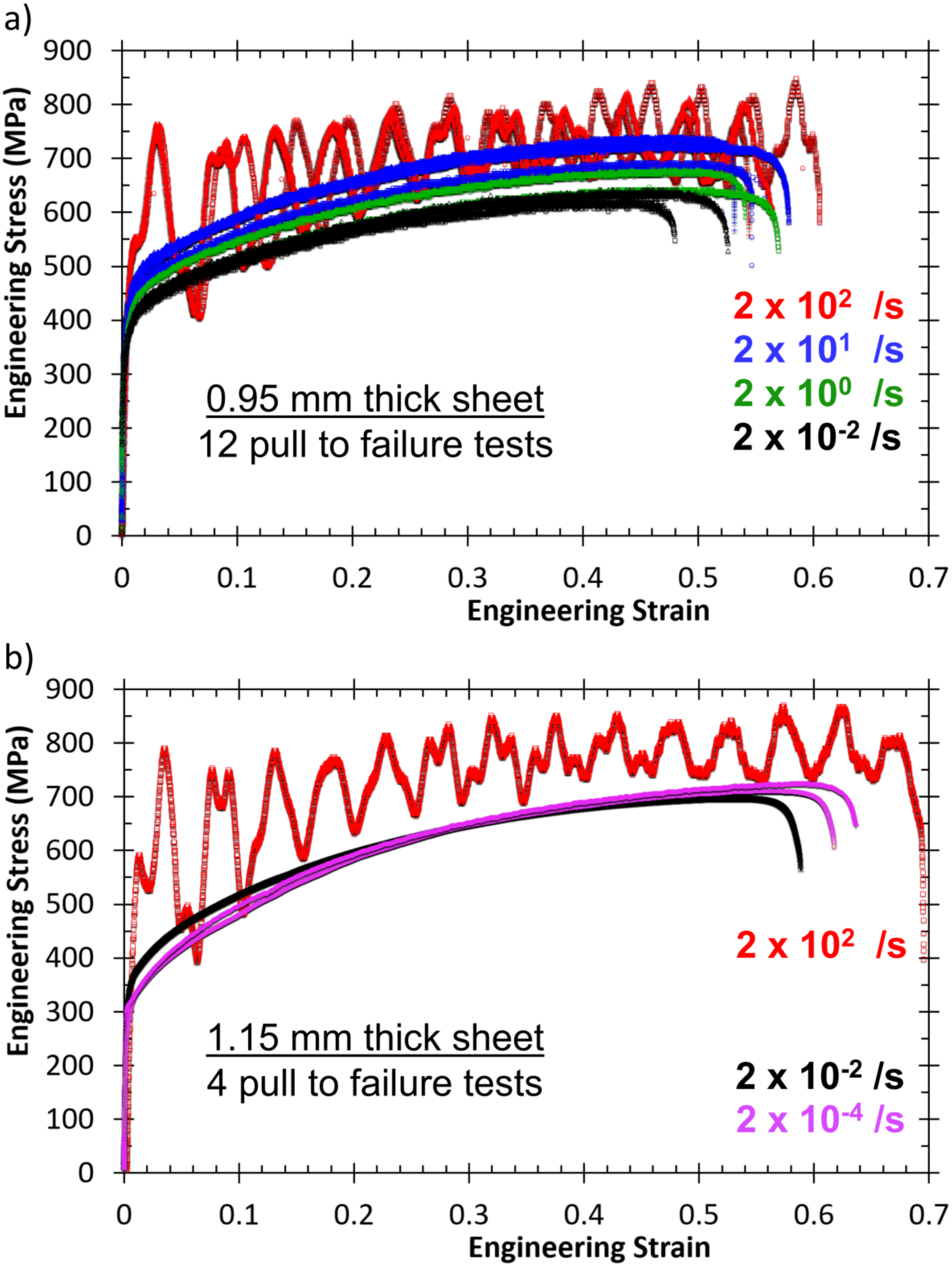

Figure A-1: Raw data of engineering stress (MPa) vs. engineering strain for the Fe-25Mn-3Al-3Si alloy when pulled to failure at strain rates of $\dot{\varepsilon} = 2x10^{-4}$ ε/s, $\dot{\varepsilon} = 2x10^{-2}$ ε/s, $\dot{\varepsilon} = 2x10^{0}$ ε/s, $\dot{\varepsilon} = 2x10^{1}$ ε/s and $\dot{\varepsilon} = 2x10^{2}$ ε/s, based on: a) 12 specimens from the 0.95 mm thick sheet and b) 4 specimens from the 1.15 mm thick sheet.

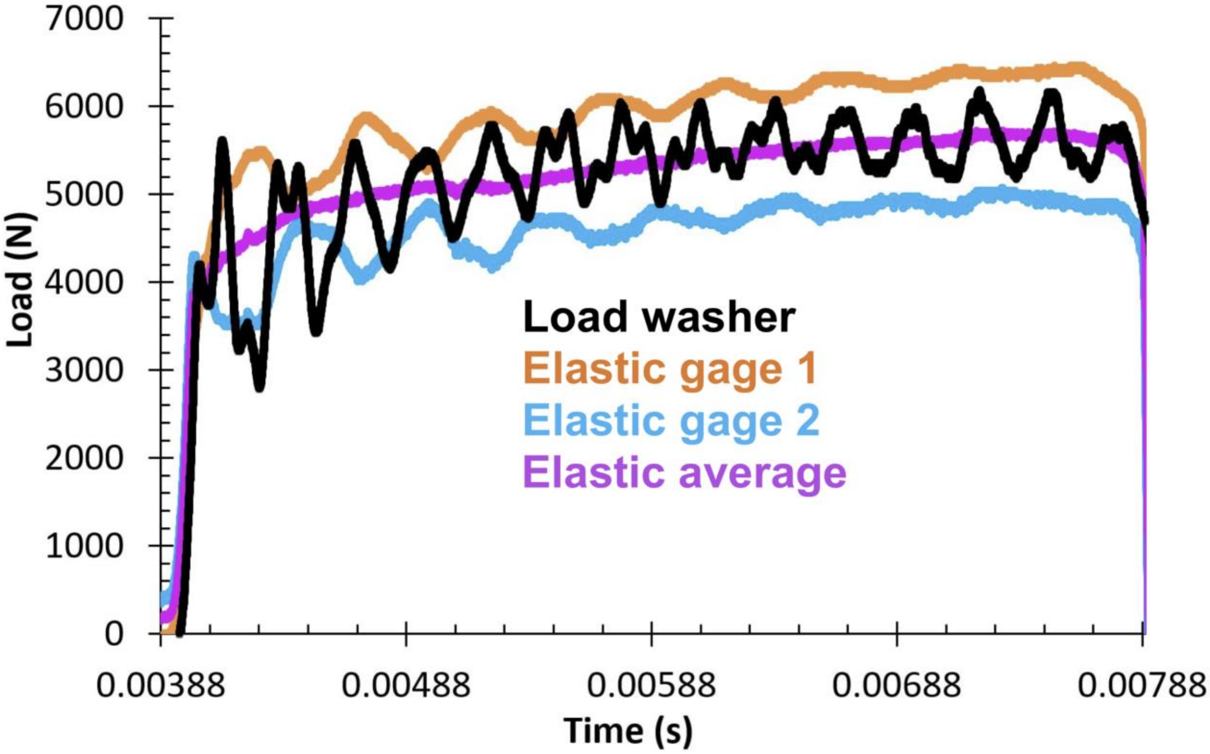

Figure A-2: Raw data of load (N) vs. time (s) for the Fe-25Mn-3Al-3Si alloy when pulled to failure at a strain rate of $\dot{\varepsilon} = 2x10^2$ ε/s using servo-hydraulic tension. Elastic strain gauges were attached on each side of the grip section. The load data from both strain gauges are averaged to reduce the amplitude of load oscillations. This tensile specimen was machined from the 1.15 mm thick sheet.

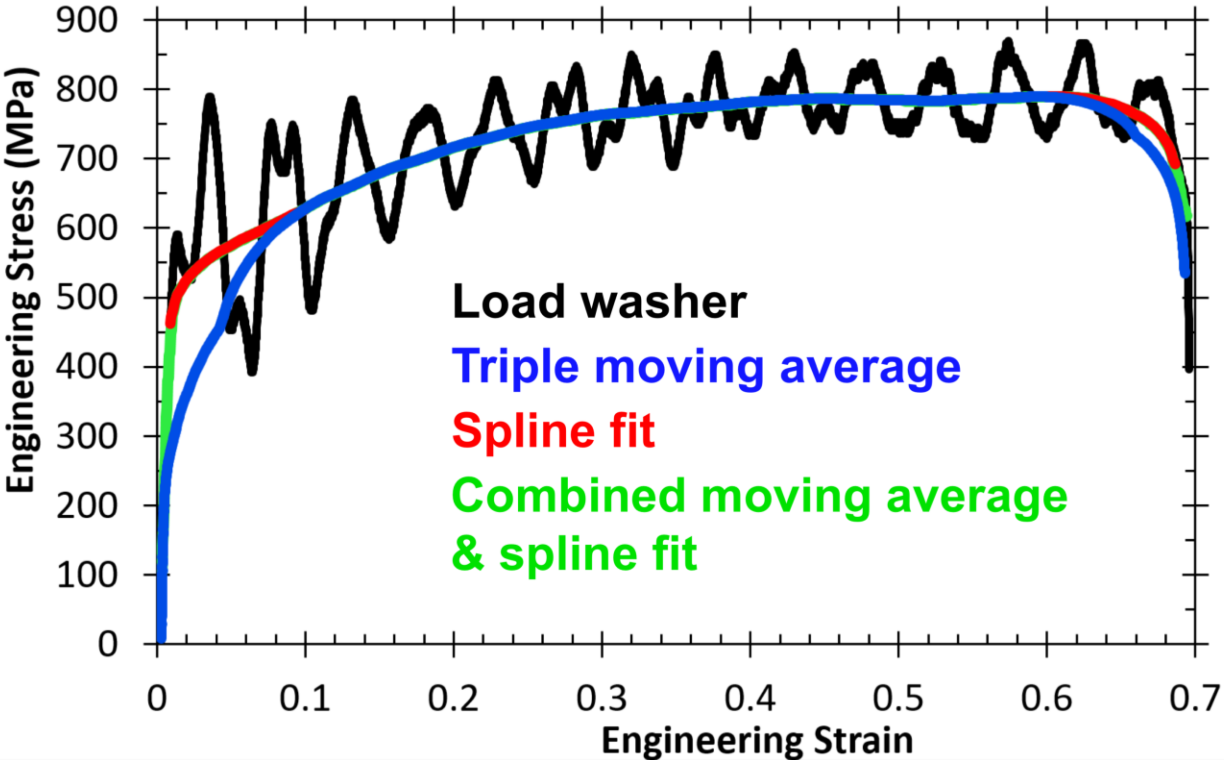

Figure A-3: Raw engineering stress (MPa) vs. engineering strain for the Fe-25Mn-3Al-3Si alloy when pulled to failure at a strain rate of $\dot{\varepsilon} = 2x10^2$ ε/s using servo-hydraulic tension. This data reduction method is based on a moving average with MATLAB®, (three iterations of smoothing), and spline fitting of the linear-elastic region and necking-fracture regions with Grapher™ software. This tensile specimen was machined from the 1.15 mm thick sheet.

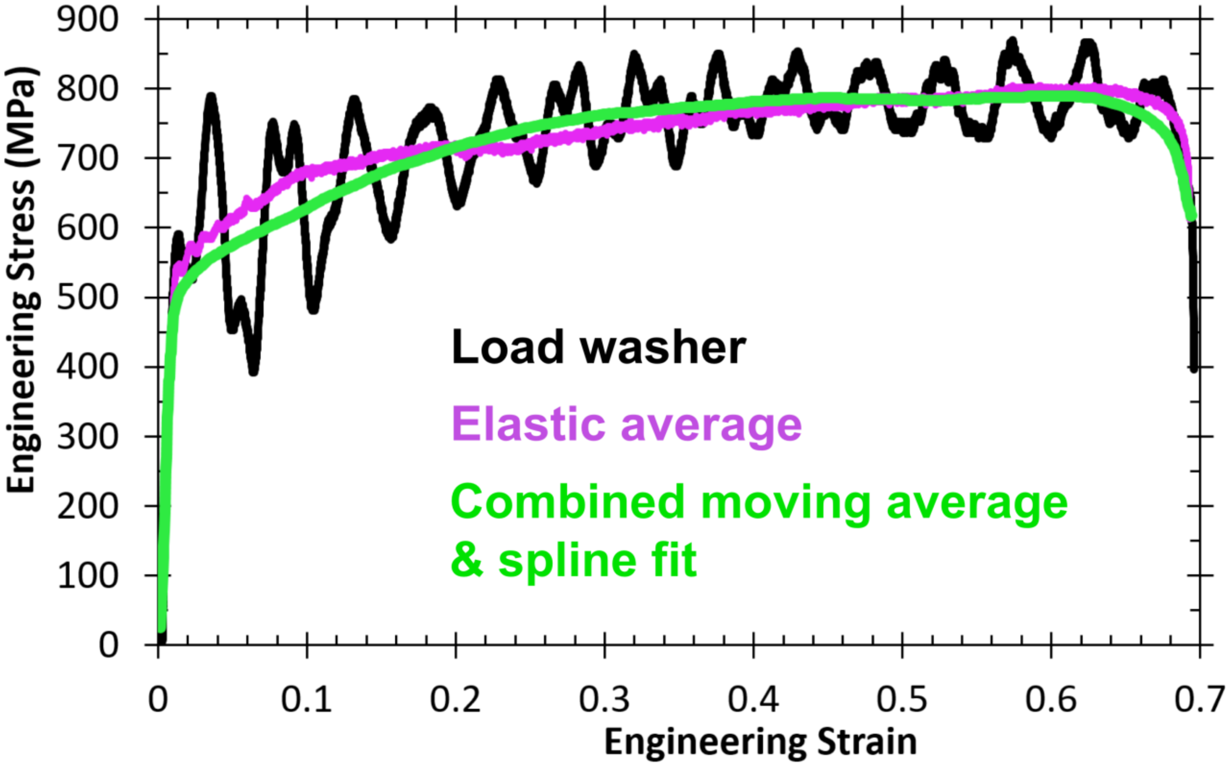

Figure A-4: A comparison of the raw load-washer data to the hardware and software-based smoothing methods, respectively presented in Figure A-2 and Figure A-3. A first attempt was made to measure load directly on the specimen grip with just one Vishay CEA-06-125UN-120 strain gauge [153] [168]. However, the load data from the grip strain gauge also exhibited large oscillations instead of a smooth load-versus-time curve, which is why other methods were investigated: two elastic gauges and the use of software-based smoothing.

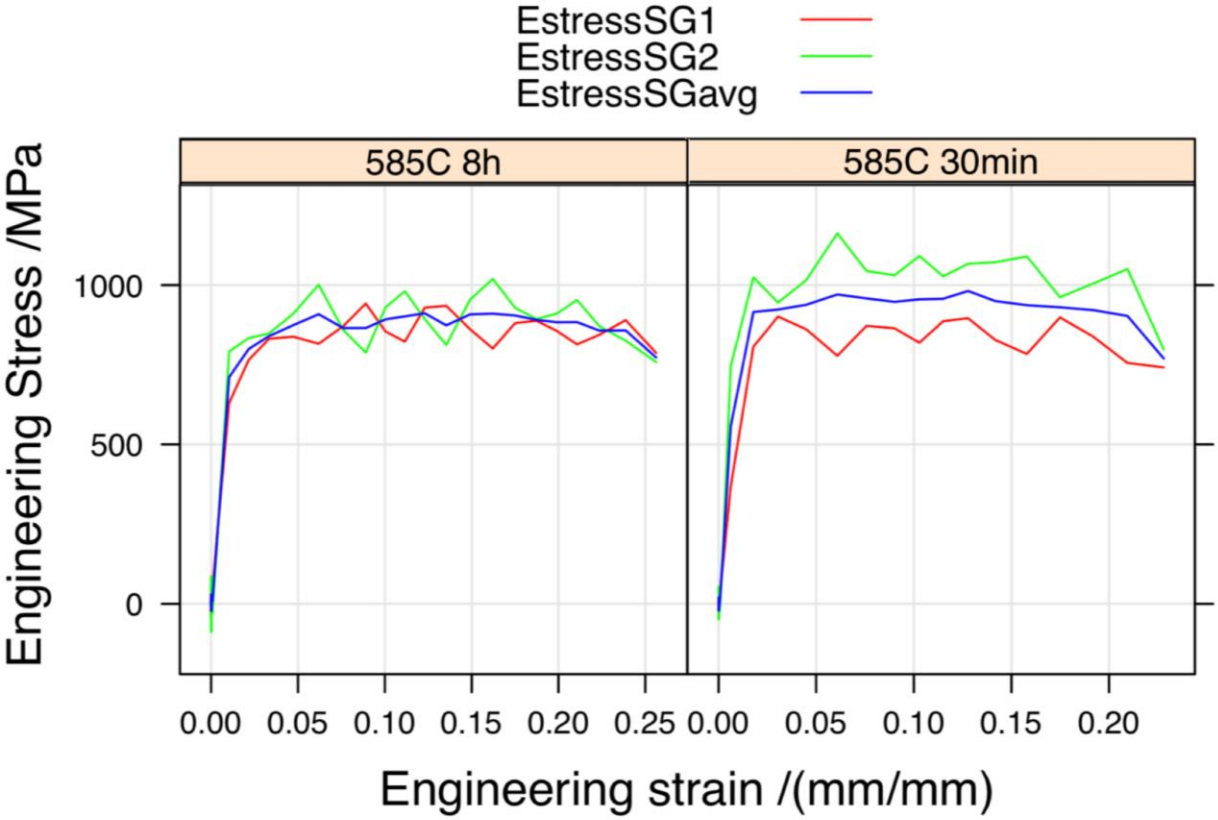

Figure A-5: Stresses calculated from each elastic strain gauge (SG) in the high-rate tests with the medium-Mn steel. SG1 faces the DIC cameras.

B. MIPAR Algorithms to Quantify Planar Defects

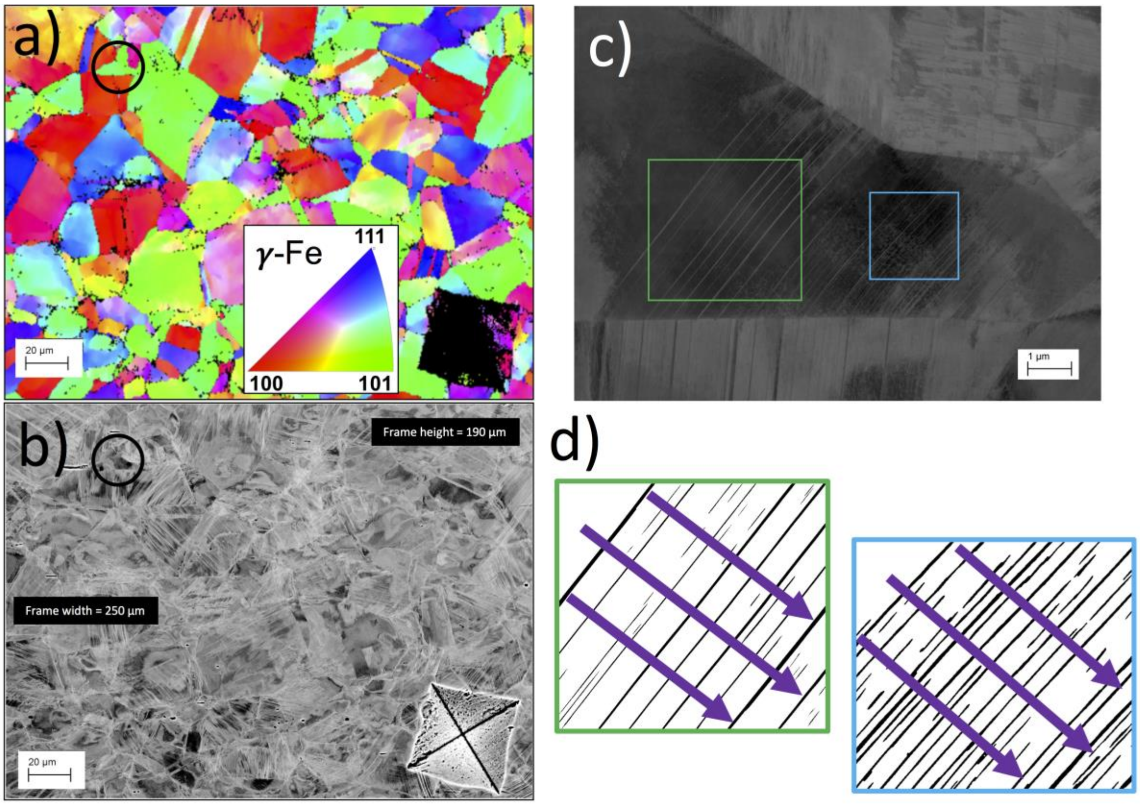

Figure B-1: Imaging techniques for SEM-based methods used to evaluate the spacing and thickness of planar defects in interrupted samples. a) EBSD survey, b) low magnification check for channeling contrast on properly oriented grains c) medium magnification ECCI scan of the grain circled in a) and b), then d) image processing.

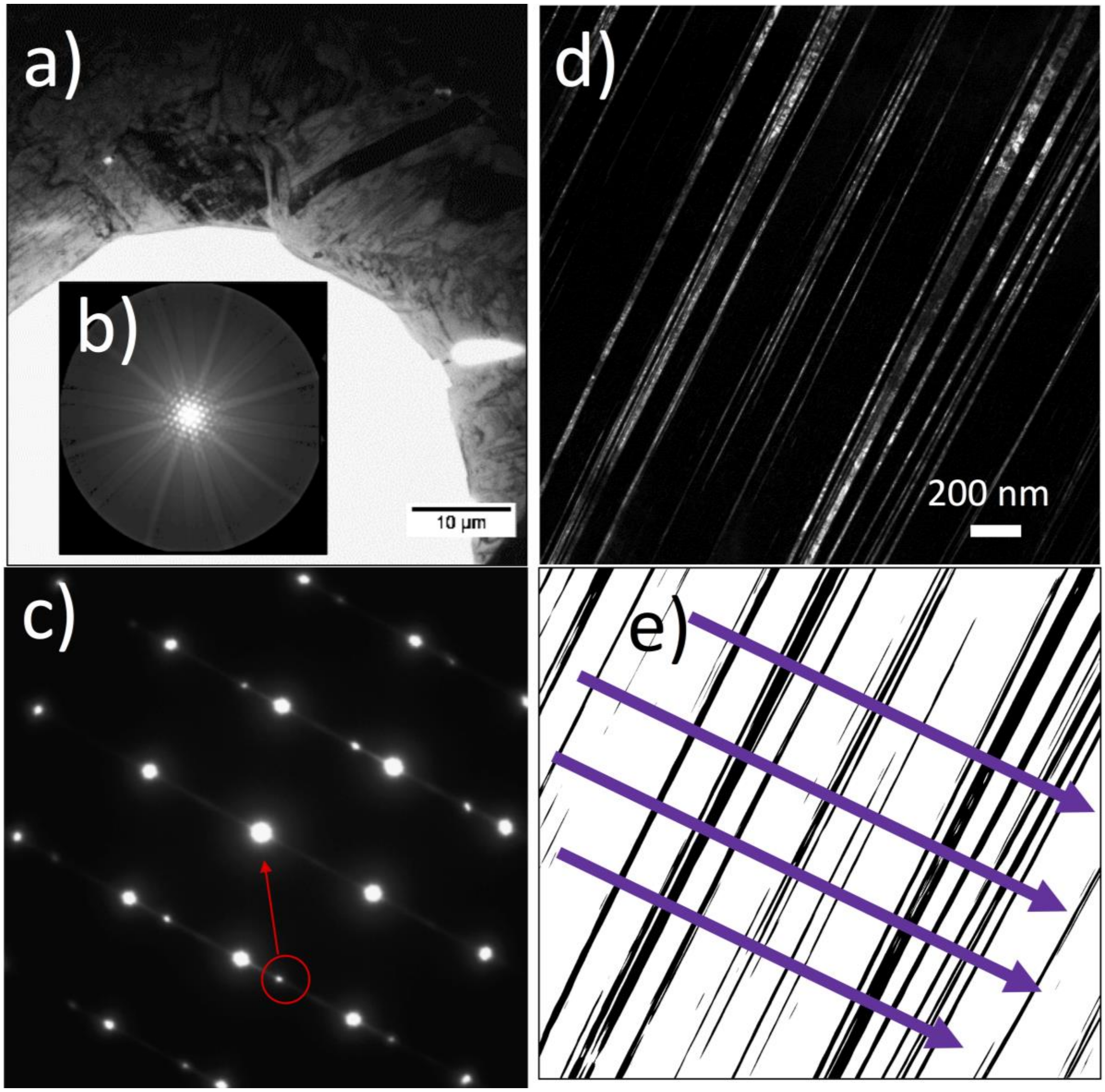

Figure B-2: Imaging techniques for TEM-based methods used to evaluate the spacing and thickness of planar defects in interrupted samples. a) BF-TEM survey, b) CBED survey, c) SAED selection of appropriate reflections (in this case twinning), d) DF-TEM imaging and e) image processing.

C. Thermal Imaging, Thermal Analysis and Fracture Surfaces

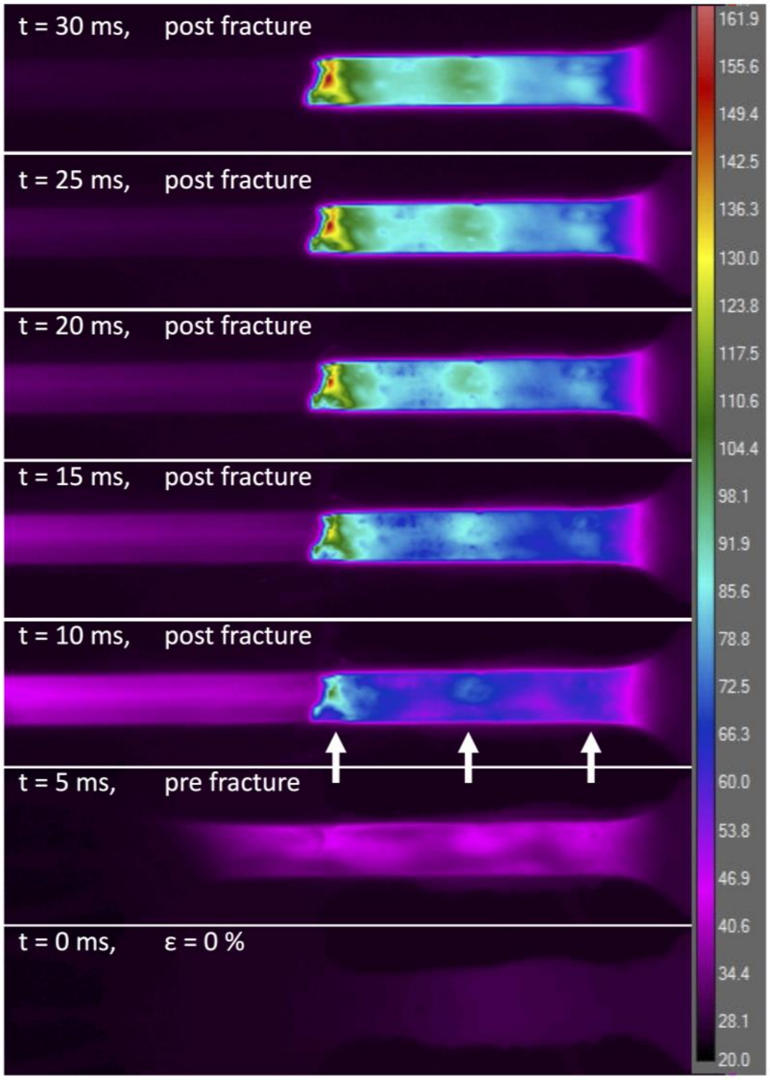

Figure C-1: Thermal images recorded at 200 fps by a calibrated infrared camera as a function of strain, with indicated time stamps corresponding to a $\dot{\varepsilon} = 2x10^2$ /s test. The arrows indicate localized hot-spots (multiple necking initiation points) with the left-most being the eventual fracture surface.

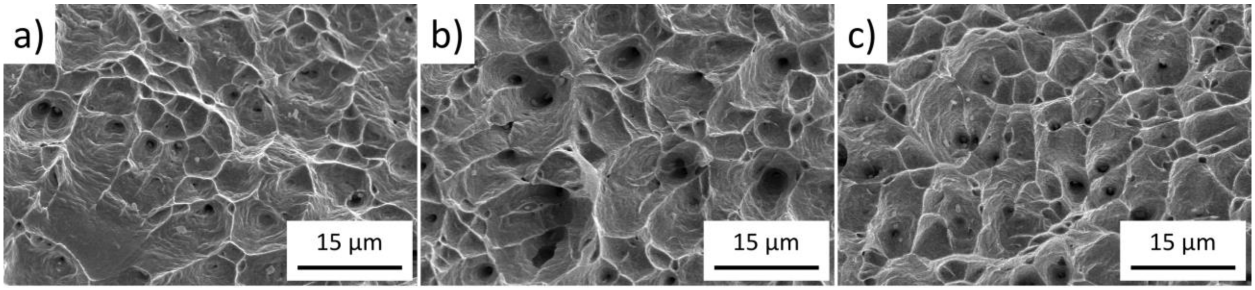

Figure C-2: SEM fracture surface images of the Fe-25Mn-3Al-3Si alloy (0.95 mm thick plate) pulled to failure at a) $\dot{\varepsilon} = 2x10^{2}$ ε/s, b) $\dot{\varepsilon} = 2x10^{1}$ ε/s and c) $\dot{\varepsilon} = 2x10^{-2}$ ε/s. All fracture surfaces showed evidence of considerable coalescence of micro-voids.

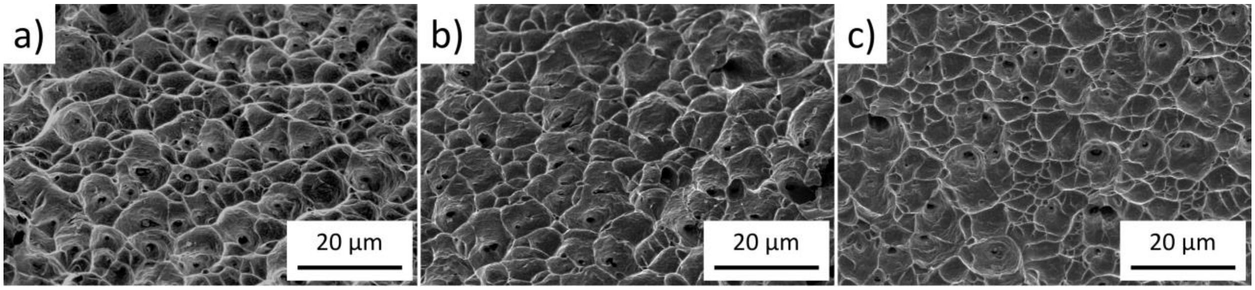

Figure C-3: SEM fracture surface images of the Fe-25Mn-3Al-3Si alloy (1.15 mm thick plate) pulled to failure at a) $\dot{\varepsilon} = 2x10^{2}$ ε/s, b) $\dot{\varepsilon} = 2x10^{-2}$ ε/s and c) $\dot{\varepsilon} = 2x10^{-4}$ ε/s. All fracture surfaces showed characteristics of extensive micro-void coalescence.

D. Medium-Mn Alloy Design Process

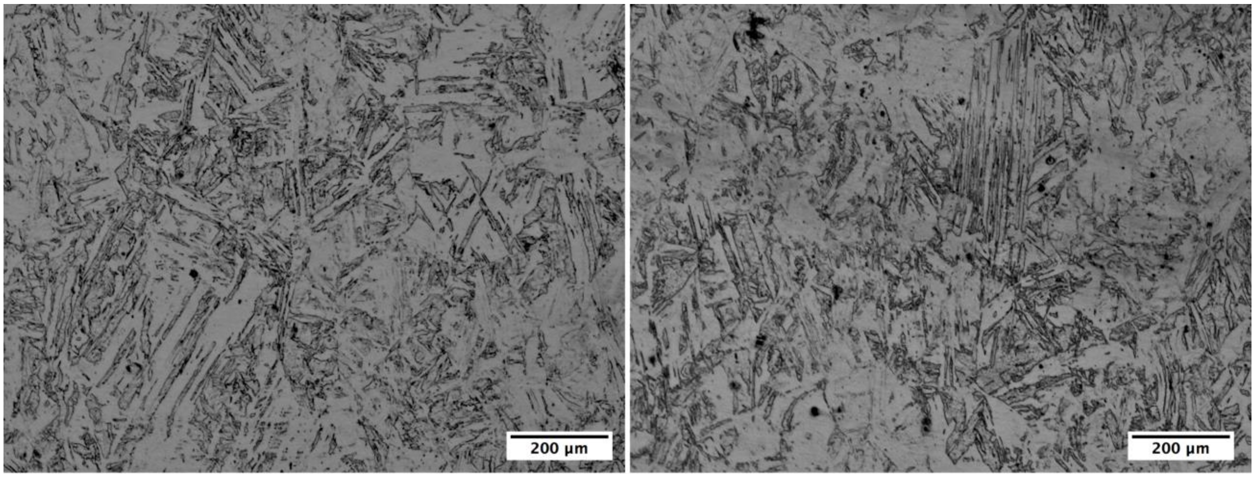

Figure D-1: Optical micrographs of the cold-rolled microstructure Fe-12Mn-3Al-0.05C (wt%) steel, after etching with 10% nital. The rolling direction is in the vertical direction.

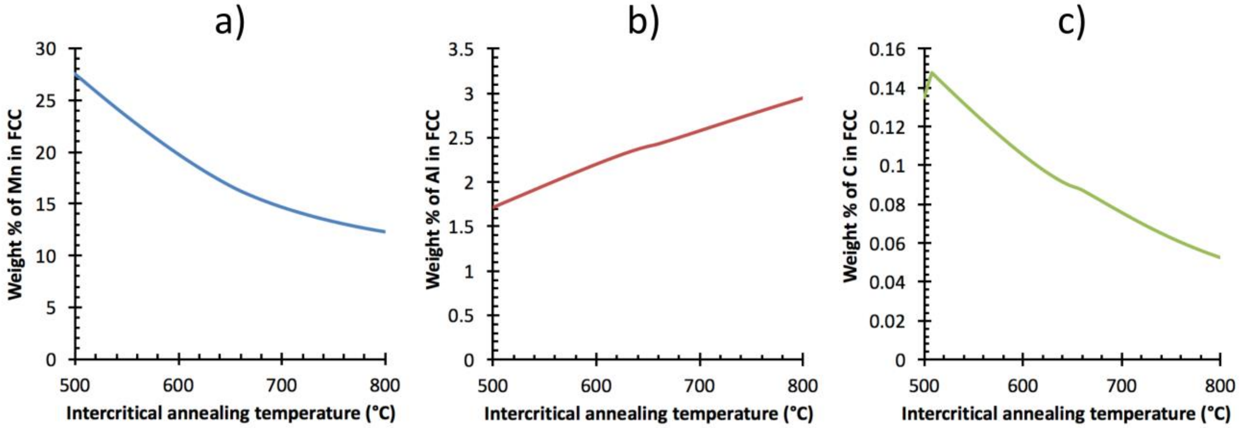

Figure D-2: Thermo-Calc® predictions of austenite composition of a) Mn b) Al and c) C, based on an FCC lattice, plotted as a function of intercritical annealing temperature for an alloy with a nominal bulk composition of Fe-12Mn-3Al-0.05C (weight %).

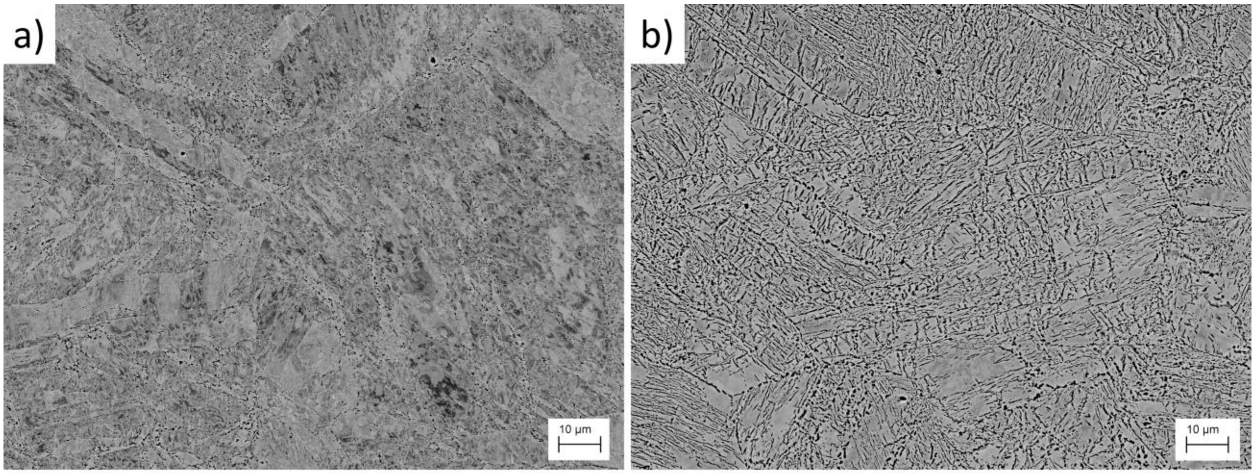

Figure D-3: Backscatter electron images of the Fe-12Mn-3Al-0.05C (wt%) steel, after annealing for a) 0.5 h and b) 8 h shows an increase in content of a dark ultrafine-grained phase (austenite).

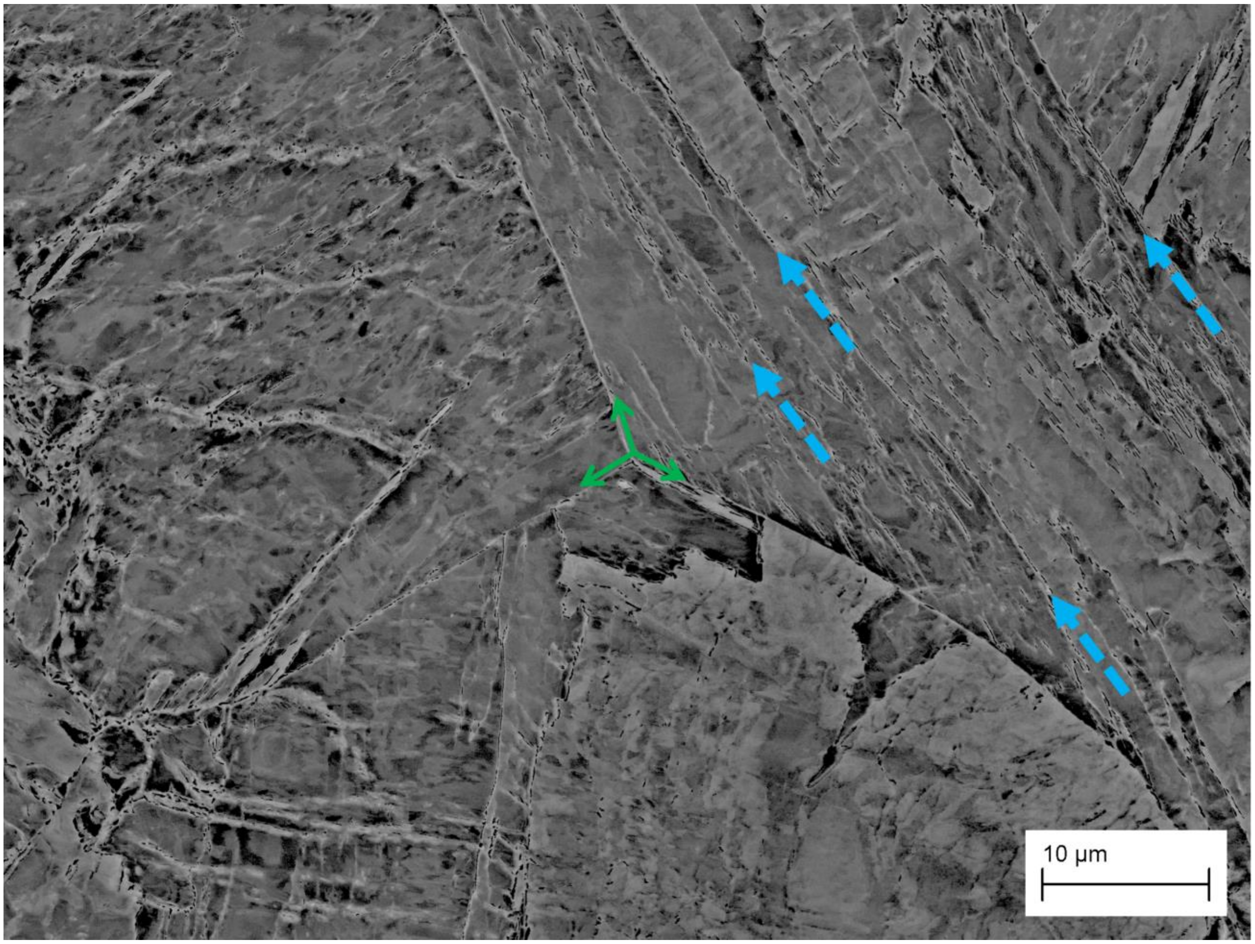

Figure D-4: Backscatter electron image of the Fe-12Mn-3Al-0.05C (wt%) steel annealed for 0.5 h and etched with 10% nital. Austenite can nucleate on prior austenite grain boundaries (solid green arrows) or parent martensite-lath boundaries (dashed blue arrows).

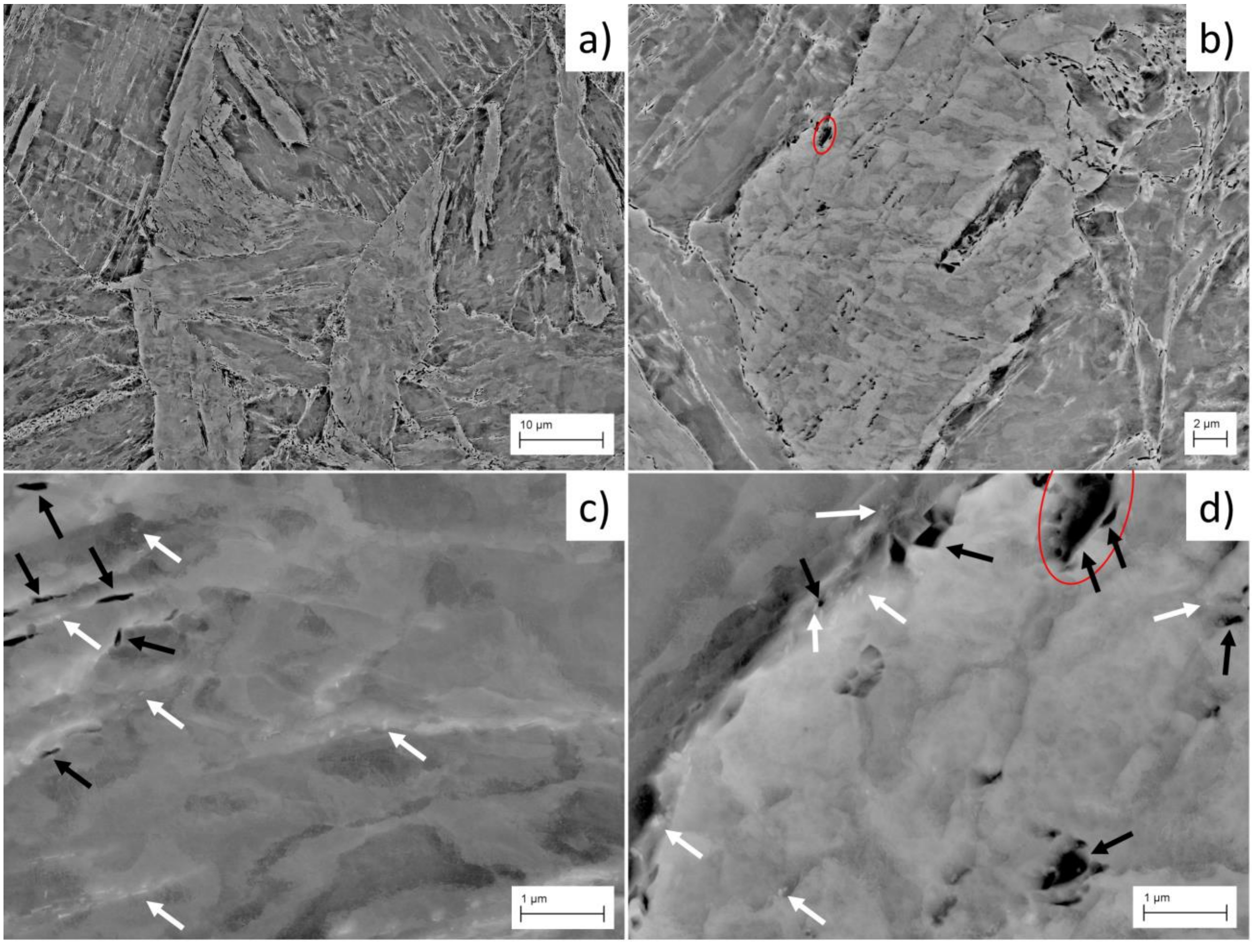

Figure D-5: Backscatter electron images of the Fe-12Mn-3Al-0.05C (wt%) steel annealed for 0.5 h and etched with 10% nital. a) and b) are medium magnification views showing that the nital etched the UFG phase. High-mag views in c) and d) of the UFG austenite (dark arrows). Other fine particles (white arrows) are also observed in close proximity to the revereted austenite, which were not etched away.

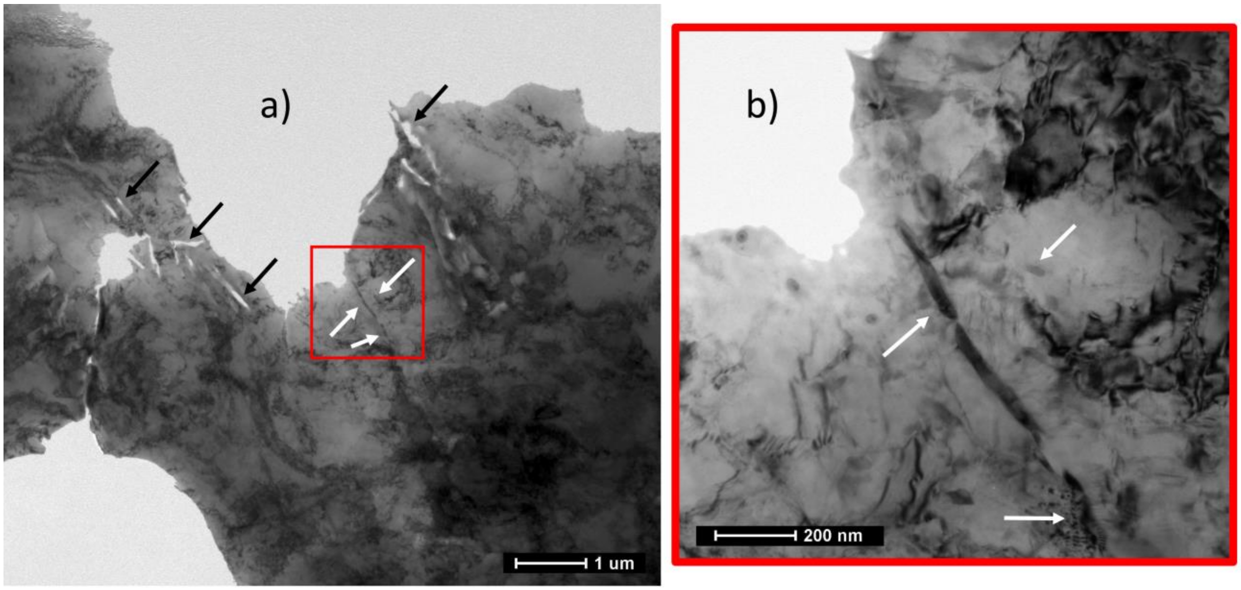

Figure D-6: BF-TEM images of the Fe-12Mn-3Al-0.05C (wt%) steel annealed for 0.5 h and electropolished. Black arrows indicate austenite that is preferentially electropolished. White arrows in a) are shown at higher magnification in b) and reveal particles that were not preferentially electropolished.

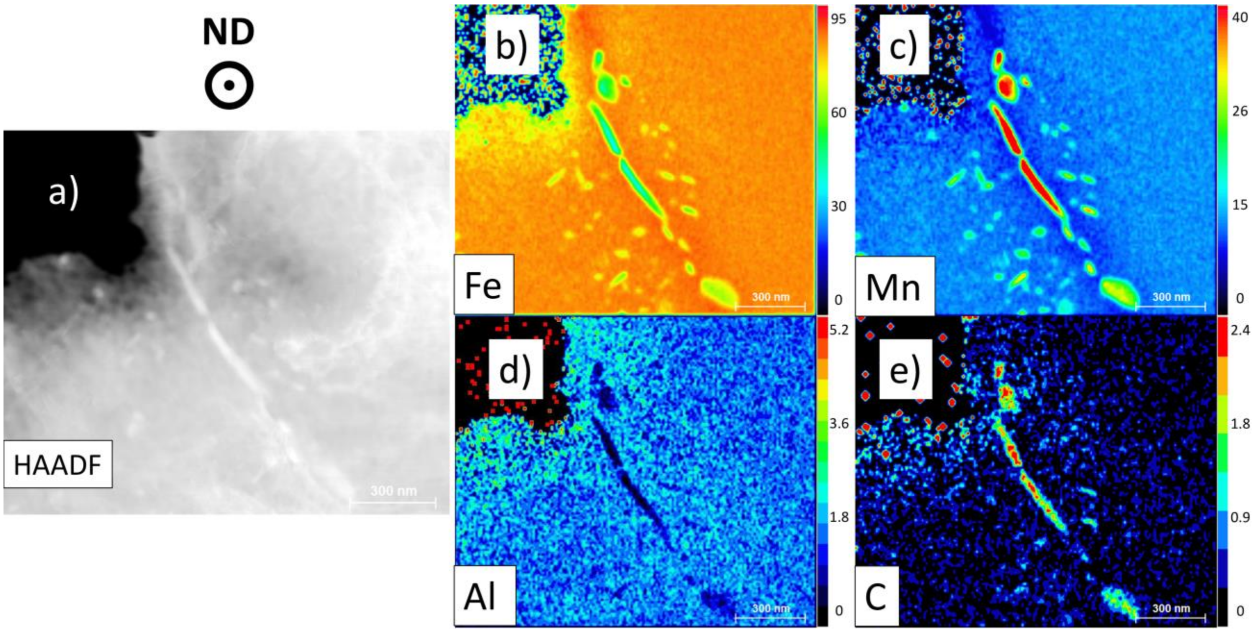

Figure D-7: STEM-EDS scans of the sample in Figure D-6. A) HAADF image and hypermaps of composition in wt% plotted for b) Fe, c) Mn, d) Al, and e) C show some of the particles are extremely rich in Mn and C as compared to other particles.

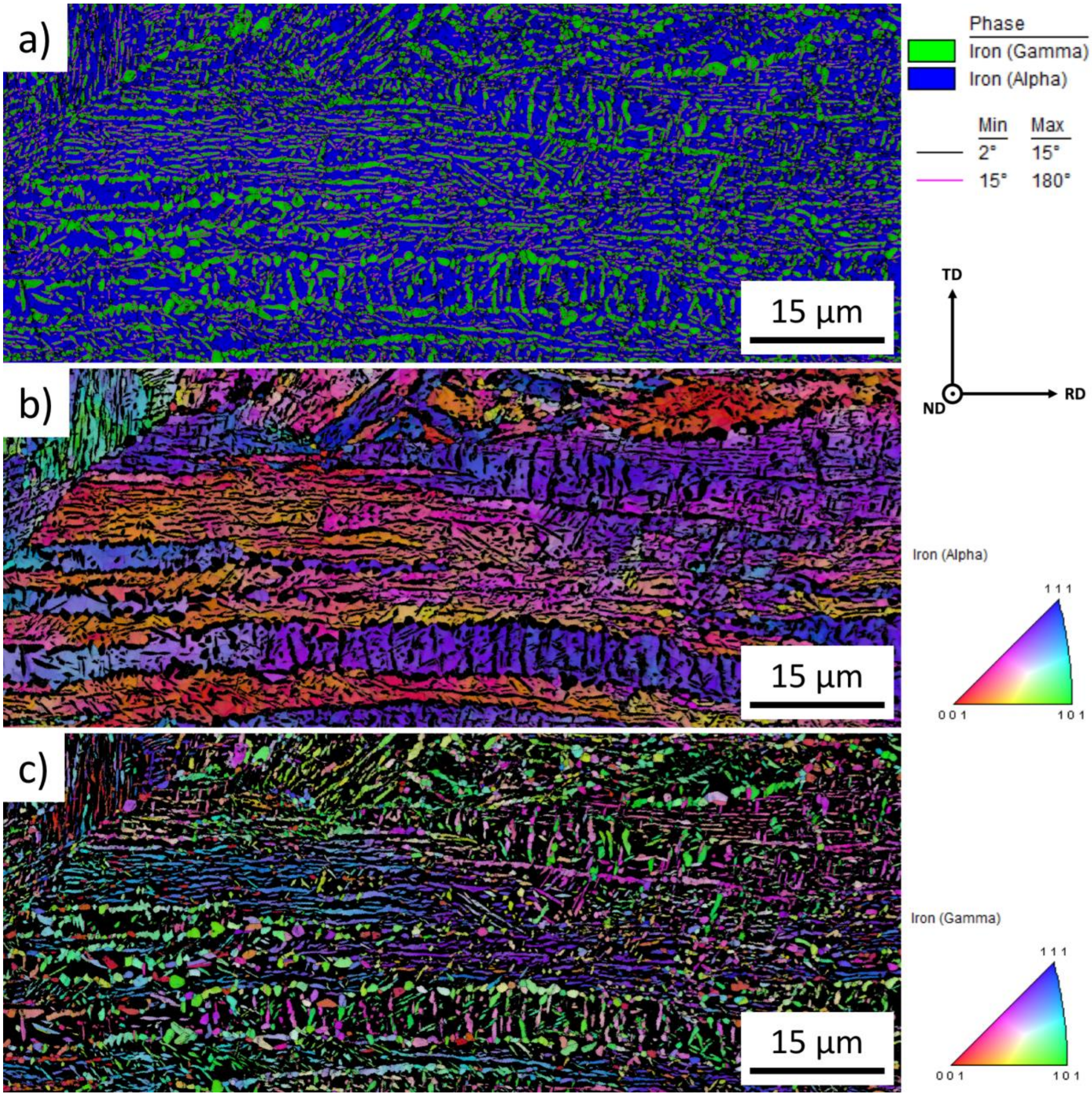

Figure D-8: Fe-12Mn-3Al-0.05C (wt%) annealed for 48 h at 585 °C. EBSD maps with a) image quality, phase and grain boundaries, b) image quality and ferrite/martensite IPF and c) image quality and austenite IPF.

E. Measurements of Lattice Constants in High-Mn Steels at Low and High Temperatures

X-ray diffraction experiments were conducted at Oak Ridge National Lab (ORNL) to study the effect of temperature on lattice constants for Fe-22/25/28Mn-3Al-3Si alloys. These results allowed for a computational collaboration at the MPIE to determine the effect of temperature on stacking fault energy. The temperature-dependent XRD patterns were collected using an X-ray diffractometer (PANAlytical X'Pert MPD Pro) with Cu Kα radiation ($\lambda_{K\alpha1}$ = 1.54060 and $\lambda_{K\alpha2}$ = 1.54443 Å), equipped with an Anton Paar XRK-900 heating stage and Oxford PheniX Cryogenic Stage. Prior to XRD measurements at each temperature, 3 minutes of waiting time was set for temperature equilibration. The 2θ step size and scan rate for each measurement were 0.0167113° and 0.107815 °/s, respectively. The XRD measurements using the heating stage were performed in an Ar environment, while those in the cryogenic stage were under vacuum.

XRD was performed to measure austenite lattice constants for three alloys (Fe-22/25/28Mn-3Al-3Si) from temperatures of 27 K to 998 K. As seen in room temperature XRD measurements in Figure E-1, increasing Mn-content decreases the two-theta diffraction angle of austenite (increases austenite lattice constant, based on Braggs' law). Figure E-2 shows that as temperature and Mn-content increases, the austenite lattice constant increases. This is due to thermal expansion and an increased austenite stability from alloying. Specific to automotive application environments, an increase in temperature from 298 to 473 Kelvin increases the austenite lattice constant of the Fe-25Mn-3Al-3Si alloy from 3.617 to 3.628 Å. Thermal expansion coefficients for each fully austenitic alloy (shown in Table E-1) were calculated using the quotient of each alloy's linear slope (provided in Table E-1) and the room temperature lattice constant (see equation E-1). Andres et al. [217][218] measured the coefficient of thermal expansion for a Fe-0.76C-0.24Si-0.91Mn-0.013P (wt. %) steel to be 2.065 x 10^{-5} K^{-1}. In this work, the thermal expansion coefficient of the 28Mn and 25Mn alloys are respectively 2.169*10^{-5} K^{-1} and 2.168x10^{-5} K^{-1}. The 28 and 25Mn alloys are also both TWIP-dominated at room temperature, while the 22Mn alloy is TRIP-dominated at room temperature and has a slightly lower thermal expansion coefficient (2.155x10^{-5} K^{-1}).

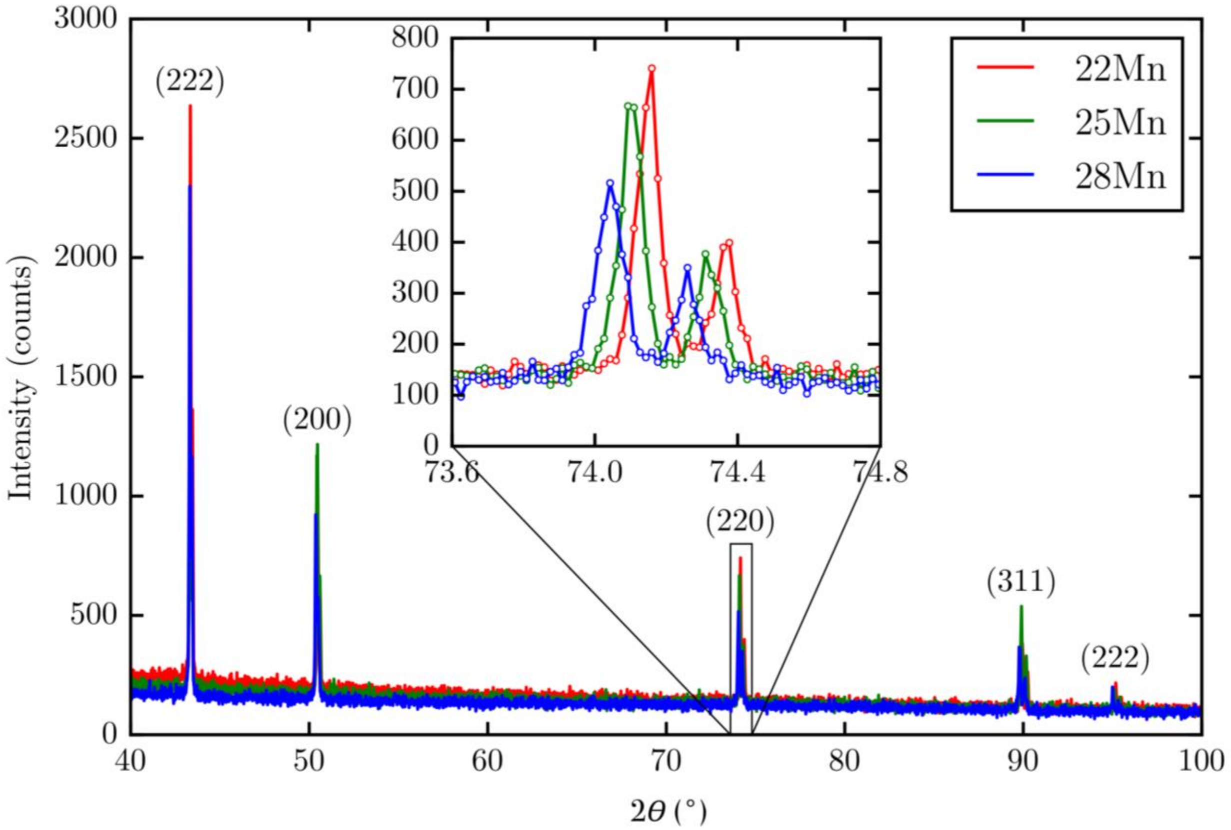

Figure E-1: XRD measurements of Fe-22/25/28Mn-3Al-3Si alloys, acquired at 298 K, with the first five allowable austenite reflections labeled. A (220) austenite inset is provided to illustrate the effect of Mn-content on the shift in diffraction angle and thus change in austenite lattice constant.

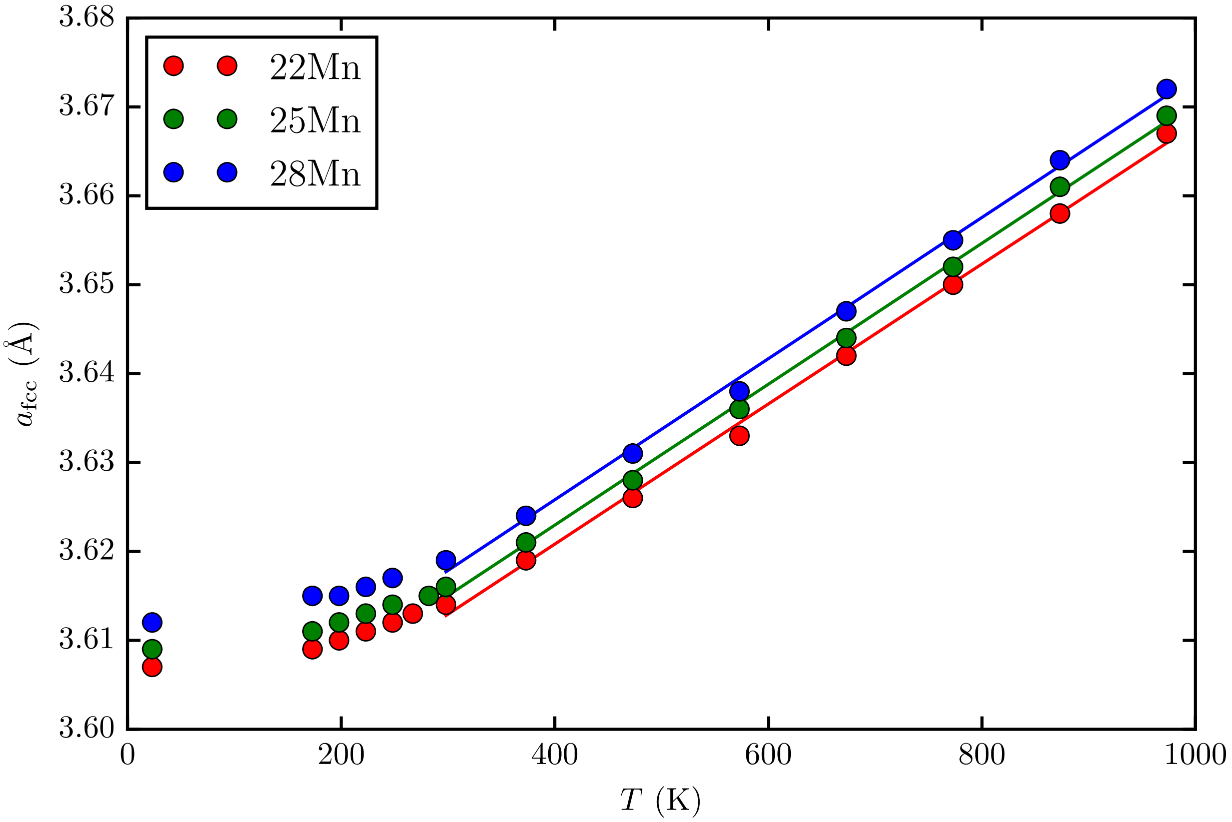

Figure E-2: Austenite lattice constants, calculated based on XRD measurements of Fe-22/25/28Mn-3Al-3Si alloys, plotted as a function of temperature (heating in Ar atmosphere and cooling under vacuum). 298 K and above linear fits yield thermal expansion coefficients.

$$\alpha_L = \frac{1}{L}\frac{dL}{dT} \qquad \text{(equation E-1)}$$

Table E-1: Thermal expansion coefficients calculated for Fe-22/25/28Mn-3Al-3Si (wt. %) alloys

	Fe-28Mn-3Al-3Si	Fe-25Mn-3Al-3Si	Fe-22Mn-3Al-3Si
Slope of linear fit in Figure E-2	0.0000785 ÅK^{-1} (R^2 = 0.996)	0.0000784 ÅK^{-1} (R^2 = 0.997)	0.0000779 ÅK^{-1} (R^2 = 0.997)
austenite lattice constant at T_{room}	3.620 Å ± 0.001	3.617 Å ± 0.001	3.615 Å ± 0.001
thermal expansion coefficient (α_L)	2.169x10^{-5} K^{-1}	2.168x10^{-5} K^{-1}	2.155x10^{-5} K^{-1}

REFERENCES

[1] J. Dykeman, “Advanced High Strength Steel - Recent Progress, Ongoing Challenges, and Future Opportunities,” in *Proceedings of the International Symposium on New Developments in Advanced High-Strength Sheet Steels*, 2013, pp. 15–28.

[2] P. J. Belanger, P. J. Hall, J. J. Coryell, and J. P. Singh, “Automotive Body Press-Hardened Steel Trends,” in *Proceedings of the International Symposium on New Developments in Advanced High-Strength Sheet Steels*, 2013, pp. 239–250.

[3] “Advanced High Strength Steel (AHSS) Application Guidelines,” *International Iron & Steel Institute, Committee on Automotive Applications*, 2009. [Online]. Available: www.worldautosteel.org.

[4] “EPA and NHTSA Set Standards to Reduce Greenhouse Gases and Improve Fuel Economy for Model Years 2017-2025 Cars and Light Trucks,” 2012. Available: https://www.epa.gov/regulations-emissions-vehicles-and-engines/final-rule-model-year-2017-and-later-light-duty-vehicle.

[5] “IIHS Crashworthiness Evaluation Programs and the U.S. Vehicle Fleet,” *Highw. Loss Data Inst. Bull.*, vol. 30, no. 7, pp. 1–10, 2013.

[6] B. De Cooman, K. Chin, and J. Kim, “High Mn TWIP steels for automotive applications,” *New Trends Dev. Automot. Syst. Eng.*, pp. 101–128, 2011.

[7] P. J. Gibbs, “Design considerations for the third generation advanced high strength steel,” Ph.D. dissertation, Colorado School of Mines, 2012.

[8] B. C. De Cooman, O. Kwon, and K.-G. Chin, “State-of-the-knowledge on TWIP steel,” *Mater. Sci. Technol.*, vol. 28, no. 5, pp. 513–527, 2012.

[9] D. Raabe *et al.*, “Alloy Design, Combinatorial Synthesis, and Microstructure Property Relations for Low-Density Fe-Mn-Al-C Austenitic Steels,” *JOM*, vol. 66, no. 9, pp. 1845–1856, 2014.

[10] M. Seth, V. J. Vohnout, and G. S. Daehn, “Formability of steel sheet in high velocity impact,” *J. Mater. Process. Technol.*, vol. 168, no. 3, pp. 390–400, 2005.

[11] S. Hiermaier, “Structures Under Crash and Impact: Continuum Mechanics, Discretization and Experimental Characterization,” New York, 2008.

[12] D. T. Pierce, J. A. Jiménez, J. Bentley, D. Raabe, and J. E. Wittig, “The influence of stacking fault energy on the microstructural and strain-hardening evolution of Fe-Mn-Al-Si steels during tensile deformation,” *Acta Mater.*, vol. 100, pp. 178–190, 2015.

[13] I. Choi, D. Son, S. Kim, D. K. Matlock, and J. G. Speer, “Strain Rate Effects on

Mechanical Stability of Retained Austenite in TRIP Sheet Steels," *SAE World Congr. Exhib.*, vol. 1, no. 1434, pp. 95–107, 2006.

[14] J. A. Jiménez, M. Carsí, O. A. Ruano, and G. Frommeyer, "Effect of testing temperature and strain rate on the transformation behaviour of retained austenite in low-alloyed multiphase steel," *Mater. Sci. Eng. A*, vol. 508, no. 1–2, pp. 195–199, 2009.

[15] J. Talonen, P. Nenonen, G. Pape, and H. Hänninen, "Effect of strain rate on the strain-induced γ → α′-martensite transformation and mechanical properties of austenitic stainless steels," *Metall. Mater. Trans. A.*, vol. 36 A, no. 2, pp. 421–432, 2005.

[16] J. A. Lichtenfeld, M. C. Mataya, and C. J. Van Tyne, "Effect of Strain Rate on Stress-Strain Behaviour of Alloy 309 and 304L Austenitic Stainless Steel," *Metall. Mater. Trans. A*, vol. 37, pp. 147–161, 2006.

[17] J. A. Rodríguez-Martínez, R. Pesci, and A. Rusinek, "Experimental study on the martensitic transformation in AISI 304 steel sheets subjected to tension under wide ranges of strain rate at room temperature," *Mater. Sci. Eng. A*, vol. 528, no. 18, pp. 5974–5982, 2011.

[18] P. Larour, "Strain Rate Sensitivity of Automotive Sheet Steels,", Ph.D. dissertation, RWTH-Aachen, 2010.

[19] Poling W., "Tensile Deformation of Third Generation Advanced High Strength Sheet Steels Under High Strain Rates", Ph.D. dissertation, Colorado School of Mines, 2016.

[20] S. Lee, Y. Estrin, and B. C. De Cooman, "Effect of the strain rate on the TRIP-TWIP transition in austenitic Fe-12 pct Mn-0.6 pct C TWIP Steel," *Metall. Mater. Trans. A.*, vol. 45, no. 2, pp. 717–730, 2014.

[21] H. K. Yang, Y. Z. Tian, Z. J. Zhang, and Z. F. Zhang, "Different strain rate sensitivities between Fe-22Mn-0.6C and Fe-30Mn-3Si-3Al twinning-induced plasticity steels," *Mater. Sci. Eng. A*, vol. 655, pp. 251–255, 2016.

[22] D. T. Pierce, "The Influence of Manganese Content and Temperature on the Relative FCC/HCP Phase Stability and Strain-Hardening Behavior of High-Manganese TRIP/TWIP Steels", Ph.D. dissertation Vanderbilt University, 2014.

[23] D. T. Pierce, J. A. Jimenez, J. Bentley, D. Raabe, C. Oskay, and J. E. Wittig, "The influence of manganese content on the stacking fault and austenite/ε-martensite interfacial energies in Fe-Mn-(Al-Si) steels investigated by experiment and theory," *Acta Mater.*, vol. 68, pp. 238–253, 2014.

[24] D. T. Pierce, J. Bentley, J. A. Jiménez, and J. E. Wittig, "Stacking fault energy measurements of Fe-Mn-Al-Si austenitic twinning-induced plasticity steels," *Scr. Mater.*, vol. 66, no. 10, pp. 753–756, 2012.

[25] D. T. Pierce, K. Nowag, A. Montagne, J. A. Jiménez, J. E. Wittig, and R. Ghisleni, “Single crystal elastic constants of high-manganese transformation- and twinning-induced plasticity steels determined by a new method utilizing nanoindentation,” *Mater. Sci. Eng. A*, vol. 578, pp. 134–139, 2013.

[26] I. Gutierrez-Urrutia and D. Raabe, “Multistage strain hardening through dislocation substructure and twinning in a high strength and ductile weight-reduced Fe-Mn-Al-C steel,” *Acta Mater.*, vol. 60, no. 16, pp. 5791–5802, 2012.

[27] Y.-K. Lee and J. Han, “Current opinion in medium manganese steel,” *Mater. Sci. Technol.*, vol. 31, no. 7, pp. 843–856, 2015.

[28] Y. F. Shen, X. X. Li, X. Sun, Y. D. Wang, and L. Zuo, “Twinning and martensite in a 304 austenitic stainless steel,” *Mater. Sci. Eng. A*, vol. 552, pp. 514–522, 2012.

[29] O. Grässel, G. Frommeyer, C. Derder, and H. Hofmann, “Phase Transformations and Mechanical Properties of Fe-Mn-Si-Al TRIP-Steels", *J. Phys. IV France*, vol. 7, no. C5, pp. 383–388, 1997.

[30] O. Grässel, L. Krüger, G. Frommeyer, and L. W. Meyer, “High strength Fe-Mn-(Al, Si) TRIP/TWIP steels development - properties - application,” *Int. J. Plast.*, vol. 16, no. 10, pp. 1391–1409, 2000.

[31] D. T. Pierce, J. A. Jiménez, J. Bentley, D. Raabe, and J. E. Wittig, “The influence of stacking fault energy on the microstructural and strain-hardening evolution of Fe-Mn-Al-Si steels during tensile deformation,” *Acta Mater.*, vol. 100, pp. 178–190, 2015.

[32] J. Ronevich, "Hydrogen embrittlment in advanced high strength steels", M.S. Thesis, Colorado School of Mines, Golden, CO, 2009.

[33] D. K. Matlock and J. G. Speer, “Design Considerations for the Next Generation of Advanced High Strength Sheet Steels,” *3rd Int. Conf. Adv. High Strength Steels*, pp. 1–8, (Springer, London), 2006.

[34] R. Schultz and A. Abraham, “Metallic material trends for North American light vehicles,” *Gt. Des. Steel Semin. Am. Iron*, 2007. Available: http://www.steelsustainability.org/~/media/Files/Autosteel/Great%20Designs%20in%20Steel/GDIS%202009/06%20-%20Metallic%20Material%20Trends%20For%20North%20American%20Light%20Vehicles.pdf.

[35] B. C. De Cooman, “Structure-properties relationship in TRIP steels containing carbide-free bainite,” *Curr. Opin. Solid State Mater. Sci.*, vol. 8, no. 3–4, pp. 285–303, 2004.

[36] D. K. Matlock and J. G. Speer, “Third generation of AHSS: microstructure design

concepts," in *Microstructure and Texture in Steels*, A. Haldar, S. Suwas, and D. Bhattacharjee, Eds. London: Springer, 2009, pp. 185–205.

[37] F. B. Pickering, "Toward Improved Toughness and Ductility," *Climax Molybdenum Dev. Co in Kyoto.*, pp. 9–32, 1971.

[38] D. K. Matlock, G. Krauss, and F. Zia-Ebrahimi, "Deformation, Processing and Structure," *ASM, Met. Park. OH*, p. 47-87, 1984.

[39] S. Lee and B. C. De Cooman, "On the selection of the optimal intercritical annealing temperature for medium Mn TRIP steel," *Metall. Mater. Trans. A Phys. Metall. Mater. Sci.*, vol. 44, no. 11, pp. 5018–5024, 2013.

[40] X. G. Wang, L. Wang, and M. X. Huang, "Kinematic and thermal characteristics of Lüders and Portevin-Le Châtelier bands in a medium Mn transformation-induced plasticity steel," *Acta Mater.*, vol. 124, pp. 17–29, 2017.

[41] B. Sun *et al.*, "Discontinuous strain-induced martensite transformation related to the Portevin-Le Chatelier effect in a medium manganese steel," *Scr. Mater.*, vol. 133, pp. 9–13, 2017.

[42] S. J. Lee, J. Kim, S. N. Kane, and B. C. De Cooman, "On the origin of dynamic strain aging in twinning-induced plasticity steels," *Acta Mater.*, vol. 59, no. 17, pp. 6809–6819, 2011.

[43] H. Luo, H. Dong, and M. Huang, "Effect of intercritical annealing on the Lüders strains of medium Mn transformation-induced plasticity steels," *Mater. Des.*, vol. 83, pp. 42–48, 2015.

[44] H. Aboulfadl, J. Deges, P. Choi, and D. Raabe, "Dynamic strain aging studied at the atomic scale," *Acta Mater.*, vol. 86, pp. 34–42, 2015.

[45] E. Emadoddin, A. Akbarzadeh, and G. H. Daneshi, "Correlation between Luder strain and retained austenite in TRIP-assisted cold rolled steel sheets," *Mater. Sci. Eng. A*, vol. 447, no. 1–2, pp. 174–179, 2007.

[46] M. Callahan, O. Hubert, F. Hild, A. Perlade, and J. H. Schmitt, "Coincidence of strain-induced TRIP and propagative PLC bands in Medium Mn steels," *Mater. Sci. Eng. A*, vol. 704, pp. 391–400, 2017.

[47] K. Davut and S. Zaefferer, "The effect of size and shape of austenite grains on the mechanical properties of a low-alloyed TRIP steel," *Steel Res. Int.*, vol. 83, no. 6, pp. 584–589, 2012.

[48] Y. Ma, "Medium-manganese steels processed by austenite-reverted-transformation annealing for automotive applications," *Mater. Sci. Technol. (United Kingdom)*, vol. 33, no. 15, pp. 1713–1727, 2017.

[49] B. Hu, H. Luo, F. Yang, and H. Dong, “Recent progress in medium-Mn steels made with new designing strategies, a review,” *J. Mater. Sci. Technol.*, vol. 33, issue 12, pp. 6–13, 2017.

[50] A. Arlazarov, M. Gouné, O. Bouaziz, A. Hazotte, G. Petitgand, and P. Barges, “Evolution of microstructure and mechanical properties of medium Mn steels during double annealing,” *Mater. Sci. Eng. A*, vol. 542, pp. 31–39, 2012.

[51] J. Han, S. J. Lee, C. Y. Lee, S. Lee, S. Y. Jo, and Y. K. Lee, “The size effect of initial martensite constituents on the microstructure and tensile properties of intercritically annealed Fe-9Mn-0.05C steel,” *Mater. Sci. Eng. A*, vol. 633, pp. 9–16, 2015.

[52] J. Han *et al.*, “The effects of prior austenite grain boundaries and microstructural morphology on the impact toughness of intercritically annealed medium Mn steel,” *Acta Mater.*, vol. 122, 2016, pp. 199–206, 2017.

[53] M. Koyama *et al.*, “Bone-like crack resistance in hierarchical metastable nanolaminate steels,” *Science*, vol. 355, pp. 1055–1057, 2017.

[54] S. Lee and B. C. De Cooman, “Annealing Temperature Dependence of the Tensile Behavior of 10 pct Mn Multi-phase TWIP-TRIP Steel,” *Metall. Mater. Trans. A Phys. Metall. Mater. Sci.*, vol. 45, no. 13, pp. 6039–6052, 2014.

[55] S. Lee, W. Woo, and B. C. de Cooman, “Analysis of the Tensile Behavior of 12 pct Mn Multi-phase ($\alpha + \gamma$) TWIP + TRIP Steel by Neutron Diffraction,” *Metall. Mater. Trans. A*, vol. 47, no. 5, pp. 2125–2140, 2016.

[56] R. Zhang, W. Q. Cao, Z. J. Peng, J. Shi, H. Dong, and C. X. Huang, “Intercritical rolling induced ultra fine microstructure and excellent mechanical properties of the medium-Mn steel,” *Mater. Sci. Eng. A*, vol. 583, pp. 84–88, 2013.

[57] S. Lee and B. C. De Cooman, “Tensile behavior of intercritically annealed ultra-fine grained 8% Mn multi-phase steel,” *Steel Res. Int.*, vol. 86, no. 10, pp. 1170–1178, 2015.

[58] M.-M. Wang, C. C. Tasan, D. Ponge, and D. Raabe, “Spectral TRIP enables ductile 1.1 GPa martensite,” *Acta Mater.*, vol. 111, no. April, pp. 262–272, 2016.

[59] Y. Zhang, L. Wang, K. O. Findley, and J. G. Speer, “Influence of Temperature and Grain Size on Austenite Stability in Medium Manganese Steels,” *Metall. Mater. Trans. A Phys. Metall. Mater. Sci.*, vol. 48, no. 5, pp. 2140–2149, 2017.

[60] O. Bouaziz, S. Allain, C. P. Scott, P. Cugy, and D. Barbier, “High manganese austenitic twinning induced plasticity steels: A review of the microstructure properties relationships,” *Curr. Opin. Solid State Mater. Sci.*, vol. 15, no. 4, pp. 141–168, 2011.

[61] K. Jeong, J. E. Jin, Y. S. Jung, S. Kang, and Y. K. Lee, "The effects of Si on the mechanical twinning and strain hardening of Fe-18Mn-0.6C twinning-induced plasticity steel," *Acta Mater.*, vol. 61, no. 9, pp. 3399–3410, 2013.

[62] G. Frommeyer, U. Brüx, and P. Neumann, "Supra-Ductile and High-Strength Manganese-TRIP/TWIP Steels for High Energy Absorption Purposes," *ISIJ Int.*, vol. 43, no. 3, pp. 438–446, 2003.

[63] G. Frommeyer and U. Brüx, "Microstructures and mechanical properties of high-strength Fe-Mn-Al-C light-weight TRIPLEX steels," *Steel Res. Int.*, vol. 77, no. 9, p. 627, 2006.

[64] Y. N. Dastur and W. C. Leslie, "Mechanism of work hardening in Hadfield manganese steel," *Metall. Trans. A*, vol. 12, no. 5, pp. 749–759, 1981.

[65] S. Allain, O. Bouaziz, and J. P. Chateau, "Thermally activated dislocation dynamics in austenitic FeMnC steels at low homologous temperature," *Scr. Mater.*, vol. 62, no. 7, pp. 500–503, 2010.

[66] S. Allain, J. P. Chateau, O. Bouaziz, S. Migot, and N. Guelton, "Correlations between the calculated stacking fault energy and the plasticity mechanisms in Fe-Mn-C alloys," *Mater. Sci. Eng. A*, vol. 387–389, pp. 158–162, 2004.

[67] J. Kim, S. J. Lee, and B. C. De Cooman, "Effect of Al on the stacking fault energy of Fe-18Mn-0.6C twinning-induced plasticity," *Scr. Mater.*, vol. 65, no. 4, pp. 363–366, 2011.

[68] S. Curtze and V. T. Kuokkala, "Dependence of tensile deformation behavior of TWIP steels on stacking fault energy, temperature and strain rate," *Acta Mater.*, vol. 58, no. 15, pp. 5129–5141, 2010.

[69] D. Raabe *et al.*, "Ab initio-guided design of twinning-induced plasticity steels," *MRS Bull.*, vol. 41, no. 4, pp. 320–325, 2016.

[70] K. Ishida and T. Nishizawa, *Trans. Jpn. Int. Met.*, vol. 15, pp. 225–231, 1974.

[71] R. E. Schramm and R. P. Reed, "Stacking fault energies of seven commercial austenitic stainless steels," *Metall. Trans. A*, vol. 6, no. 7, pp. 1345–1351, 1975.

[72] A. Dumay, J. P. Chateau, S. Allain, S. Migot, and O. Bouaziz, "Influence of addition elements on the stacking-fault energy and mechanical properties of an austenitic Fe-Mn-C steel," *Mater. Sci. Eng. A*, vol. 483–484, no. 1–2 C, pp. 184–187, 2008.

[73] A. Saeed-Akbari, J. Imlau, U. Prahl, and W. Bleck, "Derivation and variation in composition-dependent stacking fault energy maps based on subregular solution model in high-manganese steels," *Metall. Mater. Trans. A*, vol. 40, no. 13, pp. 3076–3090, 2009.

[74] M. Pozuelo, J. E. Wittig, J. A. Jiménez, and G. Frommeyer, "Enhanced mechanical

properties of a novel high-nitrogen Cr-Mn-Ni-Si austenitic stainless steel via TWIP/TRIP effects," *Metall. Mater. Trans. A*, vol. 40, no. 8, pp. 1826–1834, 2009.

[75] O. Bouaziz, S. Allain, C. P. Scott, P. Cugy, and D. Barbier, "High Manganese Austenitic Twinning Induced Plasticity Steels: A Review of the Microstructure Properties Relationships," *Curr. Opin. Solid State Mater. Sci*, vol. 15, pp. 141–168, 2011.

[76] B. C. De Cooman, Y. Estrin, and S. K. Kim, "Twinning-induced plasticity (TWIP) steels," *Acta Mater.*, pp. 1–80, 2017.

[77] D. R. Steinmetz *et al.*, "Revealing the strain-hardening behavior of twinning-induced plasticity steels: Theory, simulations, experiments," *Acta Mater.*, vol. 61, no. 2, pp. 494–510, 2013.

[78] I. Gutierrez-Urrutia and D. Raabe, "Dislocation and twin substructure evolution during strain hardening of an Fe-22 wt.% Mn-0.6 wt.% C TWIP steel observed by electron channeling contrast imaging," *Acta Mater.*, vol. 59, no. 16, pp. 6449–6462, 2011.

[79] S. Kibey, J. B. Liu, D. D. Johnson, and H. Sehitoglu, "Predicting twinning stress in fcc metals: Linking twin-energy pathways to twin nucleation," *Acta Mater.*, vol. 55, no. 20, pp. 6843–6851, 2007.

[80] A. Saeed-Akbari, L. Mosecker, A. Schwedt, and W. Bleck, "Characterization and prediction of flow behavior in high-manganese twinning induced plasticity steels: Part i. mechanism maps and work-hardening behavior," *Metall. Mater. Trans. A*, vol. 43, no. 5, pp. 1688–1704, 2012.

[81] S. L. Wong, M. Madivala, U. Prahl, F. Roters, and D. Raabe, "A crystal plasticity model for twinning- and transformation-induced plasticity," *Acta Mater.*, vol. 118, pp. 140–151, 2016.

[82] T. Jøssang, J. P. Hirth, and C. S. Hartley, "Anisotropic elasticity solutions for dislocation barriers in face-centered cubic crystals," *J. Appl. Phys.*, vol. 36, no. 8, pp. 2400–2406, 1965.

[83] R. E. Reed-Hill and R. Abbaschian, *Physical Metallurgy Principles*, Third ed. Boston: PWS Publishing Company, 1994.

[84] J. P. Hirth, *Theory of Dislocations*, 2nd ed. John Wiley and Sons, 1982.

[85] G. Gottstein, *Physikalische Grundlagen der Materialkunde*, 3rd ed. Berlin: Springer, 2007.

[86] P. B. Chowdhury, H. Sehitoglu, and R. G. Rateick, "Predicting fatigue resistance of nano-twinned materials: Part i - Role of cyclic slip irreversibility and Peierls stress," *Int. J. Fatigue*, vol. 68, pp. 277–291, 2014.

[87] L. Rémy and A. Pineau, “Twinning and strain-induced f.c.c. → h.c.p. transformation on the mechanical properties of CoNiCrMo alloys,” *Mater. Sci. Eng.*, vol. 26, no. 1, pp. 123–132, 1976.

[88] L. Rémy, “The interaction between slip and twinning systems and the influence of twinning on the mechanical behavior of fcc metals and alloys,” *Metall. Trans. A*, vol. 12, no. 3, pp. 387–408, 1981.

[89] S. Allain, J. P. Chateau, and O. Bouaziz, “A physical model of the twinning-induced plasticity effect in a high manganese austenitic steel,” *Mater. Sci. Eng. A*, vol. 387–389, pp. 143–147, 2004.

[90] T. H. Lee, E. Shin, C. S. Oh, H. Y. Ha, and S. J. Kim, “Correlation between stacking fault energy and deformation microstructure in high-interstitial-alloyed austenitic steels,” *Acta Mater.*, vol. 58, no. 8, pp. 3173–3186, 2010.

[91] M. N. Shiekhelsouk, V. Favier, K. Inal, and M. Cherkaoui, “Modelling the behaviour of polycrystalline austenitic steel with twinning-induced plasticity effect,” *Int. J. Plast.*, vol. 25, no. 1, pp. 105–133, 2009.

[92] S. Mahajan, “Critique of mechanisms of formation of deformation, annealing and growth twins: Face-centered cubic metals and alloys,” *Scr. Mater.*, vol. 68, no. 2, pp. 95–99, 2013.

[93] H. Idrissi, K. Renard, L. Ryelandt, D. Schryvers, and P. J. Jacques, “On the mechanism of twin formation in Fe-Mn-C TWIP steels,” *Acta Mater.*, vol. 58, no. 7, pp. 2464–2476, 2010.

[94] S. Miura, J. I. Takamura, and N. Narita, “Orientation Dependance of Flow Stress for Twinning in Silver Crystals,” *Trans. Jpn. Inst. Met.*, no. 9, p. 555, 1968.

[95] J. B. Cohen and J. Weertman, “A Dislocation Model for Twinning in F.C.C. Metals,” *Acta Met.*, vol. 11, no. 8, pp. 996–998, 1963.

[96] I. Gutierrez-Urrutia and D. Raabe, “Dislocation and twin substructure evolution during strain hardening of an Fe-22 wt.% Mn-0.6 wt.% C TWIP steel observed by electron channeling contrast imaging,” *Acta Mater.*, vol. 59, no. 16, pp. 6449–6462, 2011.

[97] H. Idrissi, K. Renard, D. Schryvers, and P. J. Jacques, “On the relationship between the twin internal structure and the work-hardening rate of TWIP steels,” *Scr. Mater.*, vol. 63, no. 10, pp. 961–964, 2010.

[98] G. B. Olson and M. Cohen, “A general mechanism of martensitic nucleation: Part I. General concepts and the FCC->HCP transformation,” *Metall. Trans. A*, vol. 7, no. 11, pp. 1897–1904, 1976.

[99] J. W. Brooks, M. H. Loretto, and R. E. Smallman, “In situ observations of the formation of martensite in stainless steel,” *Acta Metall.*, vol. 27, no. 12, pp. 1829–1838, 1979.

[100] D. T. Pierce, J. A. Jiménez, J. Bentley, D. Raabe, and J. E. Wittig, “Microstructure and Strain Hardening in Tensile-Tested Fe-Mn-Al-Si Steels,” vol. 21 (Suppl 3), pp. 1357–1358, 2015.

[101] B. C. De Cooman, Y. Estrin, and S. K. Kim, “Twinning-induced plasticity (TWIP) steels,” *Acta Mater.*, vol. 142, pp. 283–362, 2018.

[102] S. Cotes, A. F. Guillermet, and M. Sade, “Phase stability and fcc/hcp martensitic transformation in Fe–Mn–Si alloys Part I. Experimental study and systematics of the M and A temperatures,” *J. Alloys Compd.*, vol. 278, pp. 231–238, 1998.

[103] A. Saeed-Akbari, “Mechanism Maps, Mechanical Properties, and Flow Behavior in High-Manganese TRIP/TWIP and TWIP Steels", Ph.D. dissertation, RWTH Aachen Germany.

[104] R. L. Miller, “Ultrafine-grained microstructures and mechanical properties of alloy steels,” *Metall. Trans.*, vol. 3, no. 4, pp. 905–912, 1972.

[105] P. J. Gibbs, E. De Moor, M. J. Merwin, B. Clausen, J. G. Speer, and D. K. Matlock, “Austenite stability effects on tensile behavior of manganese-enriched- austenite transformation-induced plasticity steel,” *Metall. Mater. Trans. A Phys. Metall. Mater. Sci.*, vol. 42, no. 12, pp. 3691–3702, 2011.

[106] J. Chen, M. Lv, S. Tang, Z. Liu, and G. Wang, “Correlation between mechanical properties and retained austenite characteristics in a low-carbon medium manganese alloyed steel plate,” *Mater. Charact.*, vol. 106, pp. 108–111, 2015.

[107] H. Luo, J. Shi, C. Wang, W. Cao, X. Sun, and H. Dong, “Experimental and numerical analysis on formation of stable austenite during the intercritical annealing of 5Mn steel,” *Acta Mater.*, vol. 59, no. 10, pp. 4002–4014, 2011.

[108] S. Lee and B. C. De Cooman, “Influence of Carbide Precipitation and Dissolution on the Microstructure of Ultra-Fine-Grained Intercritically Annealed Medium Manganese Steel,” *Metall. Mater. Trans. A Phys. Metall. Mater. Sci.*, vol. 47, no. 7, pp. 3263–3270, 2016.

[109] J. Han, S.-J. Lee, J.-G. Jung, and Y.-K. Lee, “The effects of the initial martensite microstructure on the microstructure and tensile properties of intercritically annealed Fe–9Mn–0.05C steel,” *Acta Mater.*, vol. 78, pp. 369–377, 2014.

[110] J. Han and Y. K. Lee, “The effects of the heating rate on the reverse transformation mechanism and the phase stability of reverted austenite in medium Mn steels,” *Acta Mater.*, vol. 67, pp. 354–361, 2014.

[111] F. Danoix, X. Sauvage, D. Huin, L. Germain, and M. Gouné, “A direct evidence of solute interactions with a moving ferrite/austenite interface in a model Fe-C-Mn alloy,” *Scr. Mater.*, vol. 121, pp. 61–65, 2016.

[112] H. Kamoutsi, E. Gioti, G. N. Haidemenopoulos, Z. Cai, and H. Ding, “Kinetics of Solute Partitioning During Intercritical Annealing of a Medium-Mn Steel,” *Metall. Mater. Trans. A*, vol. 46, no. 11, pp. 4841–4846, 2015.

[113] J. B. Seol, D. Raabe, P. Choi, H. S. Park, J. H. Kwak, and C. G. Park, “Direct evidence for the formation of ordered carbides in a ferrite-based low-density Fe-Mn-Al-C alloy studied by transmission electron microscopy and atom probe tomography,” *Scr. Mater.*, vol. 68, no. 6, pp. 348–353, 2013.

[114] D. Raabe *et al.*, “Grain boundary segregation engineering in metallic alloys: A pathway to the design of interfaces,” *Curr. Opin. Solid State Mater. Sci.*, vol. 18, no. 4, pp. 253–261, 2014.

[115] S. Lee, S. J. Lee, and B. C. De Cooman, “Reply to comments on ‘austenite stability of ultrafine-grained transformation-induced plasticity steel with Mn partitioning,’” *Scr. Mater.*, vol. 66, no. 10, pp. 832–833, 2012.

[116] B. B. He, H. W. Luo, and M. X. Huang, “Experimental investigation on a novel medium Mn steel combining transformation-induced plasticity and twinning-induced plasticity effects,” *Int. J. Plast.*, vol. 78, pp. 173–186, 2016.

[117] S. Curtze, V. T. Kuokkala, M. Hokka, and P. Peura, “Deformation behavior of TRIP and DP steels in tension at different temperatures over a wide range of strain rates,” *Mater. Sci. Eng. A*, vol. 507, no. 1–2, pp. 124–131, 2009.

[118] G. B. Olson and M. Cohen, “A mechanism for the nucleation of strain-induced martensitic transformations* nucleation of,” *J. LessCommon Met.*, vol. 28, no. 1, pp. 107–118, 1972.

[119] D. Koistinen and R. Marburger, “A General Equation Prescribing the Extent of the Austenite-Martensite Transformation in Pure Iron-Carbon Alloys and Plain Carbon Steels,” *Acta Metall.*, vol. 7, no. 1, pp. 59–60, 1959.

[120] J. Mahieu, J. Maki, B. De Cooman, and S. Claessens, “Phase Transformation and Mechanical Properties of Si-Free CMnAl Transformation-Induced Plasticity-Aided Steel,” *Metall. Mater. Trans. A*, vol. 33, pp. 2573–2580, 2002.

[121] E. De Moor, D. K. Matlock, J. G. Speera, and M. J. Merwin, “Austenite stabilization through manganese enrichment,” *Scr. Mater.*, vol. 64, no. 2, pp. 185–188, 2011.

[122] E. De Moor, S. Kang, J. G. Speer, and D. K. Matlock, “Manganese Diffusion in Third Generation Advanced High Strength Steels,” *Proc. Int. Conf. Mining, Mater. Metall. Eng.*, pp. 1–7, 2014.

[123] R. Richman and G. Bolling, “Stress, Deformation, and Martensitic Transformation,” *Metall. Trans.*, vol. 2, p. 2451-2462, 1971.

[124] B. C. De Cooman, P. Gibbs, S. Lee, and D. K. Matlock, “Transmission electron microscopy analysis of yielding in ultrafine-grained medium Mn transformation-induced plasticity steel,” *Metall. Mater. Trans. A Phys. Metall. Mater. Sci.*, vol. 44, no. 6, pp. 2563–2572, 2013.

[125] G. B. Olson and M. Cohen, “Kinetics of strain-induced martensitic nucleation,” *Metall. Trans. A*, vol. 6, no. 3, pp. 791–795, 1975.

[126] J. A. Venables, “The Martensite Transformation in Stainless Steel,” *Philos. Mag.*, vol. 7, no. 73, pp. 35–44, 1962.

[127] R. Lagneborg, “The Martensite Transformation in 18% Cr-8% Ni Steels,” *Acta Metall.*, vol. 12, no. 7, pp. 823 – 843, 1964.

[128] P. L. Mangonon and G. Thomas, “The Martensite Phases in 304 Stainless Steel,” *Metall. Trans.*, vol. 1, no. 6, pp. 1577–1586, 1970.

[129] F. Lecroise and a Pineau, “Martensitic Transformations Induced By Plastic-Deformation in Fe-Ni-Cr-C System,” *Metall. Trans.*, vol. 3, pp. 387–396, 1972.

[130] R. T. van Tol, “Microstructural Evolution in Deformed Austenitic Twinning Induced Plasticity Steels”, Ph.D. dissertation, Delft University, 2014.

[131] S. Lee, S. J. Lee, S. Santhosh Kumar, K. Lee, and B. C. D. Cooman, “Localized deformation in multiphase, ultra-fine-grained 6 Pct Mn transformation-induced plasticity steel,” *Metall. Mater. Trans. A Phys. Metall. Mater. Sci.*, vol. 42, no. 12, pp. 3638–3651, 2011.

[132] S. Lee, K. Lee, and B. C. de Cooman, “Observation of the TWIP + TRIP Plasticity-Enhancement Mechanism in Al-Added 6 Wt Pct Medium Mn Steel,” *Metall. Mater. Trans. A Phys. Metall. Mater. Sci.*, pp. 1–8, 2015.

[133] C. Wang, W. Cao, J. Shi, C. Huang, and H. Dong, “Deformation microstructures and strengthening mechanisms of an ultrafine grained duplex medium-Mn steel,” *Mater. Sci. Eng. A*, vol. 562, pp. 89–95, 2013.

[134] M. C. McGrath, D. C. Van Aken, N. I. Medvedeva, and J. E. Medvedeva, “Work hardening behavior in steel with multiple TRIP mechanisms,” *Metall. Mater. Trans. A Phys. Metall. Mater. Sci.*, vol. 44, no. 10, pp. 4634–4643, 2013.

[135] I. Gutierrez-Urrutia and D. Raabe, “Grain size effect on strain hardening in twinning-induced plasticity steels,” *Scr. Mater.*, vol. 66, no. 12, pp. 992–996, 2012.

[136] G.E. Dieter, *Mechanical Metallurgy*, 3rd ed. Boston: McGraw-Hill, 1986.

[137] V. Kandarpa and J. W. Spretnak, “Internal Friction from Stress-Induced Ordering of Carbon Atoms in Austenitic Manganese Steels,” *Trans. Metall. Soc. AIME,* vol. 245, pp. 1439–1442, 1969.

[138] J. M. Robinson and M. P. Shaw, “Microstructural and Mechanical Influences on Dynamic Strain Aging Phenomena,” *Int. Mater. Rev.*, vol. 39, no. 3, pp. 113–122, 1994.

[139] S. T. Mileiko, “The tensile strength and ductility of continuous fibre composites,” *J. Mater. Sci.*, vol. 4, pp. 974–977, 1969.

[140] A. Ma and A. Hartmaier, “A study of deformation and phase transformation coupling for TRIP-assisted steels,” *Int. J. Plast.*, vol. 64, pp. 40–55, 2015.

[141] M. I. Latypov, S. Shin, B. C. De Cooman, and H. S. Kim, “Micromechanical finite element analysis of strain partitioning in multiphase medium manganese TWIP+TRIP steel,” *Acta Mater.*, vol. 108, pp. 219–228, 2016.

[142] O. Bouaziz and P. Buessler, “Iso-work Increment Assumption for Heterogeneous Material Behaviour Modelling,” *Adv. Eng. Mater.*, vol. 6, no. 12, pp. 79–83, 2004.

[143] S. Lee, Y. Estrin, and B. C. De Cooman, “Constitutive modeling of the mechanical properties of V-added medium manganese TRIP steel,” *Metall. Mater. Trans. A Phys. Metall. Mater. Sci.*, vol. 44, no. 7, pp. 3136–3146, 2013.

[144] M. Borsutzki, D. Cornette, Y. Kuriyama, A. Uenishi, B. Yan, and E. Opbroek, “Recommendations for Dynamic Tensile Testing of Sheet Steels,” *Int. Iron Steel Inst.*, 2005.

[145] A. Khosravifard, “Influence of High Strain Rates on the Mechanical Behavior of High Manganese Steels Abstra,” *Iranian J Mater Forming*, vol. 1, no. 1, pp. 1–10, 2014.

[146] S. Curtze, “Characterization of the Dynamic Behavior and Microstructure Evolution of High Strength Sheet Steels", Ph.D. dissertation, Tampere University of Technology, 2009.

[147] H. Mecking and U. F. Kocks, “Kinetics of flow and strain hardening,” *Acta Met.*, vol. 29, pp. 1865–1875, 1981.

[148] G. T. (Rusty) Gray, “High-Strain-Rate Deformation: Mechanical Behavior and Deformation Substructures Induced,” *Annu. Rev. Mater. Res.*, vol. 42, no. 1, pp. 285–303, 2012.

[149] D. Hull and D. J. Bacon, *Introduction to Dislocations,* 5th ed. Amsterdam: Elsevier (Butterworth- Heinemann), 2011.

[150] M. A. Meyers, *Dynamic Behavior of Materials,*New York: John Wiley & Sons. 1994.

[151] J. D. Campbell and W. G. Ferguson, “The Temperature and Strain-Rate Dependence of the Shear Strength of Mild Steel,” *Philos. Mag.*, vol. 169, no. 63–82, 1970.

[152] W. S. Lee and T. H. Chen, “Plastic deformation and fracture characteristics of Hadfield steel subjected to high velocity impact loading,” *Proc. Inst. Mech. Engrs.*, vol. 216, pp. 971–982, 2002.

[153] D. Bruce, “Dynamic Tensile Testing of Sheet Steels and Influence of Strain Rate on Strengthening Mechanisms in Sheet Steels" Ph.D. dissertation, Colorado School Mines, 2003.

[154] H. Huh, K. Ahn, J. H. Lim, H. W. Kim, and L. J. Park, “Evaluation of dynamic hardening models for BCC, FCC, and HCP metals at a wide range of strain rates,” *J. Mater. Process. Technol.*, vol. 214, no. 7, pp. 1326–1340, 2014.

[155] B. Strnadel and J. Brumek, “Effect of Tensile Test Specimen Size on Ductility of R7T Steel,” *Materials and Fabrication*, vol. 5, no. 2, pp. 2–7, 2013.

[156] D. R. Malpally, “Uncertainty Analysis of Mechanical Properties From Miniature Tensile Testing of High Strengh Steels”, Ph.D. dissertation Utah State University, 2014.

[157] X. Sun, A. Soulami, K. S. Choi, O. Guzman, and W. Chen, “Effects of sample geometry and loading rate on tensile ductility of TRIP800 steel,” *Mater. Sci. Eng. A*, vol. 541, pp. 1–7, 2012.

[158] W. J. Yuan, Z. L. Zhang, Y. J. Su, L. J. Qiao, and W. Y. Chu, “Influence of specimen thickness with rectangular cross-section on the tensile properties of structural steels,” *Mater. Sci. Eng. A*, vol. 532, pp. 601–605, 2012.

[159] K. Wang, D. Wang, and F. Han, “Effect of sample thickness on the tensile behaviors of Fe-30Mn-3Si-3Al twinning-induced plasticity steel,” *Mater. Sci. Eng. A*, vol. 642, pp. 249–252, 2015.

[160] I. F. Rajendran, “Inertia Effects on the Ductile Failure of Thin Rings,” *J. App. Mechs.*, vol. 49, pp. 31–36, 1982.

[161] I. Choi, S. Lee, D. K. Matlock, and J. G. Speer, “Strain Control during High Speed Tensile Testing,” *J. Test. Eval.*, vol. 34, no. 5, pp. 5–8, 2006.

[162] Y. Gao, C. Xu, Z. ping He, Y. lin He, and L. Li, “Response characteristics and adiabatic heating during high strain rate for TIRP steel and DP steel,” *J. Iron Steel Res. Int.*, vol. 22, no. 1, pp. 48–54, 2015.

[163] K. D. Clarke, R. J. Comstock, M. C. Mataya, C. J. Tyne, and D. K. Matlock, “Effect of strain rate on the yield stress of ferritic stainless steels,” *Metall. Mater. Trans. A Phys. Metall. Mater. Sci.*, vol. 39 A, pp. 752–762, 2008.

[164] P. Rodriguez, “Serrated Plastic Flow,” *Bull. Mater. Sci.*, vol. 6, no. 4, pp. 653–663, 1984.

[165] M. C. McGrath, D. C. Van Aken, N. I. Medvedeva, and J. E. Medvedeva, “Work hardening behavior in steel with multiple TRIP mechanisms,” *Metall. Mater. Trans. A Phys. Metall. Mater. Sci.*, vol. 44, no. 10, pp. 4634–4643, 2013.

[166] “E112-10.pdf,” in *ASTM Designation E112-10*, West Conshohocken, PA: ASTM International, 2011.

[167] J. R. Johnson, “Developing the Axisymmetric Expanding Ring: A High Strain-Rate Materials Characterization Test,” Ph.D. dissertation, The Ohio State University, pp. 1–169, 2014.

[168] L. Addessio, “The Effect of Strain Rate and Tempering on the Mechanical Properties of Low Carbon Martensite,” M.S. Thesis, Colorado School of Mines, 2007.

[169] E. Whitenton, “The NIST Kolsky Bar Data Processing System Society for Experimental Mechanics Annual Conference 2005,” *Soc. Exp. Mech. Annu. Conf.*, Portland, OR, 2005.

[170] X. Yang, L. G. Hector, and J. Wang, “A Combined Theoretical / Experimental Approach for Reducing Ringing Artifacts in Low Dynamic Testing with Servo-hydraulic Load Frames,” *Exp. Mech.*, vol. 54, pp. 775–789, 2014.

[171] D. B. Williams and C. Barry Carter, *Transmission Electron Microscopy - A Textbook for Materials Science*. 2nd edition, New York: Springer, 2009.

[172] D. R. Steinmetz and S. Zaefferer, “Towards ultrahigh resolution EBSD by low accelerating voltage,” *Mater. Sci. Technol.*, vol. 26, no. 6, pp. 640–645, 2010.

[173] I. Gutierrez-Urrutia, S. Zaefferer, and D. Raabe, “Coupling of electron channeling with EBSD: Toward the quantitative characterization of deformation structures in the SEM,” *JOM*, vol. 65, no. 9, pp. 1229–1236, 2013.

[174] S. Zaefferer, “On the formation mechanisms, spatial resolution and intensity of backscatter Kikuchi patterns,” *Ultramicroscopy*, vol. 107, no. 2–3, pp. 254–266, 2007.

[175] I. Gutierrez-Urrutia, S. Zaefferer, and D. Raabe, “Electron channeling contrast imaging of twins and dislocations in twinning-induced plasticity steels under controlled diffraction conditions in a scanning electron microscope,” *Scr. Mater.*, vol. 61, no. 7, pp. 737–740, 2009.

[176] S. Zaefferer and N. N. Elhami, “Theory and application of electron channelling contrast

imaging under controlled diffraction conditions,” *Acta Mater.*, vol. 75, no. 154, pp. 20–50, 2014.

[177] J. M. Sosa, D. E. Huber, B. Welk, and H. L. Fraser, *Integr. Mater. Manuf. Innov.*, vol. 3, p. 18, 2014.

[178] B. D. Cullity and S. R. Stock, *Elements of X-Ray Diffraction*, 3rd ed. Pearson, 2001.

[179] C. Ophus, J. Ciston, and C. T. Nelson, “Correcting nonlinear drift distortion of scanning probe and scanning transmission electron microscopies from image pairs with orthogonal scan directions,” *Ultramicroscopy*, vol. 162, pp. 1–9, 2016.

[180] A. Belianinov, Q. He, M. Kravchenko, S. Jesse, A. Borisevich, and S. V. Kalinin, “Identification of phases, symmetries and defects through local crystallography,” *Nat. Commun.*, vol. 6, p. 7801, 2015.

[181] S. Curtze and V. T. Kuokkala, “Dependence of tensile deformation behavior of TWIP steels on stacking fault energy, temperature and strain rate,” *Acta Mater.*, vol. 58, no. 15, pp. 5129–5141, 2010.

[182] S. M. Cotes, a. F. Guillermet, and M. Sade, “Fcc/Hcp martensitic transformation in the Fe-Mn system: Part II. Driving force and thermodynamics of the nucleation process,” *Metall. Mater. Trans. A*, vol. 35, no. 1, pp. 83–91, 2004.

[183] I. C. Jung and B. C. De Cooman, “Temperature dependence of the flow stress of Fe-18Mn-0.6C-xAl twinning-induced plasticity steel,” *Acta Mater.*, vol. 61, no. 18, pp. 6724–6735, 2013.

[184] M. Borsutzki, D. Cornette, Y. Kuriyama, A. Uenishi, B. Yan, and E. Opbroek, “Recommendations for Dynamic Tensile Testing of Sheet Steels,” *Intern. Iron Steel Inst.*, 2005.

[185] K. D. Clarke, “Influence of Strain Rate on the Mechanical Properties and Formability of Ferritic Stainless Steel,” M.S. Thesis, Colorado School of Mines, 2002.

[186] J. W. Christian and S. Mahajan, *Prog. Mater. Sci.*, vol. 39, pp. 1–157, 1995.

[187] N. Li *et al.*, “Localized amorphism after high-strain-rate deformation in TWIP steel,” *Acta Mater.*, vol. 59, no. 16, pp. 6369–6377, 2011.

[188] A. Saeed-Akbari, A. K. Mishra, J. Mayer, and W. Bleck, “Characterization and prediction of flow behavior in high-manganese twinning induced plasticity steels: Part II. Jerky flow and instantaneous strain rate,” *Metall. Mater. Trans. A Phys. Metall. Mater. Sci.*, vol. 43, no. 5, pp. 1705–1723, 2012.

[189] P. Sahu, S. Curtze, A. Das, B. Mahato, V. T. Kuokkala, and S. G. Chowdhury, “Stability

of austenite and quasi-adiabatic heating during high-strain-rate deformation of twinning-induced plasticity steels," *Scr. Mater.*, vol. 62, no. 1, pp. 5–8, 2010.

[190] C. M. Sellars and W. J. Tegard, ".," *Mem. Sci. Rev. Met.*, vol. 63, p. 731-746, 1966.

[191] Y. Ha, H. Kim, K. H. Kwon, S. G. Lee, S. Lee, and N. J. Kim, "Microstructural Evolution in Fe-22Mn-0.4C Twinning-Induced Plasticity Steel During High Strain Rate Deformation," *Metall. Mater. Trans. A Phys. Metall. Mater. Sci.*, vol. 46, no. 2, pp. 545–548, 2014.

[192] L. Yang and L. Lu, "The influence of sample thickness on the tensile properties of pure Cu with different grain sizes," *Scr. Mater.*, vol. 69, no. 3, pp. 242–245, 2013.

[193] Y. H. Zhao *et al.*, "Influence of specimen dimensions on the tensile behavior of ultrafine-grained Cu," *Scr. Mater.*, vol. 59, no. 6, pp. 627–630, 2008.

[194] R. W. Hertzberg, "Deformation and Fracture Mechanics of Engineering Materials." John Wiley and Sons, Hoboken, NJ, p. 810, 1996.

[195] U. F. Kocks and H. Mecking, "Physics and phenomenology of strain hardening: The FCC case," *Prog. Mater. Sci.*, vol. 48, no. 3, pp. 171–273, 2003.

[196] Y. F. Shen, N. Jia, R. D. K. Misra, and L. Zuo, "Softening behavior by excessive twinning and adiabatic heating at high strain rate in a Fe-20Mn-0.6C TWIP steel," *Acta Mater.*, vol. 103, pp. 229–242, 2016.

[197] V. Tari, A. D. Rollett, H. El Kadiri, H. Beladi, A. L. Oppedal, and R. L. King, "The effect of deformation twinning on stress localization in a three dimensional TWIP steel microstructure," *Model. Simul. Mater. Sci. Eng.*, vol. 23, no. 4, p. 45010, 2015.

[198] C.S. Barett and T.B. Massalski, *Structure of Metals*, 3rd edition. McGraw-Hill, 1966.

[199] M. K. Miller, *Atom Probe Tomography*, 1st ed. Springer US, 2000.

[200] O. Dmitrieva, P. Choi, S. S. A. Gerstl, D. Ponge, and D. Raabe, "Pulsed-laser atom probe studies of a precipitation hardened maraging TRIP steel," *Ultramicroscopy*, vol. 111, no. 6, pp. 623–627, 2011.

[201] J.J. Hren , J.I. Goldstein, and D. Joy, *Introduction to Analytical Electron Microscopy*. New York, NY: Plenum Press, 1979.

[202] P.J. Goodhew, J. Humphreys, and R. Benaland, *Electron Microscopy and Analysis*, Third. London: Taylor & Francis, 2001.

[203] E. J. Seo, L. Cho, and B. C. De Cooman, "Kinetics of the partitioning of carbon and substitutional alloying elements during quenching and partitioning (Q&P) processing of

medium Mn steel," *Acta Mater.*, vol. 107, pp. 354–365, 2016.

[204] A. Kwiatkowski da Silva, G. Inden, A. Kumar, D. Ponge, B. Gault, and D. Raabe, "Competition between formation of carbides and reversed austenite during tempering of a medium-manganese steel studied by thermodynamic-kinetic simulations and atom probe tomography," *Acta Mater.*, vol. 147, no. February, pp. 165–175, 2018.

[205] J. Chen, M. Yang Lv, Z. Yu Liu, and G. Dong Wang, "Combination of ductility and toughness by the design of fine ferrite/tempered martensite-austenite microstructure in a low carbon medium manganese alloyed steel plate," *Mater. Sci. Eng. A*, vol. 648, pp. 51–56, 2015.

[206] S. Lee, S. J. Lee, and B. C. De Cooman, "Work hardening behavior of ultrafine-grained Mn transformation-induced plasticity steel," *Acta Mater.*, vol. 59, no. 20, pp. 7546–7553, 2011.

[207] J. T. Benzing, W.A. Poling, D.T. Pierce, J. Bentley, K.O. Findley, D. Raabe and J.E. Wittig , "Effects of strain rate on mechanical properties and deformation behavior of an austenitic Fe-25Mn-3Al-3Si TWIP-TRIP steel," *Mater. Sci. Eng. A*, vol. 711, pp. 78–92, 2018.

[208] M. Stout, K. Staudhammer, J. Smith, and S. Hecker, "Effects of strain rate on deformation-induced transformation in 304 Stainless Steel: Part 1. Magnetic Measurements and Mechanical Behavior," *Metall. Trans. A*, vol. 13A, 1982.

[209] G. I. Taylor, "Plastic strain in metals," *J. Inst. Met.*, vol. 62, pp. 307–324, 1938.

[210] O. Bouaziz, S. Allain, and C. Scott, "Effect of grain and twin boundaries on the hardening mechanisms of twinning-induced plasticity steels," *Scr. Mater.*, vol. 58, no. 6, pp. 484–487, 2008.

[211] C. Y. Sun, N. Guo, M. W. Fu, and S. W. Wang, "Modeling of slip, twinning and transformation induced plastic deformation for TWIP steel based on crystal plasticity," *Int. J. Plast.*, vol. 76, pp. 186–212, 2016.

[212] A. S. J. Suiker and S. Turteltaub, "Computational modelling of plasticity induced by martensitic phase transformations," *Int. J. Numer. Methods Eng.*, vol. 63, no. 12, pp. 1655–1693, 2005.

[213] I. J. Beyerlein and C. N. Tomé, "A dislocation-based constitutive law for pure Zr including temperature effects," *Int. J. Plast.*, vol. 24, no. 5, pp. 867–895, 2008.

[214] R. Madec, B. Devincre, and L. P. Kubin, "From Dislocation Junctions to Forest Hardening," *Phys. Rev. Lett.*, vol. 89, no. 25, p. 255508, 2002.

[215] P. Hu, Y. Liu, Y. Zhu, and L. Ying, "Crystal plasticity extended models based on thermal

mechanism and damage functions: Application to multiscale modeling of aluminum alloy tensile behavior," *Int. J. Plast.*, vol. 86, pp. 1–25, 2016.

[216] Q. Wei, S. Cheng, K. T. Ramesh, and E. Ma, "Effect of nanocrystalline and ultrafine grain sizes on the strain rate sensitivity and activation volume: Fcc versus bcc metals," *Mater. Sci. Eng. A*, vol. 381, no. 1–2, pp. 71–79, 2004.

[217] C. García de Andrés, F. G. Caballero, C. Capdevila, and H. K. D. H. Bhadeshia, "Modelling of kinetics and dilatometric behavior of non-isothermal pearlite-to-austenite transformation in an eutectoid steel," *Scr. Mater.*, vol. 39, no. 6, pp. 791–796, 1998.

[218] M. Takahashi, "Reaustenisation of bainite" Ph.D. dissertation, Cambridge University, 1992.